A MODEL FOR TIME-INDEPENDENT AND TIME-DEPENDENT DAMAGE EVOLUTION AND THEIR INFLUENCE ON CREEP OF MULTIDIRECTIONAL POLYMER COMPOSITE LAMINATES

By

AMIR ASADI

A Thesis submitted to the Faculty of Graduate Studies of the University of Manitoba in partial fulfillment of the requirements of the degree of

DOCTOR OF PHILOSOPHY

Department of Mechanical and Manufacturing Engineering

University of Manitoba

Winnipeg, Manitoba, Canada

ABSTRACT

Application of polymer matrix composites in engineering structures has been steadily increasing over the past five decades. Multidirectional polymer composites are one class of continuous fiber reinforced polymer matrix composites used in aerospace structures, where the desired mechanical performance outweighs the cost. Their modulus and strength degrade with time (known as creep and creep rupture) during the service, owing to the viscos-elasticity of the polymer matrix. Additional contribution to this degradation comes from various damage modes developed in the plies of the composite with time and identified in this thesis as TDD (Time Dependent Damage). These damage modes may also develop due to process-induced residual stresses, and during loading to the service load, identified as TID (Time Independent Damage). TID influences the TDD, the creep and the creep rupture. The objective of this thesis is to develop a model to predict the evolution of TID and TDD in multiple plies of a laminate and their influence on creep. The predominant damage mode, transverse cracking, is modeled in this study. The model consists of four modules, PIS, QSL, SL, and VA. The PIS, QSL, and SL moduli predict changes in ply stresses for incremental change in temperature, stress, and time respectively, using lamination theory and assuming linear elastic behavior of the plies during an incremental step. In parallel, each module predicts the stored elastic energy in each ply after each incremental step and compares it with a critical stored elastic energy criterion to determine if a ply would crack. If fracture is predicted, the VA module based on variational analysis, is invoked to determine the crack density and the perturbation in ply stresses due to cracking. The perturbation stresses are used by the module that invoked the VA module to determine the ply stresses after cracking during the current incremental step. The model predictions for a $[\pm 45/90]_s$

laminate, at two test temperatures (80°C and 180°C) and four stresses in the range of 20–54 MPa, compare very well with experimental results validating the model.

ACKNOWLEDGEMENT

I would like to express my sincere gratitude to my advisor **Dr. Raghavan Jayaraman**, for his invaluable guidance and academic support throughout my research work.

I would like to thank **Abhishek Gupta** for training me on composite manufacturing and working with various instruments in the composites laboratory. I would also thank **Mike Boskwick** and **Kim Majury** for their technical assistance during my research.

Finally, my very special thanks to **my wife, Dorrin,** and **my family** and **friends** for their constant support and encouragement during my Ph.D.

TABLE OF CONTENTS

LIST OF FIGURES

LIST OF TABLES

LIST OF SYMBOLS

θ: orientation of a fiber in a laminate with respect to the loading direction (x-axis)

m: cos (θ)

n: sin (θ)

$\sigma_{xx,a}$: applied stress

σ_{creep}: creep stress

$\sigma_{jl}^{(k)}$: stress in ply (k) where j, l=x, y, z or j, l=1, 2, 6

$\sigma_{jl}^{P(k)}$: perturbation stress in ply (k) where j, l=x, y, z

ε_{xx}: laminate strain

$\varepsilon_{jl}^{(k)}$: strain state in ply (k) j, l=x, y, z or j, l=1, 2, 6

$e_{jl}^{(k)}$: unconstrained strain

$\varphi^{(k)}$: axial stress perturbation in ply (k)

$\eta^{(k)}$: transverse stress perturbation in ply (k)

$\psi^{(k)}$: shear stress perturbation in ply (k).

$[Q]^{(k)}$: stiffness matrix of ply (k). $[Q]_{1,2}$ along principal direction and $[Q]_{x,y}$ along global directions

$[S]^{(k)}$: compliance matrix of ply (k). $[S]_{1,2}$ along principal direction and $[S]_{x,y}$ along global directions

$[A]_{x,y}$: Stiffness matrix of the laminate along global coordinates

$[a]_{x,y}$: Compliance matrix of the laminate along global coordinates

$[T]$: Transformation matrix

N_{jl}: resultant force per unit length acting on the laminate, where j, l=x, y

M_{jl}: resultant moment per unit length acting on on the laminate, where j, l=x, y

$a^{(k)}$: half of the distance between two neighboring cracks in ply (k)

L: laminate length

h: half the thickness of the laminate

th_k: thickness of ply (k).

$\lambda^{(k)}$: crack density in ply (k)

$reg^{(k)}$: number of intact regions in ply (k)

$n^{(k)}$: number of cracks in ply (k)

$E_{jl}^{(k)}$: longitudinal or transverse modulus of ply (k) where j=l=1,2, 3 or j=l=x, y, z

$G_{jl}^{(k)}$: shear modulus of ply (k) where j, l=1, 2 or j, l=x, y, z

$v_{jl}^{(k)}$: Poisson's ratio of ply (k) where j, l=1, 2 or j, l=x, y, z

α_{jl}: coefficient of thermal expansion where j=l=1, 2

α_{jl}: Cure shrinkage coefficient where j=l=2

E_0: instantaneous modulus

E_R: rubbery modulus

E_v: viscous modulus

U_c: complementary energy

U_c^0: complementary energy of uncracked body

U_c^P: complementary energy resulting from perturbation stresses

T: temperature

t: time

E_{act}: activation energy.

R: gas constant (8.314 J/K.mole).

g_0, g_1, g_2, a_σ: nonlinear parameters in Schapery's nonlinear viscoelastic model.

ρ: density.

CHAPTER 1. INTRODUCTION

A composite material consists of two or more number of constituents and has properties better than either of its constituents. Advanced composite materials have been used for engineering structures for over 60 years. Their use in structural application has been steadily increasing owing to high specific properties and resistance to corrosion when compared to metals. Polymer composite consists of polymer matrix reinforced with high strength and high modulus fibers. A large number of available choices in fiber, resin, fiber arrangement and manufacturing method has made these composites very attractive for use in a variety of engineering applications such as military, aerospace, automotive, wind energy, civil infrastructure, building materials, and recreation and sports equipment.

1.1 Background

Based on the geometry of the reinforcement, polymer composites can be classified as particulate, discontinuous, or continuous fiber composites, as illustrated in Figure 1-1. Randomly dispersed reinforcements with aspect ratio, L/D (L: fiber length, D: fiber diameter) of 1 to 20 result in particulate composite. Discontinuous fiber composites contain short fibers with an aspect ratio of 20 to 1000, whereas continuous fiber composites contain fibers with an aspect ratio greater than 1000. Continuous fiber composites are used in structural applications in aerospace industry, where the desired mechanical performance outweighs the cost. Continuous fiber composites are further divided into two categories based on the fiber architecture, non-woven and woven (also known as textile) composite.

Aerospace composites are laminates made from lamina, which is a single layer of

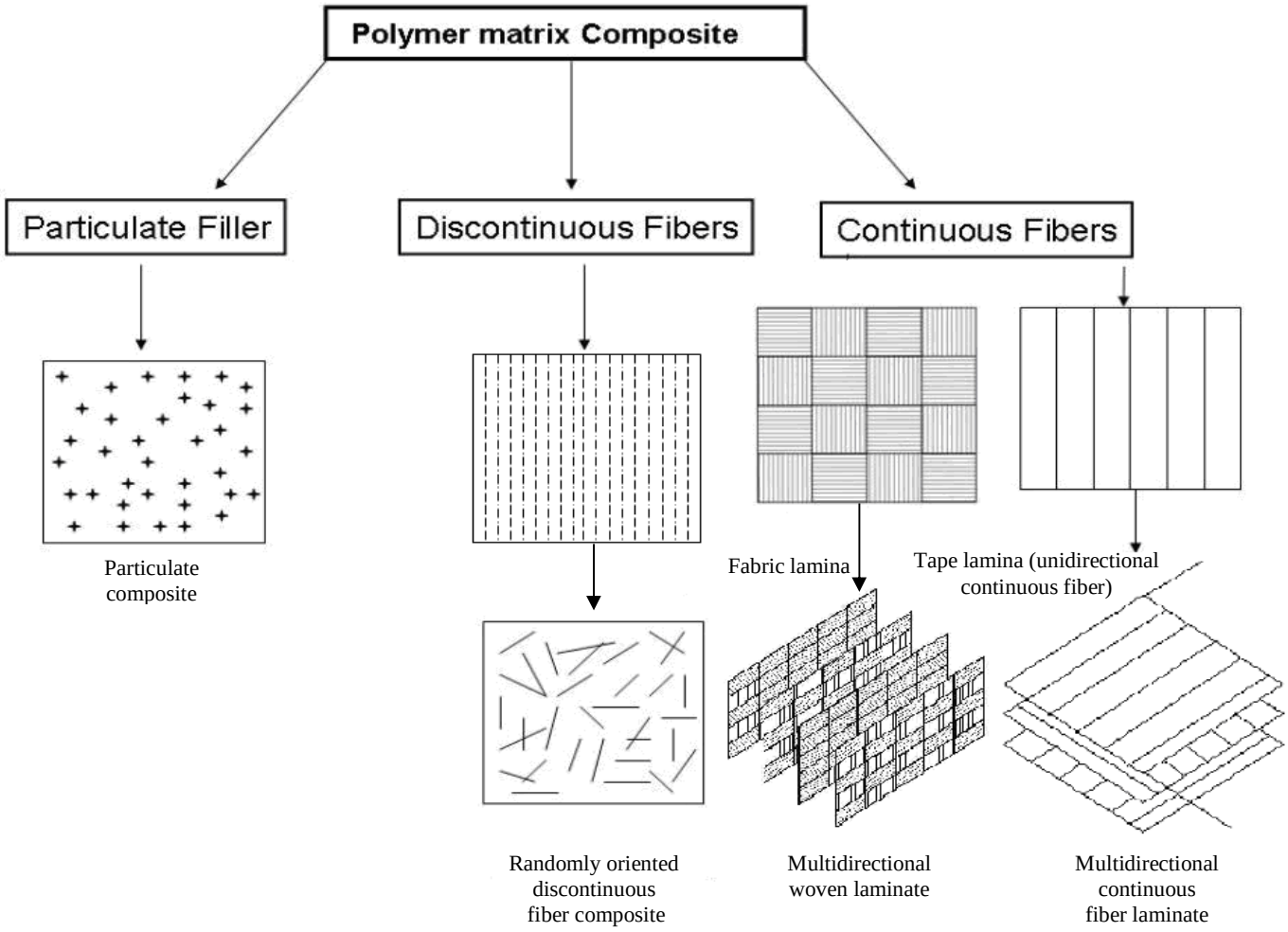

Figure 1-1 Classification of polymer matrix composites

continuous fibers impregnated with polymer resin. Unidirectional continuous fiber composite laminates may consist of more than one lamina, but the orientation of the fiber with respect to the loading direction will be the same in all layers. Multidirectional composites are laminates of unidirectional lamina layers; however, fiber orientation in each layer varies, as illustrated in Figure 1-1.

An uncured lamina is known as a pre-preg (pre-impregnated). The multidirectional composite laminate is made by stacking these pre-pregs in desired orientations and laminating them under heat and pressure in an autoclave (for aerospace applications). The pre-preg is classified based on the fiber arrangement:

a) Tape Pre-preg: A tape pre-preg is a single layer of parallel fibers impregnated with resin, as shown in Figure 1-1.

b) Fabric Pre-preg: A fabric pre-preg is formed by weaving two fiber rovings (a roving is a bundle of parallel fibers) in orthogonal direction and impregnated with resin, as shown in Figure 1-1. Since the properties of unidirectional composites are anisotropic, these types of composites are not preferred in structural design. In contrast, multidirectional composite laminates have quasi-isotropic properties and are used in engineering structures including aerospace structures. This thesis focuses on multidirectional polymer composites made from tape pre-pregs.

The modulus and strength of a unidirectional lamina will be maximum for an orientation angle of 0^o between the fiber and loading axes (denoted as [0] layer or ply) and minimum for an orientation of 90^o between the fiber and loading axes (denoted as [90] layer or ply). Hence, the modulus and strength of a multidirectional laminate depends on its stacking sequence (i.e. orientation of fibers in each layer with respect to loading direction). During loading, the ply with

least strength will fail first; however, the laminate will not fail at that First Ply Failure (FPF) load since the failure will be constrained by the outer plies with failure loads higher than the FPF load. This will result in a crack in that failed ply. Despite this failure, the failed ply will continue to bear load at locations away from the damage and will fail again (with further increase in load) until the crack density in that ply reaches a Characteristic Damage State (CDS) when the stress in that ply can no longer reach the tensile strength of that ply. With further increase in load, outer plies will crack in a similar fashion, starting with the ply with next least strength. This progressive cracking will result in progressive reduction in laminate modulus, as illustrated in Figure 1-2. The laminate will fail at an Ultimate Laminate Failure (ULF) load when the ply with the highest strength fails. While the FPF results in a conservative design, the ULF results in a pragmatic design. However, the latter requires a reliable model to predict progressive cracking and its effect on the modulus and strength of a laminate.

This damage that develops during quasi-static loading is known as Time-Independent Damage (TID) in this thesis in order to differentiate it from Time-Dependent Damage (TDD) that develops with time under constant creep load.

Various TID modes occur in multidirectional polymer composite laminates. Figure 1-3 shows transverse cracking in [90] and [-45] plies, delamination between [-45] and [+45] plies and vertical cracking in [90] plies of a $[\pm 45/90_2]_s$ laminate.

Polymer matrix composites (PMC) are viscoelastic in nature; i.e., they exhibit both elastic and viscous behavior, owing to the viscoelastic nature of the polymer matrix. Due to viscoelasticity, time-dependent degradation in modulus (creep) and strength (creep rupture) of multidirectional polymer composite laminates during service is a concern in load bearing structures. Various damage modes, observed in Figure 1-3, can also evolve with time in polymer

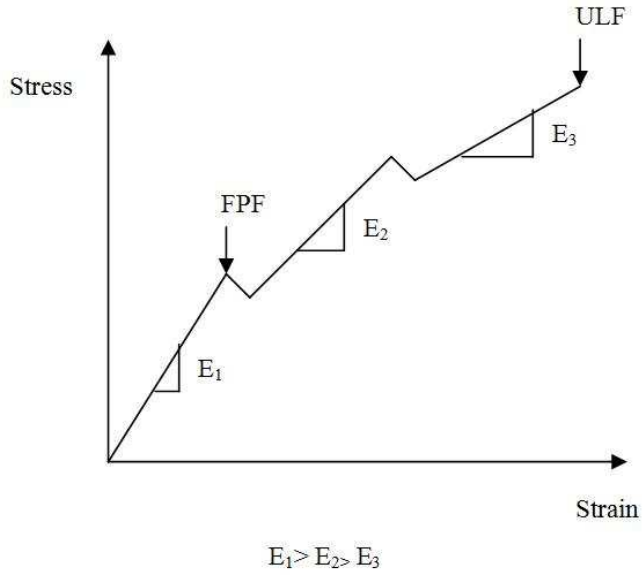

Figure 1-2: Progressive damage during quasi-static testing and its effect on modulus of polymer composites

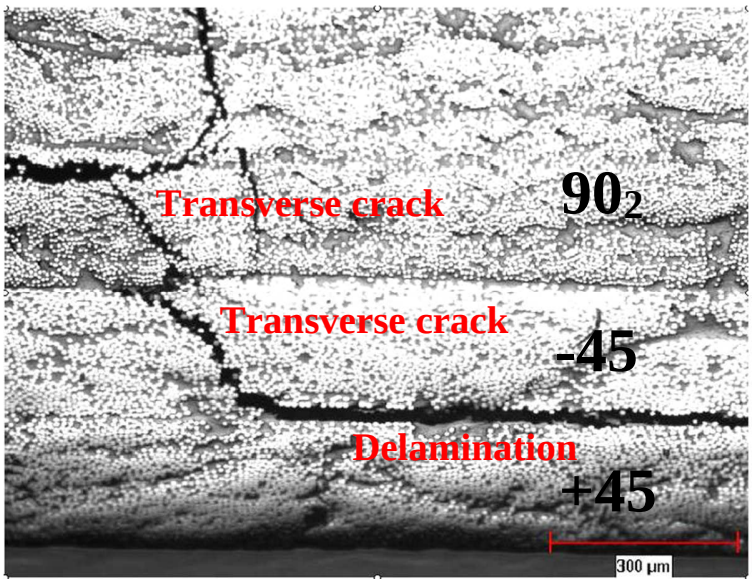

Figure 1-3: Various TID Modes in $[\pm 45/90_2]_s$ [1]

composites due to this viscoelasticity, contributing additionally to the degradation of modulus and strength with time. Dillard et al. [2] observed a discrepancy between their predictions for creep compliance and strength and the experimental results, which was reasoned to be due to extensive damage that developed during testing. Their study was the first study to highlight time-dependent damage evolution.

Balachander [3] demonstrated the influence of TDD on creep of polymer composite laminates by comparing the experimental creep results with predictions that assumed no damage, as shown in Figure 1-4. The predictions based on no-damage ("Lami" in Figure 1-4) do not agree well with experimental results. Since TID developed during loading to creep load, he accounted for its effect on modulus to explain the observed difference. Yet, the difference between the predicted ("Discounted Lami" in Figure 1-4) and experimental results increased with time, suggesting that the damage increased with creep time. Additionally, he also observed the effect of TDD on creep by comparing predictions using "Lami" and "Discounted Lami." However, he did not quantify this time-dependent damage evolution. Birur et al. [1] experimentally quantified the evolution of one damage mode (transverse cracking in [90] plies) in different stress levels with respect to time, as shown in Figure 1-5. However, they did not model its evolution as well as quantify its effect on creep and creep rupture.

Finally, FPF has also been found to be time-dependent [4]. The significance of this would be in conservative designs based on FPF. A laminate can develop damage with time even if the design stress is below FPF [4], resulting in further deterioration of modulus and strength with time.

Previous research (both experimental and theoretical) on TID and its effect on modulus of composite laminates is extensive, and a good review can be found in Ref. [5]. However, very

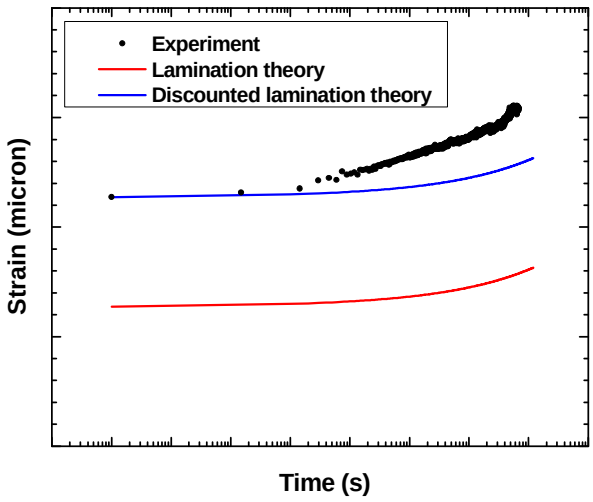

Figure 1-4: Comparison of experimental and predicted creep strain for a quasi-isotropic laminate

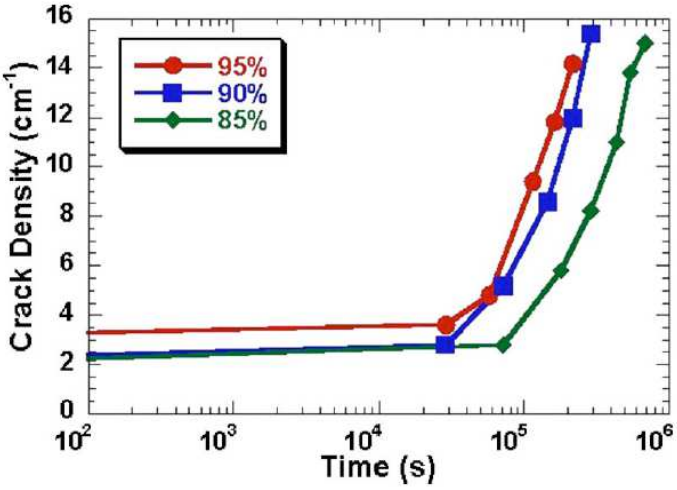

Figure 1-5: Time-dependent evolution of transverse crack density in [90] plies of [0/90/0] laminate at different stress levels at 80°C [1]

little attention has been devoted to modeling of time-dependent damage evolution and the impact of both TID and TDD on creep and creep rupture of multidirectional polymer composite laminates.

1.2 Thesis Scope

Hence, this thesis work is focused on addressing this knowledge gap by developing a model for time-dependent evolution of damage in multiple plies and its influence on creep of multidirectional polymer composite laminates. Since the creep of a laminate is influenced by both TID that develops during loading to a creep load as well as TDD that develops subsequently during creep, the model developed in this thesis accounts for the evolution and effect of both damage categories on creep. This thesis is focused on simultaneous evolution of one damage mode, transverse cracking, in multiple plies of a laminate. The developed analytical model uses the properties of unidirectional lamina (independently measured) and is validated using experimental results, generated under a wide range of stress and temperature, for (I) time-independent and time-dependent evolution of transverse cracking in multiple plies, (II) time-independent and time-dependent modulus, and (III) creep response for a representative laminate.

To the best knowledge of the author, the following outcomes of this thesis are the first in this area:

(a) An analytical model for predicting time-independent evolution of transverse cracking simultaneously in multiple plies of a composite and its influence on modulus.

(b) An analytical model for predicting time-dependent evolution of transverse cracking, simultaneously, in multiple plies of a composite. This model also accounts for process-induced stress and any TID due to this process-induced stress.

(c) An analytical model to predict the creep compliance of a composite with both TID and TDD.

1.3 Organization of Thesis

Chapter 2 includes a thorough review of the published work on categories of damage, creep, creep-rupture, and the effect of damage on creep and creep rupture and discusses both experimental and modeling work. Based on this review, knowledge gaps are identified to define the objectives of this thesis. The model developed in this thesis is presented in Chapter 3. Chapter 4 presents details on experimental procedure and simulation. Model predictions and experimental results are presented, compared, and discussed in Chapter 5. Conclusions and recommendations for further work in this area are presented in Chapter 6.

CHAPTER 2. LITERATURE REVIEW

This chapter provides a concise review of published literature on creep, creep-rupture, time-independent and time-dependent damage in polymer composites, all of which are relevant topics to the research of this thesis. It should be noted that time-dependent damage development (cracking) in a ply can be considered as creep-rupture of that ply. The intent is to identify the knowledge gaps in the area of time-dependent evolution of various damage modes and their influence on creep of multidirectional polymer composite laminates, in support of the scope and the objectives of this thesis.

First, background information is provided briefly to support the understanding of various terminologies and concepts used in this thesis. Subsequently, various damage modes and their influence on mechanical properties of composites are presented. A review of previous efforts in modeling TID and its effect on the modulus of composite laminates is presented next. This is followed by a review of published studies on creep and creep-rupture. Finally, a review of previous efforts to model time-dependent damage and its impact on creep is presented. Following a summary of current knowledge gaps, thesis objectives conclude this chapter.

While a large body of published literature in areas relevant to this thesis was examined, only selected papers are cited in the following sections. The rest are provided as bibliography at the end of this thesis.

2.1 Background Information

Composites used in structural applications are usually multidirectional composite laminates made by stacking together several laminas. Lamination theory is used to determine the

property of a multidirectional laminate, shown in Figure 2-1, using its lamina properties. Ply stresses and strains are also determined using this theory. More details on lamination theory can be found in Appendix A. The relationship between force and moment resultants for the laminate and the reference plane strains and curvatures can be written in the form of equation (2-1).

$$\begin{bmatrix} N \\ \cdots \\ M \end{bmatrix} = \begin{bmatrix} A & B \\ \cdots\cdots & \\ B & D \end{bmatrix} \begin{bmatrix} \varepsilon^0 \\ \cdots \\ \kappa \end{bmatrix} \tag{2-1}$$

Here, [A], [B] and [D] are laminate stiffness matrices. Equation (2-1) can be inverted to determine laminate strain and curvature in response to applied load and moment:

$$\begin{bmatrix} \varepsilon^0 \\ \cdots \\ \kappa \end{bmatrix} = \begin{bmatrix} a & b \\ \cdots\cdots & \\ c & d \end{bmatrix} \begin{bmatrix} N \\ \cdots \\ M \end{bmatrix} \tag{2-2}$$

where [a], [b], [c], and [d] are laminate compliance matrices and obtained from stiffness matrices, as explained in Appendix A.

2.1.1 Damage modes and their effect on modulus

Polymer composites develop damage when subjected to a load. Damage modes in polymer composite laminate can be classified as intrinsic or extrinsic [4]. Intrinsic damage modes are those that occur within a ply of a laminate (or a unidirectional lamina) and are not influenced by the laminate stacking sequence. Micro-cracking, crazing and yielding of the matrix, fiber fracture, and fiber-matrix interface failure (debonding) are examples of intrinsic damage modes.

Extrinsic damage modes are those that occur within and between the plies of a laminate and are influenced by the laminate stacking sequence. Transverse cracking (due to in-plane stresses), delamination (due to interlaminar stresses), vertical cracks (due to out-of-plane

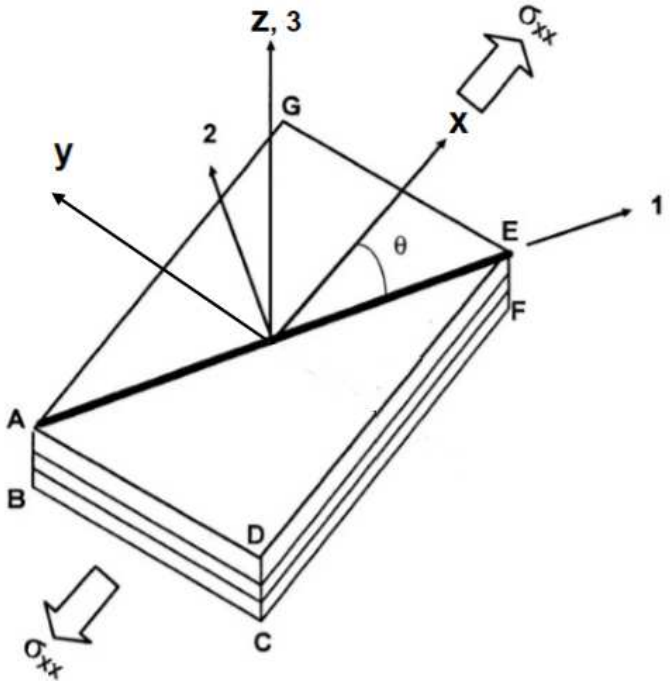

Figure 2-1: Laminate coordinate system [1]

stresses) are examples of extrinsic damage modes [1]. Extrinsic damage modes are easier to detect than intrinsic damage modes. The effect of extrinsic damage modes will be manifested as degradation in the modulus of the laminate (increase of compliance) and /or permanent strain in the laminate, as shown in Figure 1-2.

Transverse cracks, shown in Figure 2-2 and Figure 2-3, are the most common form of damage in composite laminates. Transverse cracks, also known as matrix cracks, occur in the matrix and run parallel to the fibers, transverse to the loading direction, and span the thickness and the width of a ply. When transverse stress in a ply exceeds the ultimate strength of a ply ($\sigma_{22}^{k} > \sigma_{22}^{U}$), it fails. The fracture is constrained to this ply by the stronger outer plies and is prevented from progressing along the entire thickness of the laminate. This results in transverse cracks in that ply. Transverse cracks in [0] plies are known, in the literature, as longitudinal cracks or splitting. Transverse cracks increase and reach the CDS (discussed in 1.1), as shown in Figure 2-4. At this stage, all cracks have a characteristic spacing. A number of analytical models can be found in the literature correlating the transverse crack density in [90] plies with time-independent modulus degradation [5].

Other types of damage modes can be initiated from these transverse cracks or at other locations such as free edges and ply-ply interfaces. Delamination is one damage mode, nucleated usually from the tip of transverse cracks [8-12]. Delamination, shown in Figure 2-5, has a detrimental effect on the strength of composites. This damage mode occurs when interlaminar stresses are greater than corresponding interlaminar strengths, i.e. $\sigma_{zz}^{k} > \sigma_{zz}^{U}$ or $\sigma_{xz}^{k} > \sigma_{xz}^{U}$ or $\sigma_{yz}^{k} > \sigma_{yz}^{U}$.

Vertical cracks are nucleated due to out-of-plane normal stresses (σ_{zz}) and are termed as vertical cracking to differentiate it from delamination due to interlaminar shear stresses, as

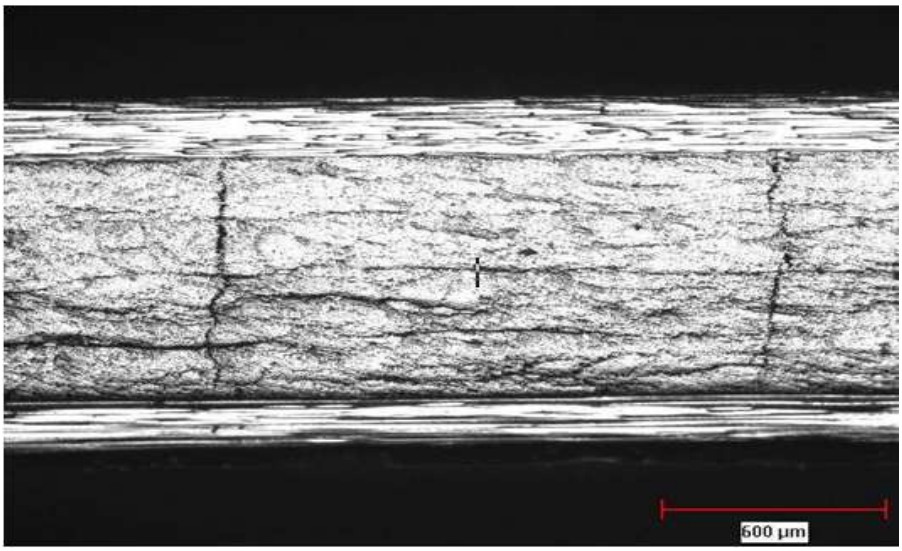

Figure 2-2: Transverse cracks in $[0/90_2]_s$ [1]

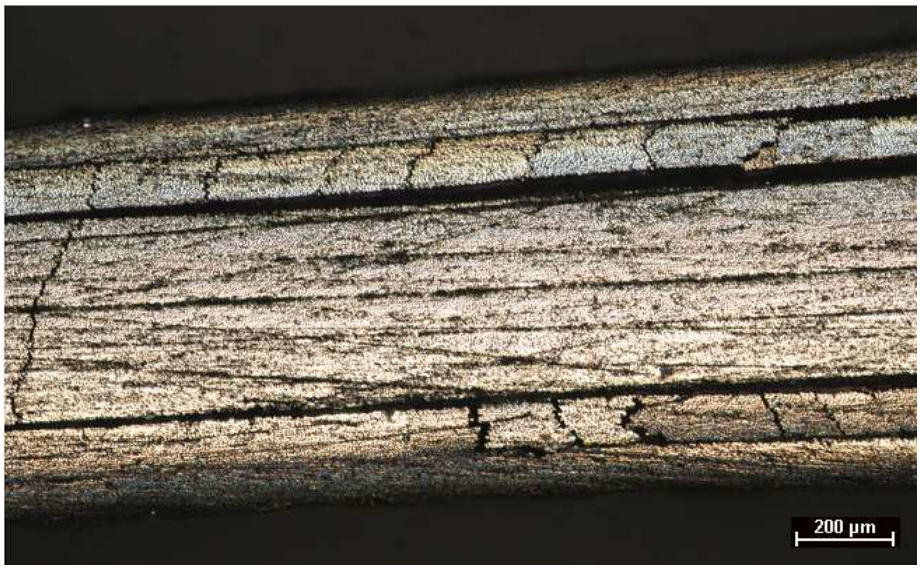

Figure 2-3: Transverse cracks in [-45] and [90] ples of $[\pm 45/90_2]_s$

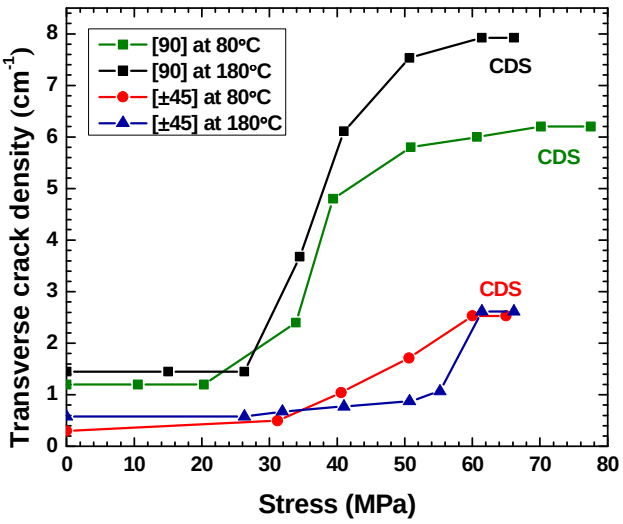

Figure 2-4: Transverse crack density evolution in [90] and [±45] plies with applied stress in $[\pm 45/90_2]_s$ at temperatures of 80 ºC and 180 ºC

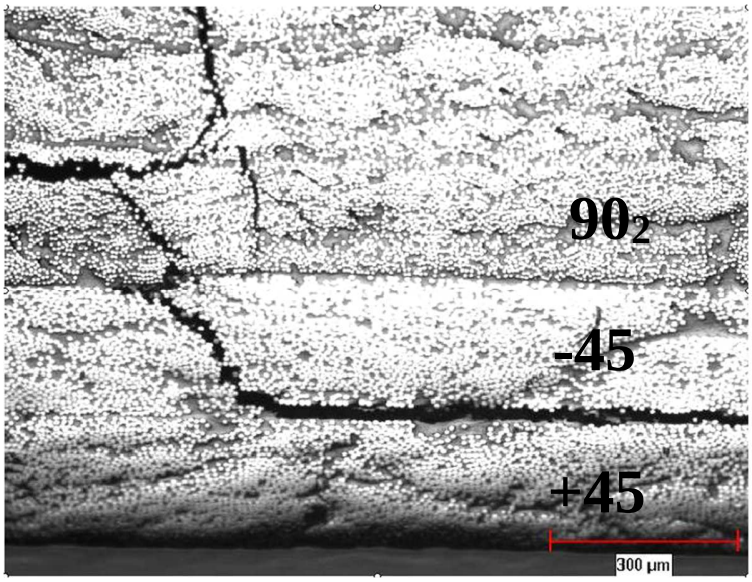

Figure 2-5: Delamination between 45 and -45 plies in $[\pm 45/90_2]_s$ [1]

shown in Figure 2-6. When $\sigma_{zz}^{k} > \sigma_{zz}^{U}$ of the plies, this damage mode occurs. Fiber fracture is nucleated when the axial stress on the fiber exceeds the axial fiber strength, i.e. $\sigma_{11}^{k} > \sigma_{11}^{U}$, as shown in Figure 2-7.

The damage state is characterized by crack density, λ, which is equal to the inverse of the distance between two neighboring cracks, 1/2a, as shown in Figure 2-8, where *2a* is the crack spacing. With increase in the crack density, the modulus of the laminate decreases, as shown in Figure 2-9.

Time-independent and time-dependent evolution of transverse cracking in multiple plies of a laminate has been focused in this study.

2.1.2 Creep and creep-rupture

When a stress of σ_o is applied to an elastic material, as shown in Figure 2-10a, it would deform elastically to a strain of ε_0, as shown in Figure 2-10b. This strain will remain constant with time and will return to zero strain state as soon as the applied stress is removed. In contrast, a viscoelastic material would exhibit a time-dependent increase in strain, ε_v, as shown in Figure 2-10c, in addition to the instantaneous elastic strain, ε_0. Upon unloading, the elastic strain will recover immediately while the viscoelastic strain will recover over a period of time. Hence, a viscoelastic material would exhibit both elastic and viscous behavior. In carbon fiber/polymer matrix composites, such as the one studied in this thesis, the carbon fibers remain elastic and do not creep. Hence, the observed creep and creep rupture in these composites is due to the viscoelasticity of the polymer matrix.

Creep is time-dependent deformation of a material under a constant load or stress, as shown in Figure 2-11 (a). The applied stress is usually well below the ultimate tensile strength of

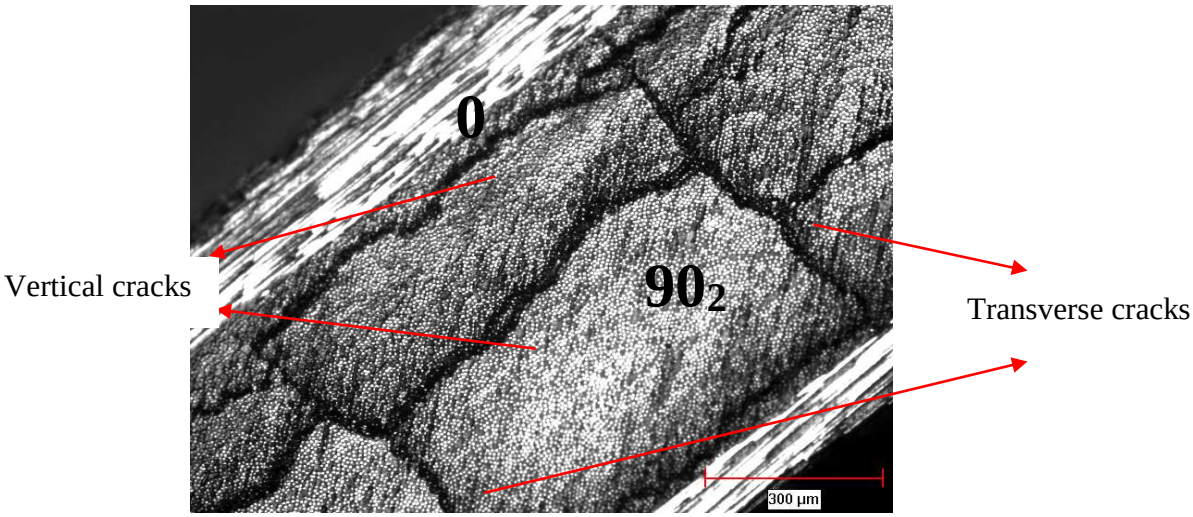

Figure 2-6 Transverse and vertical cracking in $[0/90_2]_s$ [1]

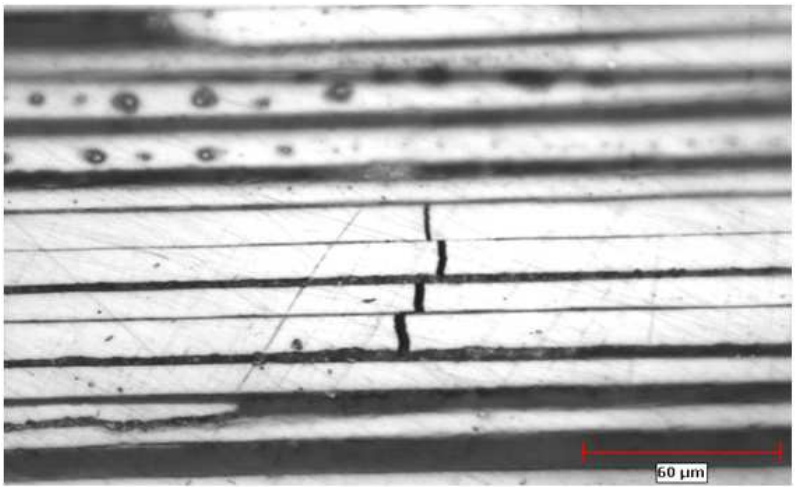

Figure 2-7: Fiber breakage in [0] plies [1]

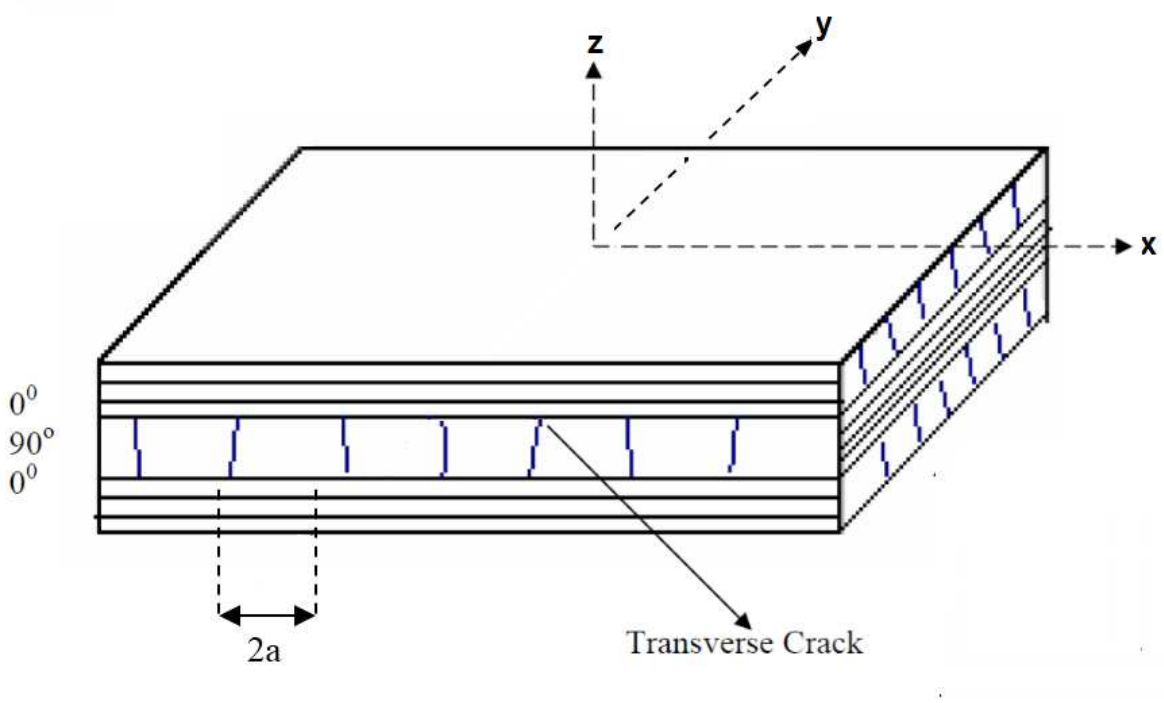

Figure 2-8: Schematic of damage state in a composite laminate $[0/90]_s$

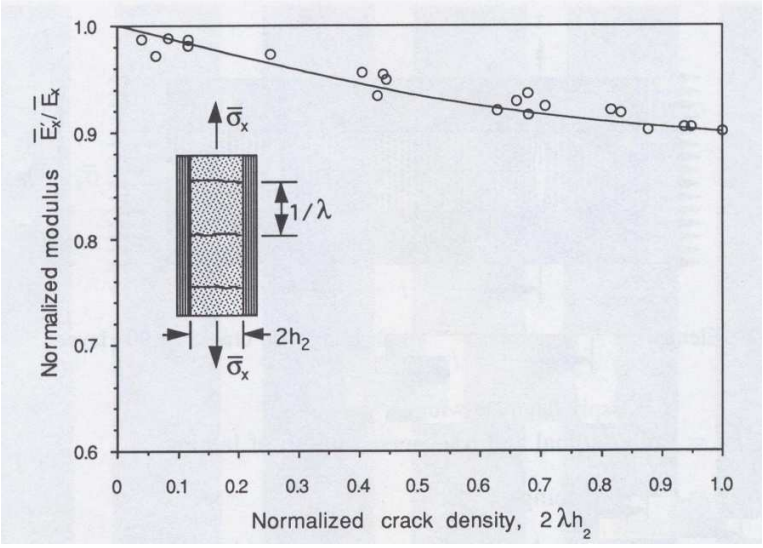

Figure 2-9: Axial modulus of cracked $[0/90_2]_s$ AS4/3501-6 laminate normalized with intact axial modulus versus transverse crack density [6]

Figure 2-10: Schematic of (a) stress profile, (b) elastic behaviour and (c) viscoelastic behavior (Figure 2-1 in Ref. [16])-Image removed due to copyright

Figure 2-11**:** Illustration of creep and creep rupture: a) Applied stress profile, and b) Measured strain and compliance as a function of creep time (Figure 1-9 in Ref. [16]) -Image removed due to copyright

material. Creep results in increase in compliance and decrease in modulus of the material, as shown in Figure 2-11(b). While creeping, a viscoelastic material may suddenly fail as shown in Figure 2-11(b) and this is termed as creep rupture. The time to failure would depend on the applied stress as shown in Figure 2-12. Creep and creep rupture are two concerns in application of polymer composite materials in load bearing structural applications. Possible excess deformation due to creep or catastrophic failure due to creep-rupture in a structural composite part necessitates the characterization of time-dependent modulus and strength for a reliable design and application of polymer composite structures.

The continuous fiber reinforcement is the backbone of a composite, which determines stiffness and strength of the composite. Since the fibers are much stiffer than the matrix, the fiber properties tend to control the response of a lamina along the direction of the fiber axis; thus, the longitudinal and in-plane transverse compliances, S_{11} and S_{12} respectively, are fiber dominated.

On the other hand, the compliances along transverse direction (perpendicular to the fiber direction) and in shear, S_{22} and S_{66} respectively, are normally matrix dominated properties because they are closely tied to the response of the matrix. Matrix properties are time-dependent while the fiber properties do not vary with time and are time-independent. Developing a model for prediction of creep thus involves prediction of time-dependent degradation of matrix-dominated properties, i.e., $S_{22}(t)$ and $S_{66}(t)$ of a unidirectional lamina. Only two out of four compliances of unidirectional lamina are time-dependent, given in equation (2-3),

$$[S(t)]_{1,2} = \begin{bmatrix} S_{11} & S_{12} & 0 \\ S_{12} & S_{22}(t) & 0 \\ 0 & 0 & S_{66}(t) \end{bmatrix} \tag{2-3}$$

Since it is time consuming to quantify this degradation experimentally for the entire service life, accelerated testing and modeling methodology is often used to predict this degradation beyond

Figure 2-12**:** Creep-rupture: applied stress versus rupture time (Figure 1-10 in Ref. [16]) - Image removed due to copyright

the experimental time window. A widely accepted method is Time-

Temperature-Superposition-Principle (TTSP), as shown in Figure 2-13. TTSP assumes that the creep curves at various temperatures during static loading of a PMC (Polymer Matrix Composite) have similar shape but are shifted with respect to time. Accelerated creep curves at various temperatures within a short experimental time-window are generated and shifted along the time-axis to generate a master curve, as shown in Figure 2-13. The master curve generated by TTSP represents the compliance of the material at a reference temperature over a period of time much longer than the experimental time-window.

Various service factors that can influence creep and creep rupture are stress, temperature, moisture and physical aging. The reader is referred to references [13-16] for more information on the influence of the various factors on creep and creep rupture. This study focuses only on the effect of temperature and stress on the creep of multidirectional composites. The compliance matrix of a unidirectional lamina, represented by equation (2-3), is input to the model for creep of multidirectional composites developed in this study. This compliance matrix has been already developed by previous students of this research group [3, 15] applying accelerated testing and TTSP methodologies mentioned above.

2.2 Published literature on TID

When the stress in a ply exceeds the FPF stress for a damage mode, the ply would develop that damage mode. The amount of damage would depend on the magnitude of the stress as well as the stacking sequence. This ply stress can be process-induced or due to applied load. This section reviews experimental studies on TID, followed by modeling studies.

Figure 2-13: Schematic illustration of Time-Temperature-Superposition-Principle (TTSP) (Figure 2-6 in Ref. [16]) -Image removed due to copyright

2.2.1 Process-induced TID

The curing process of thermoset polymer composites involves curing at a higher cure temperature and subsequently cooling to room temperature. Cross-linking during the curing process results in shrinkage of the polymer matrix of the composite. Also, the matrix contracts more than the fiber during cooling. Hence, process-induced residual stresses develop in polymer composite laminates due to mismatch in cure shrinkage and thermal contraction between the fiber and the matrix as well as between plies of a laminate. Additional contributions [17] may come from a mismatch between the composite part and the tool used to manufacture the part, as well as due to differential expansion during the ramp-up stage (if gelation occurs prior to reaching the cure temperature).

Process-induced residual stresses can result in warpage [17] and damage upon cooling from cure temperature even before mechanical loading [18, 19]. Hahn [20] developed a micromechanically based model to study the effect of residual stresses in failure of $[0_2/\pm45]_s$, cross-ply and quasi-isotropic laminates and concluded that the residual stresses resulted in early failure of [90] plies in the studied laminates. The effect of residual stresses on strength of composites was studied by Nimmer [21] and Wisnom [22] using a micromechanical model compared with finite element (FE) results and a FE model, respectively. They showed that existing residual stresses mostly affect the interface between fiber and matrix, and this is beneficial for the transverse strength of the composite by inserting compressive stresses in the interface. Formation of process-induced transverse cracking in [90] plies during a thermal load was experimentally investigated by Adams et al. [23] in cross-ply laminates. They showed that increasing thermal loading cycles led to increasing of the transverse cracks in [90] plies.

Park et al. [24] developed a shear lag based model along with critical strain energy to predict transverse cracking in multiple plies of cross ply laminates and quasi-isotropic laminates under thermal loading. The predictions of transverse crack density for thick [45] plies in quasi-isotropic laminates compared fairly well with experimental results. However, prediction of transverse cracks for [90] and [45] plies did not compare well with experiments, especially in the cases where the investigated ply group was thin. Herakovich [25], Zhao et al. [26] studied the effect of residual stress on the failure of unidirectional composites under transverse mechanical loading using a micromechanical and FE model along with a maximum stress failure criterion. The prediction showed that the existence of residual stresses can be detrimental or beneficial depending on what failure envelope the material is. Asadi and Raghavan [7] showed that the residual stress built up in the composite during the manufacturing and cooling process can nucleate transverse cracking in [90] and [45] plies of $[\pm 45/90_2]_s$ and subsequently affect the cracking progression in creep.

Fiber reinforcements are usually assumed to be elastic and are not affected by the curing process [27, 28]. However, polymer matrix is viscoelastic and depends on time, temperature, and degree of cure. Having the capability to predict process-induced damage would be useful in designing a cure process to eliminate or minimize it. This requires a model to predict process-induced residual stress and a criterion to predict failure. The former has been studied extensively by a number of researchers in the context of process-induced warpage [27-35] and viscoelastic models, [36-44] but rarely in the context of process-induced damage. For example, Wheitsman [36] studied the residual stresses during cool down from cure temperature to room temperature accounting for temperature dependence of compliances, whereas White and Hahn [38, 39] developed a viscoelastic model to account for mechanical properties dependent on time and

degree of cure to determine the residual stresses during curing and cool down process. However, while most of the papers have taken into consideration process-induced residual stress, very few studies have cited any process-induced damage or its effect on failure of composites.

2.2.2 TID due to mechanical load

Extensive experimental studies have been completed to understand the effect of ply thickness and stacking sequence on onset stress/strain for the appearance of a damage mode, CDS, and sequence of appearance of various damage modes during quasi-static loading. A very good and concise review has been authored by Narin [5]. Most studies have focused on transverse cracking in [90] plies of cross-ply laminates consisting of [0] and [90] plies. A handful of them have focused on delamination [8-12, 45-47]. Some of the earliest of these studies include those of Garrett et al. [48], Bader et al. [49], Parvizi et al. [50], Bailey et al. [51, 52], and Jones et al. [53] who carried out experiments for observation of transverse cracking in [90] plies and the effect of thickness of [90] plies on transverse cracking in cross-ply laminates.

The laminate stacking sequence and thickness of the plies affect the damage onset stress (σ_{FPF}) and evolution of transverse cracking. The onset stress for transverse cracking in $[90/0_n]_s$ with thicker [90] plies is lower than the onset stress for $[90/0_n]_s$ with thinner [90] plies. Thinner [90] ply groups can, therefore, develop higher crack density before final laminate failure. The thicker the inner [0] plies in $[90/0_n]_s$ laminates, the higher the onset stress for transverse cracking in outer [90] plies and the lower the CDS. This suggests that initiation stress for transverse cracking in [90] plies is lower for $[90_n/\theta_m]_s$ than for $[(\theta_m/90_n]_s$ laminates. $[90_n/\theta_m]_s$ have been observed to exhibit a greater tendency for delamination [5, 10], which often starts at the tip of transverse cracks [54]. Thicker [90] ply groups, in both types of layups are more delamination prone as well. If the thickness is less than a specific value, delamination would start sooner than

the transverse cracking [5].

The effect of the thickness of [90] plies on transverse cracking and delamination has been studied by Wang et al. [8, 9, 11, 12, 55, 56] and Nairn [5, 10]. They found that the load at which delamination starts depends on the laminate stacking sequence. If the neighboring plies of the cracked ply are stiffer, a higher stress is required for delamination. This is mainly because the magnitude and sign of free edge stresses, which are responsible for delamination onset, depend on the stacking sequence [56]. For instance, $[90/\pm45/0]_s$ have been found to be exhibit negligible delamination when compared to $[\pm45/0/90]_s$ because of high normal out-of- plane compressive stress, in contrast to tensile out-of-plane stress in the latter. Stacking sequence of the laminate can also affect the pattern of the transverse cracks [57]. Periodic transverse cracking in $[0_m/90_n]_s$ in contrast to staggered transverse cracking in $[90_m/0_n]_s$ has been reported by Nairn et al. [58].

Most of the studies in damage of composites are limited to transverse cracking of [90] plies in cross-ply laminates, as mentioned above. To the knowledge of the author, there are very few studies in the literature focused on simultaneous transverse cracking in multiple plies of a laminate [45, 59-61]. Simultaneous transverse cracking and delamination was in the focus of some studies for laminates other than cross-ply laminates [8-12, 45-47]. The above experimental observations have been used in developing various predictive models discussed below.

2.2.3 Models for TID

Previous research on modeling of TID evolution (specifically in [90] plies of laminates) and its effect on modulus of composite laminates is extensive and a good review can be found in

Ref. 5. Various approaches that have been used in the past to account for the effect of TID on modulus during quasi-static loading can be grouped into three categories: Ply

Discounting Models, Continuum Damage Mechanics (CDM) Models, and Elastic Analysis based Models.

Ply Discounting Models reduce the modulus of the cracked ply to near zero value and use it within the framework of lamination theory to determine the modulus of the laminate. Many studies cited in Ref. 62 and 63 fall under this category.

In the CDM approach, the damaged ply is modeled as an equivalent undamaged ply with an apparent/in-situ modulus/compliance [6]. The latter is obtained, as a function of crack density, by fitting the experimental data with the model, as shown in Figure 2-14 and Figure 2-15. Alternatively, a damage parameter is defined and used to determine the apparent modulus of the damaged ply [64, 65]. The damage parameter is determined as a function of applied stress/strain by fitting the experimental data with the model. These two modeling approaches were not used in this thesis since they lack the predictive capability.

Elastic Analysis based models determine the perturbation in ply stresses and strains due to damage and use the new stress/strain state to determine the modulus of the laminate with damage [5]. These models employ appropriate fracture criteria for ply failure, which can be grouped into three categories, strength based criteria, polynomial criteria, and energy based criteria. Elasticity based models are either analytical or numerical. Analytical models are based on shear lag analysis [48, 66-68] and variational analysis [69, 70, 85]. Numerical models involve finite element analysis [8, 9]. Since an analytical model is developed in this thesis, prior research on analytical models is reviewed here.

2.2.3.1 Shear lag analysis based models

Shear lag analysis is associated with the stress transfer from one ply to another near a crack by means of interlaminar shear deformation. Shear lag method was originally proposed by

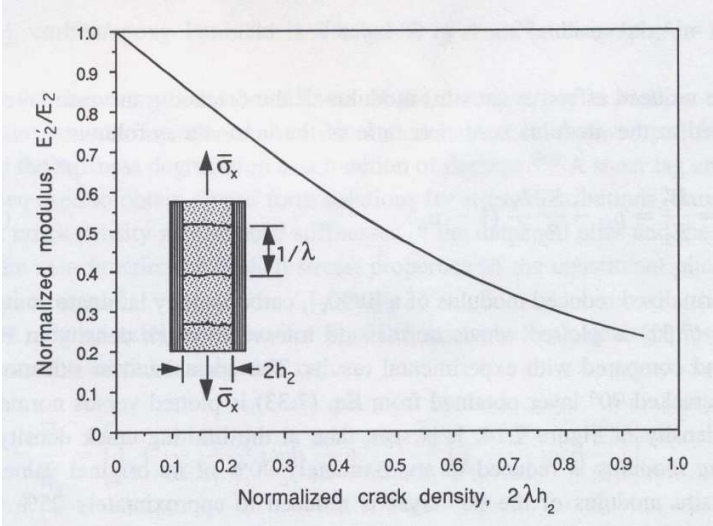

Figure 2-14: Apparent transverse modulus of an equivalent [90] ply (normalized by transverse modulus of intact [90] ply versus transverse crack density in $[0/90_2]_s$ AS4/3501-6 laminate) [6]

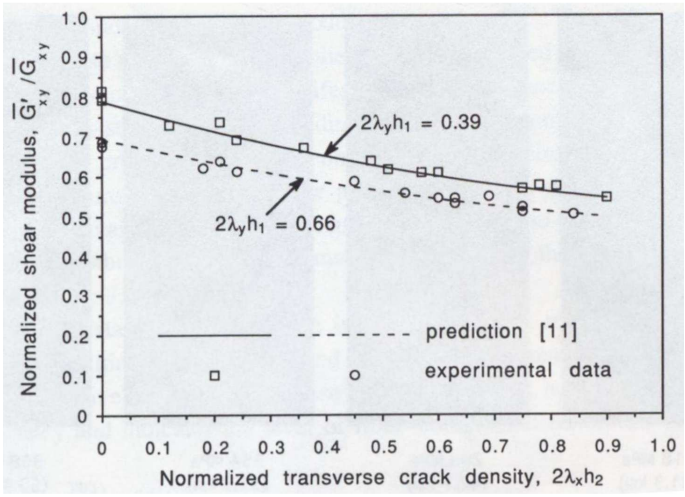

Figure 2-15: Apparent shear modulus of equivalent [90] ply (normalized shear modulus of intact [90] plies versus transverse crack density in $[0/90_2]_s$ AS4/3501-6 laminate [6]

Cox [71]. In the shear lag analysis it is assumed that 1) the fiber and matrix behavior is linear elastic, 2) the interface between fiber and matrix is perfect, and 3) no load is transferred through the fiber ends. Assume that a strain of ε is applied to a fiber embedded in a matrix. Since strain is maximum at the fiber end and minimum at the fiber center (zero for a sufficiently long fiber), there will be a shear stress distribution at the fiber-matrix interface and a tensile stress distribution in the fiber. The rate of load transfer is proportional to the difference between the axial displacement of the fiber, W_f, and corresponding displacement of the matrix if there was no fiber, W_m, as follows:

$$\frac{dF}{dx} = \gamma(W_f - W_m)$$

where γ is the shear lag parameter which depends on geometry of fiber arrangement within the matrix and material properties.

Shear-lag analysis was first introduced in composites for cross-ply laminates by Garrett and Bailey [48] to predict transverse cracking of [90] plies. Nuismer and Tan [72] used shear-lag analysis to determine the reduction in stiffness of a laminate. However, they neglected to analyze out-of-plane stress (σ_{zz}) and variation in the transverse displacement as a function of x-axis coordinate (i.e. along loading direction) to eliminate the variation of σ_{xx} along the z-coordinate, i.e. thickness of the ply. The model predictions for modulus compared well with FE results for $[\pm\theta_m/90_n]_s$ laminates with pre-existing cracks in [90] plies. Laws and Dvorak [73] used the same assumptions in their shear-lag analysis along with strain energy release rate criterion to predict stiffness loss as a function of transverse crack density in [90] plies and crack density as a function of applied load in a cross-ply laminate. The predictions of their model for transverse crack density in [90] plies of cross-ply laminates as a function of the applied load was validated through experimental results.

McCartney [74] developed a model based on shear lag analysis to predict the stress transfer and displacement distribution between the 0° and 90° plies with transverse cracks in [90] plies, as well as the dependence of mechanical properties on transverse crack density. He assumed that the tensile stress was independent of the ply thickness. Plies were divided into sub-plies of smaller thickness to improve the accuracy of analysis. The model predictions for reduction in modulus with respect to the applied load in cross-ply laminates with cracks in [90] plies compared very well with experimental results.

Flaggs [75] assumed linear variation of the in-plane displacement along thickness direction in his shear-lag analysis to predict transverse cracking of [90] plies of [±θ/90] laminates in conjunction with strain energy released rate criterion. He also indicated that the lamina strength in the laminate was dependent on the neighboring plies in the laminate. By comparing the predictions and experimental results for onset strain and stress for transverse crack in [90] plies of $[\pm\theta_m/90_n]_s$, he demonstrated that a failure criterion based on strain energy release rate provides better results compared with predictions based on strength based failure criteria. Han and Hahn [76], Lee and Daniel [67] and Daniel and Tsai [68] assumed quadratic dependence of the in-plane displacements along the transverse direction in their shear lag analysis. They developed closed form solutions for stress distribution, transverse crack density and time-independent degradation of laminate modulus in terms of in-situ modulus of the [90] plies in a cross-ply laminate with transverse cracking in [90] plies. The change in load partitioning among layers due to damage was simply interpreted in terms of change in the in-situ modulus of the damaged layers.

Fukunaga et al. [77] and Lim and Hong [78] developed a modified model based on a shear lag analysis to predict the transverse crack density and stiffness reduction of the cross-ply

laminates. Fukunaga et al. [77] incorporated a Weibull distribution in the strength of [90] plies. In their model, it was assumed that the shear stresses due to transverse cracking acted only within a thin resin-rich layer adjacent to [90] plies. Critical strain energy release rate was used as the criterion for cracking. Their model predicted the dependence of the first cracking in [90] plies on the [90] ply thickness as well as the reduction in modulus by progressive transverse cracking. Considering the thin layer adjacent to [90] plies led to better predictions compared to those shear lag models which assumed the entire [90] layer as the shear layer [49-51, 75, 76].

Lu and Liu [79] developed a modified shear lag analysis for cross-ply laminates, called interlayer shear slip theory, to investigate the effect of interfacial bonding on the behaviour of cross ply laminates. In this model, they assumed the existence of an interlaminar shear layer in contrast to other methods that assumed perfect bonding between plies. The results determined by this model for transverse deflection of a composite beam in-plane displacement and normal stress in cross-ply laminates were in good agreement with numerical results.

Berthelot [80] applied analyzed stress distribution in cross-ply laminates with transverse cracking in [90] plies. The longitudinal displacement along the transverse direction was assumed to be quadratic in [90] plies and linear in [0] plies. The displacement along the thickness in [90] plies was assumed to be a function of distance along both longitudinal and thickness directions. Model predictions for stress and strain distribution in [0] and [90] plies yielded a good agreement with FE results.

Fan and Zhang [59] proposed a model, called ECM (Equivalent Constraint Model), to predict the stress distribution in a cracked laminate. In this model, the cracked layer was replaced by an equivalent layer with in-situ mechanical properties. The model used shear lag analysis along with strain energy release rate criterion to predict the stress transfer from one layer to

another layer and hence stress distribution in all layers. This model was able to analyze only transverse cracking. The model predictions for reduction of longitudinal, transverse and shear modulus as a function of crack density of [90] plies in cross-ply and $[\pm\theta_m/90_n]$ laminates were in good agreement with experimental results. Also, the predictions for onset strain of crack compared very well with experimental results. Kashtalyan and Soutis [60, 61, 81] extended this work for other damage modes such as splitting and delamination. In contrast with the models reviewed above, this model [60, 61, 81] focused on the prediction of various damage modes in multiple plies. Stiffness reduction due to transverse cracking and splitting in cross ply laminates [60], delamination induced by transverse cracking and splitting in a cross-ply laminate [61], as well as transverse cracking in angle-ply laminates [81] were modeled and predicted. An in-situ damage effective function was introduced. These model predictions have been compared with experimental results in references [68, 82, 83]. The predicted longitudinal, transverse and shear moduli agreed well with the results published in Ref. 82 and 83 but not with those published in Ref. 68. Also, the predicted Poisson's ratio did not agree well with experimental values.

2.2.3.2. Variational analysis base models

Variational analysis is an extension of the maximum and minimum theory of ordinary functions. The goal of variational analysis (calculus of variations) is to provide upper and lower bounds for a set of exact solution. The mathematical problem of minimizing an integral is the aim of the variational analysis. *"A tentative path which differs from the actual path (exact solution) in an arbitrary but still infinitesimal degree is called "variation" of actual path and calculus of variations investigates the changes in the value of an integral caused by such infinitesimal variations of the path"* [84].

Calculus of variations deals with maximizing or minimizing functionals. Functionals are dealing with mappings from a set of functions to the real numbers and usually referred to as functions of functions. Functionals are often expressed as definite integrals involving functions and their derivatives. The interest of calculus of variations is to find the functions that make the functional a maximum or minimum.

Suppose that y(x) minimizes the following integral.

$$I[y] = \int_{x_0}^{x_1} [p(x)(y')^2 + q(x)y^2 + 2f(x)y]dx$$

$$y(x_0) = y_0, \qquad y(x_1) = y_1,$$

where p, q, and f are given continuous functions in $x_0 \le x \le x$ and p>0, and q>0. The value of I[y] is a functional (function of a function) with argument y. If the first variation of I[y] is equal to zero, the value for y(x) is determined. The first derivative of I[y] results in the following Euler-Lagrange equation:

$$-[p(x)(y')]' + q(x)y + f(x) = 0$$

The solution to the above differential equation will provide values of y(x) that would minimize I[y].

Variational analysis, applied to predict damage evolution, determines the change in the stress state due to cracking using a perturbation term in stress, which is calculated by minimizing the complementary energy using calculus of variations originally proposed by Hashin [69]. A solution based on finding an admissible stress state, which would minimize the complementary energy, results in an upper bound for strain energy. A solution based on an admissible strain state will provide a lower bound for strain energy. Studies using both methods can be found in the literature and are reviewed below.

Hashin [69] was the first to use variational analysis to develop a model to predict transverse cracking in [90] plies of a cross-ply laminate using critical strain energy release rate criterion. In his model, the stress state was taken to be a function of distance along loading direction (x-axis) but independent of distance along the out-of plane z-axis. In other words, the stress was assumed to be constant through the ply thickness. Minimizing the complementary energy (using the principle of minimum complementary energy), the two dimensional elastic stress state was determined. This was subsequently used to calculate strain energy release rate, which was subsequently compared with fracture toughness to determine if fracture occurred. Hashin's predictions for reduction in modulus with respect to crack density compared well with the experimental results.

Nairn et al. [10, 46] extended Hashin's work [69] to predict both transverse cracking and delamination induced by transverse cracks in [90] plies of cross-ply laminates. Thermal residual stresses were considered in their analysis. Transverse cracking was observed to continue until the transverse crack density reached a critical crack density at which delamination started; i.e., transition from transverse cracking to delamination occurred. The predictions for transverse crack density were in good agreement with experimental results. This model did not focus on prediction of transverse cracking or damage modes in the plies other than [90] plies.

However, Lim and Li [47] showed that Nairn and Hu [10] underestimated the energy release rate, and hence, the predicted transition was a coincidence. This is mainly because the critical strain energy release rate for delamination was much higher than that of transverse cracking in many materials, and such a transition from transverse cracking to delamination was almost impossible. Nairn [46] also derived upper and lower bounds for the energy release rate for

transverse cracking in composite laminates. He determined the admissible stress state in the laminate for the upper bound and the admissible strain state for the lower bound.

Varna and Berglund [85] also used Hashin's model and the failure criterion of the critical strain energy release rate to predict the transverse cracking in cross-ply laminates, assuming a ply-thickness dependent stress function in their variational analysis compared to Hashin's model in which the stress distribution was independent of the ply thickness. Anderssen et al. [86] also used the principle of minimum potential energy along with the critical strain energy failure criterion to determine the stiffness reduction in cross-ply laminates. This study accounted for the crack opening displacement (COD) as a part of the displacement field in the variational analysis and thus the advantage of minimizing the strain energy with respect to the crack opening displacement function. They compared the prediction for stiffness reduction as a function of crack density with FE results and results by Hashin [69] and Varna [85]. Their model predicted well the stiffness reduction for carbon/epoxy composites; however, it underestimated the stiffness reduction for glass/epoxy. Zhang and Minnetyan [87] used the principle of minimum potential energy to estimate the effective modulus of cracked $[\theta_m/90_n]_s$ and $[90_n/\theta_m]_s$ laminates with transverse cracks in [90] plies. They assumed COD to be a function of distance along both the out-of-plane (ply thickness) and loading direction compared to the model of Anderssen et al. [86] in which COD was only dependent on out-of-plane direction. They demonstrated the effect of neighboring plies of the cracked ply on the modulus reduction of the laminate by varying θ. They showed that a lower crack density $[\theta_m/90_n]_s$ had a higher modulus compared to $[90_n/\theta_m]_s$ with the same crack density. However, this trend was reversed at a higher crack density. The model predictions for stiffness reduction compared well with experimental results for AS4/epoxy and glass/epoxy composites. Farge et al. [88] experimentally studied the COD dependence of

transverse cracks in graphite/epoxy cross-ply laminates using an optical measurement of displacement field. They showed that the average COD is not dependent on stress level, and linear elasticity is still valid for a cracked laminate provided that the reduction in stiffness is considered.

Rebiere and Gamby [45] extended the variational analysis based model developed by Hashin [69] and used it with a critical strain energy release rate criterion to analyze transverse cracking and splitting as well as delamination in cross ply laminates. In addition to predicting the order of occurrence of these damage modes, it was shown that the sequence of damage modes strongly depended on ply thickness, fiber orientation in layers sandwiching the cracking layer, and properties of fiber and matrix. The predicted strain for initiation of longitudinal cracking did not agree with experimental results obtained by Bailey et al. [51]. However, the predictions were in good agreement with FE results for transverse cracking and delamination.

Recently, Vinogradov and Hashin [89] used Hashin's original method [69] for cracking of angle-ply $[\theta_m^2/\ \theta_n^1]_s$ laminates. They rotated the laminate by the angle of the cracking ply (θ-90)° about the out-of-plane axis to yield a cross-ply laminate $[(\theta_m^2-\theta_n^1+90°)_m\ /90_n°]_s$, and they used the original method for analysis of cracking of [90] plies of a cross-ply laminate. The stiffness reduction as a function of crack density was in good agreement with experimental results.

Although shear lag analysis is very simple to perform, variational analysis has a number of advantages. First, it does not have to make the assumptions used by shear-lag analysis. Unlike shear lag analysis, variational analysis does not assume the presence of an interlaminar layer for stress transformation from undamaged ply to damaged ply. Secondly, shear lag analysis assumes a certain mathematical function to define the variation of stress with distance from the crack

location. In contrast, variational analysis need not make any such assumption. Thirdly, variational analysis can be extended easily to three dimensional analysis, while shear lag analysis requires additional assumptions with regards to stress functions. In view of these advantages, variational analysis is used in this thesis.

2.2.4 Failure criterion for time-independent failure

Time-independent failure criteria, used in the models discussed in 2.2.3, can be broadly classified into three categories: strength based criterion, polynomial criterion, and energy criterion. The strength-based criterion predicts failure of a ply when the stress (strain) of the ply reaches the maximum stress (strain) for that ply. Though the strength-based criterion can explicitly predict the fracture mode, it is unable to account for the effect of the multi-axial stress state in the lamina of a laminate since strength data is mostly generated using uniaxial tests. Additionally, it cannot account for the constraint effect of outer plies on the failure stress of the cracking ply, manifested as variation in ply failure stress (magnitude of which is different from the experimental strength value) with laminate layup sequence. Hence, the strength-based failure criterion cannot predict accurately the damage occurring in a ply within a laminate.

Polynomial failure criteria such as Tsai-Hill or Tsai-Wu can be applied to multi-axial stress state; however, they cannot explicitly predict the failure mode.

The energy based criterion predicts failure when the total energy (or strain energy release rate) of a ply reaches a critical energy (or critical strain energy release rate) for that ply. Since the energy in a ply is determined using all stresses in that ply, this criterion inherently takes into account the multi-axial stress state and is used by many researchers [8-12, 45, 46, 55, 56, 58, 69, 70, 85, 87, 89]. Nairn et al. [90] evaluated their predictions based on energy and strength failure criteria, carrying out a wide range of experiments on 21 different layups, which all had [90] plies

(some of them in the middle and some of them on the surface). The results showed that a criterion based on the strain energy could provide a better prediction when compared to a strength criterion [48, 91- 93] for failure.

A recently concluded world-wide round robin exercise [62, 63] has evaluated 19 failure criteria by applying them to predict FPF and ULF of various types of laminates under various multi-axial stress states. While the accuracy of predictions varied with the model, some model predictions were better than others under certain loading conditions. Overall, the Tsai-Wu criterion was better than others. Despite this, energy criterion is used in this thesis due to the need to differentiate the failure (i.e. damage) mode.

2.3 Review on Published Studies on Creep and Creep Rupture

This section includes a review of studies on creep and creep rupture without consideration of damage, experimental studies of time-dependent damage, modeling of creep and creep-rupture with consideration of damage, and finally, failure criterion for time-dependent failure.

2.3.1 Creep and creep rupture without consideration of damage

The published literature on the creep of polymer matrices of both unidirectional and multidirectional composites is extensive, and a detailed review can be found in Ref. 3, 16. Most of the studies focused on the creep of unidirectional laminas.

Dillard et al. [2, 94] developed a creep model, based on lamination theory, to predict the creep of laminates using the creep properties of the lamina that makeup the laminate. They recorded extensive damage in their samples tested under constant load, which caused the

predictions to be lower than the experimental data. They also studied experimentally the creep rupture of the multidirectional composite laminates and modeled using the Tsai-Hill criterion and creep-rupture strength of unidirectional lamina. Discrepancy was observed between the model predictions and experimental results due to non-consideration of time-dependent damage. Their work highlighted the influence of time-dependent damage on creep and the need of its consideration in any creep model for multidirectional laminates. Using Dillard's approach [2, 94] along with a modified Kohlrausch-Williams-Watts (KWW) equation, Viswanathan [15] and Balachander [3] generated the creep compliance data of the unidirectional lamina in the linear viscoelastic region, given in equation (4-3) (described in chapter 4 in details). These creep compliance data were used in this thesis. Also, in this thesis, the focus is on time-dependent damage in creep, and hence, the review for multidirectional laminates is narrowed to those with time-dependent damage.

2.3.2 Experimental studies of time-dependent damage

There are only about 10 to 15 published papers focusing on the experimental study of time-dependent damage. Moore and Dillard [95] were the first to record experimentally the increase in transverse crack density in [90] plies of cross-ply laminates over time at room temperature at stress levels greater than FPF stress. Raghavan and Meshi [4] showed experimentally that the FPF stress was also time-dependent and that the creep of cross-ply laminates increased with the increase in transverse crack density. They carried out experiments with various strain rates to show the dependence of time-dependent matrix crack density as well as first ply failure on the strain rate at a given stress level. Nguyen and Gamby [96] experimentally concluded that a linear viscoelastic behavior of the undamaged material and a

load-rate dependent critical energy criterion can explain the loading rate dependence of FPF and cracking.

Birur et al. [1] experimentally studied the evolution of various damage modes with time in multidirectional polymer composite laminates subjected to a constant load at elevated temperatures. They investigated the influence of temperature, thickness of inner plies, and outer-ply constraint on damage evolution in six laminates with different stacking sequences by varying the layup sequence. It was observed that the sequence of evolution of the damage modes varied with the laminate stacking sequence, stress, and temperature. The different damage modes also influenced one another as well as the creep rupture time. These studies establish that polymer composite laminates develop TDD and that the creep and creep rupture of polymer composite laminates are influenced by both the viscoelasticity of the polymer matrix and the TDD.

2.3.3 Modeling of creep and creep-rupture with consideration of damage

Only a handful of studies (10-12) have focused on modeling the effect of TDD on the creep of multidirectional laminates. The models used in these studies are based on either the continuum damage mechanics (CDM) [97-99] or elastic analysis based models [96, 100-105] discussed in previous sections

Schapery [97-99] developed constitutive equations based on a continuum damage model for linear viscoelastic lamina within a laminate with growing (time-dependent) transverse cracks; however, his model did not focus on the prediction of time-dependent damage growth as well as creep of the laminate. He concluded that the homogenized constitutive equations [98] developed for linear viscoelastic unidirectional fiber composites with damage are practically the same as those for linear elastic material, regardless of whether the damage is constant or time-dependent. For specified strain histories, the current stresses depend on the current damage, but not on the

strain history. Balachander [3] modeled the creep of quasi-isotropic laminates by discounting the modulus of damaged [90] plies within the framework of a lamination theory. Figure 1-4 shows a comparison of experimental creep compliance with predicted compliance. Even though his predictions correlated reasonably with experimental results at shorter times, they diverged with increase in creep time due to the increase in crack density with time, which was not accounted for in the model.

Ahci and Talreja [100] developed a thermodynamics based model along with FE modeling for predicting the non-linear creep of woven polymer composites with pre-existing damage. Time-dependent damage evolution was not modeled in this study. They fitted the experimental data with their model to obtain the damage parameter. The predictions for creep strain compared well with experimental results for T650-35/PMR-15 composites.

Ogi et al. [102-104] developed a model based on shear lag analysis to predict the creep response of a laminate with cracks in [90] plies and used it to predict and validate the creep of a cross-ply laminate with time-dependent transverse cracking [102, 103] as well as the creep and recovery behavior of a quasi-isotropic laminate with pre-existing transverse cracks [104]. In their studies, experimental crack density was used and no appropriate model was developed to predict time-dependent increase in damage. They fitted the experimental data, for transverse crack density obtained as a function of stress and time, using a probabilistic failure model and used the latter to simulate the transverse crack density evolution with time. The model could not predict the strain in the initial portion of creep due to erroneous predicted modulus. However, the increment of creep strain during the loading was in reasonable agreement with experimental results.

Akshantala and Brinson [105] and Nguyen and Gamby [96] developed models based on variational and shear lag analyses, respectively, to predict the loading rate dependence of transverse cracking in [90] plies of cross-ply laminates during tensile testing. These studies used maximum stress and maximum strain failure criterion respectively. Akshantala and Brinson [105] did not validate the predicted crack density evolution with any experimental or numerical results. Nguyen and Gamby's model prediction for crack density as a function of the applied stress at different strain rates compared well with the experimental results for cross-ply laminates. Both studies have not been extended and validated for creep.

All the above-mentioned models, both in TID and TDD, require *a priori* knowledge on crack density for a given stress, and hence did not predict the crack evolution. Using the given crack density as input, the above models can predict the modulus or creep or stress-strain curve [45, 59, 61, 69, 70, 102, 105]. In other words, the proposed models in the literature cannot predict crack density, modulus, and strain at a given stress or time unless one of these parameters is given to the model, thus suggesting a curve fitting rather than predictive capability. Further, although there are attempts to predict simultaneous transverse cracking in multiple plies [45, 59-61], none of the reviewed models can do so.

2.3.4 Failure criterion for time-dependent failure

A comprehensive review of published failure criteria for creep rupture of unidirectional lamina can be found in Ref. 106. While there is large body of published literature on models for creep rupture of unidirectional laminates with application of a wide range of failure criterion, only a handful of studies have focused on predicting the time-dependent failure of a ply of a laminate. The criteria used in these studies are discussed below very briefly.

A maximum strength or strain criteria (using experimental creep rupture data along principal material coordinates, i.e.θ=0 or 90^o) does not yield accurate creep rupture predictions for unidirectional laminates under off-axis loading due to a multiaxial state of stress. Similarly, these criteria cannot be used to predict time-dependent failure of a ply within a laminate. Dillard et al. [2, 94] applied the Tasi-Hill criterion along with experimental creep rupture data to predict ply failure within a laminate. Once the first failure was predicted, they discounted the properties of that ply to negligible value, and hence did not predict further progressive cracking of that ply or other plies (as observed experimentally). The above approaches require experimental creep rupture data for unidirectional laminates tested along principal material coordinates. Additionally, experimental data measured under uniaxial loading may not be suitable for prediction under multiaxial loading even if either the Tsai-Hill or Tsai-Wu criterion is used. Akshantala and Brinson [105] and Ogi et al. [102-104] used maximum strength as the criterion for transverse cracking. Raghavan and Meshii [107] have developed and validated a critical stored elastic energy criterion (that is consistent with the fracture mode) for creep rupture of unidirectional lamina under uniaxial normal and shear loading. This is preferred over the strain energy release rate criterion used in Ref. 8-10, 45, 58, 69, 70, 75, 85-87, 89, 102, and 104 since the latter requires *a priori* knowledge of initial flaw size, which is an unknown. This critical stored elastic energy criterion is used in this thesis.

2.4 Summary of Literature Review, Knowledge Gap, and Motivation for Thesis

Based on this literature review, the following can be summarized:

(a) In addition to TID due to process-induced stress and quasi-static loading to creep load, various damage modes evolve with time under constant creep loading in multidirectional polymer composite laminates.

(b) These damage modes evolve in multiple plies sequentially as well as simultaneously depending on the loading conditions.

(c) Evolution of a single form of damage (namely transverse cracking), with stress, in [90] plies and its effect on time-independent modulus has been modeled. There is one study each on transverse cracking in [45] plies and sequential damage development (transverse cracking followed by delamination) in [90] plies.

(d) The effect of pre-existing transverse cracks in [90] plies on the creep of composite laminates has been modeled in a couple of studies. One of these has used experimental time-dependent transverse crack density data to model the effect of time-dependent cracking on creep.

Based on this literature review, the following knowledge gap can be identified in the area of creep of multidirectional composite laminates.

1) The time-independent and interactive evolution of various damage modes in multiple plies of a laminate, due to process-induced stress and loading to creep stress, and its effect on subsequent creep is the least understood.

2) Time-dependent and interactive evolution of various damage modes in multiple plies of a laminate, during creep, and its effect on creep is equally least understood.

3) A model to predict both categories of damages, identified in (i) and (ii), and their effect on creep is non-existent.

2.5 Thesis Objectives

Hence, the goal of the thesis is to address the knowledge gap, identified in 2.4, in the area of time-dependent evolution of various damage modes and their influence on creep response of multidirectional polymer composite laminates. Since this is a vast and very challenging area, this thesis is focused only on one damage mode (transverse cracking) and its simultaneous evolution in multiple plies of a multidirectional laminate. The objectives of this thesis to realize the above goal are as follows:

1. To develop an analytical model to predict the creep response of a multidirectional polymer composite laminate with simultaneous time-dependent evolution of transverse cracking in multiple plies. This model should be able to predict time-independent evolution of transverse cracking in multiple plies during ramping up to the desired creep load, as well as due to process-induced stress, and to account for its effect on subsequent creep.
2. To characterize experimentally a) the evolution of transverse cracking with stress (during loading) and time (during creep) in multiple plies of a composite laminate, b) time-independent and time-dependent modulus, and c) creep.
3. To validate 1 using 2.

Based on the literature review, variational analysis, combined with a critical stored elastic energy fracture criterion, is used to model the evolution of both TID and TDD. A modified lamination theory framework, incorporating the module for damage evolution, is used to predict creep of multidirectional composite laminates. Results from quasi-static tensile tests and tensile creep tests, done at two different temperatures (and two different creep stress levels) are used to validate the model.

CHAPTER 3. MODEL FOR CREEP OF MULTIDIRECTIONAL LAMINATES WITH TIME-INDEPENDENT AND TIME-DEPENDENT DAMAGE

3.1 Introduction

The stress state in the plies of a laminate depends on the curing process and loading history. Aerospace composite laminates are cured at high temperature (177°C for the composite used in this study) and cooled to room temperature. Process-Induced Stress (PIS) develops in the plies due to mismatch, among plies, in cure-induced shrinkage and CTE (Coefficient of Thermal Expansion). This PIS state in the plies would be altered during loading to creep load and the stress in the plies at the start of creep would depend both on the PIS and the applied creep load. Finally, during creep under constant load, this stress state would be further altered when the stress in the most compliant ply would gradually decrease with time (due to change in compliance with time) and that in the least compliant plies would gradually increase with time (due to transfer of the load from the former). These three zones of process and load history are illustrated in Figure 3-1. This stress state in a ply can be further modified due to cracking of that ply when the stress state in that ply reaches the limit for fracture. In this thesis the cracking appearing in zones I and II due to PIS and applied load is called TID (Time-Independent Damage), and that cracking appearing in Zone III over time due to creep is called TDD (Time Dependent Damage). Therefore, a creep model should be able to simulate the evolution of ply stress state, TID and TDD for a process and load history to predict the creep of a multidirectional composite, reliably. The model developed in this thesis has this capability.

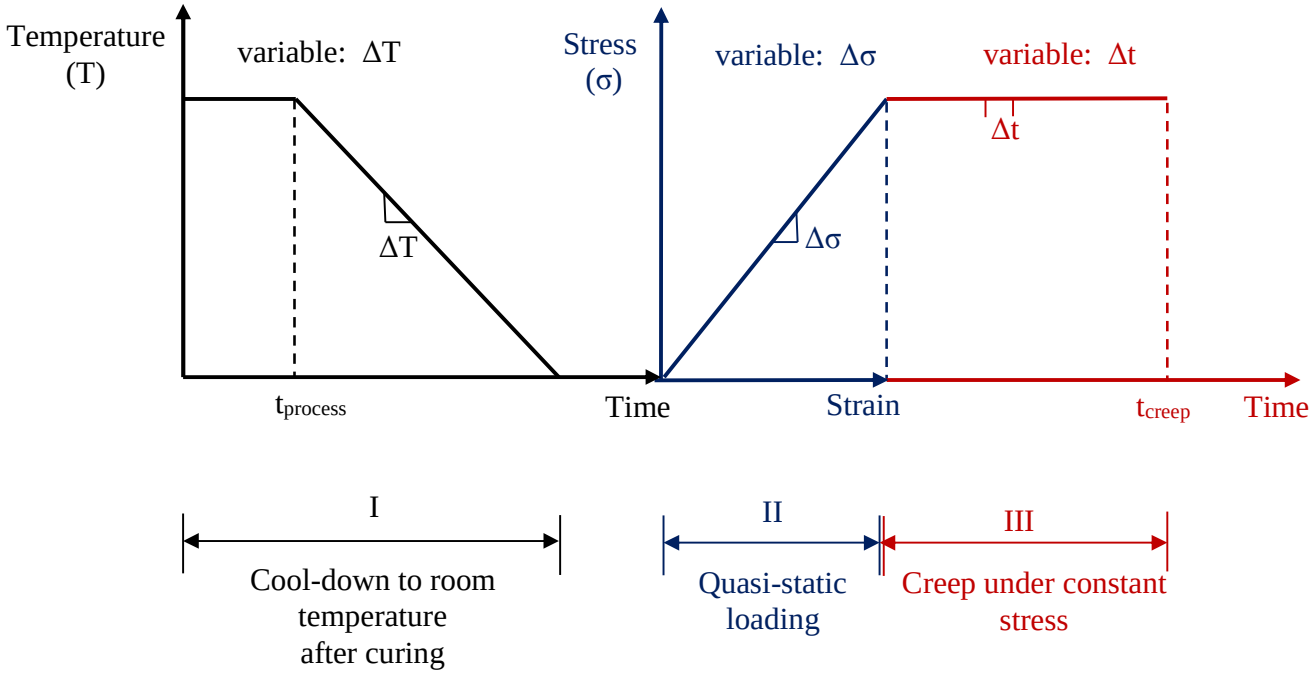

Figure 3-1: Process and load history considered in the developed model

3.2 Creep Model

A block diagram of the creep model consisting of four integrated modules developed in this thesis is provided in Figure 3-2. The PIS module predicts the process-induced stress for an imposed process history. The QSL (Quasi-Static Load) module predicts the stress state for an imposed load profile with initial values input from PIS module. The Static Load (SL) module predicts the stress state as a function of time with initial values input from the QSL module. All these modules use lamination theory, discussed in Appendix A, to predict the stress state in the plies during each incremental change in the variable relevant for a given zone, indicated in Figure 3-1. Incremental change in temperature (ΔT), load ($\Delta\sigma$), and time (Δt) are the variables corresponding to the PSI, QSL, and SL modules, respectively. This incremental analysis is required to take into account the change in material properties along with the change in the magnitude of identified variables as well as perturbation in stresses due to TID and TDD. During each incremental step, each of these modules will determine the stored elastic energy and compare it with a critical stored elastic energy limit to predict if a ply would fracture during that step. If a fracture is not predicted, the variable is changed by a pre-determined magnitude and the simulation procedure is repeated. If failure is predicted, a fourth Variational Analysis (VA) module, shown in Figure 3-2 is accessed. This module is the core of this creep model and predicts the perturbation in the stress state of a ply due to cracking and the new crack density, which would be input to the module that invoked the VA module. Using this data, the module that predicted fracture recalculates the average stress state in the plies of the laminates, average stress and strain on the laminate, and modulus/compliance of the laminate. These along with crack density are output by the PIS, QSL, and SL modules as a function of simulation variables used in those modules.

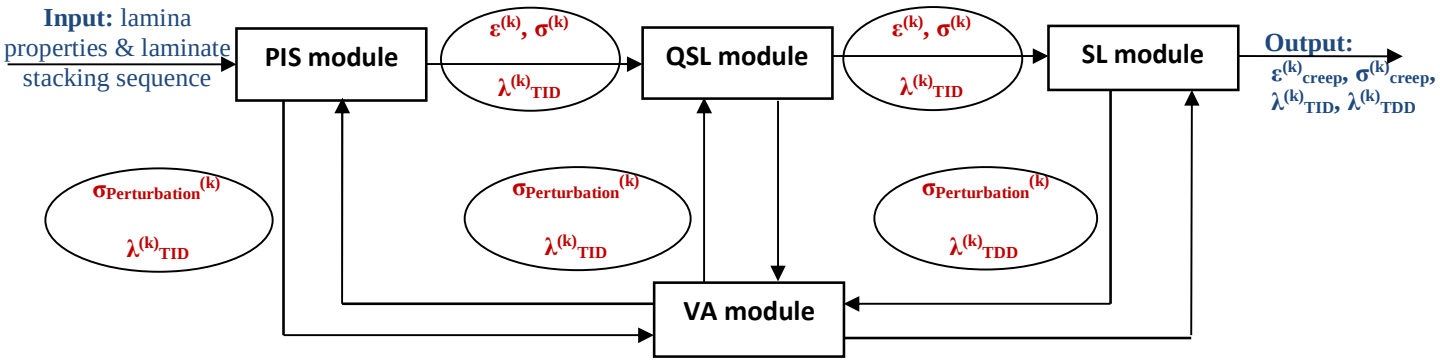

Figure 3-2: Creep model for composites with damage

The damage mode considered in this model is transverse cracking in multiple plies. Among various damage modes discussed in Chapters 1 and 2, this is the primary damage mode that occurs first and that continues to develop in multiple plies for a wide range of applied stress (during quasi-static loading) and time (during creep) before other damage modes develop resulting in ultimate laminate failure.

The features of this model, which differentiate it from published work in this area and highlight new contributions from this thesis, are listed below.

- Prediction of TID evolution in multiple plies of a laminate
- Prediction of TDD evolution in multiple plies of a laminate
- Prediction of creep of laminates with TID and TDD
- Prediction using independently measured lamina properties and without using any fitted parameter.

The five important components of this model are the four modules shown in Figure 3-2 and the fracture criterion. These are discussed in detail below, starting with the core VA module.

3.3 Variational Analysis (VA) Module

This module extends the variational analysis approach developed by Hashin [69] for TID in a ply. Differences between the current modeling approach and Hashin's approach will be highlighted by the end of this section.

When a crack occurs in one ply, the stress state in all plies of the laminate will be altered. The main goal of the variational analysis is to determine an admissible stress state that satisfies the equilibrium equations, interface continuity conditions, and traction boundary conditions.

The following assumptions are made while developing this model.

1) A transverse crack forms in a ply spanning the entire thickness and width of that ply.

2) A new crack always forms in the middle of the intact portion between two cracks in that ply, resulting in a crack spacing, $\mathbf{a^{(k)}}$, that is half of the previous value, $\mathbf{2a^{(k)}}$, shown in Figure 3-3.

3) Axial stresses (σ_{xx}) do not vary along the width, and z-axis (independent of ply thickness), i.e., constant thorough width and thickness direction.

4) Transverse cracks in [-θ] and [+θ] plies are assumed to be at the same location.

In order to derive the admissible stress field which satisfies the equilibrium and boundary conditions, the principle of minimum complementary energy was applied. Complementary energy density of a material is the area between stress-strain curve and σ-axis, i.e. $b=\int_0^\sigma \varepsilon d\sigma$, as shown in Figure 3-4, in contrast with the strain energy density which is the area under stress-strain curve, i.e. $a=\int_0^\varepsilon \sigma d\varepsilon$, as shown in Figure 3-4. The principle of minimum complementary energy will be explained further in this section.

Consider a $[\theta_m/90_n]_s$ laminate a crack density, $\lambda^{(90)}$, $\lambda^{(-\theta)}$, and $\lambda^{(+\theta)}$ in [90], [-θ], and [+θ] plies respectively, as shown in Figure 3-3. Coordicate system of the laminate is also shown in Figure 2-1. Suppose that this laminate has reached this damage state at a given load. The damage state of the ply is characterized by crack density $\lambda^{(k)}$, which is equal to $1/(2a^{(k)})$. $2a^{(k)}$ is the crack spacing for the corresponding ply (k), as shown in Figure 3-3. th_k is the thickness of each ply, and h_1 and h_2 are the distance of the top surfaces of [-θ] and [+θ] plies from the symmetry line. Although the cracks in all plies are aligned in Figure 3-3, the laminate would not fail, since cracks propagating along the width of [-45] and [+45] layers are perpendicular each other. The alignment of cracks in [-45] and [+45] layers, due to the assumption of the location of cracking (Figure 3-3), may not happen in reality, as

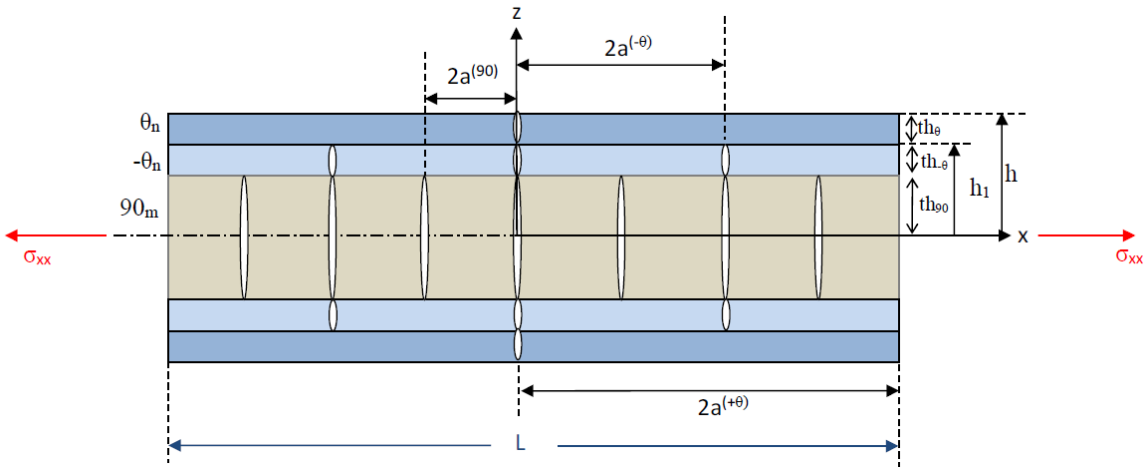

a)

Figure 3-3: a) $[\theta_m/90_n]_s$ laminate with damage in various plies

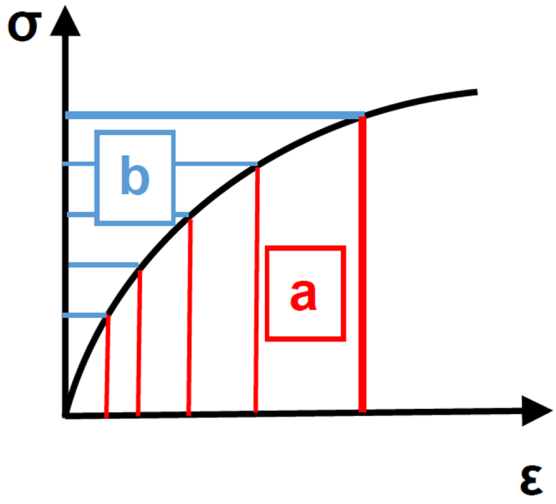

Figure 3-4: (a) Strain energy, and (b) complementary energy

shown in Figure 3-5. However, it was assumed that transverse cracks in [-θ] and [+θ] plies are at the same location. The impact of this assumption on the accuracy of prediction will be discussed in 5.4.1. It is worth mentioning that the number of cracks shown in Figure 3-3 is just for demonstration purposes.

Since crack density in various plies is the not the same at any given stress, the entire gage length of the laminate, shown in Figure 3-3, is used in modeling. Suppose that the total number of intact regions in [θ], [–θ], and [90] are $reg^{(\theta)}$, $reg^{(-\theta)}$, and $reg^{(90)}$ respectively. In other words, the total number of cracks in [θ], [–θ] and [90] are ($n^{(\theta)} = reg^{(\theta)} - 1$), ($n^{(-\theta)} = reg^{(-\theta)} - 1$) and ($n^{(90)} = reg^{(90)} - 1$) , respectively. It should be noted that the two ends of the laminate were not considered cracks since they are transferring the load through the whole laminate. When there is no crack, the plies of the laminate are in plane stress condition, and longitudinal (σ_{xx}), transverse (σ_{yy}) and shear (σ_{xy}) stresses are determined using lamination theory. Suppose that a new crack forms in a ply (e.g., [90]) of $[\theta_m/90_n]_s$ laminate. This could happen in zones I or II or III in Figure 3-1. The analysis below is for cracking in zone III under a constant creep stress (σ_{creep}); however, it is applicable to other zones too. Suppose that the crack forms during a time step Δt from t_{i-1} to t_i. The stress distribution among the plies will change. The new stress state for each ply at time t_i is given by:

$$\sigma_{jl}^{(k)}(t_i) = \sigma_{jl}^{(k)}(t_{i-1}) - \sigma_{jl}^{P(k)} \tag{3-1}$$

where $\sigma_{jl}^{(k)}(t_i)$ (j,l = x,y,z; k = θ,-θ,90) are the stresses in the k^{th} layer at t_i. $\sigma_{jl}^{(k)}(t_{i-1})$ are the stresses in the k^{th} layer at t_{i-1}, and $\sigma_{jl}^{P(k)}$ is the perturbation in the stresses of the k^{th} layer due to damage at t_i. The general form of equation (3-1) can be rewritten for each ply, as follows:

$$\sigma_{xx}^{(k)}(t_i, x) = \sigma_{xx}^{(k)}(t_{i-1}) - \sigma_{xx}^{P(k)}(x) = \sigma_{xx}^{(k)}(t_{i-1}) - \varphi^{(k)}(x) \tag{3-2}$$

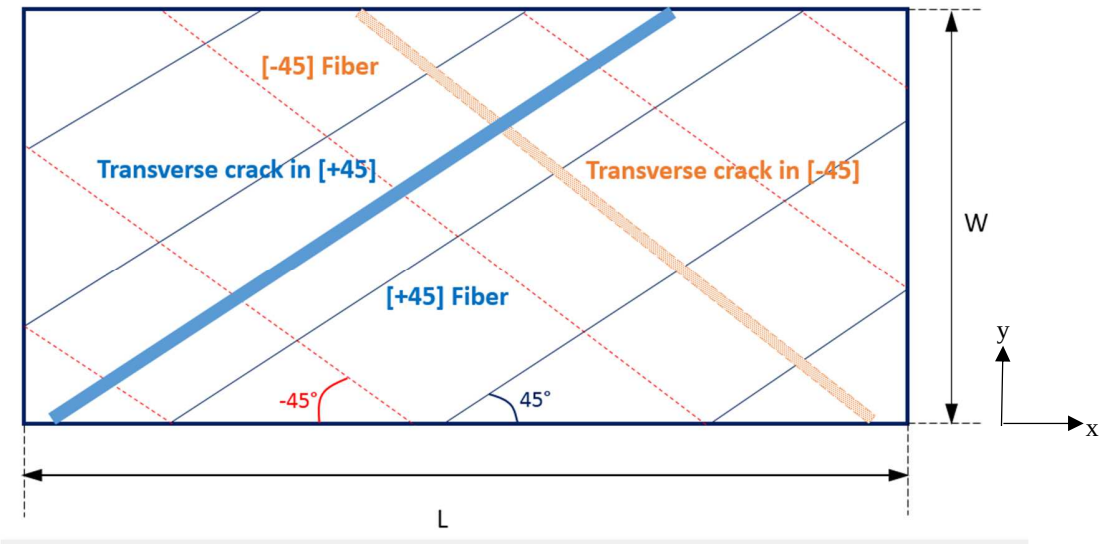

Figure 3-5: The top view of the laminate showing cracks spanning the width in [-45] and [+45] plies

$$\sigma_{xy}^{(k)}(t_i,x)=\sigma_{xy}^{(k)}(t_{i-1})-\sigma_{xy}^{P(k)}(x)=\sigma_{xy}^{(k)}(t_{i-1})-\psi^{(k)}(x) \tag{3-3}$$

$$\sigma_{yy}^{(k)}(t_i,x)=\sigma_{yy}^{(k)}(t_{i-1})-\sigma_{yy}^{P(k)}(x)=\sigma_{yy}^{(k)}(t_{i-1})-\eta^{(k)}(x) \tag{3-4}$$

where $\varphi^{(k)}(x)$, $\psi^{(k)}(x)$, and $\eta^{(k)}(x)$ are the stress perturbation terms in ply (k) along global axial, transverse and shear directions, respectively.

Once the crack occurs in a ply, the bonding between that ply and its adjacent ply vanishes at the tip of the crack. This will introduce out-of-plane normal (σ_{zz}) and shear stresses (σ_{xz} in the x-z plane and σ_{yz} in the y-z plane) as shown in Figure 3-6 for an infinitesimal element near the crack. The equilibrium equations for force balance along X, Y and Z directions are:

Along X-direction

$$(\sigma_{xx}+\frac{\partial\sigma_{xx}}{\partial x}dx)\times(dy\times dz)-\sigma_{xx}\times(dy\times dz)+(\sigma_{xy}+\frac{\partial\sigma_{xy}}{\partial y}dy)\times(dx\times dz)-\sigma_{xy}\times$$

$$(dx\times dz)+(\sigma_{xz}+\frac{\partial\sigma_{xz}}{\partial z}dz)\times(dx\times dy)-\sigma_{xz}\times(dx\times dy)=0 \tag{3-5}$$

Along y-direction:

$$(\sigma_{yy}+\frac{\partial\sigma_{yy}}{\partial y}dy)\times(dx\times dz)-\sigma_{yy}\times(dx\times dz)+\sigma_{xy}\times(dy\times dz)-(\sigma_{xy}+\frac{\partial\sigma_{xy}}{\partial x}dx)\times$$

$$(dy\times dz)-\sigma_{yz}\times(dx\times dy)=0 \tag{3-6}$$

Along z-direction:

$$(\sigma_{zz}+\frac{\partial\sigma_{zz}}{\partial z}dz)\times(dx\times dy)-\sigma_{zz}\times(dx\times dy)+(\sigma_{xz}+\frac{\partial\sigma_{xz}}{\partial x}dx)\times(dy\times dz)-\sigma_{xz}\times$$

$$(dy\times dz)+(\sigma_{yz}+\frac{\partial\sigma_{yz}}{\partial y}dy)\times(dx\times dz)-\sigma_{yz}\times(dx\times dz)=0 \tag{3-7}$$

Rewriting equations (3-5)-(3-7) will result in the equilibrium equations for a given ply (k), given in equations (3-8)-(3-10):

$$\frac{\partial\sigma_{xx}^{(k)}}{\partial x}+\frac{\partial\sigma_{xy}^{(k)}}{\partial y}+\frac{\partial\sigma_{xz}^{(k)}}{\partial z}=0 \tag{3-8}$$

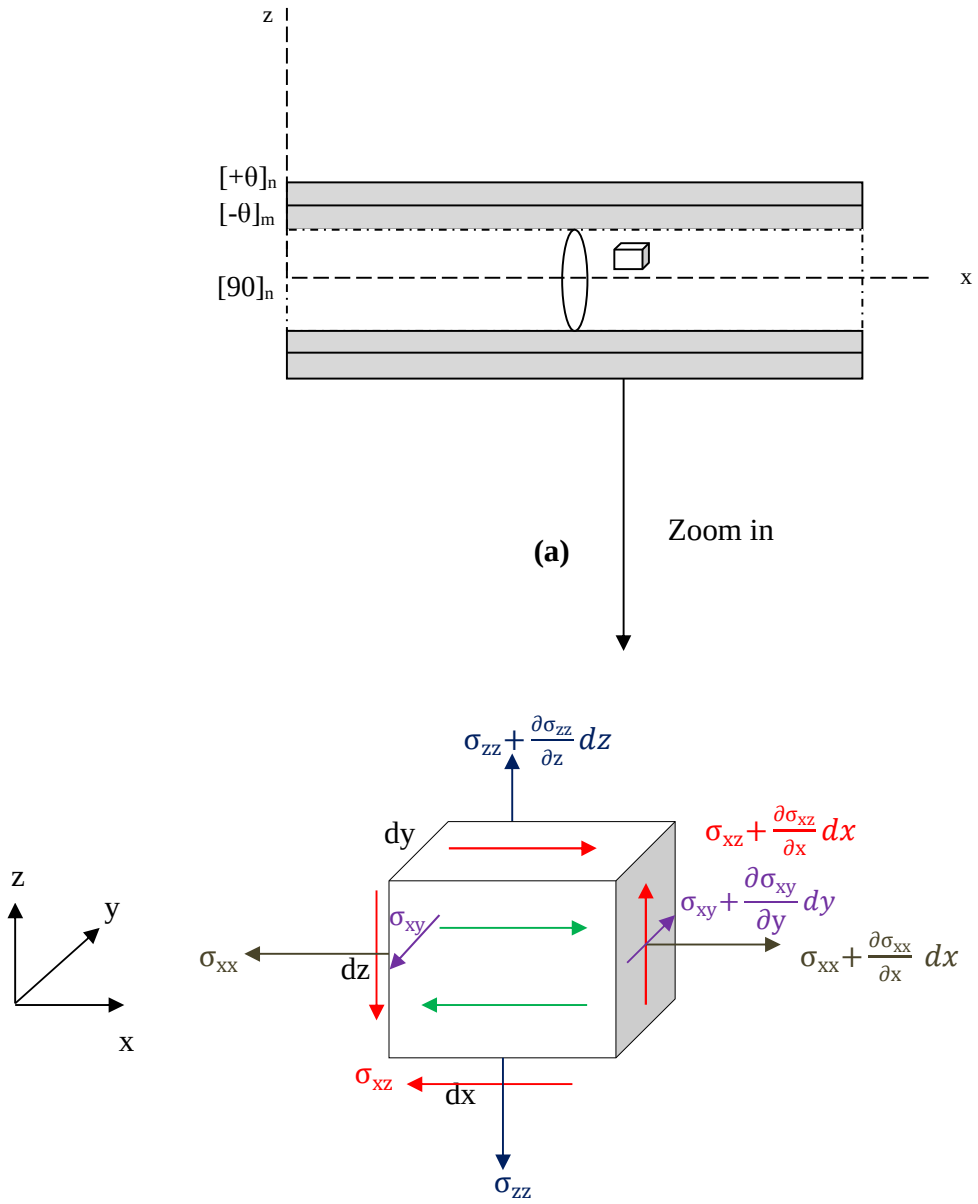
z
[+θ]n
[-θ]m
[90]n
x
Zoom in
(a)
σzz+ ∂σzz/∂z dz
dy
σxz+ ∂σxz/∂x dx
σxy+ ∂σxy/∂y dy
σxy
σxx
dz
σxx+ ∂σxx/∂x dx
z
y
x
σxz
dx
σzz
(b)

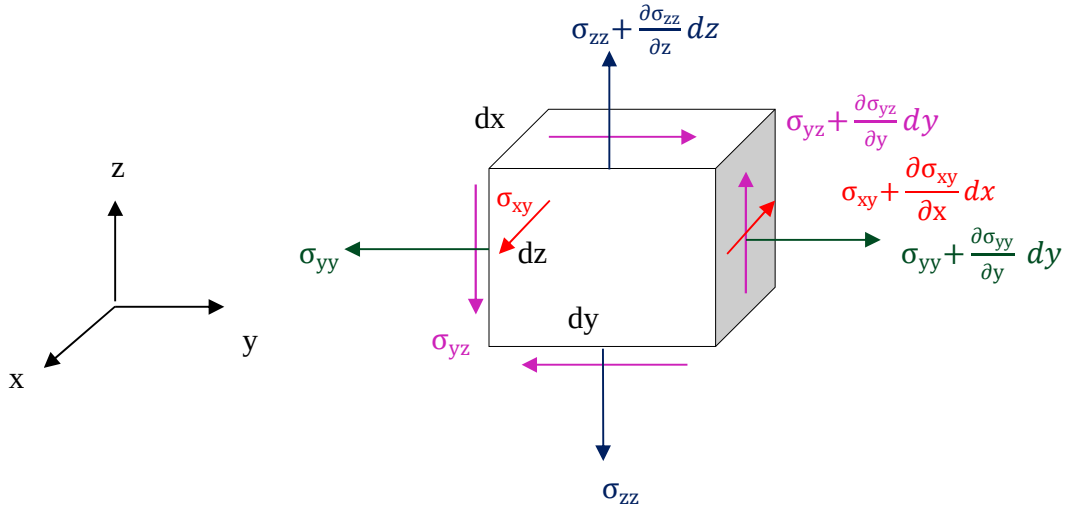

Figure 3-6: a) An element near the crack zone, b) stresses applied to the element in x-z plane view, and c) stresses applied to the element in y-z plane view

$$\frac{\partial \sigma_{xy}^{(k)}}{\partial x}+\frac{\partial \sigma_{yy}^{(k)}}{\partial y}+\frac{\partial \sigma_{yz}^{(k)}}{\partial z}=0 \tag{3-9}$$

$$\frac{\partial \sigma_{xz}^{(k)}}{\partial x}+\frac{\partial \sigma_{yz}^{(k)}}{\partial y}+\frac{\partial \sigma_{zz}^{(k)}}{\partial z}=0 \tag{3-10}$$

The boundary conditions are presented according to the coordinates system, shown in Figure 3-3. The boundary conditions on the crack surface of ply (k) i.e x= ±2 $n^{(k)}$ $a^{(k)}$ are given in equations (3-11)-(3-13).

$$\sigma_{xx}^{(k)}(\pm 2n^{(k)}a^{(k)},z^{(k)})=0 \quad or \quad \varphi_{x=\pm 2n^{(k)}a^{(k)}}^{(k)}=\sigma_{xx}^{(k)}(t_{i-1}) \tag{3-11}$$

$$\sigma_{xy}^{(k)}(\pm 2n^{(k)}\,a^{(k)},z^{(k)})=0 \quad or \quad \psi_{x=\pm 2n^{(k)}a^{(k)}}^{(k)}=\sigma_{xy}^{(k)}(t_{i-1}) \tag{3-12}$$

$$\sigma_{xz}^{(k)}(\pm 2\,n^{(k)}a^{(k)},z^{(k)})=0 \tag{3-13}$$

where $n^{(k)}$ is the number of cracks at ply (k), as defined earlier in this section ($n^{(k)}$ =1,2,...,n). The boundary conditions at the traction free surface are:

$$\sigma_{xz}^{(\theta)}(x,h)=0 \tag{3-14}$$

$$\sigma_{yz}^{(\theta)}(x,h)=0 \tag{3-15}$$

$$\sigma_{zz}^{(\theta)}(x,h)=0 \tag{3-16}$$

Symmetry with respect to the (x-y) plane requires that at the mid-point of two neighboring cracks in [90],

$$\sigma_{xz}^{(90)}(\pm n^{(90)}a^{(90)},z=0)=0 \tag{3-17}$$

and

$$\sigma_{yz}^{(90)}(\pm n^{(90)}a^{(90)},z=0)=0 \tag{3-18}$$

Traction continuity at the two interfaces (between 90 and -θ as well as between -θ and θ) requires

that shear stresses and normal stresses in the z-direction are equal across the interface at $z=th_{90}$ and $z=h_1$. At $z=th_{90}$

$$\sigma_{xz}^{(90)}(x,z=th_{90})=\sigma_{xz}^{(-\theta)}(x,z=th_{90}) \tag{3-19}$$

$$\sigma_{yz}^{(90)}(x,z=th_{90})=\sigma_{yz}^{(-\theta)}(x,z=th_{90}) \tag{3-20}$$

$$\sigma_{zz}^{(90)}(x,z=th_{90})=\sigma_{zz}^{(-\theta)}(x,z=th_{90}) \tag{3-21}$$

At $z=h_1$

$$\sigma_{xz}^{(-\theta)}(x,z=h_1)=\sigma_{xz}^{(\theta)}(x,z=h_1) \tag{3-22}$$

$$\sigma_{yz}^{(-\theta)}(x,z=h_1)=\sigma_{yz}^{(\theta)}(x,z=h_1) \tag{3-23}$$

$$\sigma_{zz}^{(-\theta)}(x,z=h_1)=\sigma_{zz}^{(\theta)}(x,z=h_1) \tag{3-24}$$

Substituting the general form of stress distribution given by equations (3-2)-(3-4) into equilibrium equations (3-8)-(3-10) and applying the boundary conditions given in (3-11)-(3-24), the stress state in each ply reduces to the following.

[90] plies:

$$\sigma_{xx}^{(90)}(t_i,x)=\sigma_{xx}^{(90)}(t_{i-1})-\varphi^{(90)}(x) \tag{3-25}$$

$$\sigma_{xy}^{(90)}(t_i,x)=\sigma_{xy}^{(90)}(t_{i-1})-\psi^{(90)}(x) \tag{3-26}$$

$$\sigma_{yy}^{(90)}(t_i,x)=\sigma_{yy}^{(90)}(t_{i-1})-\eta^{(90)}(x) \tag{3-27}$$

$$\sigma_{xz}^{(90)}(t_i,x,z)=\frac{d\varphi^{(90)}(x)}{dx}z \tag{3-28}$$

$$\sigma_{yz}^{(90)}(t_i,x,z)=\frac{d\psi^{(90)}(x)}{dx}z \tag{3-29}$$

$$\sigma_{zz}^{(90)}(t_i,x,z)=-\frac{d^2\varphi^{(90)}(x)}{dx^2}\left(\frac{z^2+h}{2}-th_{90}\right)-\frac{d^2\varphi^{(-\theta)}(x)}{dx^2}\left(\frac{h-th_{90}}{2}\right) \tag{3-30}$$

[-θ] plies:

$$\sigma_{xx}^{(-\theta)}(t_i,x)=\sigma_{xx}^{(-\theta)}(t_{i-1})-\varphi^{(-\theta)}(x) \tag{3-31}$$

$$\sigma_{xy}^{(-\theta)}(t_i,x)=\sigma_{xy}^{(-\theta)}(t_{i-1})-\psi^{(-\theta)}(x) \tag{3-32}$$

$$\sigma_{yy}^{(-\theta)}(t_i,x)=\sigma_{yy}^{(-\theta)}(t_{i-1})-\eta^{(-\theta)}(x) \tag{3-33}$$

$$\sigma_{xz}^{(-\theta)}(t_i,x,z)=\frac{d\varphi^{(-\theta)}(x)}{dx}(z-h_1)-\frac{d\varphi^{(\theta)}(x)}{dx}th_\theta \tag{3-34}$$

$$\sigma_{yz}^{(-\theta)}(t_i,x,z)=\frac{d\psi^{(-\theta)}(x)}{dx}(z-h_1)-\frac{d\psi^{(\theta)}(x)}{dx}th_\theta \tag{3-35}$$

$$\sigma_{zz}^{(-\theta)}(t_i,x,z)=-\frac{d^2\varphi^{(-\theta)}(x)}{dx^2}\frac{(h_1-z)^2}{2}+\frac{d^2\varphi^{(\theta)}(x)}{dx^2}th_\theta(z-h+\frac{th_\theta}{2}) \tag{3-36}$$

[θ] plies:

$$\sigma_{xx}^{(\theta)}(t_i,x)=\sigma_{xx}^{(\theta)}(t_{i-1})-\varphi^{(\theta)}(x) \tag{3-37}$$

$$\sigma_{xy}^{(\theta)}(t_i,x)=\sigma_{xy}^{(\theta)}(t_{i-1})-\psi^{(\theta)}(x) \tag{3-38}$$

$$\sigma_{yy}^{(\theta)}(t_i,x)=\sigma_{yy}^{(\theta)}(t_{i-1})-\eta^{(\theta)}(x) \tag{3-39}$$

$$\sigma_{xz}^{(\theta)}(t_i,x,z)=-\frac{d\varphi^{(\theta)}(x)}{dx}(h-z) \tag{3-40}$$

$$\sigma_{yz}^{(\theta)}(t_i,x,z)=-\frac{d\psi^{(\theta)}(x)}{dx}(h-z) \tag{3-41}$$

$$\sigma_{zz}^{(\theta)}(t_i,x,z)=-\frac{d^2\varphi^{(\theta)}(x)}{dx^2}\frac{(h-z)^2}{2} \tag{3-42}$$

The stress state derived in equations (3-25)-(3-42) contains three unknown perturbation functions for each layer, resulting in a total of nine unknowns. In order to determine these perturbation terms, i.e., $\varphi^{(k)}(x)$, $\psi^{(k)}(x)$ and $\eta^{(k)}(x)$, the *principle of minimum complementary energy* is applied. The principle of minimum complementary energy states [84] that, "among all

the sets of admissible stresses which satisfy the equations of equilibrium and boundary conditions, the sets of actual stress components make the complementary energy an absolute minimum." Calculus of variation is used to minimize the complementary energy function. The complementary energy U_c, in absence of displacement boundary conditions, is given by (3-43)

$$U_c = \iint \varepsilon_{ij} d\sigma_{ij} dv = \frac{1}{2} \int S_{ijkl} . \sigma_{kl} . \sigma_{ij} dv \tag{3-43}$$

where σ_{ij} and S_{ijkl} are the stress and the compliance tensors, respectively, and V is the volume of the intact regions along the gauge length of the sample, shown in Figure 3-3. Hashin [69] has shown that the complementary energy for any cracked body is equal to the summation of the complementary energy of the uncracked body (U_c^0) and the complementary energy resulting from perturbation stresses (U_c^P).

$$U_c = U_c^0 + U_c^P \tag{3-44}$$

The perturbation stress state, given by equations (3-25)-(3-42), is plugged into equation (3-43) and (3-44) to determine the perturbation functions that minimize the complementary energy of the cracked laminate. Due to symmetry with respect to mid-plane, z=0, only half of the cracked region, i.e., $0 \leq z \leq h$, is analyzed

$$U_c^P = n^{(\theta)} \int_{-a_\theta}^{a_\theta} \int_{h_1}^{h} W^{(\theta)} dzdx + n^{(-\theta)} \int_{-a_{-\theta}}^{a_{-\theta}} \int_{th_{90}}^{h_1} W^{(-\theta)} dzdx + n^{(90)} \int_{-a_{90}}^{a_{90}} \int_{0}^{th_{90}} W^{(90)} dzdx \tag{3-45}$$

where $W^{(k)}$ is the complementary energy associated with perturbation stress state in one intact portion of ply (k), and $n^{(k)}$ is the number of intact regions in ply (k). Equation (3-45) can be written in terms of stresses in various plies of the laminate, as follows:

$$U_c^P = \frac{1}{2} n^{(\theta)} \int_{-a_\theta}^{a_\theta} \int_{h_1}^{h} \{[\sigma^{P(\theta)}(t_i)]_{x,y} [S^{(\theta)}(t_{i-1})]_{x,y} [\sigma^{P(\theta)}(t_i)]_{x,y}\} dz dx +$$
$$\frac{1}{2} n^{(-\theta)} \int_{-a-_\theta}^{a-_\theta} \int_{th_{90}}^{h_1} \{[\sigma^{P(-\theta)}(t_i)]_{x,y} [S^{(-\theta)}(t_{i-1})]_{x,y} [\sigma^{P(-\theta)}(t_i)]_{x,y}\} dz dx + \quad (3\text{-}46)$$
$$\frac{1}{2} n^{(90)} \int_{-a_{90}}^{a_{90}} \int_{0}^{th_{90}} \{[\sigma^{P(90)}(t_i)]_{x,y} [S^{(90)}(t_{i-1})]_{x,y} [\sigma^{P(90)}(t_i)]_{x,y}\} dz dx$$

where $[\sigma^{P(k)}(t_i)]_{x,y}$ and $[S^k(t_{i-1})]_{x,y}$ are the perturbation stress matrix at t_i and compliance matrix at t_{i-1}, respectively. The terms of the matrices are provided below. The relationship between stress and strain is given by equation (3-47).

$$\begin{bmatrix} \varepsilon_{xx} \\ \varepsilon_{yy} \\ \varepsilon_{zz} \\ \gamma_{yz} \\ \gamma_{zx} \\ \gamma_{xy} \end{bmatrix} = \begin{bmatrix} S_{xx}^{(k)}(t_{i-1}) & S_{xy}^{(k)}(t_{i-1}) & S_{xz}^{(k)}(t_{i-1}) & 0 & 0 & S_{xs}^{(k)}(t_{i-1}) \\ S_{xy}^{(k)}(t_{i-1}) & S_{yy}^{(k)}(t_{i-1}) & S_{yz}^{(k)}(t_{i-1}) & 0 & 0 & S_{ys}^{(k)}(t_{i-1}) \\ S_{xz}^{(k)}(t_{i-1}) & S_{yz}^{(k)}(t_{i-1}) & S_{zz}^{(k)}(t_{i-1}) & 0 & 0 & S_{zs}^{(k)}(t_{i-1}) \\ 0 & 0 & 0 & S_{qq}^{(k)}(t_{i-1}) & S_{qr}^{(k)}(t_{i-1}) & 0 \\ 0 & 0 & 0 & S_{qr}^{(k)}(t_{i-1}) & S_{rr}^{(k)}(t_{i-1}) & 0 \\ S_{xs}^{(k)}(t_{i-1}) & S_{ys}^{(k)}(t_{i-1}) & S_{zs}^{(k)}(t_{i-1}) & 0 & 0 & S_{ss}^{(k)}(t_{i-1}) \end{bmatrix} \begin{bmatrix} \sigma_{xx}^P \\ \sigma_{yy}^P \\ \sigma_{zz}^P \\ \sigma_{yz}^P \\ \sigma_{zx}^P \\ \sigma_{xy}^P \end{bmatrix} \quad (3\text{-}47)$$

where $S_{jl}^{(k)}(t_{i-1})$ (k=θ, -θ, 90 and j, l=x, y, z, r, q, s), where q=yz, r=xz and s=xy, are the transformed compliance in global coordinates of the ply calculated using equation (3-48):

$$[S^{(k)}(t_{i-1})]_{j,l} = [T_2^{-1}][S^{(k)}(t_{i-1})]_{j',l'}[T_1] \quad (3\text{-}48)$$

$[S^{(k)}(t_{i-1})]_{j',l'}$ is the unidirectional creep compliance at time t_{i-1} along material coordinates of the ply, given in equation (3-49). $[T_1]$ and $[T_2]$ are transformation matrices given in equation (3-50).

$$[S_{j'l'}^{(k)}]=\begin{bmatrix} S_{11}^{(k)} & S_{12}^{(k)} & S_{13}^{(k)} & 0 & 0 & 0 \\ S_{12}^{(k)} & S_{22}^{(k)}(t_{i-1}) & S_{23}^{(k)}(t_{i-1}) & 0 & 0 & 0 \\ S_{13}^{(k)} & S_{23}^{(k)}(t_{i-1}) & S_{33}^{(k)}(t_{i-1}) & 0 & 0 & 0 \\ 0 & 0 & 0 & S_{44}^{(k)}(t_{i-1}) & 0 & 0 \\ 0 & 0 & 0 & 0 & S_{55}^{(k)}(t_{i-1}) & 0 \\ 0 & 0 & 0 & 0 & 0 & S_{66}^{(k)}(t_{i-1}) \end{bmatrix}$$

$$=\begin{bmatrix} \frac{1}{E_{11}^{(k)}} & \frac{-\nu_{12}^{(k)}}{E_{11}^{(k)}} & \frac{-\nu_{13}^{(k)}}{E_{11}^{(k)}} & 0 & 0 & 0 \\ \frac{-\nu_{12}^{(k)}}{E_{11}^{(k)}} & \frac{1}{E_{22}^{(k)}(t_{i-1})} & \frac{-\nu_{23}^{(k)}}{E_{22}^{(k)}(t_{i-1})} & 0 & 0 & 0 \\ \frac{-\nu_{13}^{(k)}}{E_{11}^{(k)}} & \frac{-\nu_{23}^{(k)}}{E_{22}^{(k)}(t_{i-1})} & \frac{1}{E_{33}^{(k)}(t_{i-1})} & 0 & 0 & 0 \\ 0 & 0 & 0 & \frac{1}{G_{23}^{(k)}(t_{i-1})} & 0 & 0 \\ 0 & 0 & 0 & 0 & \frac{1}{G_{13}^{(k)}(t_{i-1})} & 0 \\ 0 & 0 & 0 & 0 & 0 & \frac{1}{G_{12}^{(k)}(t_{i-1})} \end{bmatrix}$$

(3-49)

$$[T_1]=\begin{bmatrix} m^2 & n^2 & 0 & 0 & 0 & 2mn \\ n^2 & m^2 & 0 & 0 & 0 & -2mn \\ 0 & 0 & 1 & 0 & 0 & 0 \\ 0 & 0 & 0 & m & -n & 0 \\ 0 & 0 & 0 & n & m & 0 \\ -mn & mn & 0 & 0 & 0 & m^2-n^2 \end{bmatrix},\ [T_2]=\begin{bmatrix} m^2 & n^2 & 0 & 0 & 0 & mn \\ n^2 & m^2 & 0 & 0 & 0 & -mn \\ 0 & 0 & 1 & 0 & 0 & 0 \\ 0 & 0 & 0 & m & -n & 0 \\ 0 & 0 & 0 & n & m & 0 \\ -2mn & 2mn & 0 & 0 & 0 & m^2-n^2 \end{bmatrix}$$

(3-50)

E_{jl} (t_{i-1}), G_{jl} (t_{i-1}) and ν_{jl} (t_{i-1}) (j, l=1, 2, 3) are Young's modulus, shear modulus and Poisson's ratio along principal directions at time t_{i-1}. *m*, and *n* are sin (k) and cos (k), respectively, where k is the orientation of the fiber in the ply with respect to the global x-axis . k = 90^o, -θ, or + θ for the three ply groups of the chosen laminate.

Substituting equations (3-25)-(3-42) and (3-47)-(3-50) in equation (3-46) results in

$$W^{(90)} = n^{(90)} \int_{-a_{90}}^{a_{90}} [\frac{47}{15}\frac{(\varphi'^{(90)})^2 th^5}{E_{yy}^{(90)}(t_{i-1})} - 5\frac{\varphi'^{(90)}\varphi'^{(-\theta)} th^5}{E_{yy}^{(90)}(t_{i-1})} + \frac{4}{3}\frac{(\varphi'^{(90)})^2 th^3}{G_{xy}^{(90)}(t_{i-1})} - \frac{10}{3}\frac{\nu_{yz}^{(90)}(t_{i-1})\varphi'^{(90)}\eta^{(90)} th^3}{E_{yy}^{(90)}(t_{i-1})}$$
$$-\frac{10}{3}\frac{\nu_{xy}^{(90)}(t_{i-1})\varphi'^{(90)}\varphi^{(90)} th^3}{E_{yy}^{(90)}(t_{i-1})} + \frac{4}{3}\frac{(\psi'^{(90)})^2 th^3}{G_{yz}^{(90)}(t_{i-1})} + \frac{(\varphi^{(90)})^2 th}{E_{xx}^{(90)}(t_{i-1})} + \frac{(\eta^{(90)})^2 th}{E_{yy}^{(90)}(t_{i-1})} + \frac{9}{4}\frac{(\varphi'^{(-\theta)})^2 th^5}{E_{yy}^{(90)}(t_{i-1})} + \frac{(\psi^{(90)})^2 th}{G_{xy}^{(90)}(t_{i-1})}$$
$$+3\frac{\nu_{yz}^{(90)}(t_{i-1})\eta^{(90)}\varphi'^{(-\theta)} th^3}{E_{yy}^{(90)}(t_{i-1})} - 2\frac{\nu_{xy}^{(90)}(t_{i-1})\varphi^{(90)}\eta^{(90)} th}{E_{xx}^{(90)}(t_{i-1})} + 3\frac{\nu_{xy}^{(90)}(t_{i-1})\varphi^{(90)}\varphi'^{(-\theta)} th^3}{E_{xx}^{(90)}(t_{i-1})}]dx$$

(3-51)

$$W^{(-\theta)} = n^{(-\theta)} \int_{-a_{-\theta}}^{a_{-\theta}} [\frac{1}{40}\frac{(\varphi'^{(-\theta)})^2 th^5}{E_{yy}^{(-\theta)}(t_{i-1})} + \frac{5}{24}\frac{\varphi'^{(-\theta)}\varphi'^{(\theta)} th^5}{E_{yy}^{(-\theta)}(t_{i-1})} + \frac{1}{6}\frac{(\varphi'^{(-\theta)})^2 th^3}{G_{xy}^{(-\theta)}(t_{i-1})} - \frac{1}{6}\frac{\nu_{yz}^{(-\theta)}(t_{i-1})\varphi'^{(-\theta)}\eta^{(-\theta)} th^3}{E_{yy}^{(-\theta)}(t_{i-1})}$$
$$-\frac{1}{6}\frac{\nu_{xy}^{(-\theta)}(t_{i-1})\varphi'^{(-\theta)}\varphi^{(-\theta)} th^3}{E_{xx}^{(-\theta)}(t_{i-1})} + \frac{1}{6}\frac{(\psi'^{(-\theta)})^2 th^3}{G_{yz}^{(-\theta)}(t_{i-1})} + \frac{1}{2}\frac{(\varphi^{(-\theta)})^2 th}{E_{xx}^{(-\theta)}(t_{i-1})} + \frac{1}{2}\frac{(\eta^{(-\theta)})^2 th}{E_{yy}^{(-\theta)}(t_{i-1})}$$
$$+\frac{13}{24}\frac{(\varphi'^{(\theta)})^2 th^5}{E_{yy}^{(-\theta)}(t_{i-1})} + \frac{1}{2}\frac{(\psi^{(-\theta)})^2 th}{G_{xy}^{(-\theta)}(t_{i-1})} + \frac{1}{2}\frac{\psi'^{(-\theta)}\psi'^{(\theta)} th^3}{G_{yz}^{(-\theta)}(t_{i-1})} + \frac{1}{2}\frac{\varphi'^{(-\theta)}\varphi'^{(\theta)} th^3}{G_{xy}^{(-\theta)}(t_{i-1})} + \frac{1}{2}\frac{(\psi'^{(\theta)})^2 th^3}{G_{yz}^{(-\theta)}(t_{i-1})}$$
$$+\frac{1}{2}\frac{(\varphi'^{(-\theta)})^2 th^3}{G_{xy}^{(-\theta)}(t_{i-1})} - \frac{\nu_{yz}^{(-\theta)}(t_{i-1})\varphi'^{(\theta)}\eta^{(-\theta)} th^3}{E_{yy}^{(-\theta)}(t_{i-1})} - \frac{\nu_{xy}^{(-\theta)}(t_{i-1})\varphi'^{(\theta)}\varphi^{(-\theta)} th^3}{E_{xx}^{(-\theta)}(t_{i-1})} - \frac{\nu_{xy}^{(-\theta)}(t_{i-1})\varphi^{(-\theta)}\eta^{(-\theta)} th^3}{E_{xx}^{(-\theta)}(t_{i-1})}$$

(3-52)

$$W^{(\theta)} = n^{(\theta)} \int_{-a_{\theta}}^{a_{\theta}} [\frac{1}{40}\frac{(\varphi'^{(\theta)})^2 th^5}{E_{yy}^{(\theta)}(t_{i-1})} - \frac{1}{6}\frac{\nu_{yz}^{(\theta)}(t_{i-1})\eta^{(\theta)}\varphi'^{(\theta)} th^3}{E_{yy}^{(\theta)}(t_{i-1})} - \frac{1}{6}\frac{\nu_{xy}^{(\theta)}(t_{i-1})\varphi'^{(\theta)}\varphi^{(\theta)} th^3}{E_{xx}^{(\theta)}(t_{i-1})} + \frac{1}{6}\frac{(\varphi'^{(\theta)})^2 th^3}{G_{xy}^{(\theta)}(t_{i-1})}$$
$$+\frac{1}{6}\frac{(\psi'^{(\theta)})^2 th^3}{G_{yz}^{(\theta)}(t_{i-1})} + \frac{1}{2}\frac{(\varphi^{(\theta)})^2 th}{E_{xx}^{(\theta)}(t_{i-1})} + \frac{1}{2}\frac{(\eta^{(\theta)})^2 th}{E_{yy}^{(\theta)}(t_{i-1})} - \frac{\nu_{xy}^{(\theta)}(t_{i-1})\varphi^{(\theta)}\eta^{(\theta)} th}{E_{xx}^{(\theta)}(t_{i-1})} + \frac{1}{2}\frac{(\psi^{(\theta)})^2 th}{G_{xy}^{(\theta)}(t_{i-1})}]dx$$

(3-53)

In deriving equation (3-51)-(3-53), it is assumed that the thicknesses of all plies are the same, i.e., $th_{90}=th_{-\theta}=th_{\theta}$, and equal to *th*. It is also assumed that the laminate is transversely isotropic, and the properties in the x-z plane are the same as those in the x-y plane, as follows:

$$E_{33}(t_{i-1}) = E_{22}(t_{i-1})$$

(3-54)

$$G_{13}(t_{i-1}) = G_{12}(t_{i-1}) \quad (3\text{-}55)$$

$$\nu_{13}(t_{i-1}) = \nu_{12}(t_{i-1}) \quad (3\text{-}56)$$

$$G_{23}(t_{i-1}) = \frac{E_{22}(t_{i-1})}{2(1+\nu_{23}(t_{i-1}))} \tag{3-57}$$

where

$$\nu_{23}(t_{i-1}) = 2.45\nu_{21}(t_{i-1}) \tag{3-58}$$

Equation (3-58) derived as per according to Ref. [65]. In order to calculate the stress perturbation terms, $\varphi^{(k)}(x)$, $\psi^{(k)}(x)$, and $\eta^{(k)}(x)$, the complementary energy given by equations (3-51)-(3-53) must be minimized. The first variation of energy equations (3-51)-(3-53) with respect to each perturbation stress, i.e. $\varphi^{(k)}(x)$, $\psi^{(k)}(x)$, and $\eta^{(k)}(x)$ will provide Euler-Lagrange differential equations [109]. Since there are eight unknown perturbation stresses (no in-plane shear in [90]), eight Euler-Lagrange differential equations were derived. The solution to the derived Euler-Lagrange equations will minimize the complementary energy. The Euler-Lagrange equations for the functions $\varphi^{(k)}(x)$, $\psi^{(k)}(x)$ and $\eta^{(k)}(x)$ are given in equations (3-59)-(3-66)

$$A_1\frac{d^4}{dx^4}\varphi^{(90)}(x) + A_2\frac{d^2}{dx^2}\varphi^{(90)}(x) + A_3\varphi^{(90)}(x) + A_4\frac{d^4}{dx^4}\varphi^{(-\theta)}(x) + A_5\frac{d^2}{dx^2}\varphi^{(\theta)}(x) + A_6\frac{d^2}{dx^2}\eta^{(90)}(x) + A_7\eta^{(90)}(x) = 0 \tag{3-59}$$

$$A_6\frac{d^2}{dx^2}\varphi^{(90)}(x) + A_7\varphi^{(90)}(x) + A_{17}\frac{d^2}{dx^2}\varphi^{(-\theta)}(x) + A_8\eta^{(90)}(x) = 0 \tag{3-60}$$

$$A_9\frac{d^4}{dx^4}\varphi^{(-\theta)}(x) + A_{10}\frac{d^2}{dx^2}\varphi^{(-\theta)}(x) + A_{11}\varphi^{(-\theta)}(x) + A_{12}\frac{d^4}{dx^4}\varphi^{(\theta)}(x) + A_{13}\frac{d^2}{dx^2}\varphi^{(\theta)}(x) + A_{14}\frac{d^2}{dx^2}\varphi^{(90)}(x) + A_5\frac{d^2}{dx^2}\varphi^{(90)}(x) + A_{15}\frac{d^2}{dx^2}\eta^{(-\theta)}(x) + A_{16}\eta^{(-\theta)} + A_{17}\frac{d^2}{dx^2}\eta^{(90)}(x) + A_{25}\psi^{(-\theta)}(x) + A_{26}\frac{d^2}{dx^2}\psi^{(-\theta)}(x) = 0 \tag{3-61}$$

$$A_{15}\frac{d^2}{dx^2}\varphi^{(-\theta)}(x) + A_{16}\varphi^{(-\theta)}(x) + 6A_{15}\frac{d^2}{dx^2}\varphi^{(\theta)}(x) + A_{18}\frac{d^2}{dx^2}\eta^{(-\theta)}(x) + A_{27}\psi^{(-\theta)}(x) = 0 \tag{3-62}$$

$$A_{19}\frac{d^4}{dx^4}\varphi^{(\theta)}(x) + A_{20}\frac{d^2}{dx^2}\varphi^{(\theta)}(x) + A_{21}\varphi^{(\theta)}(x) + A_{12}\frac{d^4}{dx^4}\varphi^{(-\theta)}(x) + A_{13}\frac{d^2}{dx^2}\varphi^{(-\theta)}(x) + 6A_{15}\frac{d^2}{dx^2}\eta^{(-\theta)}(x) + A_{23}\eta^{(-\theta)} + A_{22}\frac{d^2}{dx^2}\eta^{(\theta)}(x) + A_{28}\frac{d^2}{dx^2}\psi^{(-\theta)}(x) + A_{29}\frac{d^2}{dx^2}\psi^{(\theta)}(x) + A_{30}\psi^{(\theta)}(x) = 0 \tag{3-63}$$

$$A_{22}\frac{d^2}{dx^2}\varphi^{(\theta)}(x) + A_{23}\varphi^{(\theta)}(x) + A_{24}\eta^{(\theta)}(x) + A_{31}\psi^{(\theta)}(x) = 0 \quad (3\text{-}64)$$

$$A_{32}\frac{d^2}{dx^2}\psi^{(-\theta)}(x) + A_{33}\psi^{(-\theta)}(x) + A_{34}\frac{d^2}{dx^2}\psi^{(\theta)}(x) + A_{35}\varphi^{(\theta)}(x) + A_{36}\frac{d^2}{dx^2}\varphi^{(\theta)}(x) = 0 \quad (3\text{-}65)$$

$$A_{37}\frac{d^2}{dx^2}\psi^{(\theta)}(x) + A_{38}\psi^{(\theta)}(x) + A_{39}\frac{d^2}{dx^2}\psi^{(-\theta)}(x) + A_{40}\frac{d^2}{dx^2}\varphi^{(\theta)}(x) + A_{41}\eta^{(\theta)}(x) + A_{42}\varphi^{(\theta)}(x) = 0 \quad (3\text{-}66)$$

The coefficients, A_1-A_{42}, are groupings of various terms and are given in the Appendix B. Since $\psi^{(90)}(x)$ is equal to zero (no shear stress in [90] plies), the system of the above differential equations has eight unknowns and eight differential equations.

In order to solve the derived differential equations, appropriate "imposed boundary conditions" were applied. Here, imposed boundary conditions mean constant stress rate or constant strain rate used during loading to the required creep load. Figure 3-7 shows the changes in the stress-strain curve for a finite amount of a crack growth during constant strain rate and constant stress rate loading. For a constant strain rate loading, represented by ABD in Figure 3-7, the stress drops to D when the cracking occurs at B. However, for the case of constant stress rate loading, the stress remains unchanged and the strain increases to C when cracking occurs. In view of this, it is important to use the appropriate conditions to have accurate results.

In our experiments, constant strain rate was used to load the sample to the creep load. Hence we used contant strain rate conditions in QSL module. In contrast, the load was constant during the actual creep test and hence, constant stress rate condition was used in SL module.

Due to the complexity of the derived differential equations, these equations were solved numerically using MATLAB function *bvp4c*, which has been developed to solve the boundary value problems for ordinary differential equations. This function is capable of solving a system of non-linear differential equations by defining a grid on which the solution is computed and

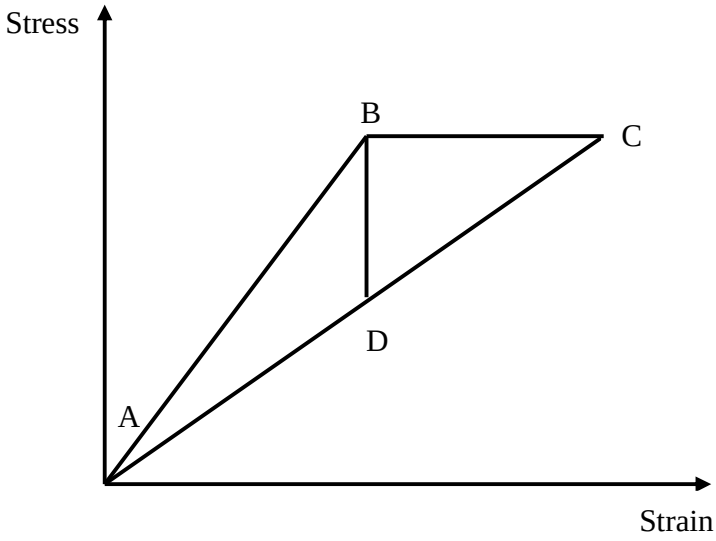

Figure 3-7: Stress-strain schematic for constant strain rate and constant load rate tests.

ABC refers to constant load rate, and ABD refers to a constant strain rate test.

compared with an initial guess. Further information on the solution procedure is provided in Section 4.5.5.1.

Once the unknown perturbation stress terms are determined, they can be substituted into equations (3-26)-(3-43) to completely define the stress state of each ply at a given temperature or applied stress or creep time upon formation of a new crack in a ply. This result is input to PIS, QSL, and SL modules, depending on which module invoked the VA module.

In order to highlight the differences between the current approach and Hashin's approach [69], a very brief introduction to Hashin's approach is given below.

Hashin used a 2-D variational analysis to determine the stress state of each ply due to transverse cracking in [90] plies of a cross-ply laminate, shown in Figure 3-8. Since the cross ply laminate has two ply groups ([0] and [90]), six stress perturbation terms are required to determine the stress state. However, there is no shear coupling in cross-ply laminates; hence, two perturbation terms associated with shear vanish. He also assumed zero perturbation in stress along the y direction. Hence, he considered only two perturbation terms to address the change in axial stress in both plies, due to transverse cracking in [90], which is given in equations (3-67) and (3-68).

$$\sigma_{xx}^{(90)} = \sigma_{xx}^{0(90)} - \sigma_{xx}^{P(90)} = \sigma_{xx}^{0(90)} - \zeta_1(x) \tag{3-67}$$

$$\sigma_{xx}^{(\theta)} = \sigma_{xx}^{0(\theta)} - \sigma_{xx}^{P(\theta)} = \sigma_{xx}^{0(\theta)} - \zeta_2(x) \tag{3-68}$$

where $\sigma_{xx}^{0(90)}$ and $\sigma_{xx}^{0(\theta)}$ are initial stresses before cracking, and $\zeta_1(x)$ and $\zeta_2(x)$ are stress perturbation terms for [90] and [0], respectively. He assumed a constant load rate condition (i.e. stress on the laminate before and after cracking is the same) which allows writing one perturbation term based on the other using force balance, as follows:

$$\sigma_{xx}^{(0)}\, th_0 + \sigma_{xx}^{(90)}\, th_{90} = \sigma_{xx}^{0(0)}\, th_0 + \sigma_{xx}^{0(90)}\, th_{90} = \sigma_{xx}\, h \tag{3-69}$$

.

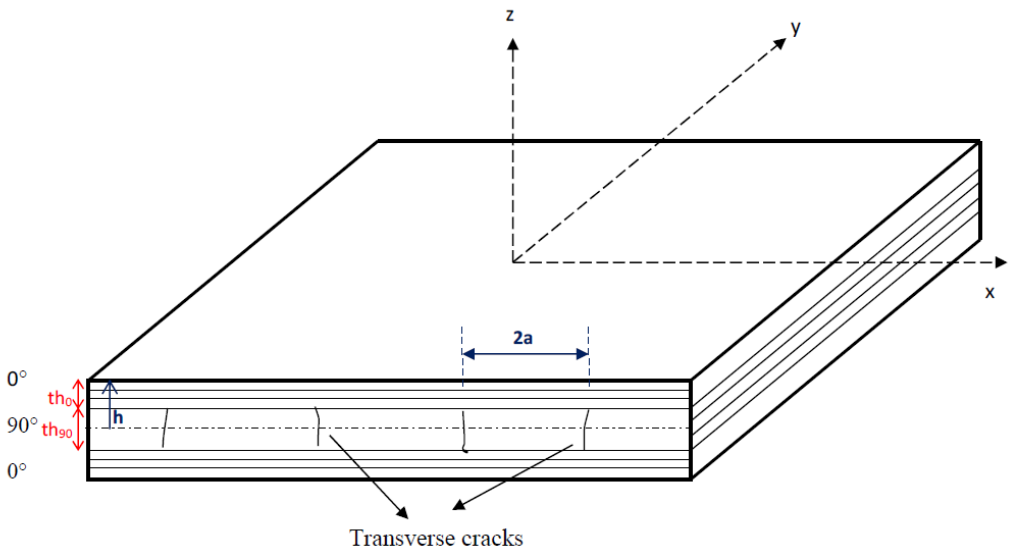

Figure 3-8: A damaged $[0/90]_s$ laminate used in Hashin's analysis

where, th_0, $th_{90,}$ and h are the thicknesses of [0], [90], and laminate respectively. Substituting equation (3-69) in (3-67) and (3-68) results in:

$$\xi_2(x) = -\frac{th_{90}}{th_0}\frac{\sigma_{xx}^{0(90)}}{\sigma_{xx}^{0(0)}}\xi_1(x) \tag{3-70}$$

In contrast, the present analysis considers cracking in all three plies of the laminate, i.e., θ, -θ, and 90 where θ is not equal to zero. Also, the current analysis considers perturbation in in-plane normal, transverse and shear stresses independently due to cracking at each ply. In other words, Hashin used one stress perturbation term per ply and determined the stress field by minimizing the complementary energy. However, in the current analysis three stress perturbation terms per ply are defined, and hence, a total of nine unknown stress perturbation terms are determined based on the principle of minimum complementary energy. In addition, while Hashin's analysis solves for a constant load rate condition, the present analysis solves for a constant strain-rate condition during ramping up to creep load (as well as during thermal loading in Zone I) and for a constant load rate condition after reaching the creep load. Furthermore, while Hashin's analysis can be applied only for TID prediction, the present analysis can be applied for prediction of both TID and TDD.

Finally, while the current analysis is capable of predicting the crack density, the corresponding stress state, and the laminate modulus, Hashin's approach merely determines the stress state for a given crack density and modulus.

3.4 Process-Induced Stress (PIS) Module

This module calculates the process-induced residual stresses and transverse crack density in each ply during cooling down from the process temperature to room temperature, as illustrated

in Figure 3-9. The variable in this module is ΔT. Due to the influence of temperature on the properties of the lamina, as well as the possibility of ply cracking due to induced residual stress, the temperature is decreased incrementally and the ply stress state is determined after each step decrement in temperature.

Using lamination theory, the unconstrained thermal strains of each ply are determined using equation (3-71)

$$e_{jl} = \alpha_j \left(T - T_{cure}\right) \qquad j = l = 1, 2 \tag{3-71}$$

$$e_{jl} = \varepsilon_{Cure\,Shrinkage} \qquad j = l = 2 \tag{3-72}$$

where e_{jl} in equation (3-71) is unconstrained thermal strain, α_{jl} is thermal expansion coefficients and T is temperature, and e_{jl} in equation (3-72) is the unconstrained cure shrinkage strain. Having transferred these strains to global coordinates to obtain $[e_T]_{x,y}^{(k)}$, thermal stresses and moments of the laminate are subsequently calculated using the equations (3-73) and (3-74).

$$[N_T]_{x,y} = \sum_{k=1}^{n} [Q]_{x,y}^{(k)} [e_T]_{x,y}^{(k)} th_k \tag{3-73}$$

$$[M_T]_{x,y} = \sum_{k=1}^{n} [Q]_{x,y}^{(k)} [e_T]_{x,y}^{(k)} z_k . th_k \tag{3-74}$$

where th_k and z_k are the thickness and the distance of the mid-point of the ply from the reference plane, respectively. $[Q]_{x,y}^{(k)}$ in case of thermal part is dependent on temperature; however, in the case of a cure-induced part it is calculated at cure temperature. The residual stress due to cure shrinkage strain along the transverse direction was calculated using the transverse modulus of the composite at T_{cure} and the cure shrinkage strain. This stress was added to the transverse residual stress due to thermal strain. This procedure was adopted since residual stress due to cure shrinkage would be cured-in at the cure temperature and should not change during cool down.

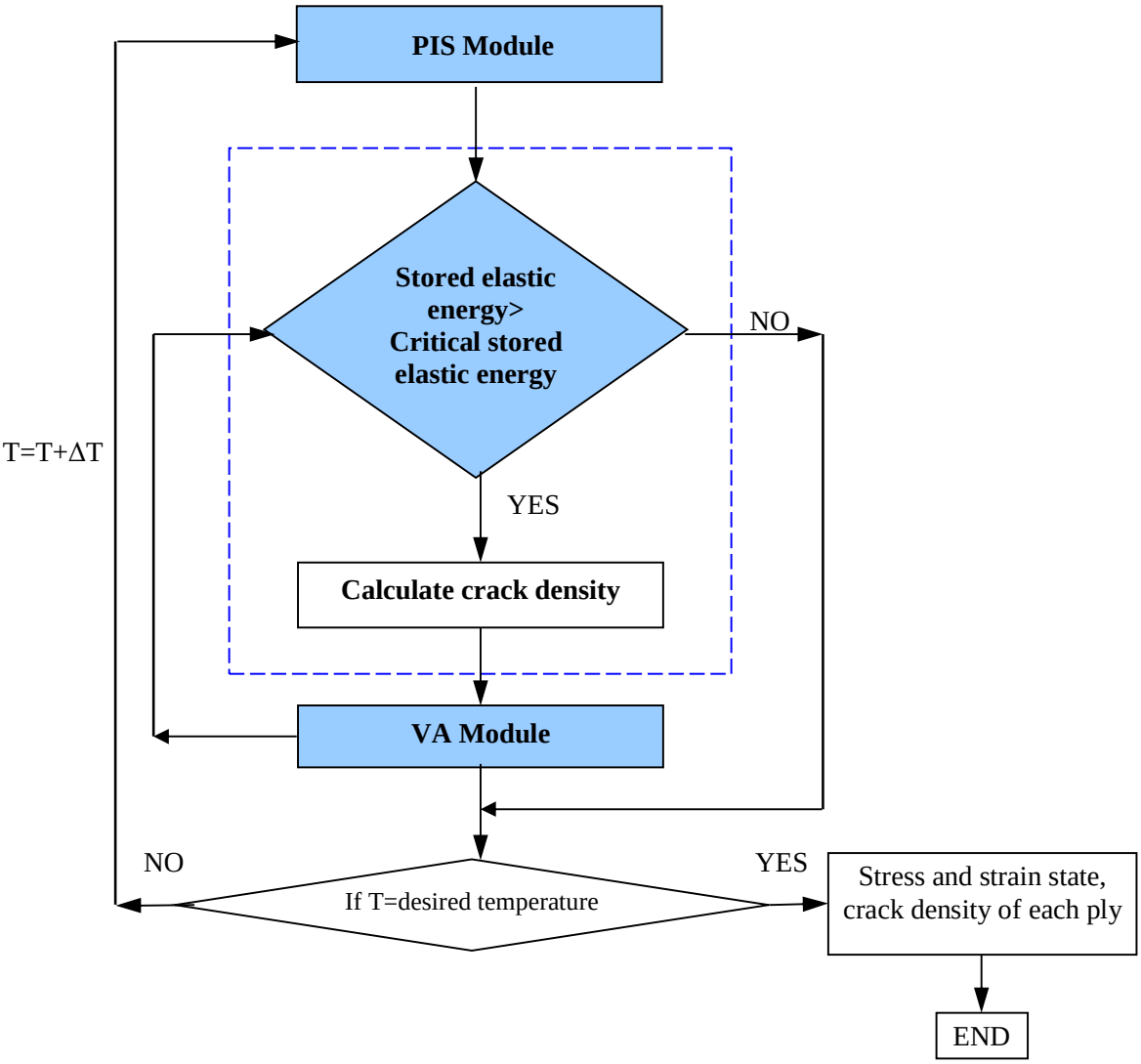

Figure 3-9: The PIS module

The longitudinal residual stress due to cure shrinkage was assumed to be negligible due to the large difference in the fiber modulus and resin modulus at cure temperature.

Due to the axial of loading [D] matrix is zero. Further, due to symmetric laminate used in this thesis, [B] is also zero, and only [A] and [a] matrices are non-zero. [A] and [a] are the stiffness and compliance matrices at the current temperature and are calculated using the relationships explained in Section 2.1.1. The strains of the laminate are calculated using equation (3-75).

$$[\varepsilon^0]_{x,y} = [a]_{x,y}[N_T]_{x,y} \tag{3-75}$$

Thermal strains and residual stresses in an individual ply are determined using the equations (3-76) and (3-77).

$$[\varepsilon_R]_{x,y}^{(k)} = [\varepsilon^0]_{x,y}^{(k)} - [e_T]_{x,y}^{(k)} \tag{3-76}$$

$$[\sigma_R]_{x,y}^{(k)} = [Q]_{x,y}^{(k)}[\varepsilon_R]_{x,y}^{(k)} \tag{3-77}$$

Equations (3-76) and (3-77) are applied to the thermal and cure-induced parts separately to provide process-induced strain and stress that comprises both cure-induced and thermal parts. Figure 3-9 depicts the procedure of predicting crack density and final stress state of each ply and laminate strain during cool-down. During cooling down from the cure temperature to room temperature, at each ΔT ($\Delta T=T_i-T_{i-1}$ where T_i and T_{i-1} are the current and previous temperatures), the stress and strain state of each ply is determined using equations (3-76) and (3-77). Then, the stored elastic energy in each ply is determined and compared with a critical stored elastic energy criterion to determine if that ply would fail or not. If the calculated stored elastic energy is equal to or greater than the critical stored elastic energy, cracking is deemed to have occurred. If failure is predicted, the crack number of the failed ply is increased by one crack, i.e. $n_i^{(k)} = n_{i-1}^{(k)} + 1$ and

the new crack density of $\lambda_i^{(k)}$ is determined where $n_{i-1}^{(k)}$ are the crack numbers of the ply at $T_{i-1,}$ and $\lambda_i^{(k)}$ are the crack density of the ply at T_i. Then, the VA module discussed in Section 3.3 is invoked using the new crack spacing (i.e., $1/n_i^{(k)}$) to determine the perturbation in the ply stress state as well as the final stress state of the ply after cracking. Then, the stress state of the ply is averaged, and the stored elastic energy using the average stresses is re-calculated and compared with the fracture criterion. This procedure is repeated until the stored elastic energy of each ply reaches a lower value than the critical stored elastic energy of that ply. Details on this procedure are presented in 3.5. The imposed boundary condition on the VA module is constant stress rate loading.

The output of this module is process-induced stress and crack density at each ply and laminate strain which is input to the QSL module as shown in Figure 3-2. It is worth mentioning that the output laminate stress will be zero, while the laminate strain is not zero.

3.5 Quasi Static Load (QSL) Module

This module predicts the change in ply stress and crack density during loading to creep load under constant displacement (i.e. strain) rate. The variable in this module is $\Delta\sigma$ where $\Delta\sigma=\sigma_{xx,\,i} - \sigma_{xx,\,i-1}$ ($\sigma_{xx,\,i-1}$ refers to the previous stress and $\sigma_{xx,\,i}$ is the current stress). The laminate strain, ply stress states and cracking, due to manufacturing-induced residual stress, predicted by the PIS module are input to this module. The modeling approach for the case of no process-induced cracking is discussed first, followed by the approach for the case of process-induced cracking.

Figure 3-10 shows the flow chart of the QSL module. Consider a laminate without any predicted process-induced damage at the start of loading, $\sigma_{xx,\,i-1}$, i.e., a load per unit width of $N_{jl,\,i-1}$, where j, l = x,y. Using lamination theory, represented by equations (2-4) to (2-13), the load per unit width-strain relationship for the laminate with process-induced stress is given in equations (3-78) and (3-79).

$$\begin{bmatrix} N_{xx} \\ N_{yy} \\ N_{xy} \end{bmatrix}_{i-1} = \begin{bmatrix} A_{xx} & A_{xy} & A_{xs} \\ A_{xy} & A_{yy} & A_{ys} \\ A_{xs} & A_{ys} & A_{ss} \end{bmatrix}_{i-1} \begin{bmatrix} \varepsilon^0_{xx} \\ \varepsilon^0_{yy} \\ \gamma^0_{xy} \end{bmatrix}_{i-1} + \begin{bmatrix} B_{xx} & B_{xy} & B_{xs} \\ B_{xy} & B_{yy} & B_{ys} \\ B_{xs} & B_{ys} & B_{ss} \end{bmatrix}_{i-1} \begin{bmatrix} \kappa_{xx} \\ \kappa_{yy,} \\ \kappa_{xy} \end{bmatrix}_{i-1} - \begin{bmatrix} N_{xx,T} \\ N_{yy,T} \\ N_{xy,T} \end{bmatrix} \tag{3-78}$$

$$\begin{bmatrix} M_{xx} \\ M_{yy} \\ M_{xy} \end{bmatrix}_{i-1} = \begin{bmatrix} B_{xx} & B_{xy} & B_{xs} \\ B_{xy} & B_{yy} & B_{ys} \\ B_{xs} & B_{ys} & B_{ss} \end{bmatrix}_{i-1} \begin{bmatrix} \varepsilon^0_{xx} \\ \varepsilon^0_{yy} \\ \gamma^0_{xy} \end{bmatrix}_{i-1} + \begin{bmatrix} D_{xx} & D_{xy} & D_{xs} \\ D_{xy} & D_{yy} & D_{ys} \\ D_{xs} & D_{ys} & D_{ss} \end{bmatrix}_{i-1} \begin{bmatrix} \kappa_{xx} \\ \kappa_{yy} \\ \kappa_{xy} \end{bmatrix}_{i-1} - \begin{bmatrix} M_{xx,T} \\ M_{yy,T} \\ M_{xy,T} \end{bmatrix} \tag{3-79}$$

where $\varepsilon^0_{jl,i-1}$ and $\kappa_{jl,i-1}$ (j, l=x, y) are the mechanical strains. ($[N_T]_{x,y}$, $[M_T]_{x,y}$) represent thermal load per unit width given in equations (3-73) and (3-74). Since $[B]_{x,y,\,i-1}$ is zero due to symmetric lay-up, the strain of the laminate for in-plane loading is

$$[\varepsilon^0]_{x,y,i-1} = [a]_{i-1}\{[N]_{x,y,i-1} + [N_T]_{x,y}\} \tag{3-80}$$

and the stress in each ply is given by

$$\begin{bmatrix} \sigma_{xx} \\ \sigma_{yy} \\ \sigma_{xy} \end{bmatrix}^{(k)}_{i-1} = \begin{bmatrix} Q_{xx} & Q_{xy} & Q_{xs} \\ Q_{xy} & Q_{yy} & Q_{ys} \\ Q_{xs} & Q_{ys} & Q_{ss} \end{bmatrix}^{(k)}_{i-1} \left\{ \begin{bmatrix} \varepsilon^0_{xx} \\ \varepsilon^0_{yy} \\ \gamma^0_{xy} \end{bmatrix} - \begin{bmatrix} e_{xx,T} \\ e_{yy,T} \\ e_{xy,T} \end{bmatrix} \right\} \tag{3-81}$$

where $[e_{jl,T}]$ (j, l=x, y) are transformed unconstrained thermal strains and unconstrained strains induced in curing, given in equation (3-72). The stored elastic energy in each ply is determined and compared with a critical stored elastic energy criterion to determine if that ply would fail or

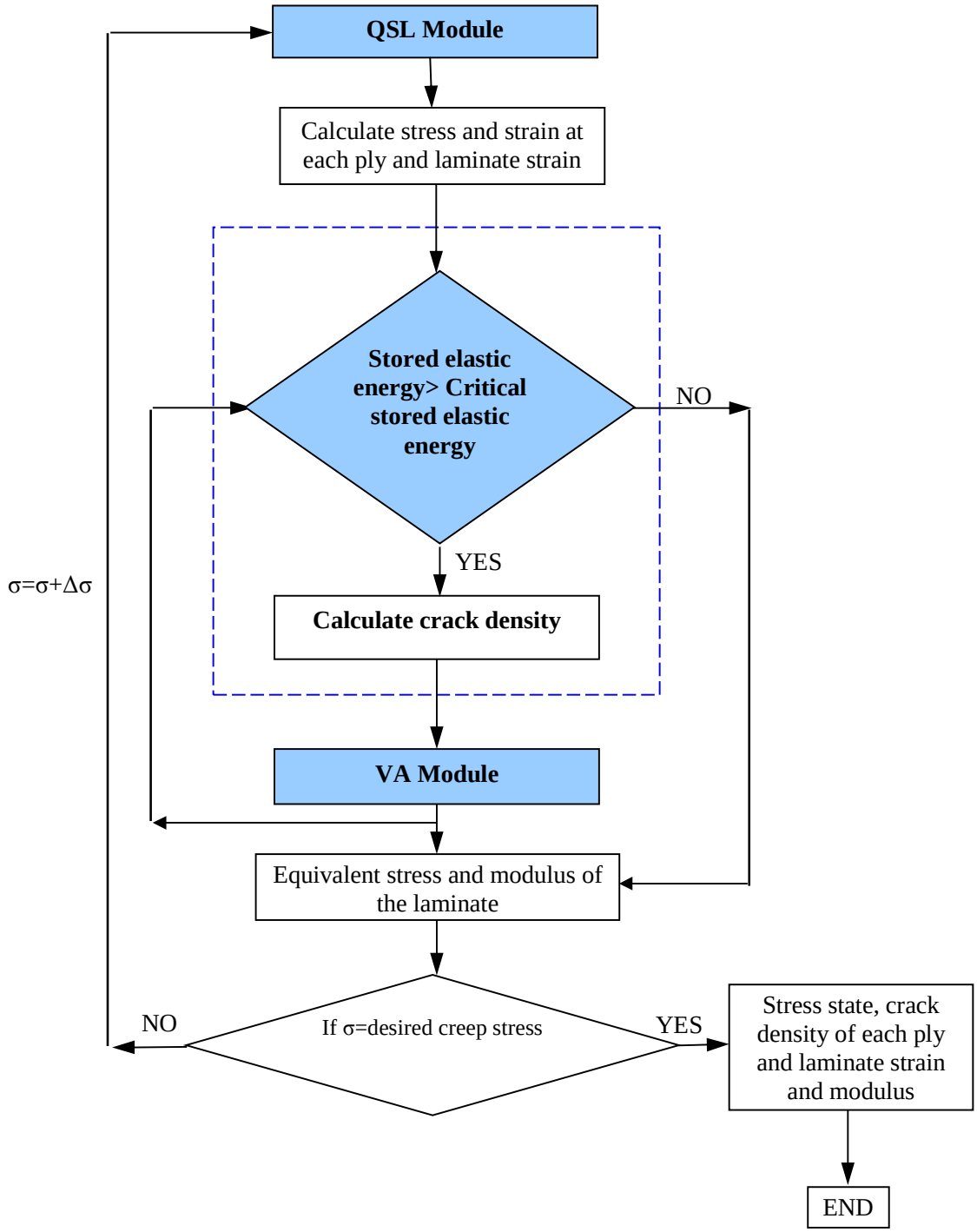

Figure 3-10: Flow chart for QSL module

not. If no cracking is predicted, the stress, i.e., the load per unit width, is incremented such that the new stress is $\sigma^0_{xx,\ i} = \sigma_{xx,\ i-1} + \Delta\sigma$, as shown in Figure 3-11. The increment of strain corresponding to $\Delta\sigma$, i.e., increment in load per unit width, is determined using equation (3-82).

$$[\Delta\varepsilon^0]_{x,y} = [a]_{x,y,i-1}[\Delta N]_{x,y} \tag{3-82}$$

Then, the stress state at each ply ($[\sigma^0]^{(k)}_{x,y,i}$) corresponding to the increase of laminate strain is determined and added to the previous stress state of the ply, as given in equation (3-83-a) and (3-83-b).

$$[\Delta\sigma]^{(k)}_{x,y} = [Q]^{(k)}_{x,y}[\Delta\varepsilon^0]_{x,y} \tag{3-83-a}$$

$$[\sigma^0]^{(k)}_{x,y,i} = [\sigma^0]^{(k)}_{x,y,i-1} + [\Delta\sigma]^{(k)}_{x,y} \tag{3-83-b}$$

The stored elastic energy is, subsequently, calculated using the stress state in a ply, given in equation (3-83). At each step, if the calculated stored elastic energy in a ply is equal or greater than the critical stored elastic energy, cracking is deemed to have occurred in that ply. The crack density of the ply at $\sigma_{xx,\ i-1}$ is $\lambda^{(k)}_{i-1}$ which is equal to zero. The new crack density $\lambda^{(k)}_i$ of the cracked ply at $\sigma^0_{xx,\ i}$ is calculated by adding one crack to the existing cracks of that ply (i.e., $n^{(k)}_i = n^{(k)}_{i-1} + 1$). The new crack density and stress state of that ply are input to the VA module to determine the perturbation in the stress state of that ply due to this cracking and the new stress after cracking. Since the new stress state of the ply varies along longitude and thickness of that ply (see equations (3-25)-(3-42)) depending on the distance from the location of the crack, the stress is averaged. Then, the stored elastic energy for each ply is re-calculated using the new stress state determined by the VA module and compared with its critical stored elastic energy to see if any of the plies would fail again under this new stress state. This procedure is repeated

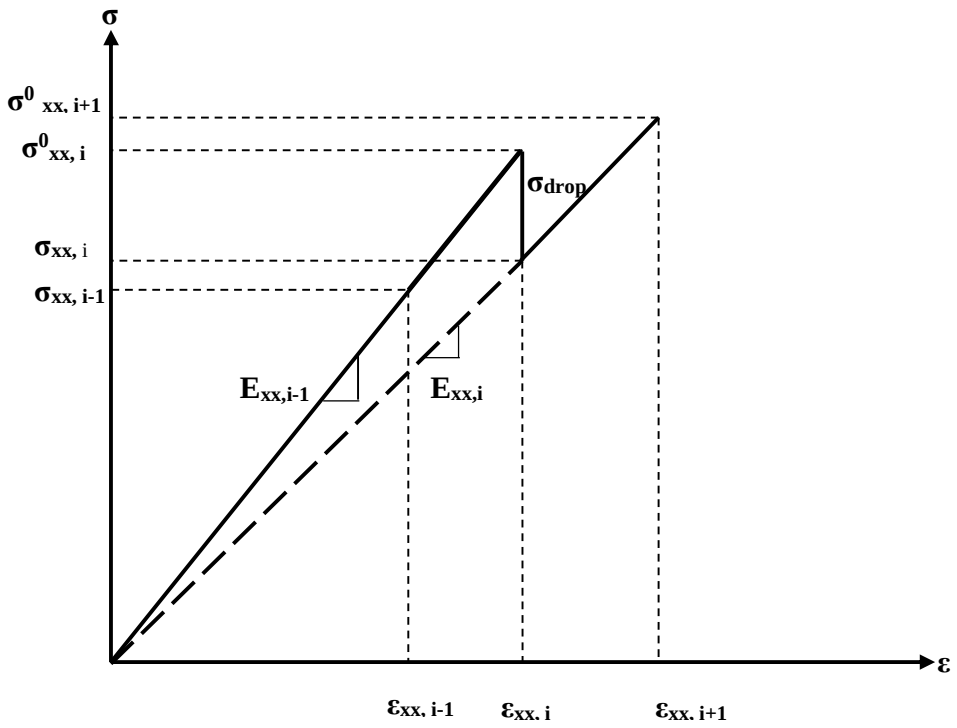

Figure 3-11: Stress-strain curve for a constant strain rate test

until all plies reach an energy level lower than the critical energy. The above procedure ensures that no more cracking will occur.

Subsequently, the overall laminate stress after cracking of a ply or plies needs to be calculated. Since the imposed boundary conditions in the VA module is a constant strain rate, the stress of the laminate would drop after cracking from $\sigma^0_{xx,\,i}$ to $\sigma_{xx,\,i}$ at a constant laminate strain of $\varepsilon_{xx,\,i}$ as shown in Figure 3-11. After the stress state of each ply has been determined using the VA module, the equivalent axial stress of the laminate stress $\sigma^{\varepsilon_i(L)}_{equivalent}(\sigma_{xx,\,i})$, corresponding to the new ply stress state (predicted by the VA module) and constant strain of $\varepsilon_{xx,\,i,}$ is determined using equation (3-84).

$$\sigma_{xx,i} = \sigma^{\varepsilon_{xx,i}(L)}_{equivalent} = \frac{1}{2h}\sum_{k=1}^{n} th_k\left(\sigma^{(k)}_{xx} + \sigma^{(k)}_{xy} + \sigma^{(k)}_{xz}\right) \tag{3-84}$$

The ply stresses in equation (3-85), i.e., $\sigma^{(k)}_{jl}$ (j, l = x, y, z) in the above equation, correspond to average stress in the ply obtained by averaging the distribution in the ply stress state predicted by the VA module over the length of the ply or the length of the intact portion. The average stress of a ply (k) is calculated using equation (3-85).

$$\sigma^{(k)}_{jl,i} = \frac{1}{th_k}\frac{1}{2a^{(k)}}\int_{z_k}^{z_k+th_k}\int_{2(n^{(k)}-1)a^{(k)}}^{2(n^{(k)})a^{(k)}}\sigma^{(k)}_{jl,i}(x,z)\,dxdz \tag{3-85}$$

where $n^{(k)}$ and $2a^{(k)}$ are the total numbers of intact regions and distances between two neighboring cracks in ply (k), respectively, as shown in Figure 3-3.

The modulus of the cracked laminate is determined using the equivalent load given in equation (3-84) and (3-85) and the laminate strain as follows.

$$E^{\varepsilon_{xx,i}}_{xx} = \frac{\sigma^{\varepsilon_{xx,i}(L)}_{equivalent}}{\varepsilon_{xx,i}} \tag{3-86}$$

During the next stress increment, $\Delta\sigma$ will be added to this equivalent stress to obtain the new laminate stress, $\sigma^0_{xx,\,i+1}$. At this stress, the intact regions between two neighboring cracks in a ply are considered for further analysis. The [a] matrix is updated with the new modulus for the cracked laminate, i.e,. $E_{x,i}$ as per equation (3-87), and then input to equation (3-82).

$$[a]_{x,y,i+1} = \begin{bmatrix} \frac{1}{hE_{xx,i}} & a_{xy} & a_{xs} \\ a_{xy} & a_{yy} & a_{ys} \\ a_{xs} & a_{ys} & a_{ss} \end{bmatrix} \tag{3-87}$$

The above procedure is repeated until the desired creep load is reached.

If there is process-induced damage, a very small strain is applied to the laminate. The crack density and stress state of each ply are input to the VA module. Subsequently, the perturbation in the stress state due to cracking and the new stress of each ply after cracking are determined. Then, the equivalent load and the modulus of the cracked laminate are determined using equation (3-84) and (3-86) respectively. This modulus will be assumed to be the modulus of the cracked laminate at load equal to zero. Then, the above procedure will be repeated.

The laminate strain, modulus, crack density, and stress state of each ply will be input to the SL module.

3.6 Static Load (SL) Module

This module predicts the creep of the laminate as well as the TDD. The laminate strain, ply stress state and crack density (TID), predicted by the QSL module at the end of loading to the desired creep load, are input to this module, and these are taken as the value at the start of creep (creep time, t=0). The variable in this module is Δt. The creep for a desired time period is

simulated in incremental time steps, $\Delta t=t_i-t_{i-1}$ (t_{i-1} refers to the previous creep time and t_i is the current creep time). Two assumptions were made in this program: 1) ply stress remains constant during a time step Δt and corresponds that of the previous time (t_{i-1}), and 2) ply compliance for a time-step Δt corresponds that of the previous time (t_{i-1}). Two possible cases are that a) no cracking will be predicted by the QSL module, and b) cracking will be predicted by the QSL module. Both cases are discussed below.

The flow chart for this module is provided in Figure 3-12. Consider a laminate without any damage at the start of creep, $t_{i-1}=0$ (creep time starts at end of loading to creep load). Let the time be incremented by Δt to t_i. The total laminate strain at t_i is determined by calculating the creep during Δt and adding to the strain at t_{i-1}. The creep during Δt is determined using lamination theory as discussed below.

Dillard et al. [2, 94] developed the first model based on lamination theory to predict the creep compliance of multidirectional laminates using the creep compliance of unidirectional laminates and the orientation of fibers in the plies with respect to the loading axis. This modeling approach has been adapted in the model developed in this thesis to determine the laminate strain, as well as ply stresses and strains due to creep, for an undamaged ply or intact regions of a cracked ply.

Assuming that the change in the ply stress during Δt is not large enough to change the creep compliance (note that the material is non-linear viscoelastic, and the creep compliance changes with stress), the creep of the laminate during Δt is determined using the creep compliances of the plies at t_{i-1}. The latter is determined using the creep model for unidirectional lamina provided as input and the ply stress state at t_{i-1}. The compliance matrix of the ply given in equation (A-1) is updated to correspond to the unidirectional creep compliances at t_{i-1} along

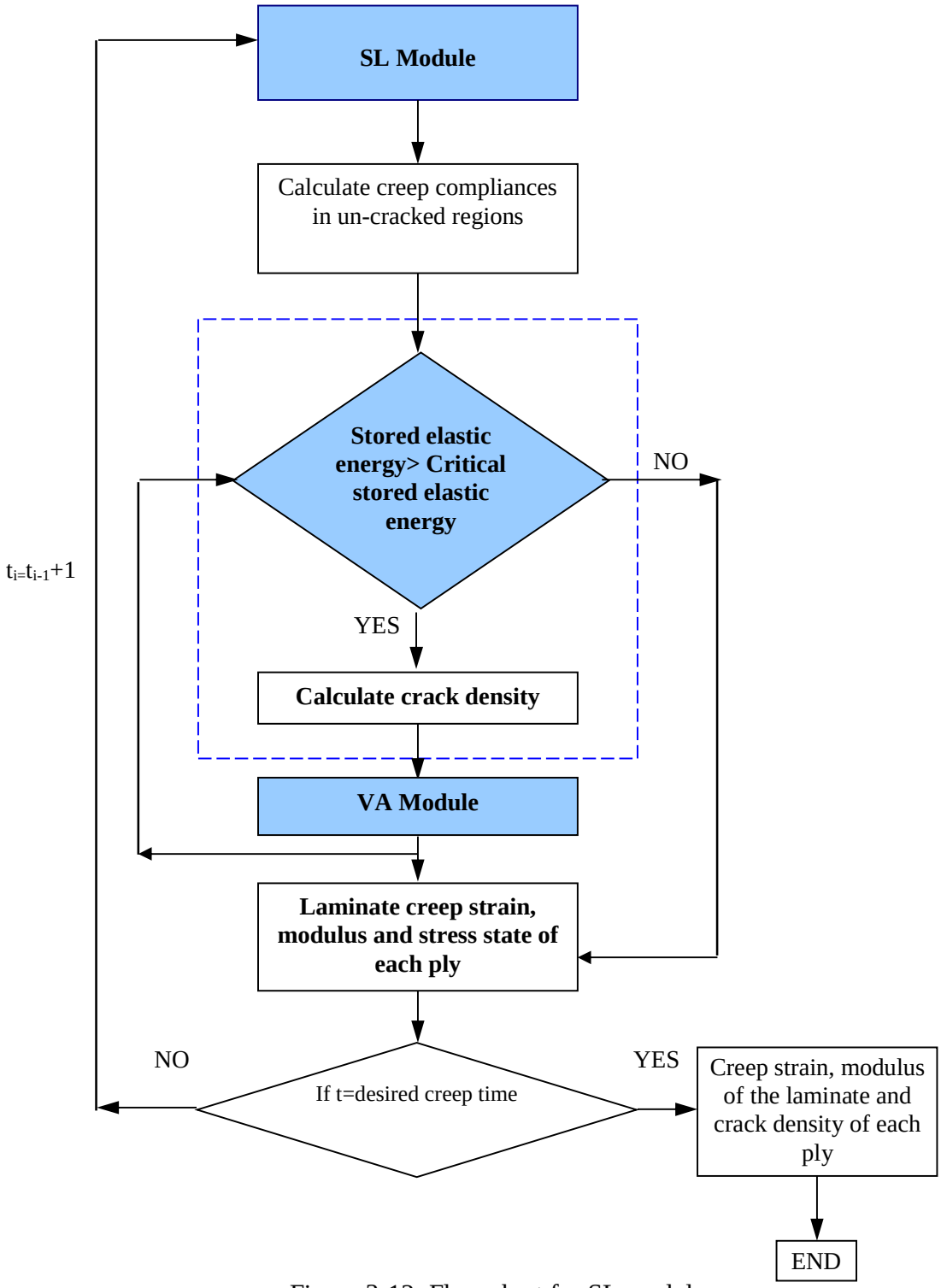

Figure 3-12: Flow chart for SL module

principal coordinates and is given in equation (3-88).

$$[S(t_{i-1})]_{1,2}^{(k)} = \begin{bmatrix} S_{11} & S_{12} & 0 \\ S_{12} & S_{22}(t_{i-1}) & 0 \\ 0 & 0 & S_{66}(t_{i-1}) \end{bmatrix}^{(k)} \tag{3-88}$$

For creep of a unidirectional lamina with fibers oriented at an angle (k) to the loading axis, the above equation is modified as follows.

$$\begin{bmatrix} S_{xx}(t_{i-1}) & S_{xy}(t_{i-1}) & S_{xs}(t_{i-1}) \\ S_{xy}(t_{i-1}) & S_{yy}(t_{i-1}) & S_{ys}(t_{i-1}) \\ S_{xs}(t_{i-1}) & S_{ys}(t_{i-1}) & S_{ss}(t_{i-1}) \end{bmatrix}^{(k)} = [T_3]^{-1} \begin{bmatrix} S_{11} & S_{12} & 0 \\ S_{12} & S_{22}(t_{i-1}) & 0 \\ 0 & 0 & S_{66}(t_{i-1}) \end{bmatrix}^{(k)} [T_3] \tag{3-89}$$

where $[T_3]$ is the transformation matrix given in (3-90):

$$[T_3] = \begin{bmatrix} m^2 & n^2 & 2mn \\ n^2 & m^2 & -2mn \\ -mn & mn & m^2 - n^2 \end{bmatrix} \tag{3-90}$$

m and *n* are sin (k) and cos (k), respectively, where κ is the orientation of the fiber in the ply with respect to the global x-axis . k = 90^o, -θ, or + θ for the three ply groups of the chosen laminate.

Due to the difference in the orientation of the fibers in various plies, the unconstrained creep of various plies of a laminate would be different; however, they are constrained to deform together as a part of the laminate. The difference between the actual laminate strain and the unconstrained strain results in residual stress in that ply and alters the ply stress state, which is predicted as follows. First the equivalent load that would result in unconstrained strain in all plies is determined using equation (3-91).

$$[\Delta N]_{x,y} = \Sigma [Q(t_{i-1})]_{x,y}^{(k)} [\Delta \varepsilon]_{x,y} \tag{3-91}$$

where ΔN and Δε are corresponding to the equivalent load and unconstrained strain of the laminate with respect to the global axes during Δt respectively. $[Q(t_{i-1})]_{x,y}^{(k)}$ is the stiffness matrix

of ply (k) at time t_{i-1}. The unconstrained strain with respect to the principal axes is calculated as per equation (3-92).

$$[\Delta\varepsilon]_{1,2} = [\sigma(t_{i-1})]^{(k)}_{1,2}[\Delta S]_{1,2} \tag{3-92}$$

where $[\sigma(t_{i-1})]^{(k)}_{1,2}$ is the ply stress in the principal axes at time $t_{i-1,}$ and $[\Delta S]_{1,2}$ is the difference in compliance between time t_i and t_{i-1}. $[\Delta\varepsilon]_{x,y}$ is calculated by transforming $[\Delta\varepsilon]_{1,2}$ to the global axes using equation (3-93).

$$\begin{bmatrix} \varepsilon_{11} \\ \varepsilon_{22} \\ \frac{1}{2}\gamma_{66} \end{bmatrix} = [T_3] \begin{bmatrix} \varepsilon_{xx} \\ \varepsilon_{yy} \\ \frac{1}{2}\gamma_{xy} \end{bmatrix} \tag{3-93}$$

The increase in laminate strain due to this equivalent load is determined using equation (3-94) and added to the laminate strain at t_{i-1} to get the laminate strain at t_i as per equation (3-95).

$$[\Delta e]_{x,y} = [a(t_{i-1})]_{xy}[\Delta N]_{x,y} \tag{3-94}$$

$$\varepsilon(t_i) = \varepsilon(t_{i-1}) + [\Delta e]_{x,y} \tag{3-95}$$

where $[a(t_{i-1})]$ is the laminate compliance at t_{i-1}. The ply stress at t_i is determined using equation (3-96).

$$[\sigma(t_i)]^{(k)}_{1,2} = [Q(t_{i-1})]^{(k)}_{1,2}[\varepsilon(t_i)]^{(k)}_{1,2} - [\Delta\varepsilon]^{(k)}_{1,2} \tag{3-96}$$

where $[\varepsilon(t_i)]^{(k)}_{1,2}$ is the transformed form of strain calculated in equation (3-95) with respect to the principal axes of the ply, and $[\Delta\varepsilon]^{(k)}_{1,2}$ is the unconstrained strain of the ply given in equation (3-92).

The stored elastic energy at each ply is calculated based on the ply stress state at $t_{i,}$ given in equation (3-96), and creep compliances at $t_{i,}$ calculated in equation (3-87), and compared with

the critical stored elastic energy. The critical elastic energy is determined as a function of time as per the procedure discussed in the next section and input to the model. If the stored elastic energy is less than the critical elastic energy for cracking at t_i, then no failure is predicted. The time is incremented by Δt to $t_{i+1,}$ and the above procedure is then repeated.

If the calculated stored elastic energy is equal to or greater than the critical elastic energy for cracking at $t_{i,}$ cracking in that ply is deemed to have occurred. This will lead to a sudden increase in laminate strain at t_i ($\varepsilon_{xx,\ 2i}$ in Figure 3-13) in addition to an increase in strain due to creep during the duration from t_{i-1} to t_i ($\varepsilon_{xx,\ 1i'}$ in Figure 3-13). This would also alter the ply stress state determined using equation (3-96). Both the increase in laminate strain and change in ply stress state due to cracking are predicted as follows using the VA module. The number of cracks of that ply is increased by one, i.e., $n_i^{(k)} = n_{i-1}^{(k)} + 1$, to obtain the new crack density of the cracked ply at $t_{i,}$ i.e., $\lambda_i^{(k)}$. The new crack density at t_i and the current stress state of the plies at t_i given by equation (3-96) is input to the VA module to determine the perturbation stress and new stress state for the plies at t_i after cracking. Using the latter, the stored elastic energy for each ply is calculated again using the average stress state of the ply calculated in equation (3-85) (as explained in Section 3.5), and is compared with the critical elastic energy at t_i to determine if it would fail again. This procedure is repeated until the stored elastic energy of that ply reaches a value lower than the critical elastic energy to ensure that no further cracking would occur at that time. The crack density corresponding to t_i is recorded.

The ply stress state determined by the VA module is used to determine the laminate strain after cracking at t_i ($\varepsilon_{xx,\ 2i}$ in Figure 3-13) as follows. Since the load is maintained at a constant load or stress rate during creep, the increase in strain due to cracking should occur at constant load, i.e., from A to C in Figure 3-13. However, C can also be reached by following the path

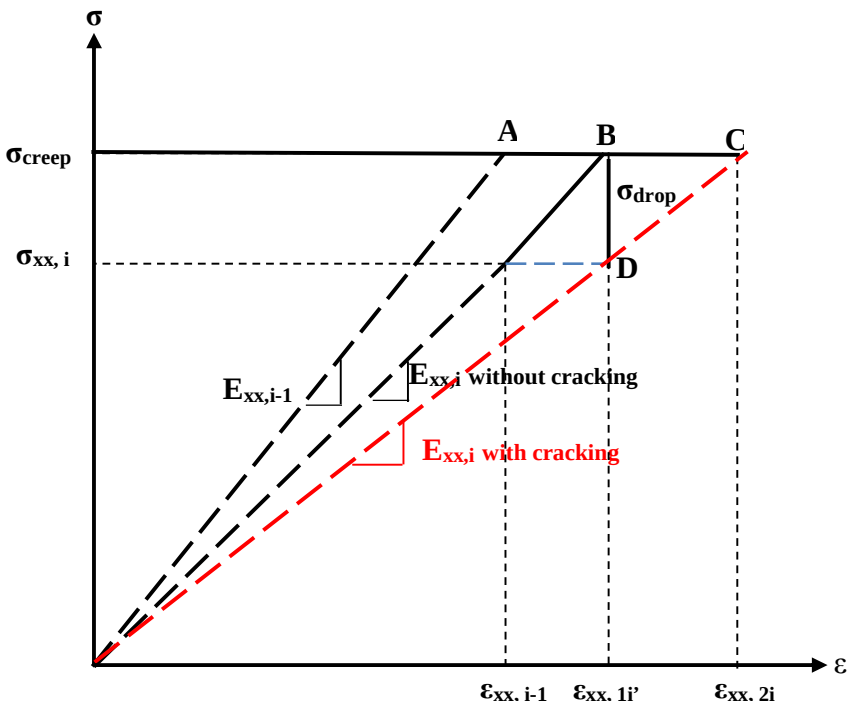

Figure 3-13: Stress-strain curve for a constant load (stress) rate test

ABDC, i.e. allowing the stress to drop first at constant strain due to cracking at point B and then increasing the load back to the creep load level. This is similar to the procedure used in the QSL module to predict the composite response under a constant strain rate, and is used to determine the increase in strain due to cracking at t_i. It is worth mentioning that increase in the strain from A to B is due to creep and from B to C is due to cracking.

When a ply fails at a constant strain ($\varepsilon_{xx,\,1i'}$ in Figure 3-13), the stress on the laminate drops from σ_{creep} to $\sigma_{xx,\,i}$, as shown in Figure 3-13. $\sigma_{xx,\,i}$ is obtained by determining the equivalent axial stress of the laminate using the ply stress state at $t_{i,}$ as determined by the VA module as per equation (3-97).

$$\sigma_{xx,i} = \sigma^{(L)}_{equivalent}(t_i) = \frac{1}{2h}\sum_{k=1}^{n} th_k\left(\sigma^{(k)}_{xx} + \sigma^{(k)}_{xy} + \sigma^{(k)}_{xz}\right) \tag{3-97}$$

The average ply stress in equation (3-97) is obtained by averaging the distribution in ply stress state predicted by the VA module over the length of the ply or the length of the intact portion given in equation (3-85). The modulus of the laminate is determined using equation (3-98) obtained by substituting equation (3-97) into equation (3-87) as given in equation (3-95).

$$E^{t_i}_{xx} = \frac{\sigma^{(L)}_{equivalent}(t_i)}{\varepsilon_{xx,1i}} \tag{3-98}$$

The drop in stress, σ_{drop} ($=\sigma_{creep} - \sigma^{(L)}_{equivalent}(t_i)$), is added to the equivalent stress to bring the load back to creep load, and the increase in strain due to cracking at t_i is determined as per equation (3-99).

$$\Delta\varepsilon = \frac{\sigma_{creep} - \sigma^{(L)}_{equivalent}(t_i)}{E^{t_i}_{xx}} \tag{3-99}$$

This is added to $\varepsilon_{1i'}$ to get the total laminate strain ε_{2i}, at t_i. Using this strain, the compliance matrix of the laminate is updated according to equation (3-87). Subsequently, the next time

increment is applied, and the procedure is repeated until the desired creep time is reached, and thus laminate creep strain and TDD are obtained for the desired time period.

If there is damage predicted by the QSL module, the modulus and strain of the laminate, the stress state, and crack density at each ply at the desired creep load are input from the QSL module to the SL module at creep time equal to zero. Then, the above procedure will be repeated until reaching the desired creep load.

The laminate creep strain, modulus, crack density and stress state of each ply will be the output of the SL module.

3.7 Fracture Criterion

A critical stored elastic energy criterion is used in this model for predicting fracture and thus damage in a ply. This was developed by Raghavan and Meshii [110-112] and applied successfully to predict creep rupture of unidirectional laminates at various stresses and temperatures. Note that this criterion, developed to predict time-dependent failure, is equally applicable to predict time-independent failure. For the sake of completeness, the details of this criterion, developed by Raghavan and Meshii [110-112] are presented below.

According to this criterion, there exists a critical value for the stored elastic energy in a composite lamina, and the latter would fail when this limit is exceeded during loading or creep. A polymer composite is a viscoelastic material, exhibiting both elastic and viscous deformation. Hence, the total energy at fracture (for example the area under the stress-strain curve obtained by tensile testing) would be the sum of the elastic energy stored in the material as well as the energy dissipated in deforming the material to fracture. According to the above criterion, the value for stored elastic energy at fracture would be the critical value, and the model framework, developed

by Raghavan and Meshii [110-112] to extract this value from tensile test results, is presented below.

Far below glass transition temperature T_g (glass transition temperature is a temperature below which a polymer behaves like a brittle solid and above which it behaves like a rubber), a polymer matrix of a polymer composite has a very high resistance to chain segmental motion and consequently behaves like a brittle solid. With an increase in temperature from a temperature below T_g, the polymer becomes progressively softer due to overcoming of the viscous resistance to polymer chain motion. At temperatures above T_g, the polymer matrix approaches a rubbery state. This behaviour was modeled by a framework shown in Figure 3-14. The two resistive elements 1 and 2 represent the elastic and viscous resistance, respectively, to polymer chain motion, while the dash pot represents viscous deformation within a polymer. The stiffness of the element 1 that represents elastic resistance is termed as rubbery modulus (E_R). The stiffness of the element 2 that represents viscous resistance is termed as viscous modulus (E_V). Both can be measured by dynamic mechanical thermal analysis (DMTA), as follows. A DMTA test result (storage modulus as a function of temperature) is shown in Figure 3-15. Well below T_g, the modulus corresponds to a glass solid (E_0). Above T_g, the modulus reaches a constant value (plateau), E_R. During the transition from a glass solid to a rubber the modulus of the polymer matrix drops by a magnitude, E_V, as shown in Figure 3-15. It should be noted that the directions and indices corresponding t o global coordinate system are left out to make it easier for reading. This procedure is applicable to any loading and direction.

At the instant of application of a constant creep stress (if it is applied instantaneously),

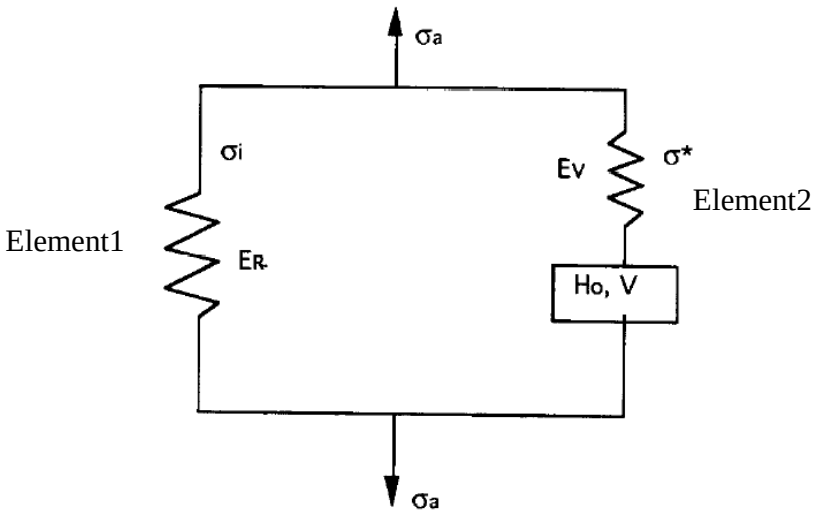

Figure 3-14: Schematic of the model proposed by Raghavan and Meshii [113]

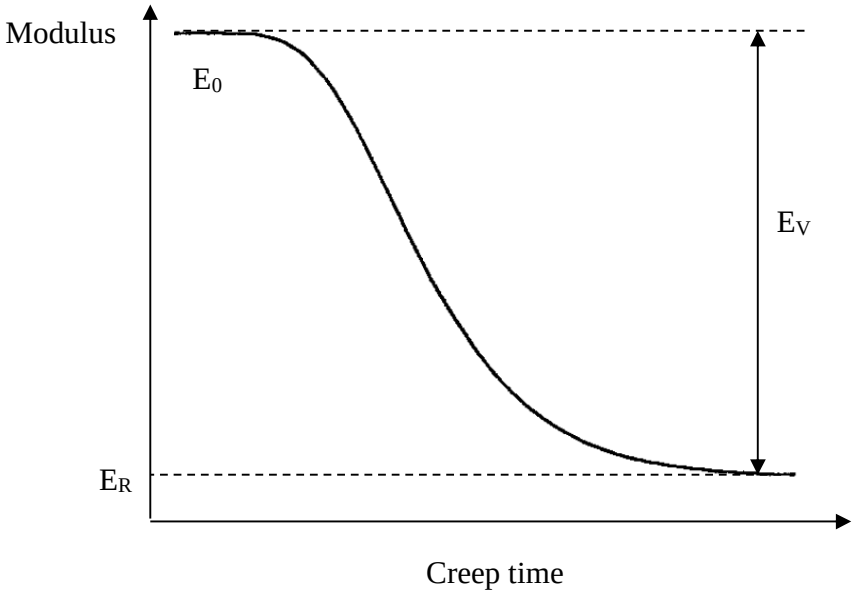

Figure 3-15: Schematic variation of modulus of a polymer composite as per model in Figure 3-14

there is no chain segmental motion (creep), and the instantaneous modulus (E_0) of the composite will be given by

$$E_0 = E_R + E_V \tag{3-100}$$

The applied creep stress is partitioned into an internal stress σ_i in element 1, and effective stress σ^* in element 2. Viscous deformation (creep) progresses with time under the influence of effective stress σ^* and temperature. As creep progresses, the effective stress decreases while the internal stress increases. The relationship among applied creep stress, and internal and effective stresses satisfies the following relationship,

$$\sigma_a = \sigma_i(t) + \sigma^*(t) \tag{3-101}$$

where σ_a is applied creep stress.

The fracture criterion developed by Raghavan and Meshii [110-112] predicts the fracture of a polymer composite when the total stored elastic energy in the two resistive elements 1 and 2 is equal or greater than the critical stored elastic energy. At a given creep stress, internal and effective stresses are determined as a function of time, using E_R , E_V, and creep strain as per equations (3-102) and (3-103).

$$\sigma_i(t) = E_R \times \varepsilon(t) \tag{3-102}$$

$$\sigma^*(t) = \sigma_a - \sigma_i(t) \tag{3-103}$$

The total elastic stored energy in the composite at time t is the sum of the elastic energies stored in resistive elements, as per equation (3-104):

$$U_R(t) = \frac{[\sigma_i(t)]^2}{2E_R} \qquad \text{and} \qquad U_V(t) = \frac{[\sigma^*(t)]^2}{2E_V} \tag{3-104}$$

The total stored elastic energy at time t is given by:

$$U_e(t) = U_R(t) + U_V(t) \tag{3-105}$$

At any given creep time, this total stored elastic energy in a ply is compared to the critical stored elastic energy for that ply to determine if that ply would fail or not.

If the time-dependent terms in the above equations are replaced with time-independent terms, we get equations to determine stored elastic energy in a ply in QSL or PIS modules.

3.7.1 Determination of critical stored elastic energy for fracture

The critical stored elastic energy is determined using the results of the tensile tests at the desired temperature. ε(t) in equation (3-102) is replaced with fracture strain (ε^U), while $\sigma_a(t)$ in equation (3-103) is replaced with fracture stress (σ^U), as follows.

$$\sigma_i^U = E_R \times \varepsilon^U \tag{3-106}$$

$$\sigma^{*U} = \sigma^U - \sigma_i^U \tag{3-107}$$

Substituting equations (3-106) and (3-107) into (3-100) and (3-105), the critical stored elastic energy at the desired temperature is determined, which is subsequently compared with the stored elastic energy of the ply to predict the cracking in the PIS and QSL modules.

In the SL module, critical stored elastic energy should be determined as a function of time. In other words, ε(t) in equation (3-102) is replaced with fracture strain ($\varepsilon^U(t)$), and $\sigma_a(t)$ in equation (3-103) is replaced with fracture stress (σ^U (t)). Consequently, the time-dependent internal ($\sigma_i^U(t)$) and effective ($\sigma^{*U}(t)$) stresses required to calculate critical stored elastic energy are determined using equations (3-108) and (3-109).

$$\sigma_i^U(t) = E_R \times \varepsilon^U(t) \tag{3-108}$$

$$\sigma^{*U}(t) = \sigma^U(t) - \sigma_i^U(t) \tag{3-109}$$

Since the creep rupture time would vary from a few hours to a number of years depending on the creep stress and temperature, it is not practical to obtain strain corresponding to

creep rupture using creep tests. Instead, it was obtained using constant strain rate testing. The time to reach a fracture strain is obtained by dividing the strain rate by the fracture strain. The practical boundary of the usable strain rates limits to the range of 10^{-2} s^{-1} to 10^{-4} s^{-1}. In order to expand this range, tests were done at temperatures higher than the reference temperature in the range of 10^{-2} s^{-1} to 10^{-4} s^{-1}. Subsequently, these strain rates were converted to equivalent strain rates at the reference temperature using the activation energy (E_{act}) and Arrhenius relationship between the strain rate and the temperature given in equation (3-110).

$$\dot{\varepsilon} = Ae^{\frac{-E_{act}}{RT}} \tag{3-110}$$

where $\dot{\varepsilon}$ is the strain rate, A is the pre-exponential constant, R is the gas constant, and T is the temperature in kelvin.

Activation energy was measured using dynamic mechanical testing at multiple frequencies (1-100 Hz), while ramping the sample temperature at a rate of 1ºC/min to 320ºC. The glass transition temperature (T_g) for each frequency was obtained from these results. The slope of the plot of the natural log of frequency versus $1/T_g$ (1/K) is equal to $-E_{act}/R$, and E_{act} is determined from it. The strain rates at different temperatures were converted to equivalent strain rate data at a reference temperature using equation (3-111) derived from equation (3-110).

$$\dot{\varepsilon}_{T_{ref}} = \dot{\varepsilon}_T \exp\left[\frac{-E_{act}}{R}\left(\frac{1}{T_{ref}} - \frac{1}{T}\right)\right] \tag{3-111}$$

where $\dot{\varepsilon}_T$ and $\dot{\varepsilon}_{T_{ref}}$ are the strain rates at the desired temperature (T) and the reference temperature (T_{ref}), respectively. The experimental fracture strain at the T_{ref} was divided by the equivalent strain rate at T_{ref} to yield the time to fracture and thus $\varepsilon^U(t)$. Time dependent critical

stored elastic energy is calculated by substituting equations (3-108) and (3-109) into equation (3-104) and (3-105).

$$U_{failure}(t) = U_R^U(t) + U_V^U(t) \tag{3-112}$$

where

$$U_R^U(t) = \frac{[\sigma_i^U(t)]^2}{2E_R} \quad \text{and} \quad U_V^U(t) = \frac{[\sigma^{*U}(t)]^2}{2E_V} \tag{3-113}$$

In order to determine rubbery modulus at the desired temperature, equation (3-113) is used

$$\frac{E_R^{T_1}}{E_R^{T_2}} = \frac{T_{ref}}{T_2} \tag{3-114}$$

where $E_R^{T_K}$ is the rubbery modulus at temperature T_K. Using dynamic mechanical analysis results (DMA), the temperature dependence of the instantaneous modulus (E_0) is determined. Using this and equation (3-100), the viscous modulus at T_{ref} is determined.

CHAPTER 4. EXPERIMENTAL AND SIMULATION DETAILS

4.1 Introduction

This chapter presents details on material, composite manufacturing, test coupon preparation and testing procedure, and simulation steps for the model developed in Chapter 3.

4.2 Material and Laminate

F263-7 epoxy resin reinforced with Toho G30-500 carbon fiber composite was used in this study. This material is used by aerospace companies to manufacture composite parts. The composite material was supplied by Hexcel Corporation in the form of 42'' wide unidirectional pre-preg tape, which was used to manufacture unidirectional and multidirectional composite panels. $[\pm 45/90_2]_s$ laminate was chosen for this study for model validation, as shown in Figure 4-1. The laminate layup most widely used in aerospace parts is the quasi-isotropic layup, $[0/\pm 45/90_2]_s$. Presence of [0] layers reduces the creep rate and the creep magnitude during an experimental time window (days to weeks) that is reasonably accessible. Hence, $[\pm 45/90_2]_s$ without [0] layers was used in this thesis in order to record a magnitude of creep, during experimental time window, that is sufficient for model validation. Additional unidirectional laminates were used to generate critical energy data, input to the model. Creep data for unidirectional laminates, input to the model, was generated by previous two students [3, 15] of the Composite Materials and Structures Research Group (CMSRG) of the University of Manitoba.

Figure 4-1: Manufactured $[\pm 45/90_2]_s$ laminate

4.3 Manufacturing of Test Coupons

4.3.1 Manufacturing of composite panels

Various steps in manufacturing of composite panels are as follows:

***a) Hand layup*:** First, the pre-preg, packed in a vacuum-sealed bag and stored in a freezer at - 25°C, was removed and allowed to thaw and reach room temperature. Then, it was cut into 12"×12" sheets. Cut sheets were manually stacked as per desired stacking sequence to yield unidirectional ($[0]_6$, $[30]_8$, $[45]_8$, $[60]_8$ and $[90]_{10}$) and multidirectional laminates $[\pm\theta_m/90_n]_s$ (e.g. $[\pm45/90_2]_s$). Orientation of the fibers in each ply with respect to global reference axes is illustrated in Figure 2-1.

b) Vacuum bag Assembly: Two aluminum tool plates were cleaned with alcohol and coated with Frekote©, a silicone-based release agent supplied by Dexter Corporation, USA or SAFELEASE 30 supplied by Airtech International, USA. After enough time was allowed between two coats to enable drying, stacked layers of the prepreg were placed between two steel tool plates and bagged, as shown in Figure 4-2. In order to enable easy removal of the cured panel a release film, WL5200B-P3-001-48"-100'-SHT, supplied by Airtech, was used between the pre-preg and the tool. Peel plies, RELEASE EASE 234TFP 38" supplied by Airtech, were used between the pre-preg and the release film in order to prevent transfer of silicone from the release film on to the panels as well as create a surface texture, which aided in subsequent bonding of the strain gages and the end-tabs. A breather cloth was used to provide a path for air and volatiles from the stacked pre-preg to escape to the vacuum port. This stack was placed on the bottom plate of a two-part mold and covered with a silicone pad to create a vacuum bag as shown in Figure 4-2.

c) Autoclave curing: The vacuum assembly was held and heated between the platens of a

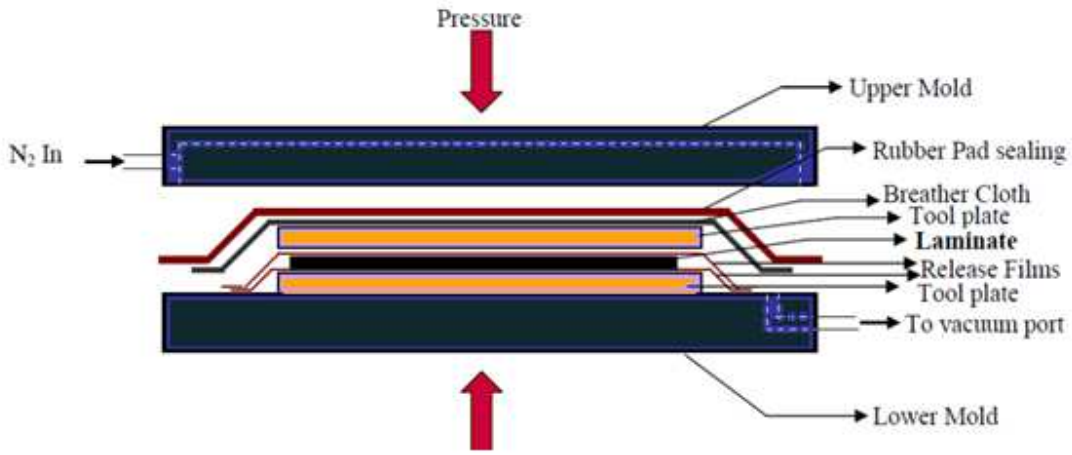

Figure 4-2: Schematic of the mold assembly for simulated autoclave curing of the composite panels

50 ton Carver hydraulic hot press, shown in Figure 4-3, and subjected to an autoclave cure cycle shown in Figure 4-4. The temperature was ramped at a rate of 3° C/min until the platens of the hydraulic hot press reached 177 °C, and the mold assembly was held at this temperature for two hours, while autoclave pressure was simulated by pressurizing the mold to 85 psi using nitrogen gas. While the space between the top cover and the vacuum bag was pressurized, the space between the vacuum bag and the bottom plate was held under vacuum to aid in the removal of entrapped air and volatiles from the pre-preg layers. The vacuum was held until 80°C. It was subsequently cut and pressure was applied. After curing for two hours, the mold was cooled down to room temperature, the pressure was released, and the panel was removed from the mold.

d) Post Curing: After the completion of the cure cycle, the laminate was post-cured at 220°C for four hours in an oven to complete the cross-linking of any monomers that did not cross-link during the curing process. Samples from the post-cured composite were tested in a Differential Scanning Calorimeter (DSC) to confirm that the curing process was complete. No residual exothermic heat was observed, as shown in Figure 4-5, confirming complete cross-linking during the curing process.

4.3.2 Volume fraction determination

Creep data for unidirectional laminates, generated by two previous students [3, 15] of the CMSRG of the University of Manitoba, was used as input in this study. Additionally, the critical stored elastic energy data for unidirectional laminates was generated as a part of this thesis. Hence, the fiber volume fraction in the new panels, manufactured as a part of this study, was measured and confirmed to be the same as that published in the Ref. 3, and 15. The volume fraction of composite panels was determined using water displacement method, described below.

Figure 4-3: Carver hydraulic hot press used in manufacturing of composite panels

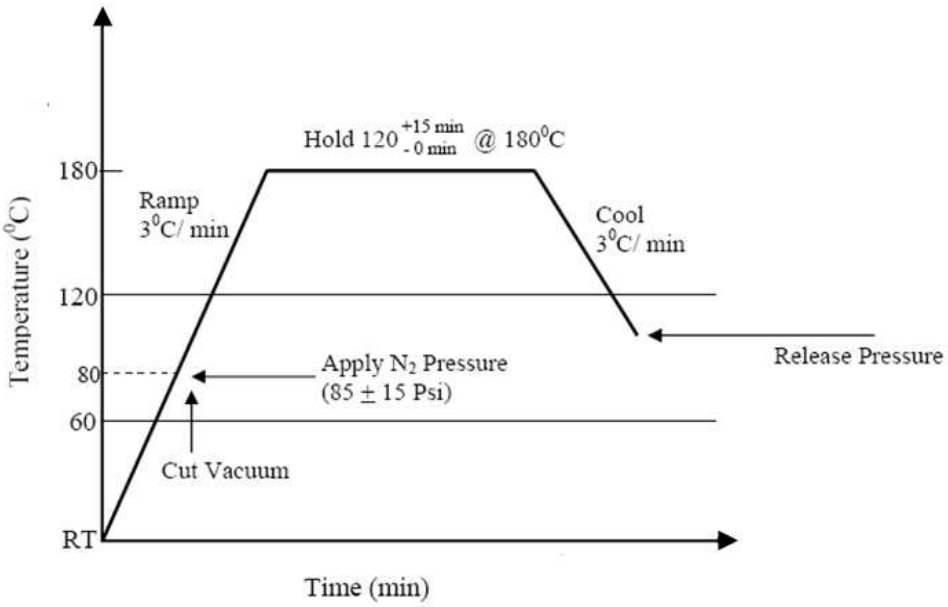

Figure 4-4: Cure cycle used in composite panels manufacturing

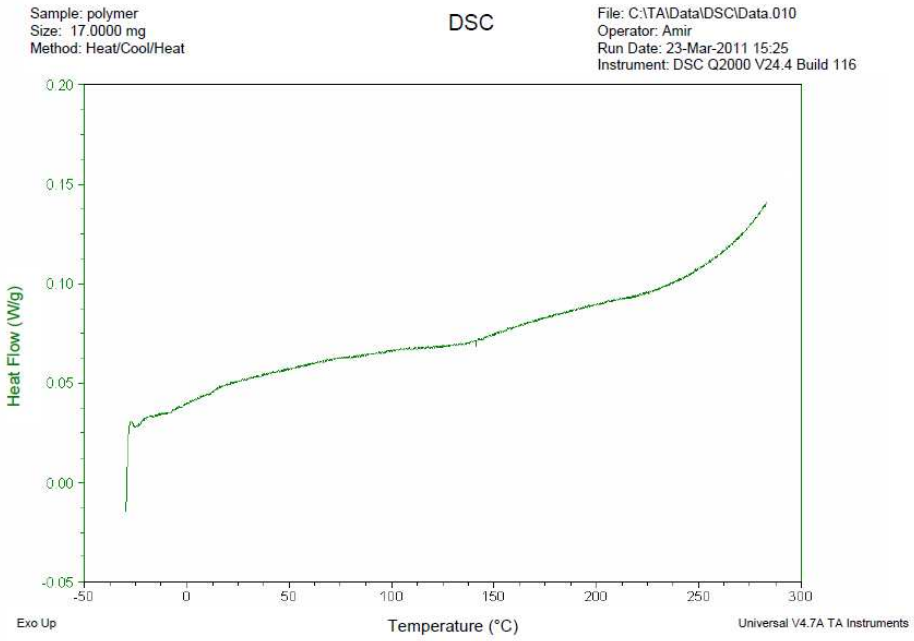

Figure 4-5: DSC test result for a post cured $[\pm 45/90_2]_s$

4.3.2.1 Water displacement method

This method, described in ASTM standard D-792 [114] was used to determine the specific density of the composite. This method consisted of the following steps:

1. Weigh the specimen in air to the nearest 0.1 mg.
2. Weigh a metal wire partially submerged in water.
3. Suspend the specimen using the wire and measure the weight of the specimen fully submerged in water with a partially submerged wire.
4. Determine the specific density of the specimen at 23°C using the following equation (4-1):

$$\rho = 0.9975 \times \frac{a}{a + w - b} \tag{4-1}$$

where

ρ = Specific density of composite (g/cm^3).

a = Weight of the specimen, in air (g).

b = Weight of the fully immersed specimen and partially immersed wire in water (g).

w = Weight of partially immersed wire in water (g).

0.9975 is a conversion factor used to convert density from kg/m^3 to specific density at room temperature in g/cm^3**.** Two samples from each manufactured unidirectional panel, $[0]_6$, $[30]_8$, $[45]_8$, $[60]_8$, and $[90]_{10}$, were tested to measure the average density of the manufactured composites. Using the rule of mixtures equation (4-2) for density, the fiber volume fraction (V_f) of the composite was calculated. Specific density and V_f results are tabulated in Table 4.1.

$$\rho_c = V_f \rho_f + (1 - V_f)\rho_m \tag{4-2}$$

where ρ_c, ρ_f, and ρ_m are composite, fiber and polymer matrix densities, respectively. The density of Toho G30-500 carbon fiber and F263-7 epoxy resin are 1.7 g/cm^3 and 1.267 g/cm^3

Table 4-1. Summary of fiber volume fraction test results for the manufactured composite panels

Composite	Sample	Composite Density (gr/cm^3)	Fiber Volume Fraction (%)
$[0]_6$	1	1.50	54
	2	1.53	60
$[30]_8$	1	1.52	58
	2	1.51	56
$[45]_8$	1	1.53	60
	2	1.52	58
$[60]_8$	1	1.54	63
	2	1.51	56
$[90]_{10}$	1	1.54	63
	2	1.52	58
Average		1.52	58

respectively.

4.3.3 Test coupon preparation

a) Tabbing: Tabs were bonded to both ends of the tensile test coupons to avoid crushing of the coupons during gripping. Woven carbon fiber epoxy composite laminates, (F263-8/T300), were used as tabs and were manufactured using a manufacturing procedure similar to the one discussed in 4.3.1. After their edges were chamfered to 7°, the tabs were bonded to the edges of the panels using Dexter Corporation's BMI 9873 adhesive and being put through the Carver hydraulic press at a temperature and pressure of 180°C and 2 tons respectively. The process time was one hour to allow the adhesive to flow and cure. The panel with edge-bonded tabs was then allowed to cool down to room temperature under pressure.

b) Cutting: Test coupons, with dimensions of 127 mm in length × 12.7 mm in width as shown in Figure 4-6, were cut from the panels using a slow-speed 39-1471 Handimet I cutter from Buehler Ltd with a feed rate of 6 mm/min. A slow feeding rate is desirable to avoid any overheating of the saw and damage to the coupon edges. The panel was held on to the cutting platform using double sided tape.

c) Polishing: Edges of all coupons were ground and polished to enable viewing of damage that developed during testing. The edges were progressively ground using 80, 180, 240, 320, 400, 600 and 1200 grit silicon carbide papers. Subsequently, they were polished using 6 µm and 1 µm alumina powder. The polished surfaces were thoroughly cleaned and wiped using ethyl alcohol to remove all loose particles.

d) Strain gauging: Strain gauges of type EA-06-250AE-350, CEA-06-125UT-350, WK-06-250BT-350, and WK-06-125TM-350, manufactured by Micro Measurements Group Inc., were used to measure strain during tensile and creep testing. While the first two were used for

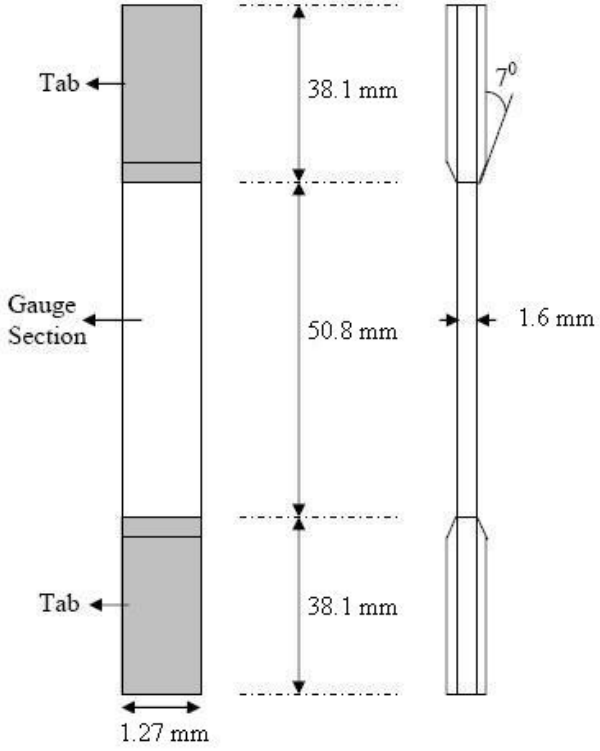

Figure 4-6: Sample geometry

tensile testing at room temperature, the others were used for tensile and creep testing at elevated temperatures. All strain gages were bonded to the test coupons using M-Bond 610 supplied by the strain gage manufacturer. Prior to bonding the strain gauges to the test coupon, the desired area was cleaned using M-prep Conditioner A (alkaline) followed by M-prep Neutralizer B (acidic). The bonded strain gages were cured under spring-clamp pressure at 180°C for 2 hours. The test coupon was allowed to cool down to room temperature in the oven. The clamp was removed and the coupon was post cured at 220°C for 2 hours to ensure that the adhesive was completely cured and to prevent any residual curing of adhesive during testing. A strain gauged sample is shown in Figure 4-7.

4.4 Tests

4.4.1 Thermo-mechanical analysis (TMA) tests

Cure shrinkage strain (perpendicular to the fibers in a prepreg) and coefficient of thermal expansions (CTE) values are required to determine the process-induced stress within the plies of the laminate. The transverse cure shrinkage strain for the composite prepreg was measured using TA Instruments' Q400 Thermo Mechanical Analyzer (TMA) shown in Figure 4-8.

Isothermal tests were carried out at 177°C (the cure temperature for the composite) for 120 minutes, and the shrinkage strain was measured as a function of time as shown in Figure 4-9.The maximum cure shrinkage was measured to be 0.014. The cure kinetics of F263-7 epoxy resin was determined using TA Instruments' Q2000 DSC and was modeled by an n^{th} order model using equation (4-3).

$$[\frac{d\alpha}{dt} = Zexp(\frac{-E}{RT})(1-\alpha)^n] \quad (4\text{-}3)$$

The model parameters, Z, E and n, are 1.787×10^{-7} s^{-1}, 85.4 $kJmol^{-1}$, and 1.14 respectively. This

Figure 4-7: A strain gauged sample

Figure 4-8: TA Instruments' Q400 Thermo Mechanical Analyzer (TMA)

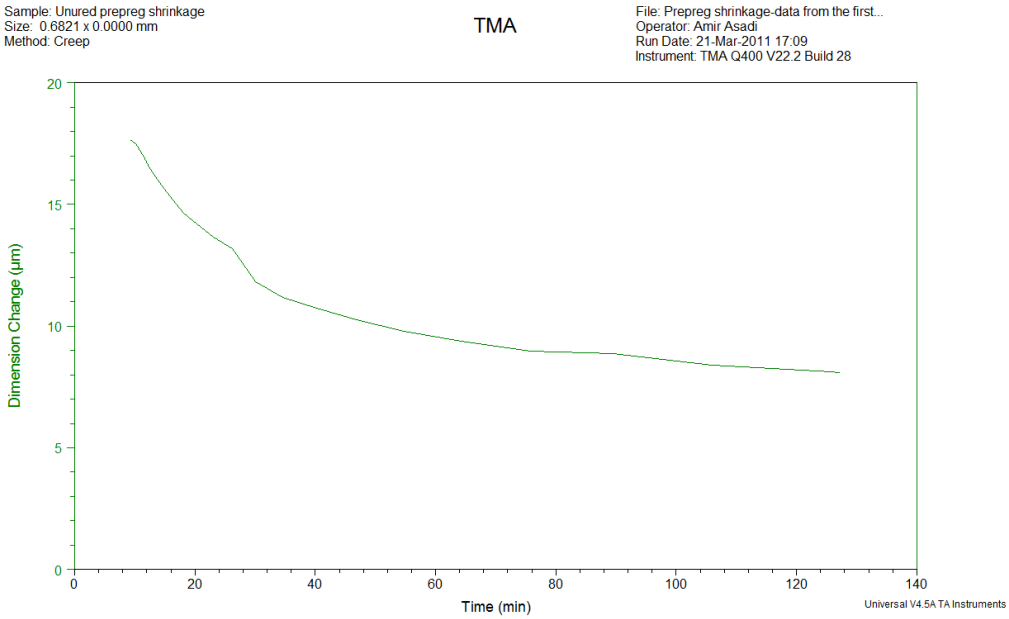

Figure 4-9: Cure shrinkage strain measured using TMA

model was used along with TMA data to define cure shrinkage as a function of degree of cure.

Test coupons from cured [0°] and [90°] unidirectional composite laminates were used to measure the thermal expansion coefficients along longitudinal (α_{11}) and transverse directions (α_{22}) to the fiber axis, using ramp tests, at 3°C/min in the temperature range of 0°C and 250°C, using the TMA. The values of CTE of the completely cured composite were measured as 1.42×10^{-7} and 2.68×10^{-5} $°C^{-1}$ for longitudinal and transverse directions respectively. Both data were input to the PIS module.

4.4.2 Dynamic mechanical analysis (DMA) tests

DMA tests were carried out to measure the glass transition temperature (T_g), instantaneous modulus, the rubbery modulus, and the activation energy, described in Sections 3.7 and 4.5.3 using TA instruments' Q800 DMA, shown in Figure 4-10. Tests were conducted using a film tension clamp. The equipment was capable of exerting a load up to 18 N and can be operated in the temperature range of -150°C to 600°C.

The coupons were ramped at 1°C/min, in the temperature range of RT (Room Temperature) to 320°C. Simultaneously, the samples were subjected to a sinusoidal load at a constant frequency of 10 Hz, and the modulus of the samples was measured as a function of temperature. A typical DMA curve for $[90]_8$ unidirectional samples are shown in Figure 4-11. Two tests were carried out for each sample.

4.4.3 Tensile tests

Tensile tests were conducted, using on-axis [0] and off-axis [θ] unidirectional composite coupons, to determine the modulus, strength, and fracture strain at different temperatures below the glass transition temperature (T_g). All test coupons were soaked at 270 °C (Glass to Rubber

Figure 4-10: TA instruments' Q800 Dynamic Mechanical Analyzer

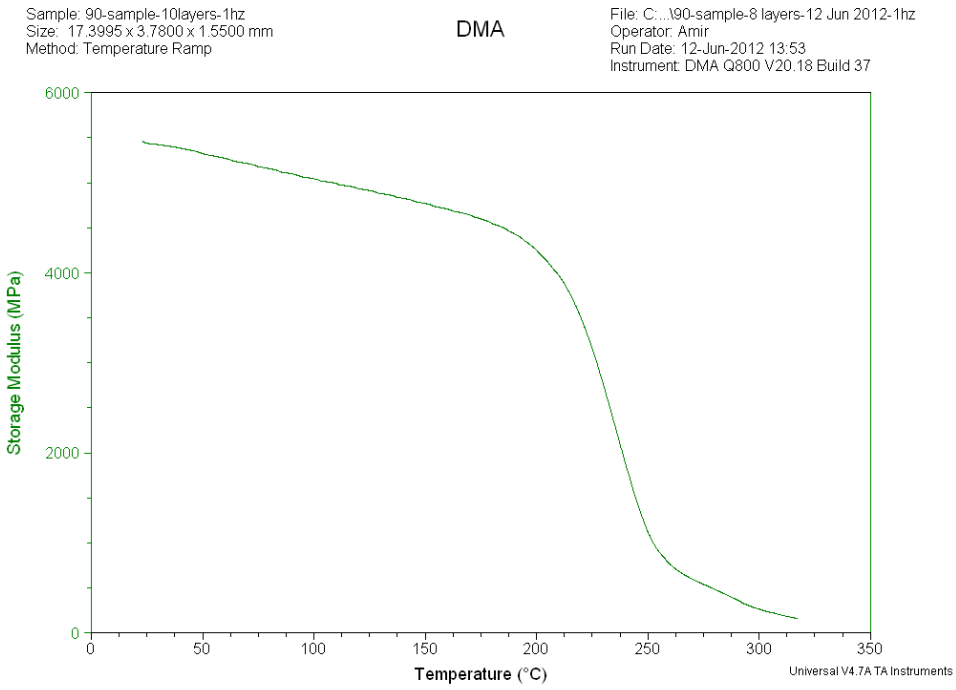

Figure 4-11: DMA test result for unidirectional $[90]_8$ sample

transition temperature) for 15 minutes prior to testing to erase any physical aging. The coupons were tested immediately after erasing the memory. Even though the laminates did not have any process-induced cracks after post-curing, the above mentioned memory erasure step introduced a few cracks in some coupons. Yet, erasing of physical aging to eliminate its influence on mechanical properties is necessary.

Tensile tests were carried out per ASTM D 4762-04 using Instron's servo-electric 8562 universal testing frame, shown in Figure 4-12. . The load frames were equipped with a ±25 kN load cell and a high- temperature oven capable of reaching a temperature of 350 °C and maintaining the set temperature within ±1°C. During ramping up to a desired temperature, the instrument was under load control and was programmed to maintain a zero load. Load cell was maintained at room temperature using cooling water, circulated through the pull rod, to avoid load fluctuations due to heating of the load cell during high temperature tests. After equilibrating at the desired temperature, the coupons were loaded at a constant strain rate of 10^{-4} s^{-1} to failure. Information on the specimens and temperature used in this testing is provided in Table 4-2.

A dummy composite coupon (material, layup and strain gauge identical to those used in the test coupon) was used, in half-bridge configuration, to off-set the effect of temperature fluctuation during testing on strains measured using strain gauges. The dummy coupon with bonded strain gage was under no load and was held close to the test coupon. The load and strain data for the dummy coupons and test coupons were acquired using National Instruments' SCXI data acquisition system and Lab View software.

4.4.4 Repetitive tensile tests

Repetitive tensile tests were used to record time-independent evolution of transverse crack density in multiple plies with increase in applied stress. These tests were also used to

Figure 4-12: Instron's 8562 servo-electric frame with environmental chamber.

Table 4-2. Tensile test plan

Composite	Number of coupons	Temperature			
		22°C	80°C	180°C	220°C
$[0]_6$		3	3	3	3
$[30]_8$		3	3	3	3
$[45]_8$		3	3	3	3
$[60]_8$		3	3	3	3
$[90]_{10}$		3	3	3	3

determine the change in the in-plane Poisson's ratio, ν_{xy}, with increase in the applied stress, with the load being increased in increments of 7-10 % of UTS (Ultimate Tensile Strength). After each load increment, the specimen was unloaded so that the polished edge of the specimen, CDEF shown in Figure 2-1, could be examined using a Nikon digital microscope to record the transverse crack density in [90] and [±θ] plies over a gauge length of 50.8 mm. The tests were carried out at 80°C and 180°C. Information on the specimens and temperature used in this testing is provided in Table 4-3.

4.4.5 Creep and time-dependent damage tests

Creep tests were carried out using Instron's screw driven 5500R and servo-electric 8562 universal testing frames, shown in Figure 4-13. The Instron 5500R machine was controlled using Bluehill software (version 2.5) and was equipped with a ±25 kN load cell and an oven, similar to the Instron 8562. The chamber was capable of reaching a temperature of 300°C. The instrument was equipped with a water cooled pull rod for high temperature tests and was kept under load control during ramp-up and equilibration. The specimens were loaded to the desired creep load at a constant strain rate of 10^{-4} s^{-1}, and after reaching the desired creep load, the machine was switched to load control mode. Creep tests were carried out at various tensile creep stress levels in the range of 45 to 54% of UTS at 80°C, and 22 to 26% of UTS at 180°C. Information on the specimens and temperature used in this testing is provided in Table 4-4.

A second set of samples was used to record time-dependent damage, so at regular time intervals, the specimens were unloaded and examined under a microscope for damage. A dummy composite coupon (with material, layup and strain gauge identical to those used in the test coupon) was used, in half-bridge configuration, to off-set the effect of temperature fluctuation during testing on strains measured using strain gauges. The dummy coupon with a bonded strain

Table 4-3. Repetitive tensile test plan

Composite	Test Type	No. of test coupons	Temperature	
			80°C	180°C
$[\pm 45/90_2]_s$	Crack density versus stress		2	2
$[\pm 45/90_2]_s$	Poisson's ratio variation with crack density		1	N/A

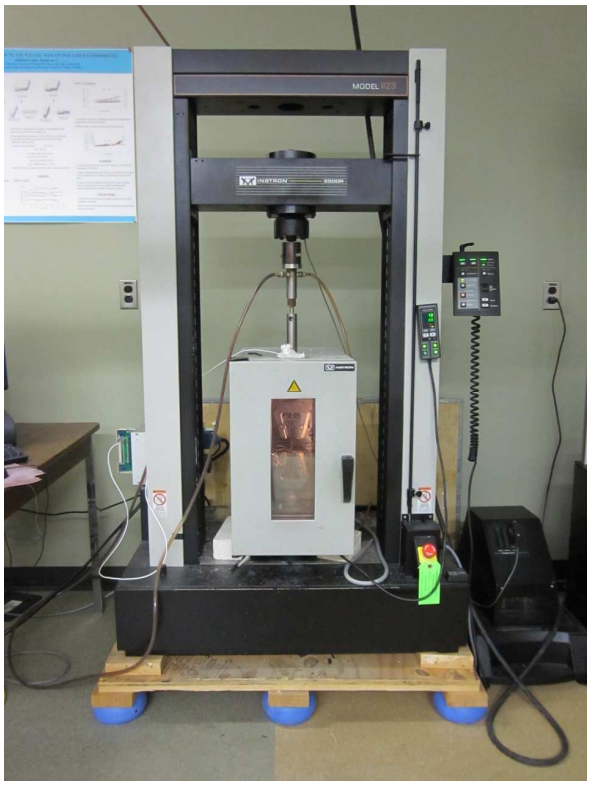

Figure 4-13: Instron's 5500R screw- driven test machine

Table 4-4. Creep and time-dependent damage test plan

Composite	Test Type		Temperature			
			80°C		180°C	
			Stress (MPa)			
			45	54	20	25
$[\pm45/90_2]_s$	Creep	No. of tests coupons	1	1	1	1
$[\pm45/90_2]_s$	Time-dependent transverse crack density characterization		45		25	
		No. of tests coupons	1		1	

gauge was under no load and was held close to the test coupon. The two strain gages on the dummy coupons and the test coupons were connected to DAQ system, and the load and strain data were acquired using National Instruments' SCXI data acquisition system and Lab View software.

4.4.6 Data acquisition

The SCXI-1000 data acquisition system from National Instruments USA, was used to collect the strain and load data during tensile and creep tests. This system consisted of a SCXI-1121 signal conditioning module fitted into a SCXI- 1000 chassis and connected to a SCXI-1321 terminal block. The DAQ unit was connected to a PCIe-6251 multifunctional DAQ board and fitted in to a computer using a shielded cable. A Labview based program was used for data sampling and logging at different rates during tests, with the data sampling rate set to 1000 kHz while the logging rate was varied from 1 data point per sec to 1 data point per 300 sec. The hardware was programmed to acquire four independent parameters (strain, load, position and time) simultaneously for each test.

4.4.7 Damage analysis

Nikon's Eclipse LV100 optical microscope shown in was used for damage analysis of tested samples. This microscope was equipped with objective lenses with magnifications of X2.5- X50 and an eyepiece with a magnification of X10. It was then attached to Nikon's DS-Fi1 camera to capture the images of the samples, which were viewed and analyzed using Nikon's NIS-Elements Basic Research-3.0 image analysis software.

4.5 Simulation Details

The model presented in Chapter 3 to predict TID and TDD evolution in multiple plies

and their influence on creep of a multidirectional polymer composite laminate was programmed using MATLAB. Lamina properties, the laminate stacking sequence, ply thickness, creep stress, temperature, creep compliance of unidirectional lamina, critical stored elastic energy and the activation energy for creep were input to the program.

Details on the input data, simulation parameters such as time and stress step-size, and MATLAB programs are provided in this section.

4.5.1 Input for simulation

4.5.1.1 Mechanical properties, laminate and test details

Mechanical properties of the material used in the thesis were acquired using the tensile tests tabulated in Table 4-2. Tensile tests were conducted for $[0]_6$, $[30]_8$, $[45]_8$, $[60]_8$, and $[90]_{10}$ unidirectional composites at temperatures of RT, 80°C, 180°C and 220°C, and the results of these tests are given in Figure 4-14. The mechanical properties determined from these tests are tabulated in Table 4-5. A $[\pm 45/90_2]_s$ laminate with a ply thickness of 0.132 mm was used to obtain the predictions for creep strain, TID and TDD, which were compared with the experimental results. Creep stresses were in the range of 22 to 55% of UTS, i.e., 45 MPa and 54 MPa for 80°C, and 20 MPa and 25 MPa for 180°C. These stresses were chosen based on the observation in repetitive tensile testing to avoid damage modes other than transverse cracking.

Temperature dependence of experimentally measured longitudinal (S_{11}), transverse (S_{22}), and shear compliances (S_{66}) was empirically modeled, as shown in equation (4-4).

$$S_{11}(T) = 8.3 \times 10^{-3} \quad (GPa^{-1})$$

$$S_{22}(T) = 0.099 + \exp(4.27 \times 10^{-6}\ T) \quad (GPa^{-1}) \quad (4\text{-}4)$$

$$S_{66}(T) = \exp(-0.0209 - 0.009T + 1.476 \times 10^{-5}T^2) \quad (GPa^{-1})$$

The longitudinal compliance, S_{11}, was observed to be independent of temperature. Tempretures

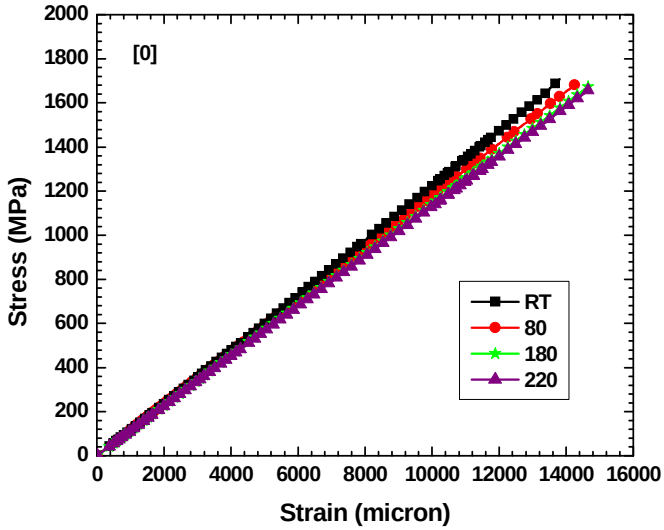
[0]
Stress (MPa)
Strain (micron)
RT
80
180
220
0
200
400
600
800
1000
1200
1400
1600
1800
2000
0
2000
4000
6000
8000
10000
12000
14000
16000

a)

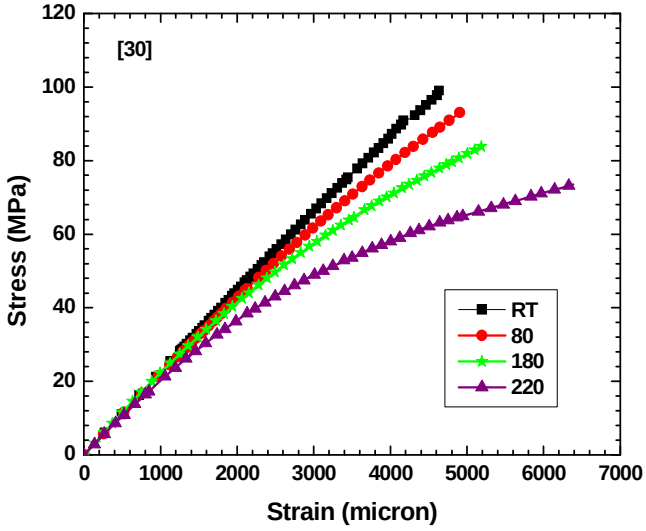
[30]
Stress (MPa)
Strain (micron)
RT
80
180
220
0
20
40
60
80
100
120
0
1000
2000
3000
4000
5000
6000
7000

b)

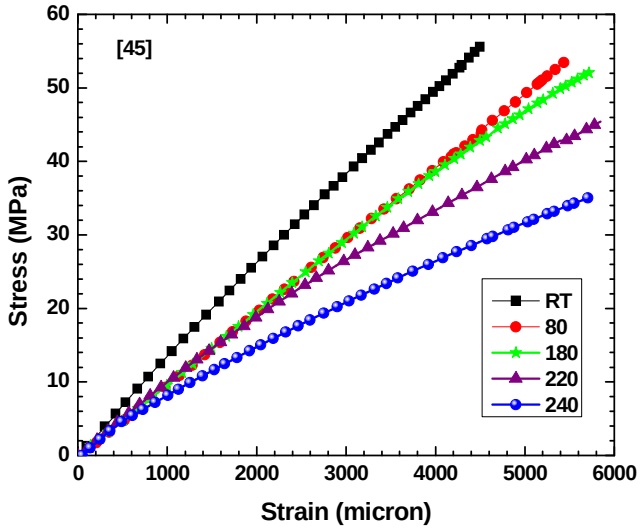
[45]
Stress (MPa)
Strain (micron)
RT
80
180
220
240
0
10
20
30
40
50
60
0
1000
2000
3000
4000
5000
6000

c)

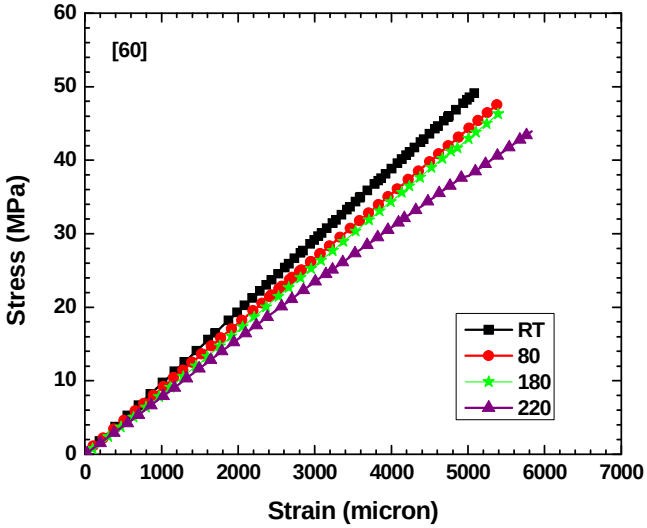
[60]
Stress (MPa)
Strain (micron)
RT
80
180
220
0
10
20
30
40
50
60
0
1000
2000
3000
4000
5000
6000
7000

d)

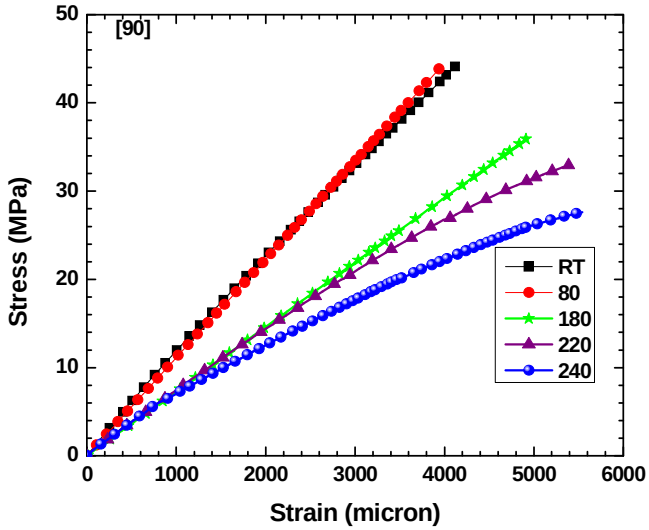

e)

Figure 4-14: Tensile test results for a) $[0]_6$, b) $[30]_8$, c) $[45]_8$, d) $[60]_8$, and e) $[90]_{10}$ at different temperatures in the range of RT to 220°C

Table 4-5. Mechanical properties of Toho G30-500 /F263-7 composite

Longitudinal modulus (E_{11})-GPa	Transverse modulus (E_{22})-GPa	Shear modulus (G_{12})-GPa	Major Poisson's ratio (ν_{12})
120±3	10±1	5±1	0.3±0.1

are in Kelvin

4.5.1.2 Lamina creep compliances

The creep compliance data of the unidirectional lamina in the linear viscoelastic region, i.e., $S_{11}(t)$, $S_{22}(t)$ and $S_{66}(t)$, generated previously by Balachander [3] and Viswanathan [15], were used in the simulation as input. The creep compliances were modeled using a modified Kohlrausch-Williams-Watts (KWW) given by equation (4-5). Since it was not possible to obtain these data for the entire service life of the composite, Balachander [3] and Viswanathan [15] employed the Time-Temperature Superposition Principle (TTSP), as previously discussed in 2.1.3.

$$S_{ij,c}(t) = g_0 S_0 + g_1 g_2 \Delta S(1 - \exp(-[(\frac{t}{a_\sigma \tau})^c]) \qquad (i = j = 1, 2, 6) \tag{4-5}$$

where t is the creep time and S_0 is the instantaneous compliance. ΔS, τ, and c are constants, as tabulated in Table 4-6, obtained by fitting the creep master curve in the linear viscoelastic region (creep stress < 7 MPa) for the unidirectional lamina using this equation. This model was found to fit the master creep curves better than other models such as the original KWW or power law. Mechanical analogs were not used to model the creep curve since they cannot be used for extrapolation beyond the experimental time window used to obtain the creep data. g_0, g_1, g_2 and a_σ are the nonlinear parameters defined by Schapery's nonlinear viscoelastic model [97]. These nonlinear parameters are equal to one in the linear viscoelastic region of polymer matrix; however, they are dependent on temperature and stress in the nonlinear viscoelastic region of polymer matrix, as described by equation (4-6).

$$\{g_0, g_1, g_2, a_\sigma\} = \begin{cases} 1 & \text{Linear visoelastic region} \\ f(\sigma, T) & \text{Non-linear visoelastic region} \end{cases} \tag{4-6}$$

The nonlinear parameters were obtained using experimental creep data generated for

Table 4-6. Values of parameters of modified KWW equation

Parameters	80°C		180°C	
	$S_{22}(t)$	$S_{66}(t)$	$S_{22}(t)$	$S_{66}(t)$
S_0 (MPa^{-1})	1.0×10^{-4}	2.07×10^{-4}	1.40×10^{-4}	2.53×10^{-4}
ΔS (MPa^{-1})	0.002675	0.002113	0.002413	0.002037
τ (min)	3.88×10^{12}	2.5416×10^{7}	1.4336×10^{8}	9.5326×10^{5}
c	0.2863	0.3638	0.2873	0.3457

unidirectional lamina in the nonlinear viscoelastic region by Gupta [16]. Creep curves in the non-linear viscoelastic region (creep stress > 7 MPa) and equation (4-4) were used to obtain the non-linear parameters using the data reduction procedure discussed in Ref. 16. These parameters were used as input in this study. The values for these constants are tabulated in Table 4-6 for 80°C and 180°C. Nonlinear parameters g_0, g_1, g_2, and a_σ were 1 while calculating the parameters in Table 4-6. Some of the non-linear parameters were dependent on both stress and temperature. This dependence was empirically modeled. These parameters for transverse ($S_{22}(t)$) and shear ($S_{66}(t)$) creep compliances are given below.

$$\left.\begin{aligned} g_0 &= 1.0414 \\ g_1 &= 0.0414\sigma_{22} + 1.0175 \\ g_2 &= 0.001\sigma_{22}T + 0.0143\sigma_{22} + 0.0071T + 0.4391 \\ a_\sigma &= 0.0003\sigma_{22}T - 0.0308\sigma_{22} - 0.0041T + 1.2134 \end{aligned}\right\} \text{ for } S_{22} \qquad (4\text{-}7)$$

$$\left.\begin{aligned} g_0 &= 0.005\sigma_{66} + 0.9754 \\ g_1 &= 0.0055\sigma_{66} + 0.9774 \\ g_2 &= 0.0018\,T - 0.1342\sigma_{66} - 0.0053T + 1.3044 \\ a_\sigma &= 0.0002\sigma_{66}T - 0.0502\sigma_{66} - 0.0027T + 1.2676 \end{aligned}\right\} \text{ for } S_{66} \qquad (4\text{-}8)$$

where T is in °C and σ is in MPa.

4.5.2 Cure shrinkage and thermal expansion

The input value for the transverse cure shrinkage strain, measured as per the procedure discussed in Section 4.4.1, was 0.014. The longitudinal cure shrinkage was found to be negligible.

The measured longitudinal (α_{11}) and transverse (α_{22}) thermal expansion coefficients were 1.42×10^{-7} and 2.68×10^{-5} °C^{-1} respectively. These values were input to the model.

4.5.3 Critical stored elastic energy for fracture

The procedure required to calculate critical stored elastic energy, has been explained in 3.7. The measured rubbery, instantaneous and viscous moduli for [0], [90] and [45] unidirectional plies are given in Table 4-7. Since the simulations were done at 80°C and 180°C, the instantaneous (E_0), the rubbery (E_R) and the viscous (E_V) modulus values at these temperatures are tabulated in Table 4-8. The rubbery modulus (E_R) at different temperatures was determined using equation (3-102), whereas the instantaneous modulus (E_0) for each temperature was determined using equations (4-9)-(4-11) given in Table 4-8, using DMA tests. The viscous modulus was determined using equation (3-100).

The activation energy, E_{act}, was experimentally determined to be 191.78 kJ/mol and 283.65 kJ/mol for [90] and [45] unidirectional samples respectively, using the procedure discussed in 3.7 and DMA test results at multiple frequencies shown in Figure 4-15 (a). The activation energy was determined from the slope of the plots in Figure 4-15 (b-c). Figure 4-16 and Figure 4-17 show the failure strain ($\varepsilon^u(t)$) and stress ($\sigma^u(t)$) as a function of time for [90] plies at 80°C and 180°C, respectively. The failure strain and stress for [45] plies at 80°C and 180°C are shown as a function of time in Figure 4-18 and Figure 4-19, respectively. These values were obtained using the tensile data plotted in Figure 4-16 and the procedure described in 3.7. Using these data in Figures 4-17-4-21 and Table 4-8 and the procedure described in 3.7, the time-dependent critical stored elastic energy along with fitted curves for [90] and [45] laminates was calculated at 80°C and 180°C and is plotted in Figure 4-20 and Figure 4-21 respectively. The fitted equations for time-dependent fracture energy for both [90] and [45] plies are given below. The coefficient of determination (R^2) for all the fitted curves was more than 0.98.

$$U^{(90)U}_{80^0C}(t) = 0.103333\exp\left(\frac{-t}{2.4131\times10^{11}}\right)^{0.105} \qquad (4\text{-}12)$$

Table 4-7: Instantaneous and rubbery moduli obtained from DMA

Material	E_0: GPa @ 295 K	E_R: GPa @ T_g+40 K	E_V: GPa @ 295 K
Toho G30-500/ F263-7 –$[90]_{10}$	10	0.60	9.40
Toho G30-500/ F263-7 –$[0]_6$	120	15.74	104.26
Toho G30-500/ F263-7 –$[45]_8$	12.50	0.80	11.20

Table 4-8: Instantaneous, rubbery and viscous moduli values at different temperatures

Material	T (K)	E_0 (GPa)	E_R (GPa)	E_V (GPa)
Toho G30-500/ F263-7 –$[90]_{10}$	295	10	0.60	9.40
	353	9.68*	0.72	8.96
	453	9.14*	0.92	8.22
Toho G30-500/ F263-7 –$[0]_6$	295	120	15.74	104.26
	353	113.08**	18.77	94.31
	453	100.94**	24.08	76.86
Toho G30-500/ F263-7 –$[45]_8$	295	12.50	0.80	11.70
	353	11.82***	0.95	10.87
	453	10.64***	1.22	9.42

* $E_0^{(90)}(T) = 10.12 - 5.47\times10^{-3}\,T$ (4-9)

** $E_0^{(0)}(T) = 122.79 - 121.37\times10^{-3}\,T$ (4-10)

*** $E_0^{(45)}(T) = 12.77 - 11.84\times10^{-3}T$ (4-11)

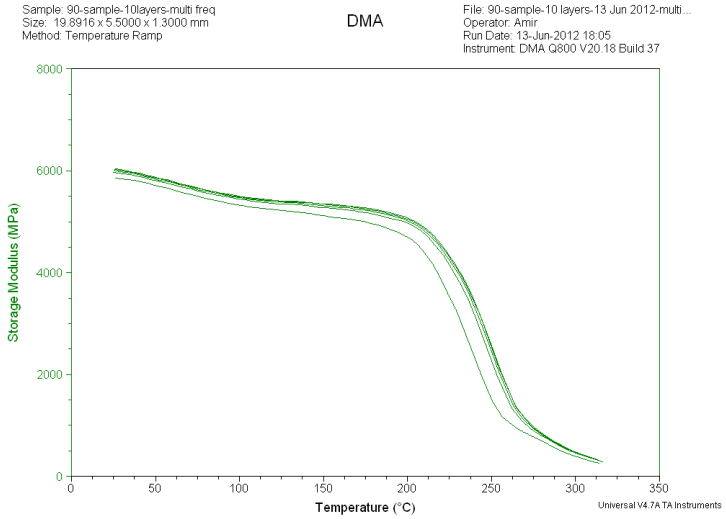
Sample: 90-sample-10layers-multi freq
Size: 19.8916 x 5.5000 x 1.3000 mm
Method: Temperature Ramp
DMA
File: 90-sample-10 layers-13 Jun 2012-multi...
Operator: Amir
Run Date: 13-Jun-2012 18:05
Instrument: DMA Q800 V20.18 Build 37
Storage Modulus (MPa)
Temperature (°C)
Universal V4.7A TA Instruments

a)

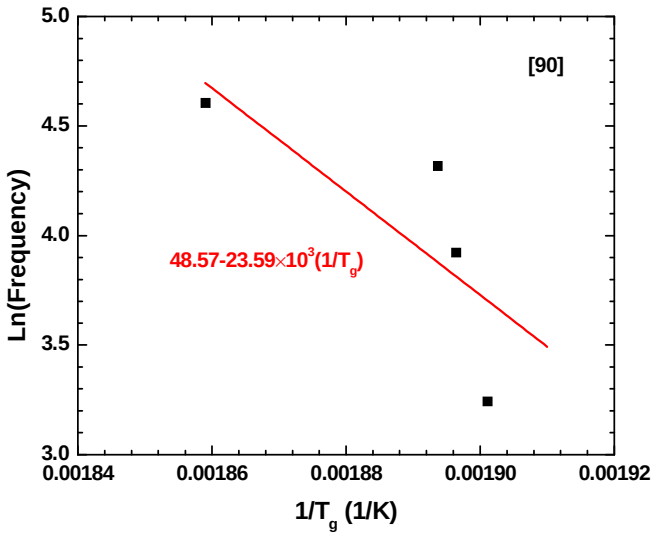
[90]
48.57-23.59×10^3(1/T_g)
Ln(Frequency)
1/T_g (1/K)

b)

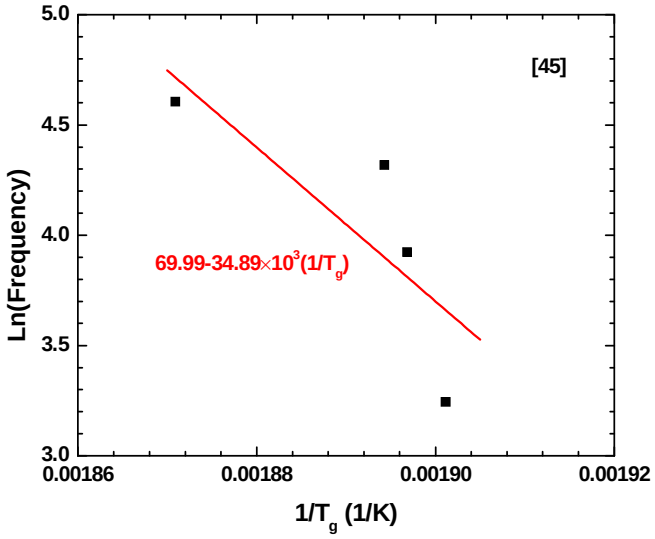

c)

Figure 4-15: a) DMA test results [90] at multiple frequencies, b) Arrhenious plot for $[90]_6$ laminate, and c) Arrhenious plot for $[45]_4$ laminate

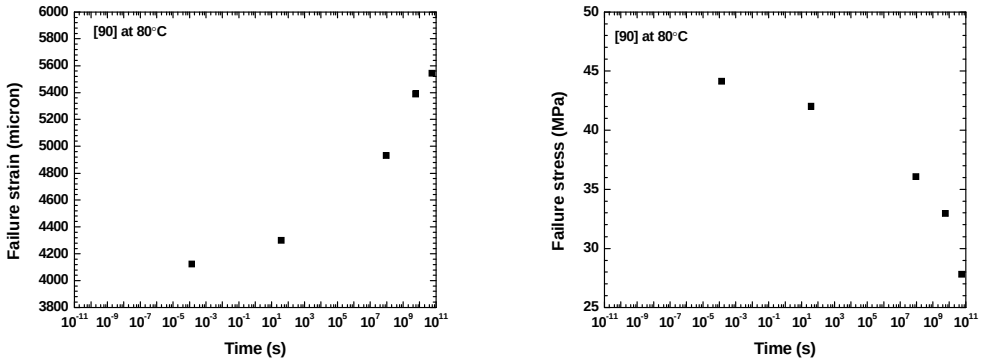

Figure 4-16: Variation of failure strain and stress data and with time for $[90]_6$ laminate at 80°C

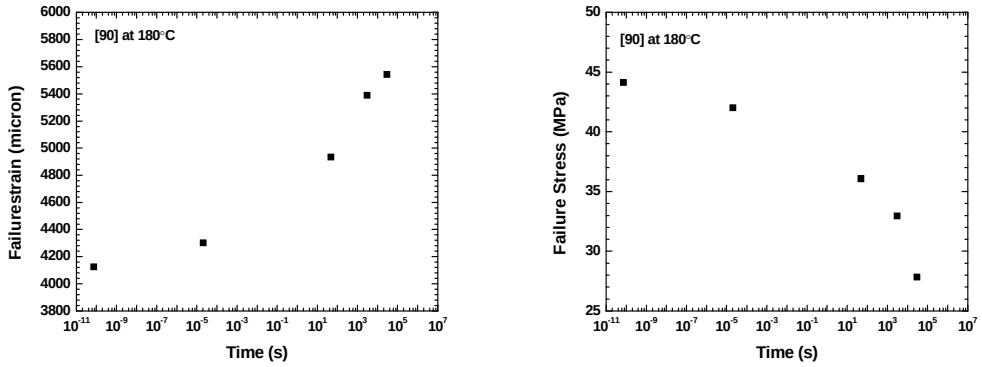

Figure 4-17: Variation of failure strain and stress with time for $[90]_6$ laminate at 180°C

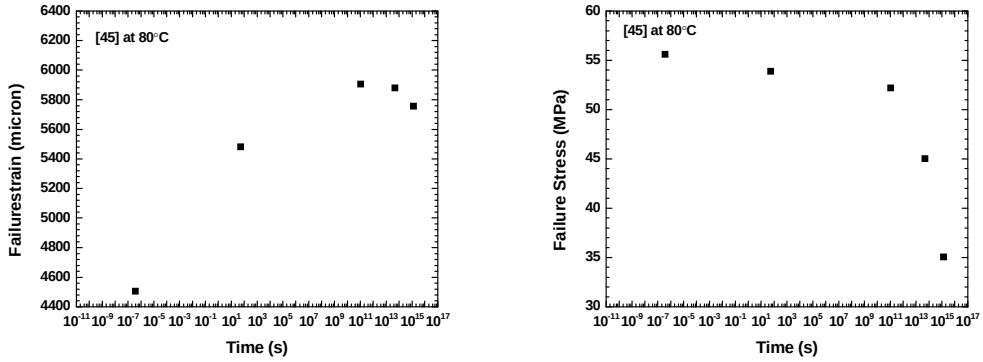

Figure 4-18: Variation of failure strain and stress with time for $[45]_4$ laminate at 80°C

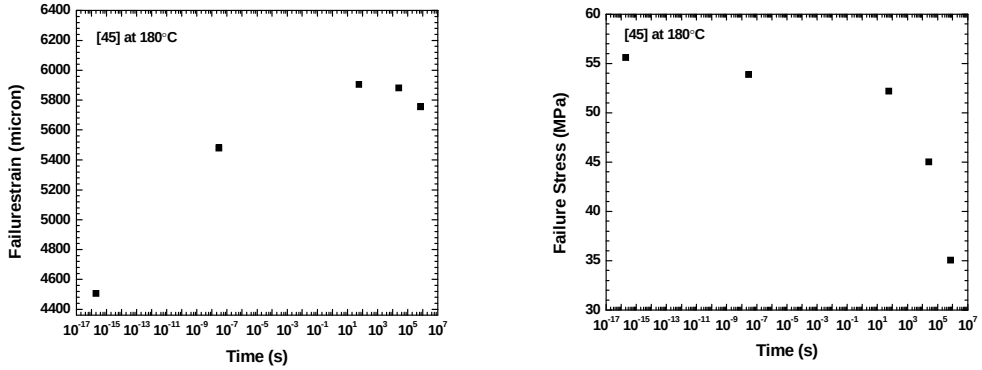

Figure 4-19: Variation of failure strain and stress with time for $[45]_4$ laminate at 180°C

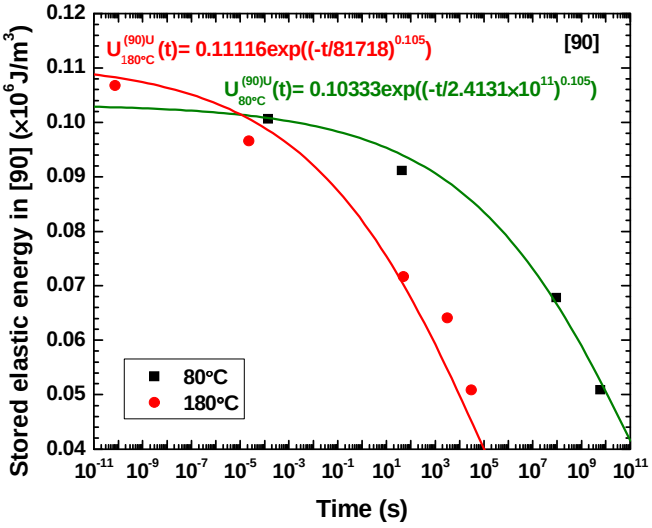

Figure 4-20: Time-dependent critical stored elastic energy per unit volume for $[90]_6$ laminate along with the fitted curves

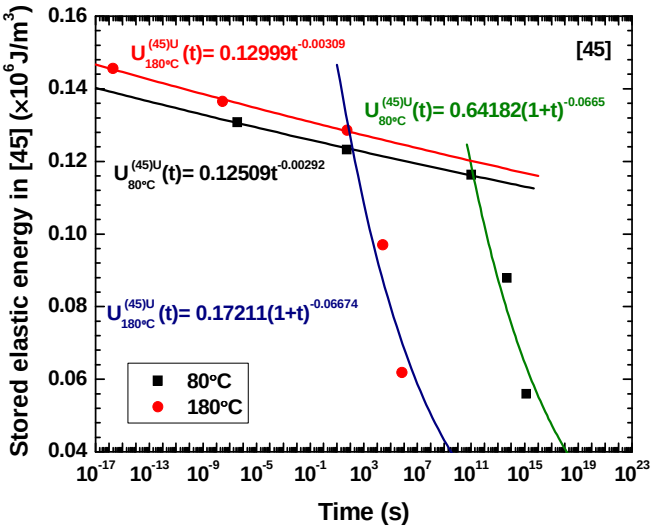

Figure 4-21: Time-dependent critical stored elastic energy per unit volume for $[45]_4$ laminate along with the fitted curves

$$U^{(90)U}_{180^0C}(t) = 0.111 \exp\left(\frac{-t}{81718}\right)^{0.105} \quad (4\text{-}13)$$

$$U^{(45)U}_{80^0C}(t) = 0.125t^{-0.003} \qquad t < 10^{11}\ s \quad (4\text{-}14\ (a))$$

$$U^{(45)U}_{80^0C}(t) = 0.642(1+t)^{-0.066} \qquad t \geq 10^{11}\ s \quad (4\text{-}14(b))$$

$$U^{(45)U}_{180^0C}(t) = 0.129\,t^{-0.003} \qquad t < 60\,s \quad (4\text{-}15(a))$$

$$U^{(45)U}_{180^0C}(t) = 0.172(1+t)^{-0.066} \qquad t \geq 60\,s \quad (4\text{-}15(b))$$

4.5.4 Simulation using MATLAB

The creep model and its four modules, discussed in Chapter 3, were programmed in MATLAB. The influence of various simulation parameters used in the MATLAB program, such as time step during creep modeling and stress step during loading to the creep load, on convergence to the optimal solution was studied. A temperature step size of -1°C, a stress-step size of 1 MPa and a time-step size of 10s for the first 24 hours and 1000s until the end of creep time, i.e. 333 hours, were found to be optimal. It was observed that values smaller than the selected did not change the accuracy of the simulation. Depending on the computer capability, the simulation time varied. Using a computer with 36 GB RAM and an Intel ® Xenon ® processor E5645 CPU, the simulation times for PIS, QSL, and SL modules were approximately 5 minutes, 2.5 hours, and 1 day.

4.5.5 Details on MATLAB program of PIS, QSL and SL Modules of the Creep Model

4.5.5.1 VA Module

The VA module solves the differential equations (3-59)-(3-66) using the *bvp4c* function in MATLAB. This function generates a numerical solution which is continuous in the interval

[a,b] in which the boundary value problems for ordinary differential equations (ODE) has been defined. *bvp4c* uses a collocation method which considers certain nodes in the interval of [a,b] and provides an approximate solution on those nodes. *bvp4c* is capable of solving ODEs with higher order and with multiple boundary values. The error tolerance can be defined in bvp4c and depends on the difficulty of the problem. Error tolerance of 10^{-4} was used in the VA module. More details on this function can be found in Ref. 115..

In the VA module, each ply of the laminate is divided into the same size intact regions; the number of intact regions will be equal to the number of a ply which has the maximum cracks +1. For example, if [90] has the maximum number of cracks among all the plies, the intact regions are determined as $n^{(90)}+1$ for all the plies where $n^{(90)}$ is number of cracks in [90] ply and the size of these intact regions are equal to $L/n^{(90)}+1$, where L is the laminate length. 175 Nodes are placed between and at the boundaries of these intact regions, and boundary values for stresses are assigned to these nodes. Using these boundary values at the location of these nodes, the differential equations are solved with an error range of 10^{-4}.

To start with, all plies will have one intact region. Nodes are also placed at the ends of the plies in the laminate as shown in Figure 4-22 (a) and the imposed boundary conditions are imposed at these nodes (zero perturbation). The stress in each ply at these nodes, for a given applied load to the laminate, is determined using lamination theory. The whole laminate are divided into same size intact regions and the nodes are located on the boundaries of the intact regions. When a crack occurs, it is located on a pre-defined node. The number of nodes are are updated with the number of cracks.

When FPF occurs in [90] plies, the crack is placed at the center of the [90] plies as shown in Figure 4-22 (b), and the boundary conditions corresponding to this crack, i.e., perturbation

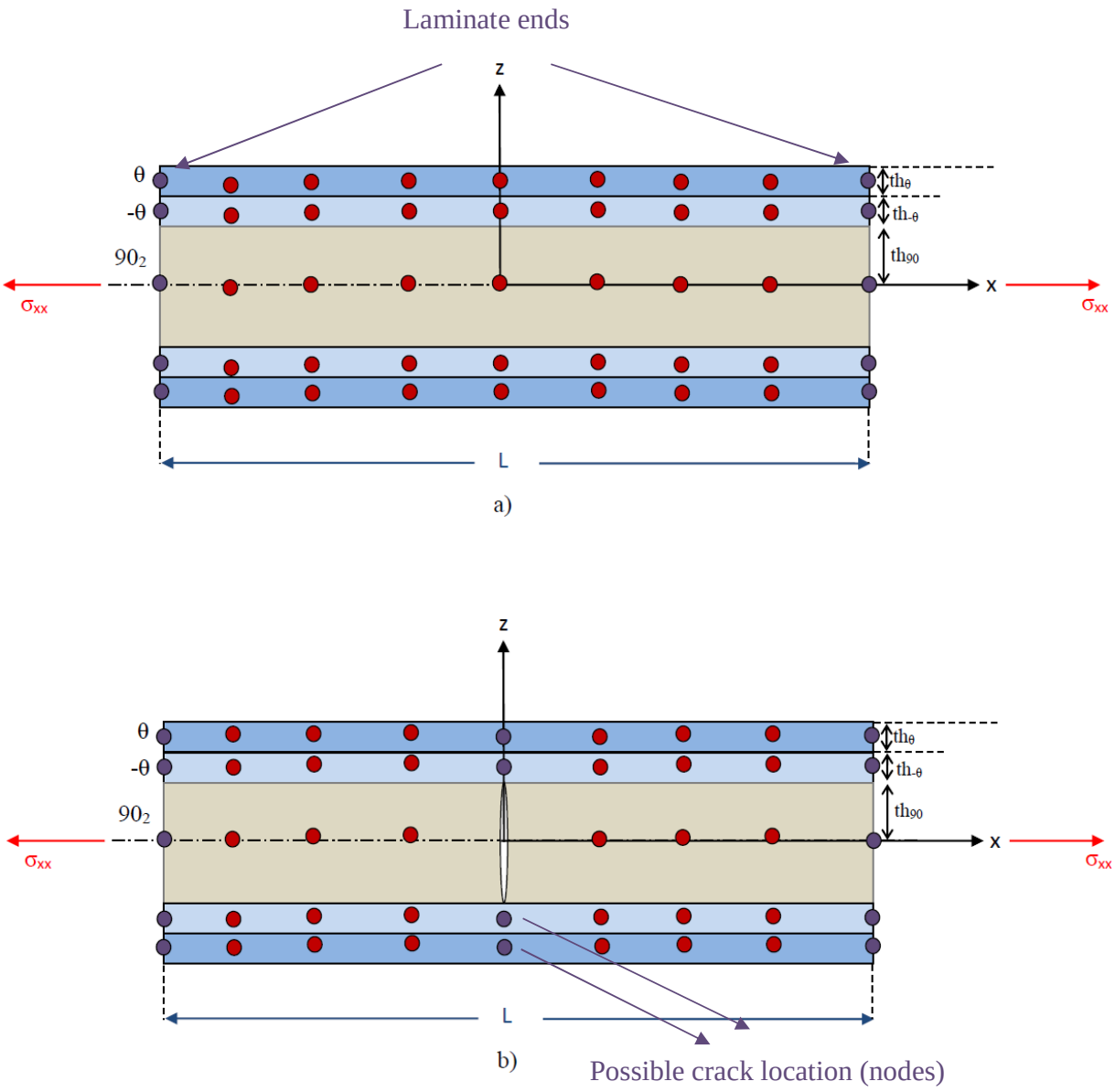
Laminate ends
z
θ
-θ
90_2
th_θ
$th_{-\theta}$
th_{90}
x
σ_{xx}
σ_{xx}
L
a)
z
θ
-θ
90_2
th_θ
$th_{-\theta}$
th_{90}
x
σ_{xx}
σ_{xx}
L
b)
Possible crack location (nodes)

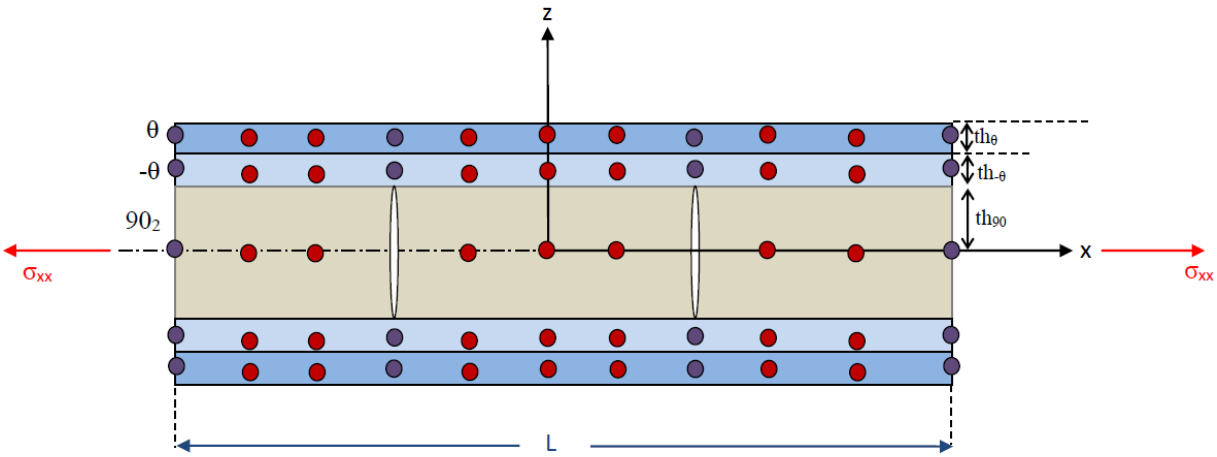

c)

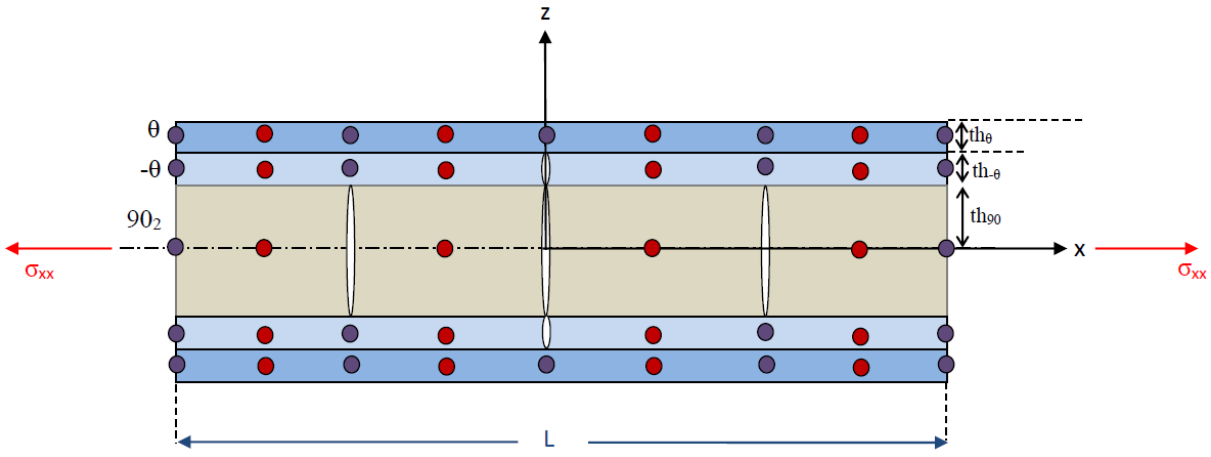

d)

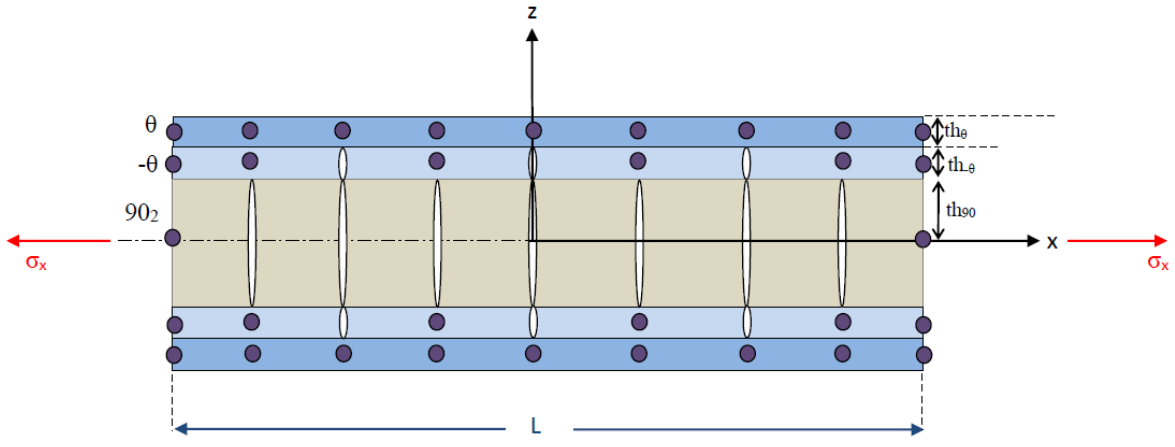

e)

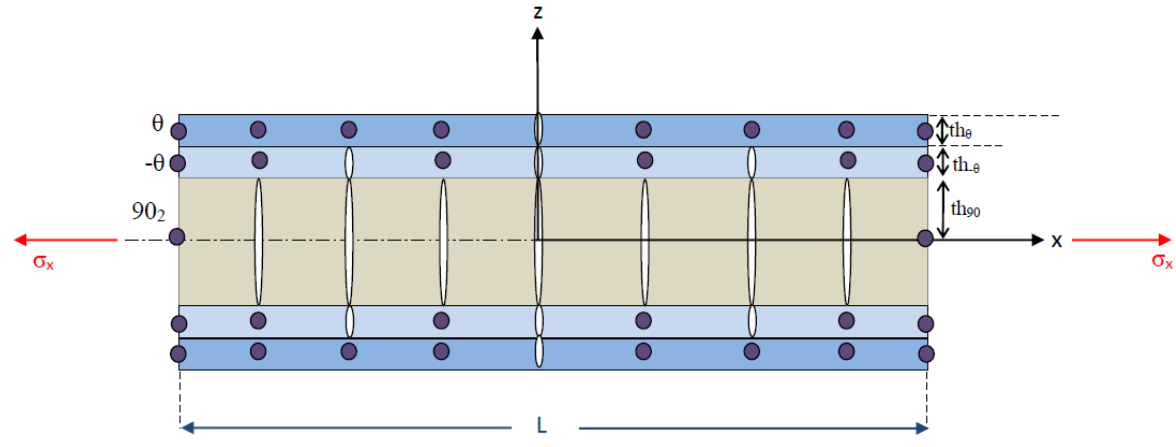

f)

Figure 4-22: Simulation of damage progression, (a) Intact Laminate, (b) FPF in [90] plies, (c) Multiple cracks in [90] plies, (d) FPF in [-45] plies, (e) Multiple cracks in [-45] plies, and (f) FPF in [+45] plies

stresses of $\varphi^{(90)}$, are set equal to the stress in that ply before cracking. Stress is then set to zero in the crack face, as equations (3-11) and (3-12) are assigned to the node at this location. It is to be noted that the crack number is increased by 1 whenever a ply fails, as per assumption. The nodes are placed in [±45] plies at locations above and below the crack in [90] plies as shown in Figure 4-22 (b). Determining the boundary values for these nodes in [±45] plies are a challenge since they are not known *a priori*. Moreover, the boundary values for [-45] plies would be different from those of [+45] plies due to the proximity of [-45] plies to cracks in [90] plies. This is supported by the experimental data presented in Section 5.3.4; the transverse cracking in [-45] plies started at a lower stress than that in [+45] plies. Based on this, the boundary values for the nodes in [±45] above and below the crack location in [90] were approximately determined and entered as the boundary conditions in the program. This will be discussed in detail in Section 5.4.1. The perturbation stresses and the stress state at these locations are still to be determined, though the solution to the differential equations yields the distribution in perturbation stresses due to cracking and the stress state in each ply of the laminate. Using this distribution, the average stress in each ply is determined as per equation (3-85), and all nodes including those at the ends are reset with these average values. The laminate stress is determined using these ply stresses, and the laminate modulus after cracking is determined using this new laminate stress and the laminate strain before fracture (constant strain rate condition) as per equation (3-86) for QSL module and (3-98) for SL module. The strain energy in each ply is re-calculated using this average stress and compared with critical stored elastic energy. If a crack is predicted, the crack number is increased by 1 as shown in Figure 4-22 (c), the same size intact regions are created, the location of cracks are updated at the boundaries of the intact regions, and the above procedure is repeated until no further cracking of that ply is predicted. This ensures that the

above-mentioned assumption of crack increment by 1 does not introduce any error in prediction. If no further cracking is predicted, the stress state and crack density are input to the working module that invoked the VA module.

The placement of cracks and nodes for FPF in [-45] plies, damage progression in [-45] plies, and FPF in [+45] plies are illustrated in Figure 4-22 (d), (e), and (f) respectively. Although the cracks in all plies are aligned in Figure 4-22 (f), the laminate would not fail since cracks propagating along the width of [-45] and [+45] layers are perpendicular each other. The final laminate failure is caused by delamination between these two layers followed by failure of fibers in each of these layers. These two failure modes and hence final laminate failure are not predicted in this thesis. The alignment of cracks in [-45] and [+45] layers due to the assumption of the location of cracking as shown in Figure 4-22 (f) may not happen in reality (as explained in Chapter 3), and the impact of this on the accuracy of prediction will be discussed in the next chapter.

The flow chart in Figure 4-25 details the various programming steps for the VA module, discussed above and in Section 3.3.

Step 1. The average stress state, $\sigma^{(k)}_{jl,\, i-1}$ (j, l=x, y) and the number of cracks, $n^{(k)}_{i-1}$, in each ply are input.

Step 2: Differential equations derived in equations (3-59) – (3-66) are programmed using the *bvp4c* function in MATLAB.

Step 3: The whole laminate is divided into the intact regions ($Intact\_Reg^{(L)}_{i-1}$) corresponding to the crack numbers of a ply (e.g. $n^{(90)}_{i-1}$), which has the maximum number of cracks ($n^{(max)}_{i-1}$), i.e., $Intact\_Reg^{(L)}_{i-1} = n^{(max)}_{i-1}+1$. Cracks are located at the boundaries of each intact region.

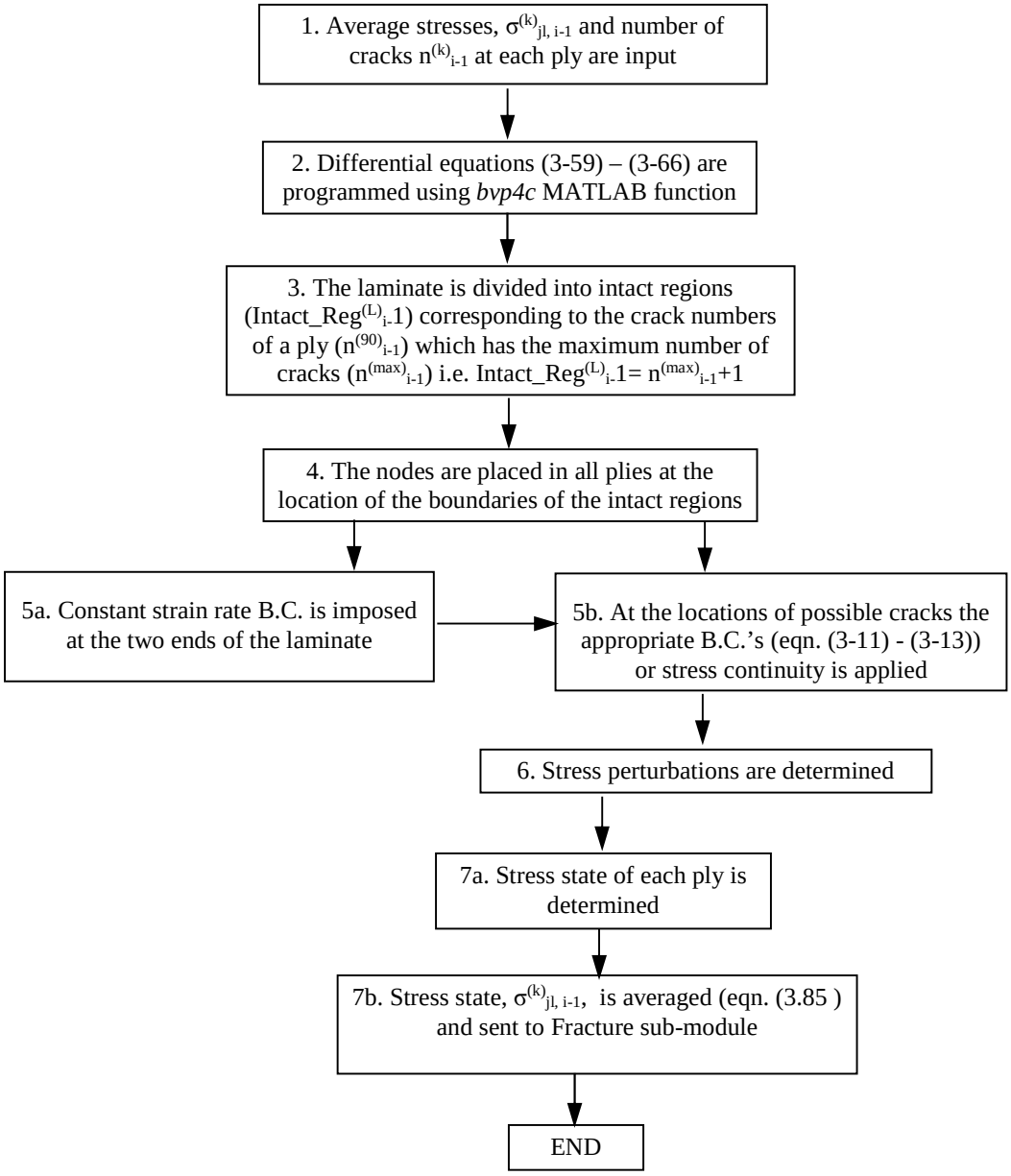

Figure 4-23: Flow chart for simulation of VA module

Step 4: Nodes are placed in all plies at the location of the boundaries of the intact regions. Cracks are located at these nodes and the boundary conditions are applied at these nodes.

Step 5a: A constant strain rate boundary condition is imposed at the two ends of the laminate, which are considered to be intact in order to transfer the applied load to the laminate. This requires that the perturbation stress at these two locations be zero; in other words, the stress at these locations is equal to the applied stress.

Step 5b: At the nodes for all plies, appropriate B.C.'s (equations (3-11 - (3-13)) in case of cracks, or continuity in case of no cracks, is applied. In other words, if there is a crack at a node, the perturbation stresses are defined such that the $\sigma^{(k)}_{xx}$, $\sigma^{(k)}_{xy}$, and $\sigma^{(k)}_{xz}$ at the crack surface of that ply are zero. The appropriate B.C.'s, as explained earlier, are applied in the corresponding nodes in other intact plies.

Step 6: The stress perturbations are determined.

Step 7a: The stress distribution in each ply is determined which is the output of this module.

Step 7b: The stresses are further averaged using equation (3-85) and sent to the fracture sub-module to ensure that the stored elastic energy of each ply is lower than the critical stored elastic energy. If the stored elastic energy of one ply is greater than the critical stored elastic energy of that ply, one crack is added to the existing cracks of the ply using the Fracture sub-module, and the VA module is invoked again by the working module (e.g. PIS or QSL or SL). Steps 1 to 7 are then repeated.

4.5.5.2 Fracture sub-module

The flow chart in Figure 4-25 details the various programming steps for the prediction of the ply failure, discussed in Section 3.7.

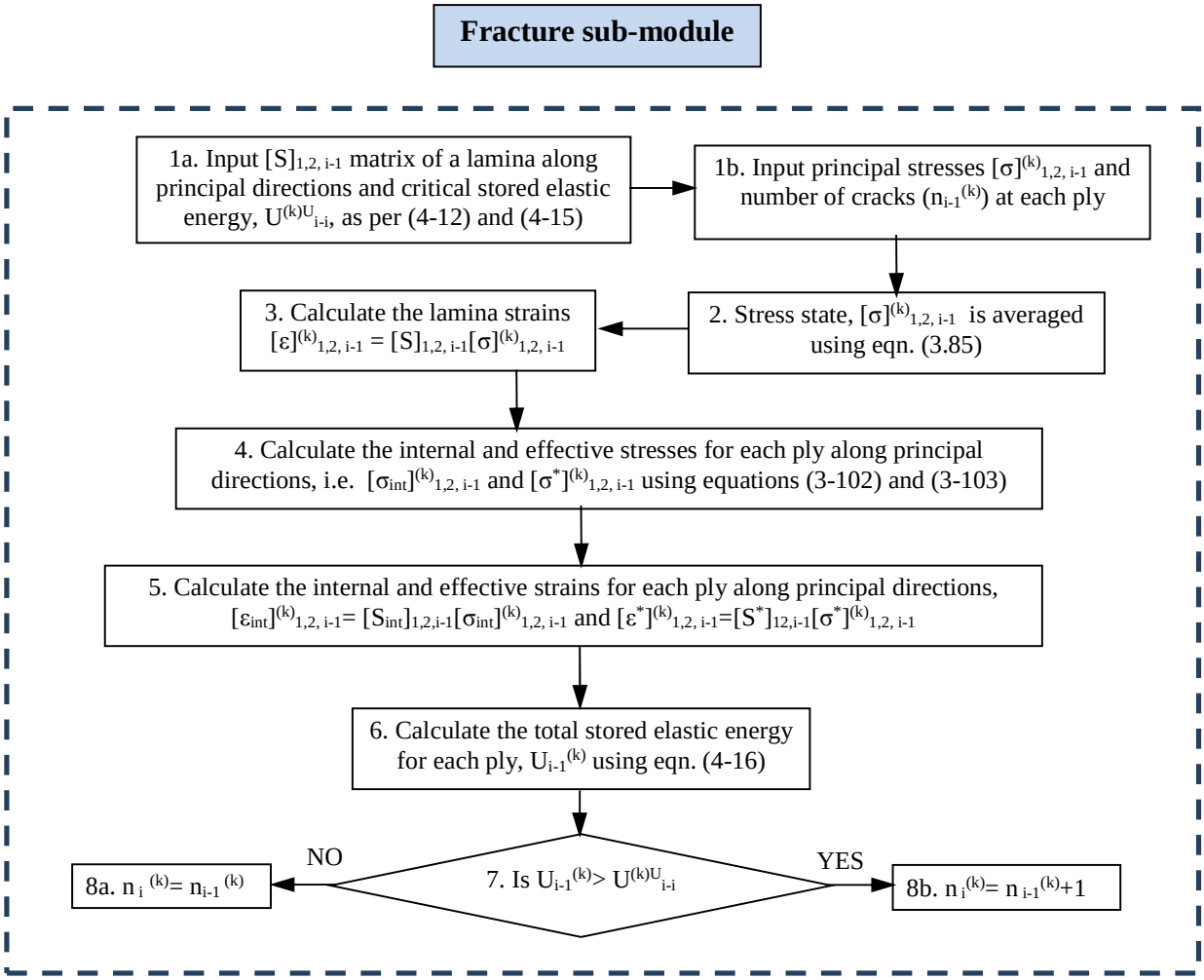

Figure 4-24: Flow chart for simulation of fracture criterion

Step 1a. The $[S]_{1,2,\ i-1}$ matrix of a lamina along principal directions and critical stored elastic energy $U_{cr,\ i-1}^{(k)}$ for each ply is input as per equations (4-12) - (4-15).

Step1b. The principal stresses $[\sigma]^{(k)}_{1,2,\ i-1}$ and number of cracks ($n_{i-1}^{(k)}$) at each ply are input from any of the four modules.

Step 2: The stresses are averaged using equation (3-85).

Step 3: The principal strains in each ply, $[\varepsilon]^{(k)}_{1,2,\ i-1}$, are determined using $[S]_{1,2,i-1}[\sigma]^{(k)}_{1,2,\ i-1}$.

Step 4: The internal and effective stresses for each ply along principal directions, i.e., $[\sigma_{int}]^{(k)}_{1,2,\ i-1}$ and $[\sigma^*]^{(k)}_{1,2,\ i-1,}$ are calculated using equations (3-102) and (3-103).

Step 5: The internal and effective strains for each ply along principal directions, i.e., $[\varepsilon_{int}]^{(k)}_{1,2,\ i-1}$ and $[\varepsilon^*]^{(k)}_{12,\ i-1,}$ are calculated using equations $[S_{int}]_{1,2,i-1}[\sigma_{int}]^{(k)}_{1,2,\ i-1}$ and $[S^*]_{1,2,i-1}[\sigma^*]^{(k)}_{1,2,\ i-1}$ respectively. $[S_{int}]_{1,2}$ and $[S^*]_{1,2}$ are calculated using the DMA tests results as tabulated in Table 4-7, and Table 4-8.

Step 6: Stored elastic energy for each ply, $U_{i-1}^{(k)}$ are determined using the internal and effective stresses and strains as per equation given below

$$U_{i-1}^{(k)} = \left[\frac{1}{2}(\sigma_{l,\text{int}}\varepsilon_{l,\text{int}}) + \frac{1}{2}(\sigma_l^*\varepsilon_l^*)\right] \qquad l = 1,2,6 \tag{4-16}$$

Equation (4-16) determines the elastic energy stored along the principal directions. The strain used in the calculation of the stored elastic energy is the residual strain in each ply as per given in equation (3-76).

Step 7: Stored elastic energy is compared with critical stored elastic energy.

Step 8: If the stored elastic energy is equal to or greater than the critical stored energy, the number of cracks is increased by one crack, i.e., $n_i^{(k)} = n_{i-1}^{(k)}+1$; if no cracking is predicted, the crack density will remain the same.

The output of this sub-module is crack density in each ply.

4.5.5.3 PIS module

The flowchart, detailing various simulation steps of the PIS module, described in Section 3.4, is given in Figure 4-25. Process-induced stresses due to CTE and cure shrinkage mismatch among various plies was determined during cooling from the cure temperature of (177°C) to room temperature. The output of this module, which will be input into the QSL module, includes the thermal strain of the laminate, the ply residual stresses, and the crack density in each ply due to residual stresses. The simulation steps are as follows:

Step 1: Initially the program reads the laminate layup, lamina properties, cure temperature, and creep temperature, cure shrinkage strain and thermal expansion (α_{11} and α_{22}); all properties are along the principal directions of the lamina.

Step 2a: Determine the S and Q matrices of a ply at the cure temperature along principal directions.

Step 2b: Determine the S and Q matrices of a ply at the current temperature, T_{i-1} along principal directions.

Step 3: The stiffness matrices, [A], [B], [D] and compliance matrices [a], [b], and [d] of the laminate are determined using the stiffness and compliance matrices of the laminas that make up the laminate as per equation (A-12). Only [A] and [a] matrices are used here due to the nature of the laminate and loading.

Step 4: The unconstrained thermal and cure-induced strains in each ply, $[\varepsilon_T]_{1,2}$, are calculated using equation $[\varepsilon_T]_{1,2}=[\alpha]_{1,2}\times[\Delta T]$ and $[\varepsilon_{Cure}]_{1,2}=[0;\varepsilon_{CureShrinkage};0]$, respectively.

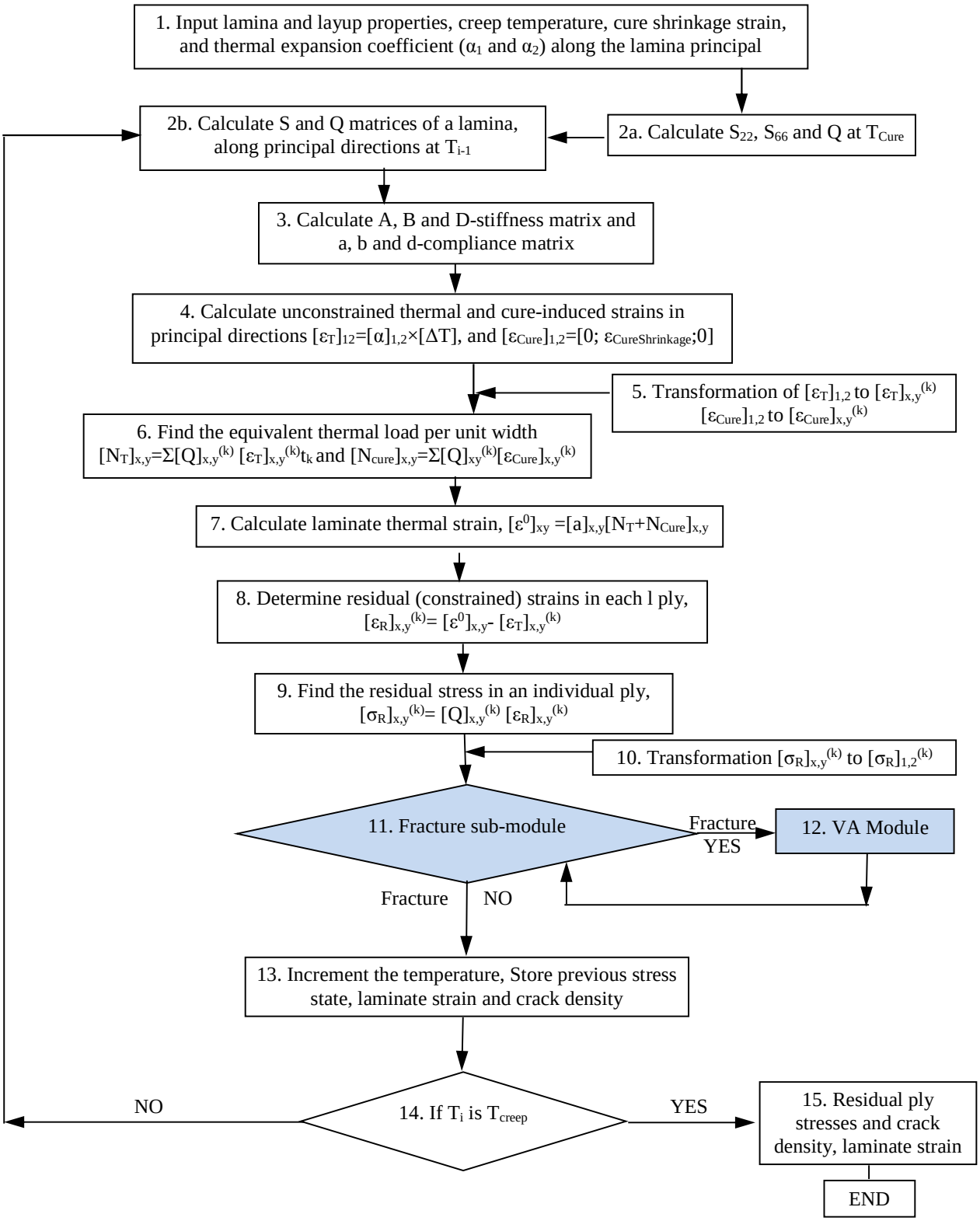

Figure 4-25: Flow chart for simulation of PIS Module

Step 5: The unconstrained thermal and cure-induced strains in each ply, $[\varepsilon_T]_{1,2}$, $[\varepsilon_{Cure,}]_{1,2}$ are transformed from principal coordinates to global coordinates $[\varepsilon_T]_{x,y}^{(k)}$ and $[\varepsilon_{Cure}]_{x,y}^{(k)}$, using the transformation matrix T_3 given in equation (3-90).

Step 6: The equivalent thermal load per unit width, corresponding to these unconstrained thermal and cure shrinkage strains in plies of the laminate, are calculated using $[N_T]_{x,y}=\Sigma[Q]_{x,y}^{(k)}[\varepsilon_T]_{xy}^{(k)}t_k$ and $[N_{cure}]_{x,y}=\Sigma[Q]_{x,y}^{(k)}[\varepsilon_{Cure}]_{x,y}^{(k)}$ and where t_k is the ply thickness.

Step 7: Using [a] matrices, strains in the laminate (which is also the strain in each ply), due to thermal and cure-induced loads, are calculated using $[\varepsilon^0]_{x,y}=[a]_{x,y}[N_T+Nc]_{x,y}$.

Step 8: Residual (i.e. constrained) strains in each ply are calculated using the laminate strain and unconstrained strains in global axes $[\varepsilon_R]^{(k)}_{x,y} = [\varepsilon^0]_{x,y} - [\varepsilon_T]^{(k)}_{x,y}{}^{k}$.

Step 9: Using the residual strains calculated in step 8 and the stiffness matrix of each ply $[Q_{xy}]^k$, the residual stresses in an individual ply are calculated using $[\sigma_R]_{xy}^{(k)}= [Q]_{xy}^{(k)}\ [\varepsilon_R]_{xy}^{(k)}$ where $[\varepsilon_R]^{(k)}_{x,y} = [\varepsilon^0]_{x,y} - [\varepsilon_T]^{(k)}_{x,y}{}^{k}$.

Step 10: The residual stresses calculated in step 9 are transformed from global axes $[\sigma_R]_{x,y}^{(k)}$ to principal axes $[\sigma_R]_{1,2}^{(k)}$ using the transformation matrix $T_{3,}$ given in equation (3-90).

Step 11: The fracture sub-module is invoked to determine if a ply would crack.

Step 12: If fracture occurs, the VA module is invoked to determine the stress state of each ply. The ply stresses are returned to the fracture sub-module to make sure that no more cracking is possible.

Step 13: The laminate strain, stress, and crack history of each ply is stored.

Step 14: A check is made to see if the desired temperature has been reached. If not, the temperature is incremented by -1°C, and steps 2 to 14 are repeated until the desired temperature is reached.

Step 15: The output of this module includes the laminate strain, the residual stresses and the crack densities in the plies.

4.5.5.4 QSL Module

This module predicts the ply stresses after each load (stress) increment during ramping to creep load, as discussed in Section 3.5. It uses the laminate strain and the residual stress output from the PIS module as the starting value. The simulation steps are highlighted in the flowchart in Figure 4-28. This module increases the load incrementally to capture the FPF. Also, an iteration loop is included to ensure convergence in ply stresses after each load increment since the composite material is non-linear viscoelastic. The ply stresses are subsequently input into the fracture sub-module and VA Module to predict the perturbation stress, the new stress state, and the crack density in each ply. The output of this module, including the laminate strain and modulus, ply stresses, and crack density in each ply, are subsequently input into the SL Module. The simulation steps are as follows:

Step 1: Initially the program reads the laminate layup, lamina properties, laminate strain, ply stresses and ply crack densities output from the PIS Module, stress-step size, and the applied creep load, σ_a.

Step 2: The S and Q matrices of a lamina along principal material directions at the creep temperature are determined.

Step 3: The laminate stiffness [A] and compliance [a] matrices are determined using the stiffness and compliance matrices of the lamina that make up the laminate, as per equation (A-12).

Step 4: The stress of the laminate is incremented.

Step 5: The incremental laminate strain corresponding to the increase in the laminate stress is calculated using $[\Delta\varepsilon_e]_{x,y} = [a]_{x,y}[\Delta N]_{x,y}$.

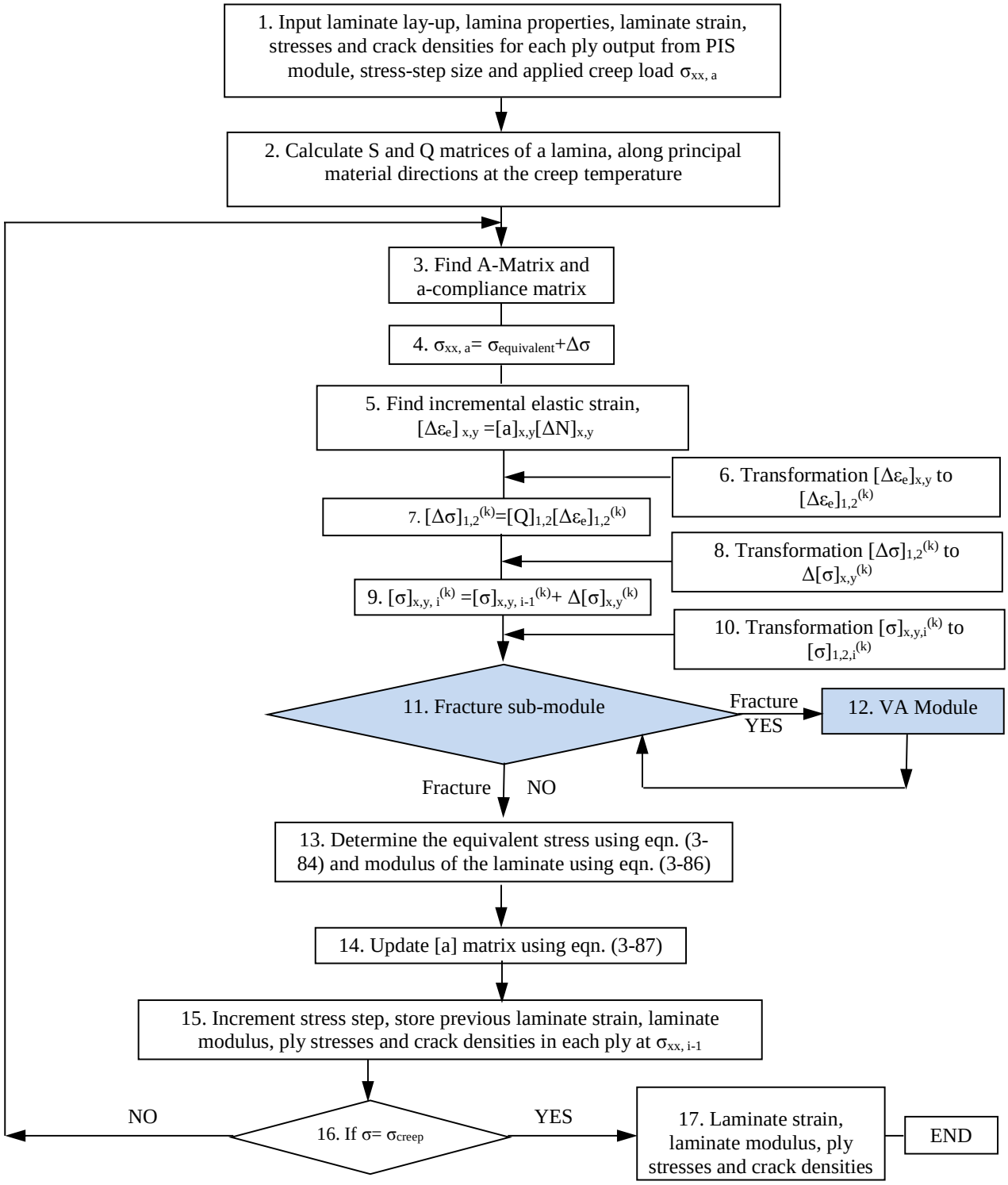

Figure 4-26: Flow chart for simulation of QSL Module

Step 6: The incremental laminate strain $[\Delta\varepsilon_e]_{x,y}$ is transformed to determine the incremental ply strains along principal directions $[\Delta\varepsilon_c]_{1,2}^{(k)}$ (where (k) corresponds to the individual

ply), using the transformation matrix T_3 given in equation (3-90).

Step 7: The incremental stress $[\Delta\sigma]_{1,2}^{(k)}$ in each ply is calculated using $[\Delta\sigma]_{1,2}^{(k)} = [Q]_{1,2}$ $[\Delta\varepsilon_e]_{1,2}^{(k)}$.

Step 8: The incremental stress in principal coordinates $\Delta[\sigma]_{1,2}^{(k)}$is transformed to global coordinates $\Delta[\sigma]_{x,y}^{(k)}$ using the transformation matrix T_3 given in equation (3-90).

Step 9: The stress in each ply is determined by adding the incremental stress in each ply calculated in Step 8 to the previous stress of the ply using $[\sigma]_{x,y,\,i}^{(k)} = [\sigma]_{x,y,\,i-1}^{(k)} + \Delta[\sigma]_{x,y}^{(k)}$.

Step 10: The stresses in each ply determined in step 9 $[\sigma]_{x,y,\,i}^{(k)}$ are transformed into principal coordinates using the transformation matrix T_3, given in equation (3-90).

Step 11: Using the stresses in the principal coordinates, the fracture sub-module is applied to determine if a ply would crack.

Step 12: If fracture occurs, the VA module is invoked to determine the stress state in each ply. The ply stresses are returned to the fracture sub-module to make sure that no more cracking is possible.

Steps 13: The equivalent stress on the laminate and the laminate modulus, after load drop due to cracking, is calculated using equations (3-84) and (3-86), respectively.

Step 14: The [a] matrix for the next step is updated using equation. (3-87) and the laminate modulus determined in Step 13.

Step 15: The laminate strain, the laminate modulus, the ply stresses, and the crack densities are stored to be the values corresponding to the current stress level.

Step 16: A check is made to see whether it has reached the desired creep stress. If not, the stress is incremented, and steps 3 to 16 are repeated until reaching the desired creep stress.

Step 17: The output of this simulation, includes the laminate strain, the laminate modulus, the ply stresses, and the crack densities in all plies, which are subsequently input into the SL Module.

4.5.5.5 SL Module

The simulation steps of the SL module, discussed in Section 3.6, are illustrated in the flowchart, shown in Figure 4-27. This module calculates the creep compliance, the ply stresses and the creep strain of the laminate. The input from the QSL module to the SL Module are the laminate strain, the laminate modulus, the ply stresses, and the ply crack density at the instant of reaching the creep load.

The creep time corresponding to this instance is taken to be zero and is incremented. In the intact regions between cracks, the creep compliance and stress states, of each ply corresponding to the new time are determined. Using this value, the fracture criterion is applied to determine if a ply would crack. If cracking is predicted, the VA Module is accessed to determine the perturbation stresses as well as new stress state in each ply. The simulation steps are as follows:

Step 1: Initially, the program reads the laminate modulus, the laminate strain, the ply stresses, and the crack densities output from the QSL Module as well as the time-step size, and the applied creep load, $\sigma_{xx,a}$.

Step 2: The S and Q matrices of the lamina at ply stresses corresponding to the current creep time, t_i and the creep temperature are determined along principal directions.

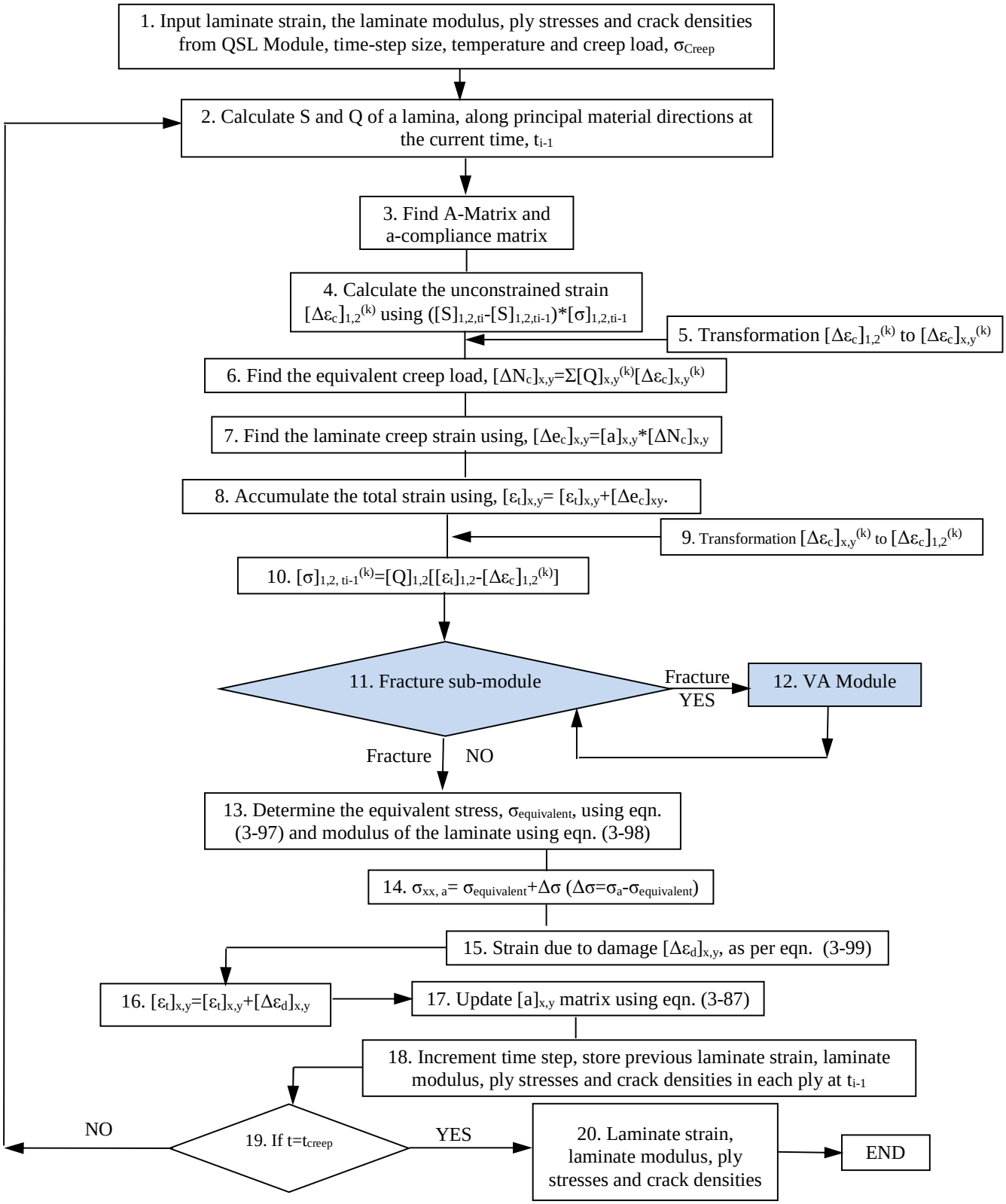

Figure 4-27: Flow chart for simulation of SL module

Step 3: The laminate stiffness [A] and compliance [a] matrices are determined using the stiffness and compliance matrices of the lamina that make up the laminate, as per equation (A-12).

Step 4: The incremental unconstrained strain $[\Delta\varepsilon_c]_{1,2}^{(k)}$ in each ply (where k corresponds to the individual ply) for the time-step Δt is calculated using the difference between lamina compliance for the current and previous time, t_i and t_{i-1} respectively, and the stress in that ply using $([S]_{1,2,ti}-[S]_{1,2,ti-1})*[\sigma]_{1,2,ti-1.}$ It is assumed that the stress in the ply remains constant during Δt.

Step 5: The unconstrained strain calculated at each ply, $\Delta[\varepsilon_c]_{1,2}^{(k)}$, is transformed to global coordinates $\Delta[\varepsilon_c]_{x,y}^{(k)}$, using the transformation matrix, T_3 given in equation (3-90).

Step 6: The incremental load corresponding to incremental strain in each ply is added to yield the equivalent creep load acting on the laminate, $[\Delta N_c]_{x,y}=\Sigma[Q]_{x,y}^{(k)}[\Delta\varepsilon_c]_{x,y}^{(k)}$.

Step 7: The increment in laminate creep strain is determined using the product of laminate compliance [a] and the equivalent creep load, $[\Delta e_c]_{x,y}=[a]_{x,y}*[\Delta N_c]_{x,y}$.

Step 8: The laminate strain is determined by adding the incremental strain to the strain at previous time, $[\varepsilon_t]_{x,y} = [\varepsilon_t]_{x,y}+[\Delta e_c]_{xy}$.

Step 9: The total strain and the unconstrained strain at each ply, $[\varepsilon_t]_{x,y}$ and $[\Delta\varepsilon_c]_{xy}^{(k)}$, respectively, are transformed from global coordinates to principal coordinates, $[\varepsilon_t]_{1,2}$ and $[\Delta\varepsilon_c]_{1,2}^{(k)}$ respectively, using the transformation matrix T_3 given in equation (3-90).

Step 10: The stresses in individual plies, $[\sigma]_{1,2,\ ti-1}^{\ (k)}$, are determined using stiffness for each ply and the difference between total strain and incremental creep strain, $[Q]_{1,2}[[\varepsilon_t]_{1,2}-[\Delta\varepsilon_c]_{1,2}^{(k)}]$.

Step 11: Using these stresses and laminate strain, the fracture sub-module is invoked to determine if a ply would crack.

Step 12: If fracture occurs, the VA module is invoked to determine the stress state of each ply. The ply stresses are returned to the fracture sub-module to make sure that no more cracking is possible.

Step 13: The equivalent stress on the laminate and the laminate modulus after load drop due to cracking is calculated using equations (3-97) and (3-98) respectively.

Step 14: The laminate stress is increased back to the creep load from the load after cracking.

Step 15: The increase in laminate strain in step 14 is the strain due to the damage, $[\Delta\varepsilon_d]_{x,y}$, (see equation (3-99)).

Step 16: This strain is added to the total strain calculated in Step 8 to get the total strain of the laminate due to both creep and damage, i.e. $[\varepsilon_t]_{x,y}=[\varepsilon_t]_{x,y}+[\Delta\varepsilon_d]_{x,y}$.

Step 17: The [a] matrix for the next step is updated using equation (3-87) together with the laminate modulus determined in Step 13.

Step 18: The laminate strain, the laminate modulus, the ply stresses, and the crack densities are stored to be the values corresponding to the current time level.

Step 19: The time is checked to see if it has reached the desired creep time. If not, the time is incremented, and steps 2 to 19 are repeated until reaching the desired creep stress.

Step 20: The output of this simulation includes the laminate strain, the laminate modulus, the ply stresses, and the crack densities in all plies of the laminate.

CHAPTER 5. RESULTS AND DISCUSSION

5.1 Introduction

This chapter presents and compares the experimental results with predictions, for time-independent (TID) and time-dependent (TDD) transverse cracking of individual plies as well as creep, in a $[\pm 45/90_2]_s$ laminate to validate the model presented in Chapter 3. While the first section of this chapter is focused on TID, due to process-induced stress and loading, and its effect on time-independent modulus, the second section is focused on TDD and its effect on creep.

5.2 Process-Induced Residual Stress and Damage

As stated in Section 3.2, process-induced residual stress and TID due to this stress was predicted and used as input to QSL module. The composite test coupons were subjected to a complex thermal cycle. After curing at 177^{o}C, the composite panels were post cured at 220^{o}C. Subsequently, the tabs were bonded to the test them at 177^{o}C before cutting the test coupons from them. This was followed by bonding of strain gages at 177^{o}C. Finally, they were heated to 270^{o}C to erase the effect of physical aging during storage. Note that after each temperature treatment they were cooled to room temperature.

The majority of the test coupons did not show any damage after going through above-mentioned thermal cycles. One sample exhibited cracking in [90] plies after being heated to 270^{o}C. The crack density was 0.5 cm^{-1}.

Process-induced residual stresses would be introduced only during the initial cure and subsequent post cure since any difference in expansion/contraction due to difference in CTE and cure shrinkage among various plies of the laminate would be cured-in due to cross-linking of the polymer matrix. Contribution due to tool-part interaction during curing [17] is ignored here. Additional contributions may come from constrained expansion and contraction during bonding of tabs and strain gages. Subsequent heating and cooling without any chemical reaction (as in the case of erasure of physical aging) would not alter the residual stress state due to above contributors, unless there is a substantial stress relaxation that can occur during slow heating/cooling and long hold times.

Simulation of process-induced stress, incorporating all of the above-mentioned contributions, is beyond the scope of this thesis. Since the majority of contribution comes from curing and post curing, the process-induced stress due to curing and post curing was modeled. The post curing temperature of 220^{o}C was used as the start temperature for cool down in order to determine the process-induced stress during cool down. The predicted process-induced stresses, at 22^{o}C, 80^{o}C, and 180^{o}C are tabulated in Table 5-1. The residual stress, σ_x, at 22^{o}C in [90] plies, determined by Gupta [16] for the same laminate manufactured using the same material, is 41.6 MPa and it compares well with predicted value of 39.8 MPa. The slight difference between these two values is related to the slight difference between the mechanical properties of the material used. This supports the above-mentioned assumption with respect to contributors to the process-induced stress. Based on this stress state, this module did not predict any damage due to process-induced stress, which is confirmed by lack of any damage in the majority of specimens. The cause for the minimal damage observed in few specimens (Figure 5-1) is not understood at this time; possible reasons are physical aging during storage before testing and defects introduced

Table 5-1: Predicted residual stresses for [90] and [45] plies of $[\pm 45/90_2]_s$ laminate at various temperature

	[45]			[-45]			[90]	
Temp.	**σ_1 (MPa)**	**σ_2 (MPa)**	**τ_6 (MPa)**	**σ_1 (MPa)**	**σ_2 (MPa)**	**τ_6 (MPa)**	**σ_1 (MPa)**	**σ_2 (MPa)**
22°C	-106.9	45.9	9.3	-106.9	45.9	-9.3	21.07	39.8
80°C	-80.4	34.6	7.0	-80.4	34.6	-7.0	15.8	29.9
180°C	-67.7	28.5	5.4	-67.7	28.5	-5.4	14.1	25.0
	ε_1	**ε_2**	**γ_6**	**ε_1**	**ε_2**	**γ_6**	**ε_1**	**ε_2**
22°C	-8.9×10^{-4}	5.3×10^{-3}	1.9×10^{-3}	-8.9×10^{-4}	5.3×10^{-3}	-1.9×10^{-3}	6.7×10^{-5}	4.4×10^{-3}
80°C	-6.7×10^{-4}	4.0×10^{-3}	1.4×10^{-3}	-6.7×10^{-4}	4.0×10^{-3}	-1.4×10^{-3}	5.0×10^{-5}	3.3×10^{-3}
180°C	-6.3×10^{-4}	4.1×10^{-3}	1.4×10^{-3}	-6.3×10^{-4}	4.1×10^{-3}	-1.4×10^{-3}	5.5×10^{-5}	3.4×10^{-3}

due to manufacturing of the test coupons. The residual stress increased with decrease in test temperature, which is to be expected. The influence of this residual stress on TID during quasi-static loading and TDD and creep is discussed further in the following sections.

5.3 Experimental Results for Time-Independent Damage (TID) Evolution and Reduction in Modulus during Quasi-Static Tensile Testing

Experimental results for the TID and its effect on modulus, during loading to creep load are presented.

5.3.1 TID modes

All plies of the $[\pm 45/90_2]_s$ laminate, namely [90], [-45] and [+45], developed various modes of damage during quasi-static loading up to the laminate failure. Transverse cracking in multiple plies of the laminate is shown in Figure 5-1. The transverse cracking started first in [90] plies. The location of transverse cracks in [-45] plies were mostly at the tip of cracks in [90] plies due to stress concentration. However, the location of transverse cracking in [+45] plies were staggered with respect to the cracks in [-45] plies. Figure 5-2 shows evolution of various modes of damage at various stress levels, during quasi-static loading at 180°C, in a representative region of the $[\pm 45/90_2]_s$ laminate. Damage usually starts as transverse cracking in [90] plies. With increase in the applied stress, transverse cracking in [-45] and [+45] plies follows and during final stages of loading, vertical cracking in [90] and delamination between [90] and [-45], and between [-45] and [+45] occur.

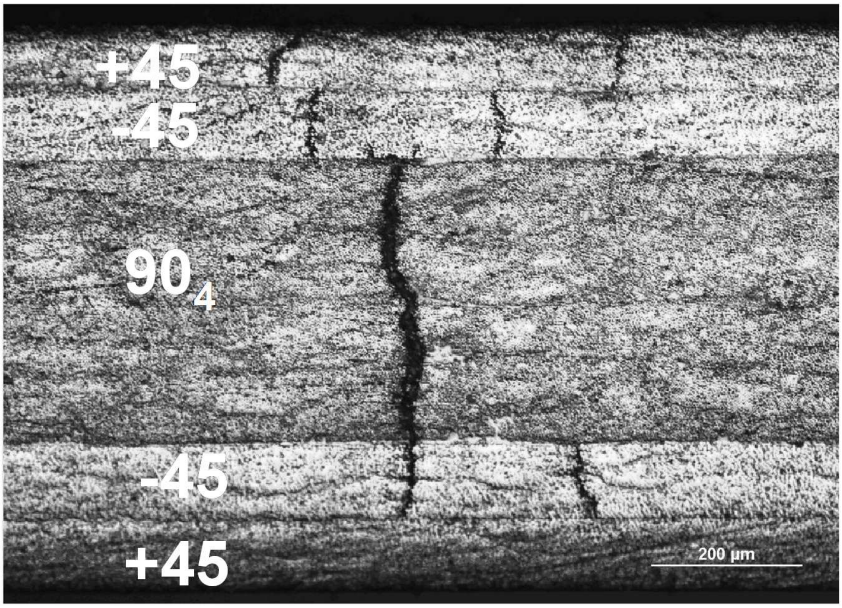

Figure 5-1: Transverse cracks in [90] and [±45] plies

a) 0 MPa

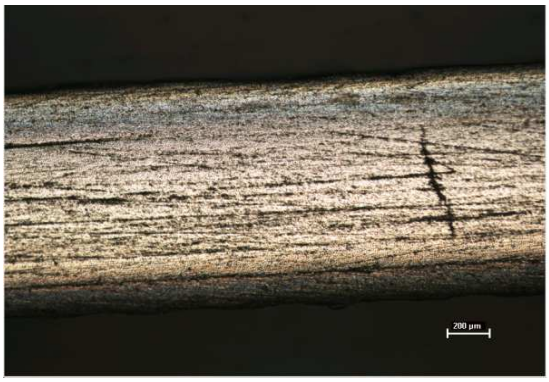

b) 50 Mpa

c) 70 MPa

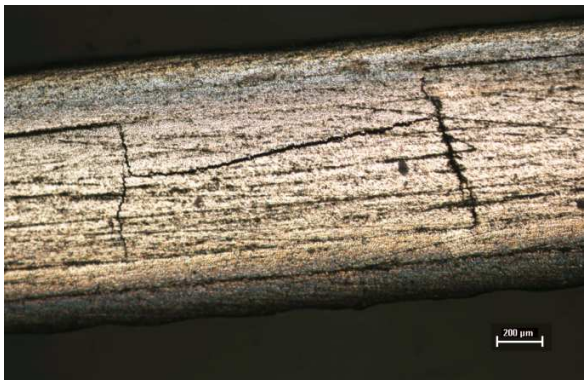

d) 90 MPa

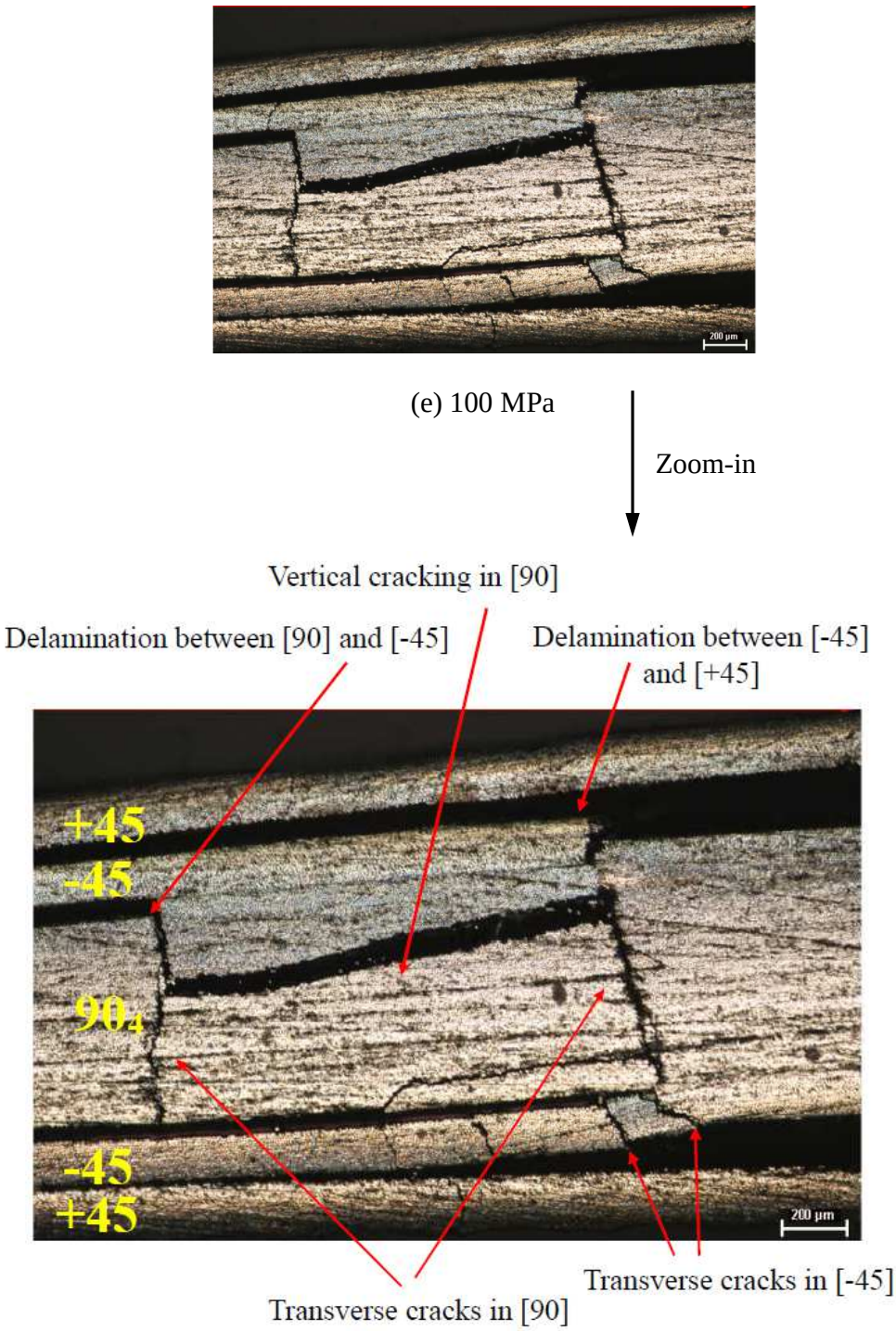

Figure 5-2: Progressive damage in $[\pm 45/90_2]_s$ during quasi-static loading at 180°C

5.3.2 Tensile test results

Repetitive tensile tests were carried out to record the evolution of transverse crack density with applied stress as well as FPF (First Ply Failure) stress for all damage modes. Representative tensile stress–strain plots at 80°C and 180 °C are provided in Figure 5-3 and Figure 5-4, respectively. The curves became increasingly non-linear with increase in stress due to increase in damage. Permanent strain observed upon unloading is due to damage and is related to crack opening displacement (COD) introduced permanently in the laminate upon cracking. The increase in permanent strain with increase in applied stress points to increase in the extent of damage. The fracture stress and strains as well as the permanent strain for both 80°C and 180°C are tabulated in Table 5-2. The fracture stress and strain at 80°C were 97±5 MPa and 7850±300 micro strains respectively. Fracture stress and strains at 180°C were 99±2 MPa and 8266+375 micro strains. The permanent strains were 750±340 and 293±98 micro strains respectively.

5.3.3 Distribution in crack spacing

The number of cracks along the edges of the specimens were determined using a digital microscope. Instead of a single value, the spacing between transverse cracks exhibited a distribution, as shown in Figure 5-5 and Figure 5-6 for [90] plies of a laminate tested at 80°C. It can be observed from Figure 5-5 that the crack spacing at a stress varied widely and this scatter decreased with increase in applied stress due to the increase in crack density. The frequency of crack spacing during the loading was determined by grouping the cracks in bins, as shown in Figure 5-6. The range of crack spacing for each bin was determined using pre-selected crack spacing increment. Three increments, namely 200, 500, and 1000 μm, were chosen to select the value that would yield the distribution faithfully. For example, the range of crack spacing for bin of 200 μm increment was 0-200 μm (crack spacing< 200 μm), 201–400 μm (200 μm < crack

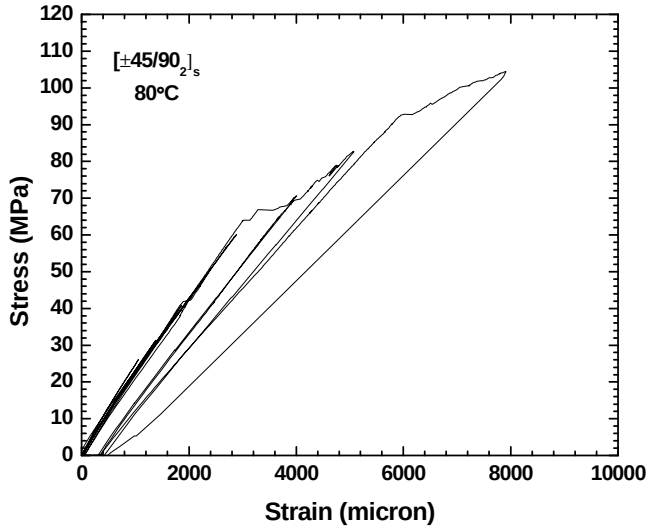

Figure 5-3: Representative results from repetitive tensile tests at 80°C

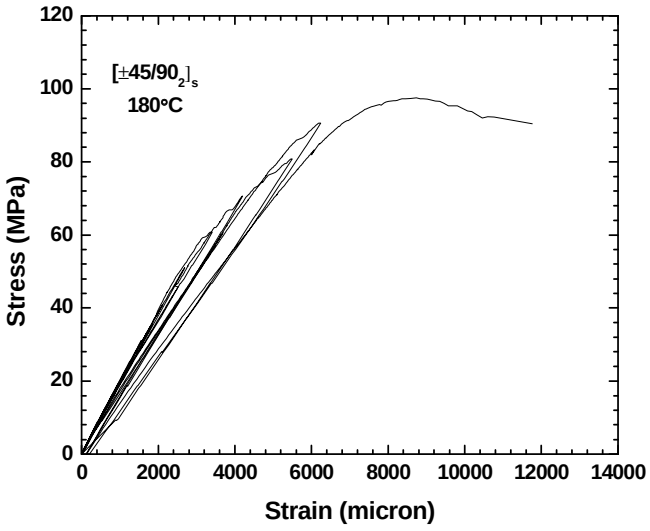

Figure 5-4: Representative results from repetitive tensile tests at 180°C

Table 5-2: Fracture stress and strain as well as permanent strain at 80°C and 180°C

Temperature	Fracture stress (MPa)	Fracture strain (micron)	Permanent strain (micron)
80°C	97±5	7850±300	750±340
180°C	99±2	8266+375	293±98

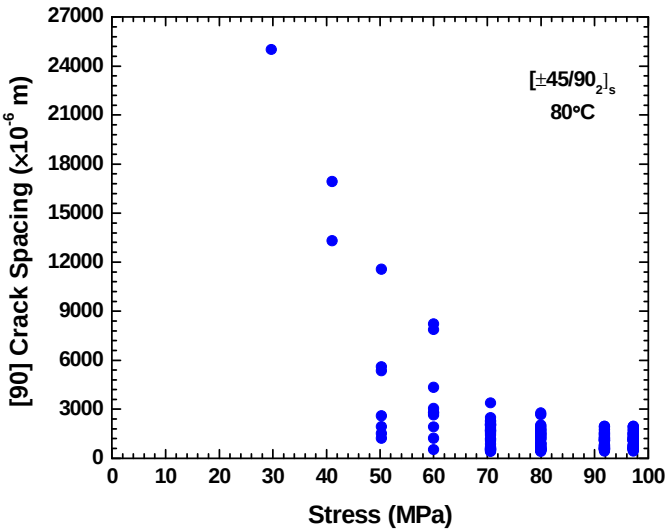

Figure 5-5: Crack spacing in [90] plies as a function of applied stress for $[\pm 45/90_2]_s$ at 80°C

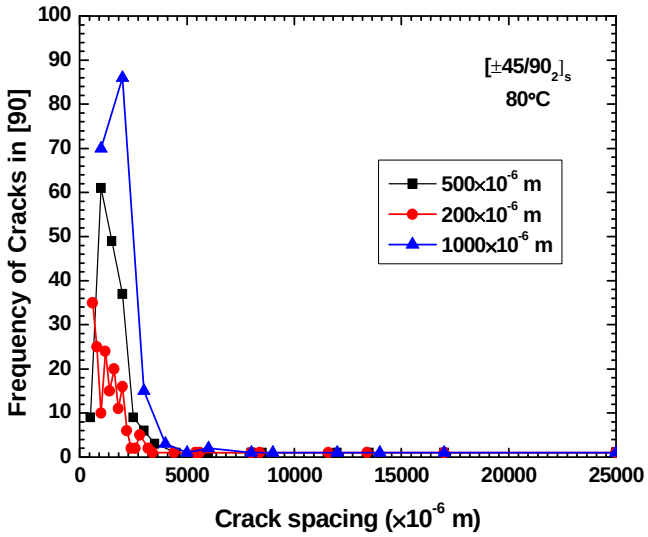

Figure 5-6: Frequency of cracks spacing in [90] plies of $[\pm 45/90_2]_s$ during the loading at 80°C

spacing < 400 μm), 401– 600 μm (400 μm < crack spacing < 600 μm), etc. The distribution in crack spacing, determined using this methodology, is plotted as a function crack spacing in Figure 5-6 during the loading from 0 to 100 MPa at 80°C. A bin value of 500 μm reproduces the normal distribution well. The peak occurred at a crack spacing of 1000 μm. This peak shifted to the right (i.e. higher crack spacing) in lower stresses.

Figure 5-7 shows the maximum and the minimum and the average crack spacing in [90] plies of the laminate tested at 80°C. All of them decreased rapidly with increase in stress and reach a plateau value.

The model developed in this thesis does not have the capability to include such distribution in crack spacing and has assumed a constant crack spacing. Hence, the transverse crack density, plotted in the rest of the figures of this chapter, was determined by dividing the number of cracks by the gage length over which those cracks were counted. The impact of this assumption on the accuracy of prediction will be discussed later in this chapter.

5.3.4 TID evolution

The transverse crack density in [90] plies, recorded for the two edges of a sample tested at 80°C is plotted in Figure 5-8 as a function of the applied stress. Superposition of the data suggests that the cracks traversed the entire width of the [90] plies and the laminate. The transverse crack density in Side 2 reached a plateau, which is commonly known as Characteristic Damage State (CDS). However, the probability of occurrence of this state in a sample depends on the interactive effect of other modes of damage that evolve simultaneously during loading. Hence, while the CDS is observed on one side, it is not observed on the other side, as observed in Figure 5-8.

The experimental transverse crack density in [-45] and [+45] plies of the same test

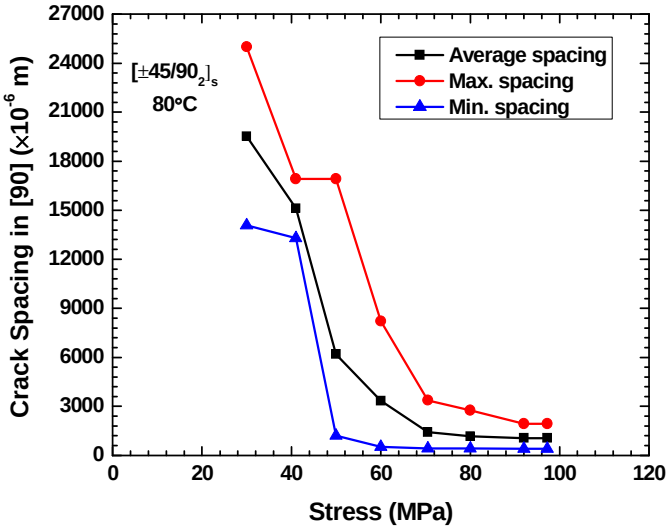

Figure 5-7: Maximum, minimum, and average crack spacing in $[\pm 45/90_2]_s$ at 80°C

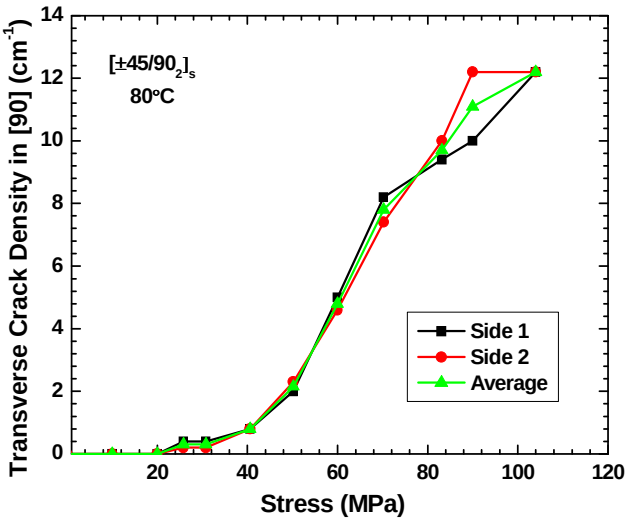

Figure 5-8: Experimental transverse crack density evolution with stress in [90] plies of a $[\pm 45/90_2]_s$ laminate at 80°C (sample 2)

coupon is plotted in Figure 5-9 and Figure 5-10 respectively. While the [90] plies were together at the center of the laminate, [±45] plies were on either side of the reference plane of the laminate, as observed in Figure 5-1. Hence, the observed crack density in the [45] plies on either side of the reference plane is identified in Figure 5-9 and Figure 5-10 as “top” and “bottom” for each side of the laminate. For each of these top or bottom plies, the crack density was determined for both edges (similar to the case of [90] plies), identified as “side1” and “side2.”

Unlike [90] plies, the crack density on one edge was different from that of the other edge for both [-45] and [+45] ply groups. This indicates that the cracks did not propagate along the entire width of the ply and the laminate. Further, the FPF stress and the crack density for the top ply were different than those for the bottom ply, for both [-45] and [+45] ply groups.

Crack density in [-45] plies adjacent to [90] plies was higher than the crack density in [+45] plies on the surface of the laminate. The average FPF stress for transverse cracking of [-45] plies was higher than that for [90] plies; the average FPF stress for [+45] plies was higher than that for [-45] plies. The above observations are consistent with expected trend since perturbation in stress in [-45], due to cracking in [90] plies, would be more than that in [+45] plies due to its proximity to [90] plies as well as the constraint on both surfaces, unlike the [+45] plies that have no constraint on one (top) surface. This causes the [-45] plies to start cracking before [+45] plies. The perturbation in stresses in [+45], due to the cracking of [-45] as well as [90] plies, would influence cracking of [+45] plies. Owing to the differences in FPF stress as well as the interactive effect of cracking of one ply on the cracking of other plies, the evolution of transverse crack density widely differed in the three plies, as observed in Figure 5-8, Figure 5-9, and Figure 5-10. It can be inferred from Figure 5-8, that the transverse crack densities on both edges of the [90] plies are the same until about 60-70 MPa and start to deviate from one

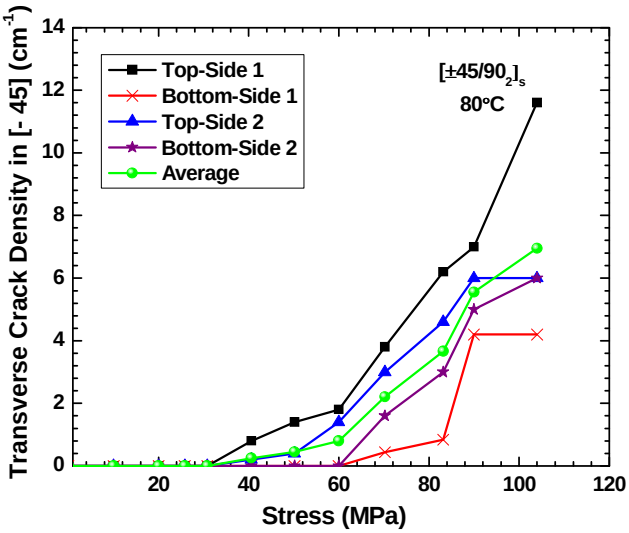

Figure 5-9: Experimental transverse crack density evolution with stress in [-45] plies of a $[\pm 45/90_2]_s$ laminate at 80°C

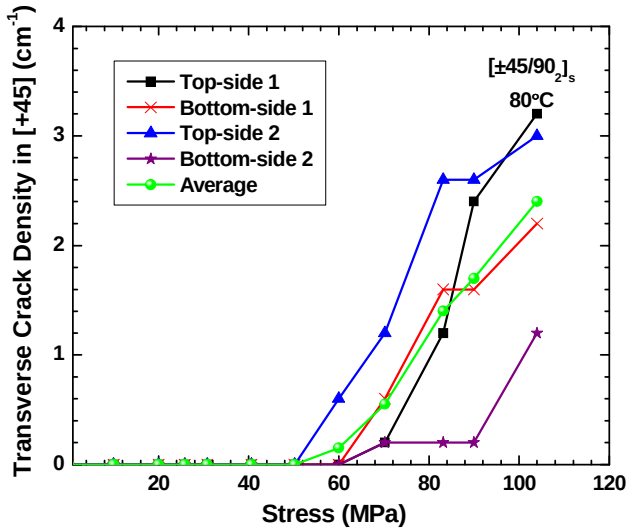

Figure 5-10: Experimental transverse crack density evolution with stress in [+45] plies of a $[\pm 45/90_2]_s$ laminate at 80°C

another beyond this stress range, when substantial cracking of [±45] plies happens. The rate of increase in crack density in [90] plies on side 1 decreases when the crack density in [-45] plies on side 1 increases. This supports the above reasoning that crack evolution in three ply groups influences one another. As mentioned before, most of the cracks developed in [-45] were aligned with the cracks in [90], which is believed to be due to the stress concentration at the tip of [90] ply cracks.

Such stress concentrations and stochastic nature of cracking, superposed with the interactive influence of cracking mentioned above, is believed to be the reason for the difference in the crack density between top and bottom plies as well as between two edges of a ply, for both [-45] and [+45] ply groups.

The average crack density for a given ply group was obtained by averaging the values for both edges of a ply. In case of [-45] and [+45] ply groups, the crack densities for the top and bottom plies were averaged to obtain an average crack density for each ply group. The average crack densities at 80°C, for [90], [-45] and [+45] ply groups of the $[\pm 45/90_2]_s$ laminate, is plotted as a function of the applied stress in Figure 5-11 to Figure 5-13 for the three tested samples. The results at 180°C are plotted in Figure 5-14 and Figure 5-15 for the two tested samples. Since [-45] plies were adjacent to [90] plies, higher transverse crack density was developed compared with [+45] plies, as shown in Figure 5-8 to Figure 5-15.

While Figure 5-8 to Figure 5-10 highlight the variation in transverse crack density evolution within a sample at 80 C, Figure 5-11 to Figure 5-13 highlight the variation in transverse crack density evolution from sample to sample. While samples 1 and 3 exhibited a CDS in [90] plies, none of the other two ply groups exhibited a CDS. The maximum crack density in [90] plies in sample 2 was higher than that in sample 1, which had a crack density

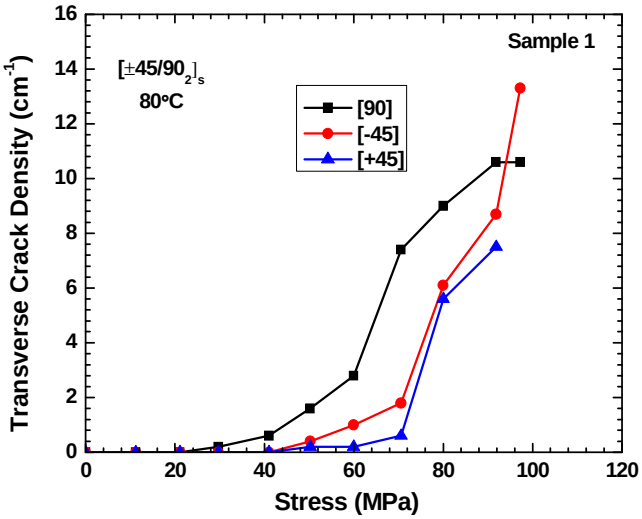

Figure 5-11: Transverse crack density evolution in [90], [-45], and [+45] plies of sample 1 at 80°C

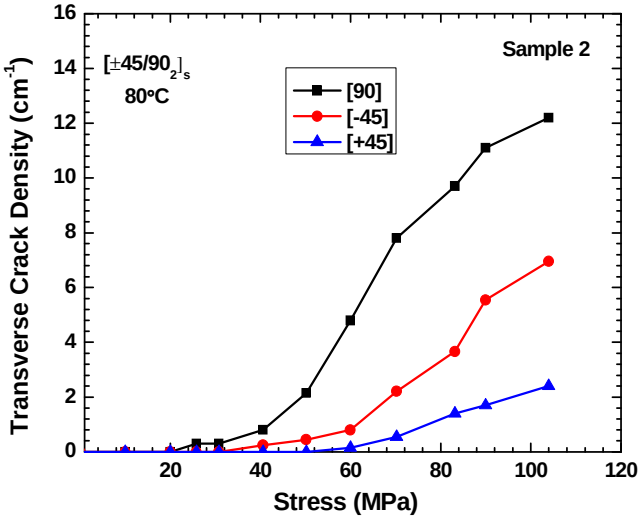

Figure 5-12: Transverse crack density evolution in [90], [-45], and [+45] plies of sample 2 at 80°C

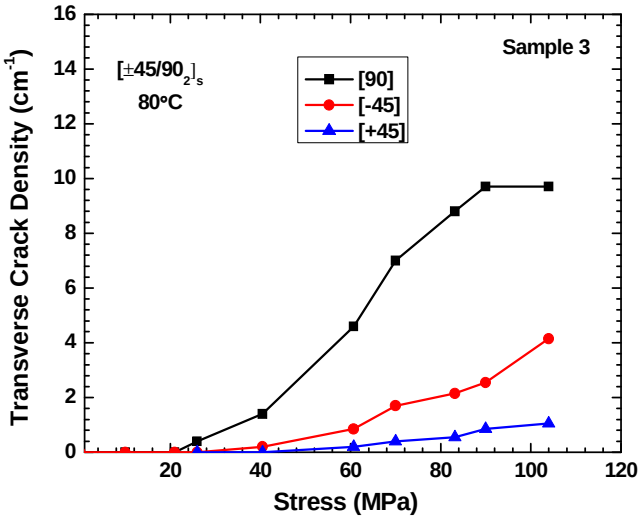

Figure 5-13: Transverse crack density evolution in [90], [-45], and [+45] plies of sample 3 at 80°C

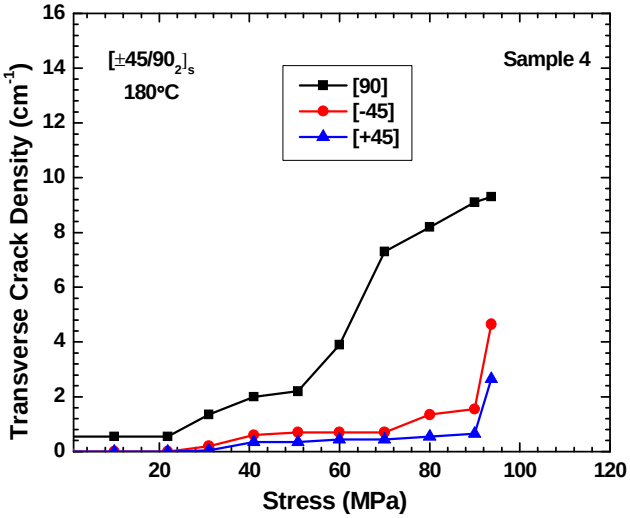

Figure 5-14: Transverse crack density evolution in [90], [-45], and [+45] plies of sample 4 at 180°C

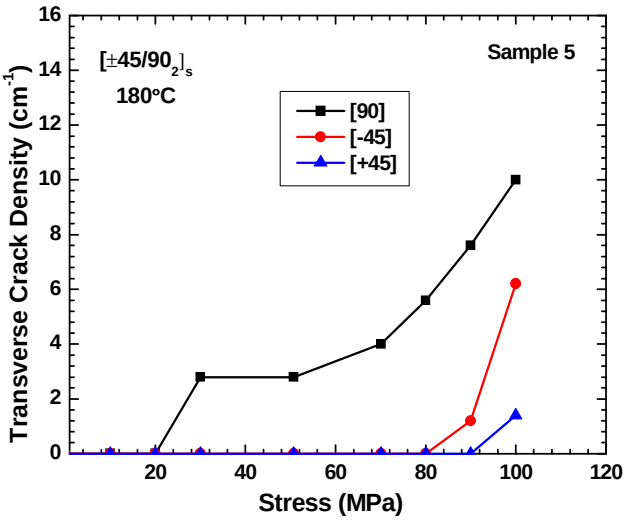

Figure 5-15: Transverse crack density evolution in [90], [-45], and [+45] plies of sample 5 at 180°C

higher than that in sample 3. The maximum crack density in [±45] ply groups in sample 1 was higher than that in sample 2 and that in sample 2 was higher than that in sample 3. This difference among samples is believed to be due to two main causes. Interaction of transverse cracking among plies, discussed above is one possible cause. Development of other damage modes, such as vertical cracking and delamination that alter the stress distribution and consequently cracking in the plies, is the second possible cause.

In sample 1, the vertical cracking in [90] plies started at 70 MPa and the delamination between [-45] and [90] plies as well as that between [-45] and [+45] plies started at 80 MPa. In sample 2, the vertical cracking started at 60 MPa; however, the delamination between [90] and [-45] plies and that between [-45] and [+45] started at 70 MPa. Since delamination would alter the ply stress state and the hence, the propensity for transverse cracking, the delamination at lower stress levels is believed to have resulted in lower transverse crack density in [±45] ply groups in sample 2. Applying similar reasoning, the higher transverse crack density in [±45] ply groups in sample 1 is attributed to its lower level of delamination (due to a higher FPF stress for delamination) than that in sample 2. The lower maximum transverse crack density in [±45] ply groups of sample 2 has resulted in higher maximum transverse crack density in [90] plies. Similarly, the higher maximum transverse crack density in [±45] ply groups of sample 1 has resulted in lower maximum transverse crack density in [90] plies.

The FPF stress values for sample 3 were 60 MPa for vertical cracking, 70 MPa for delamination between [90] and [-45], and 83 MPa for delamination between [-45] and [+45] plies. Despite similar FPF stress values,, delamination in sample 3 at failure was more extensive than that in sample 2 (as well as sample 1). Due to this, the maximum transverse crack density, in [90] and [45] ply groups of sample 3 was lower than that of samples 1 and 2.

The average transverse crack density evolution at 180^{o} C for each of the two tested samples is plotted in Figure 5-14 Figure 5-15 to highlight the effect of temperature on crack evolution. A substantial difference in crack evolution, due to the test temperature, is observed. This is believed to be due to the effect of test temperature on the process-induced residual stress, the modulus, and the critical stored elastic energy of the plies of the laminate. It can be inferred from Figure 5-14 that the FPF stress for transverse cracking in [90] plies was not different from that at 80°C; however the FPF stresses for transverse cracking in [±45] ply groups were much higher (80 MPa). Sample 4 had process-induced transverse crack in [90] plies before cracking, which reduced the FPF stress for [±45] ply groups as well as influenced the crack evolution. Unlike 80^{o}C, no CDS in [90] plies was observed at 180^{o}C and the maximum crack density at fracture at 180^{o}C was lower than that at 80^{o}C. In sample 4, the vertical cracking in [90] plies started at 60 MPa and the delamination between [90] and [-45] plies as well as that between [-45] and [+45] plies started at 70 MPa. In sample 5, the vertical cracking in [90] plies, the delamination between [90] and [-45] plies, and the delamination between [-45] and [+45] plies started at 80 MPa. Similar to the case for 80^{o}C, this difference in FPF stress values for vertical cracking and delamination is believed to be the reason for the difference between the maximum transverse crack density values for [90] and [±45] ply groups in the two samples.

The average of crack densities of all tested samples is plotted in Figure 5-16 and Figure 5-17 and for 80^{o}C and 180^{o}C respectively. The average FPF stress values for various damage modes and the maximum crack density are tabulated in Table 5-3. Since the repetitive tensile tests were completed with stress increments of 5 MPa at 80^{o}C and 10 MPa at 180^{o}C, the FPF values in Table 5-3 correspond to the stress levels beyond which the first damage was recorded. The average FPF (First Ply Failure) stresses for transverse cracking in [90], [-45], and [+45] plies

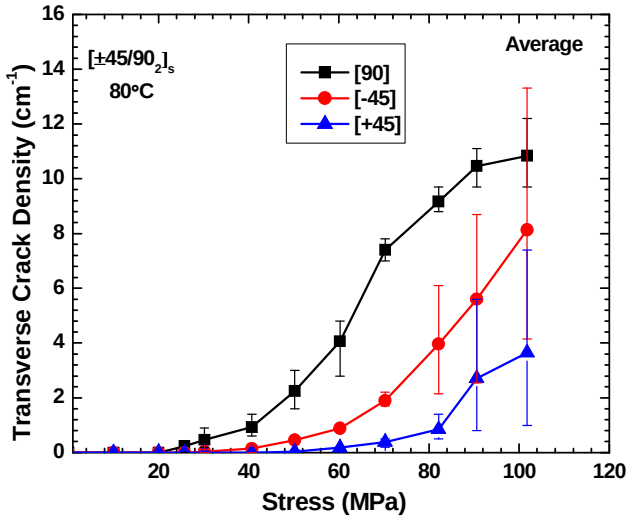

Figure 5-16: Average transverse crack density in [90], [-45], and [+45] plies at 80°C

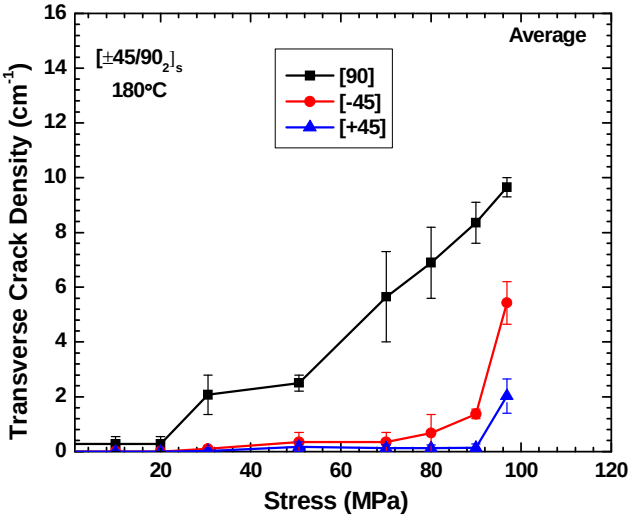

Figure 5-17: Average transverse crack density in [90], [-45], and [+45] plies at 180°C

Table 5-3: Average FPF stress and maximum transverse crack density for various plies of the laminate at two tested temperatures

Temperature	80°C		180°C	
Layer	FPF stress (MPa)	Max. CD (cm^{-1})	FPF stress (MPa)	Max. CD (cm^{-1})
[90]	28±2	11±1	31±1*	9.6±0.4
[-45]	45±5	8.1±4.5	60±30	5.4±0.8
[+45]	55±5	3.6±3	65±35	2.0±0.8

* Sample 4 at 180°C had process-induced cracking of 0.5 cm^{-1}

of samples tested at 80°C were 28±2 MPa, 45±5 MPa, and 55±5 MPa respectively. The vertical cracking in [90] plies started at 65±5 MPa. The delamination between [90] and [-45] started at 73±5 MPa and that between [-45] and [+45] plies occurred at 73±5 MPa. The average FPF stresses for transverse cracking in [90], [-45], and [+45] plies of samples tested at 180°C were 31±1 MPa, 60±30 MPa, and 65±35 MPa in [+45] plies, respectively. The vertical cracking in [90] plies started at 70±10 MPa. The delamination between [90] and [-45] plies as well as between [-45] and [+45] plies occurred at 75±5 MPa.

5.3.5 Effect of TID on the laminate modulus

The modulus of the laminate, measured during re-loading step (after unloading to determine the crack density at a stress level) of the repetitive tensile tests, is plotted in Figure 5-18 and Figure 5-19 as a function of the applied stress for 80°C and 180°C respectively. The modulus at zero load corresponds to the initial slope of the stress-strain curve determined using a strain range of 0.2%. This initial modulus varied from 18.2 GPa to 26.4 GPa with an average value of 22 GPa. It is believed that the difference in the modulus values are due to the difference in the strain rate of the tests.

For all the samples the modulus started to decrease only after FPF in [90] plies and continued to decrease until laminate failure due to increase in damage. The rate of decrease in modulus varied among samples due to variation in crack evolution, discussed in the previous section. The maximum decrease in experimental laminate modulus at 80°C is 16%, 33%, and 22% for samples 1, 2, and 3 respectively. The average decrease in experimental modulus for the laminate at 80°C is 24%.

At 180°C, the initial modulus at zero load varied from 18.0 GPa to 20.3 GPa with an average value of 19.2 GPa. Similar to the observations at 80°C, the modulus started to decrease

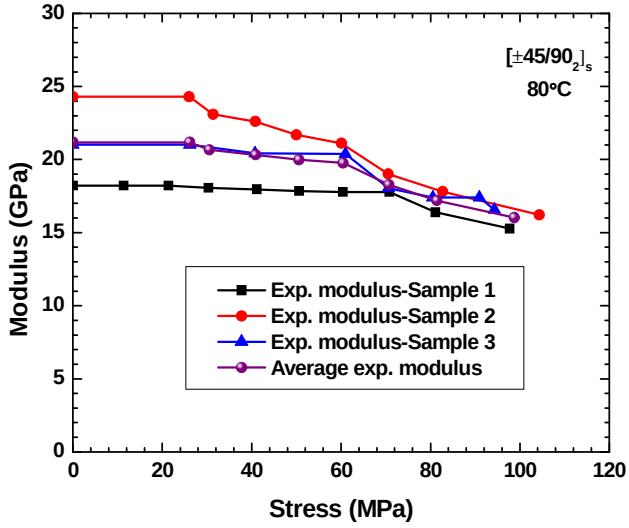

Figure 5-18: Modulus of the $[\pm 45/90_2]_s$ laminate as a function of stress at 80°C

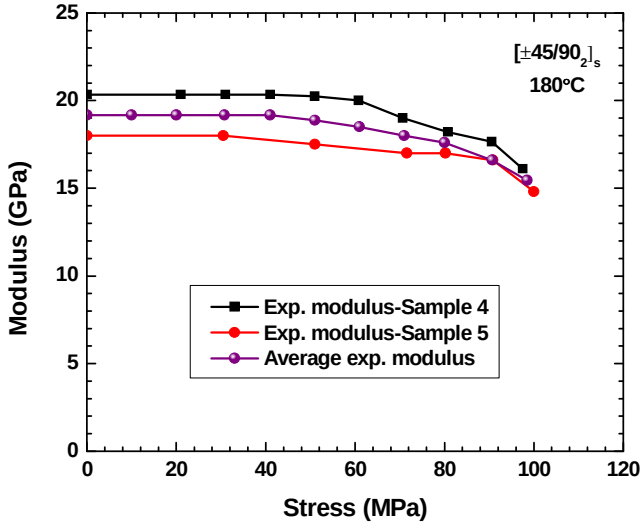

Figure 5-19: Modulus of the $[\pm 45/90_2]_s$ laminate as a function of stress at 180°C

only after FPF in [90] plies and continued to decrease until laminate failure due to increase in damage. The maximum decrease in experimental laminate modulus at 180°C is 22%, and 20% for samples 4, and 5 respectively. The average decrease in experimental modulus for the laminate at 180°C is 21%.

5.4 Predicted Results for TID and Model Validation

The presentation and discussion on experimental TID evolution, in the previous section, highlights the following

1) Crack evolution in various ply groups influence one another.
2) Crack evolution varies even within a ply group in a sample as well as from sample to sample.
3) Cracks do not traverse the entire width of [-45] and [+45] ply groups of the laminate.
4) Crack spacing in a ply exhibits a distribution, rather than a constant value.
5) Crack evolution varies with temperature.

Developing a model that can simulate all of these experimentally observed features is a very difficult task. In order to reduce the level of complexity, the following simplifications were used in developing the model.

(a) Crack evolution does not vary within a ply group

(b) Cracks, once formed, traverse the entire width of the ply and the laminate.

(c) Crack spacing is constant

Predicted results are presented, discussed, and compared with experimental results, in the following sections, to validate the model.

5.4.1 Ply stress perturbation due to cracking

A representative plot of the distribution in axial perturbation stress in all three plies of the laminate, predicted by the VA module at 43 MPa and 180°C, is shown in Figure 5-20. For this testing condition, only [90] plies cracked and the transverse crack density in [90] plies was 2.6 cm^{-1}. While Figure 5-20 (a) shows all cracks within the gage length, Figure 5-20 (b) shows the axial stress perturbation around a single crack in [90] plies. The perturbation was maximum at the crack location ($\varphi^{(90)}_{max}$) and decreased to zero away from the crack. A positive value would subtract from the stress state of that ply (a negative value would add to the existing stress state of that ply). The values for axial perturbations (φ) in three plies, at crack locations, were input as the boundary values to solve the equations (3-59)-(3-66) using the solution discussed in Chapter 4. Their values at other locations as well as the values for other two perturbations (ψ and η) at all locations were predicted using the model discussed in Chapter 3.

When [90] plies crack, the axial stress in [90] plies would be reduced to zero at the crack location while the axial stress in [±45] plies would be increased at that crack location. The average axial stress in [90] plies just before reaching a crack density (e.g. for 2.6 cm^{-1} in Figure 5-20) was taken to be the perturbation stress ($\varphi^{(90)}_{max}$) in [90] plies at the crack location, which would reduce the axial stress at these locations in [90] plies to zero.

Determining the boundary values ($\varphi^{(-45)}_{max}$ and $\varphi^{(+45)}_{max}$) for [45] plies was more difficult due to the following reasons. These values depend on the distributions in $\varphi^{(-45)}$ and $\varphi^{(+45)}$, which are not known *a priori* since they are dependent on the distributions in other unknown perturbation stresses (ψ and η) in all plies. Moreover, the values for $\varphi^{(-45)}$ (hence, $\varphi^{(-45)}_{max}$)would be different from the values for $\varphi^{(+45)}$ due to the proximity of [-45] plies to cracks in [90] plies. This is supported by the experimental data presented in Section 5.3.4; the transverse cracking in

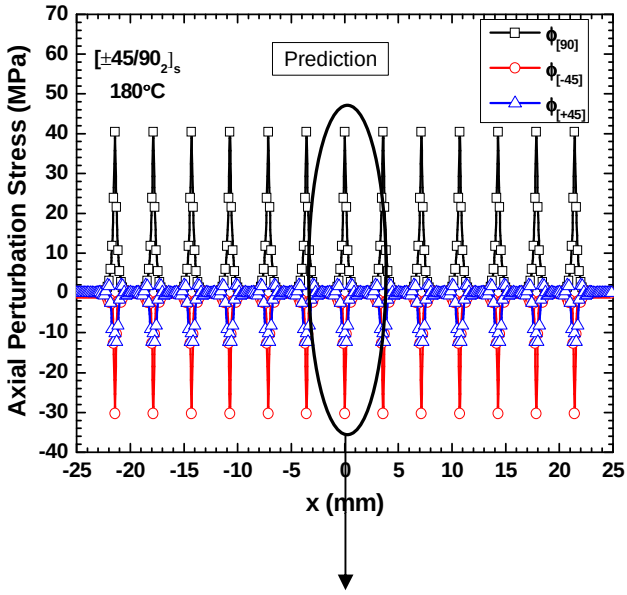

a)

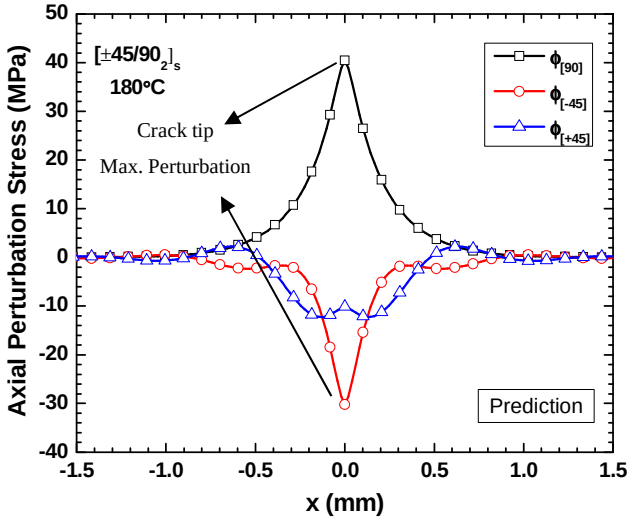

b)

Figure 5-20: Distribution of axial perturbation stresses a) through the gauge length, b) between two cracks in [90]- crack density in [90], [-45] and [+45] of 2.6 cm^{-1}, 0 cm^{-1}, and 0 cm^{-1} respectively at 43 MPa and 180°C

[-45] plies started at a lower stress than that in [+45] plies. Variation in the perturbation stress with thickness is one possible reason for the early cracking of [-45] plies. A second reason is the role of stress concentration, since the cracks in [-45] plies were found to originate from the tips of the cracks in [90] plies at many locations. Hence, these values were determined approximately as follows.

The net change in axial perturbation of the plies should be equal to the net decrease in axial laminate stress, at the instant of cracking and constant laminate strain, as per equation (5-1)

$$\varphi^{(+45)}V^{(+45)} + \varphi^{(-45)}V^{(-45)} + \varphi^{(90)}V^{(90)} = \Delta\sigma \tag{5-1}$$

where $V^{(k)}$ is the volume fraction of ply (k) in the laminate and

$$\Delta\sigma = \sigma_{xx}^{0} - \sigma_{xx} = \frac{1}{h}\left[\varepsilon_{xx}(A_{xx}^{0} - A_{xx}) - \varepsilon_{yy}(A_{xy}^{0} - A_{xy})\right] \tag{5-2}$$

The superscript "0" corresponds to values for stiffness constants of the laminate before cracking. Equation (5-1) can be modified as shown in equation (5-3) to account for the partitioning of the perturbation stress between [-45] and [+45] plies.

$$\varphi^{(+45)}V^{(+45)} + a_1\varphi^{(-45)}V^{(-45)} + \varphi^{(90)}V^{(90)} = \Delta\sigma \tag{5-3}$$

where $a_1 = \varphi^{(-45)}/\varphi^{(+45)}$.

$$\varphi^{(+45)} = \frac{\Delta\sigma}{V^{(+45)}(1+a_1)} - \frac{V^{(90)}\varphi^{(90)}}{V^{(+45)}(1+a_1)} \tag{5-4}$$

$$\varphi^{(-45)} = a_1\varphi^{(+45)} \tag{5-5}$$

The above equations are applicable to either a location in the ply or to the entire ply if average values for the perturbations are used. Since the perturbation is distributed rather than concentrated at the crack location, the values for $\varphi^{(-45)}_{max}$ and $\varphi^{(+45)}_{max}$ at locations above or

below the cracks in [90] plies will be less than that obtained using equations (5-4) and (5-5) Hence, these equations can be modified as

$$\varphi^{(+45)} = b_1.\left[\frac{\Delta\sigma}{V^{(+45)}(1+a_1)} - \frac{V^{(90)}\varphi^{(90)}}{V^{(+45)}(1+a_1)}\right] \tag{5-6}$$

$$\varphi^{(-45)} = b_1.a_1\varphi^{(+45)} \tag{5-7}$$

where b_1 is the fraction of the partitioned stress in [±45] plies concentrated at locations, above or below the cracks in [90] plies.

The axial perturbation distribution plotted in Figure 5-20 have been obtained using a_1 =3 and b_1 =0.5. The transverse and in-plane shear perturbation stresses in all three plies are plotted in Figure 5-21 and Figure 5-22 respectively. Again, the perturbation is maximum at the crack location and decreases rapidly to zero away from the crack. Due to the decrease in the longitudinal (along x-axis) laminate stress (at a constant laminate strain), after cracking in [90] plies, the ply stresses along the transverse (y-axis) direction would also decrease. Hence, the transverse perturbation stress at crack location is positive in [90] plies. Due to the loss of constraint from the [90] plies to transverse deformation of the [±45] plies at the crack location, the transverse stresses in [±45] plies would also decrease and hence, the transverse perturbation stresses in [±45] plies are also positive at the crack location. However, at locations away from the crack, the axial perturbation stresses in [±45] plies are negative (see Figure 5-20 (b)) indicating an increase in the axial stresses due to cracking. Since the plies are intact at these locations, the transverse stresses should also increase due to constraint to transverse deformation and hence, the transverse perturbation stresses in [±45] plies should also be negative. This is believed to be the reason for the change in the sign of the transverse perturbation stresses in [±45] plies from positive to negative before decreasing to zero at locations farther away from the

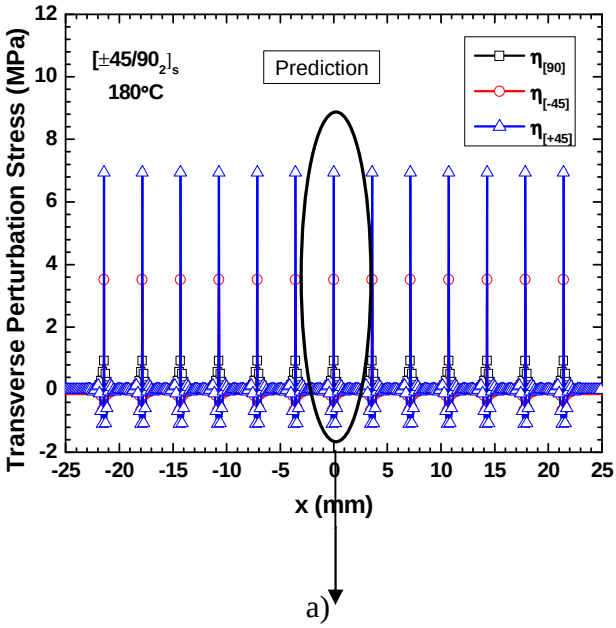

a)

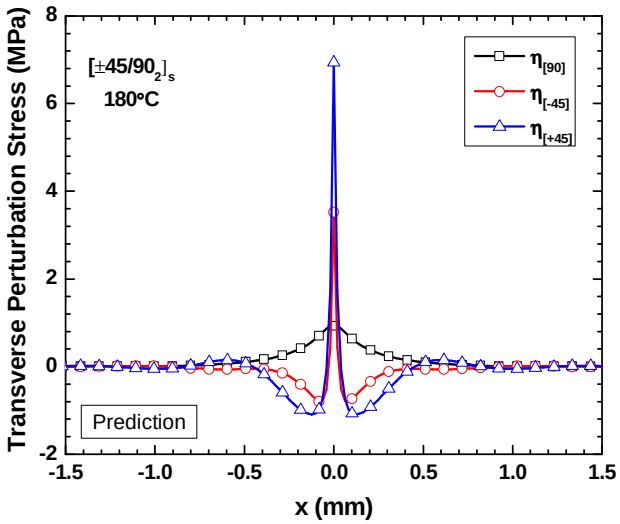

b)

Figure 5-21: Distribution of transverse perturbation stresses a) through the gauge length, b) between two cracks in [90]- crack density in [90], [-45] and [+45] of 2.6 cm^{-1}, 0 cm^{-1}, and 0 cm^{-1} respectively at 43 MPa and 180°C

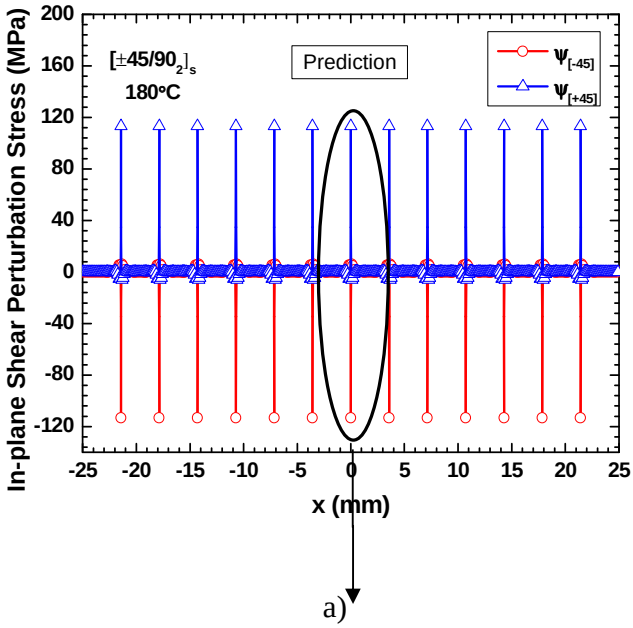

a)

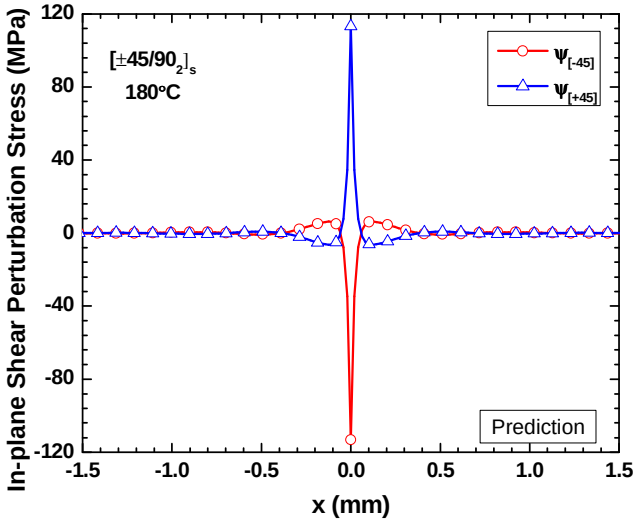

b)

Figure 5-22: Distribution of shear perturbation stresses a) through the gauge length, b) between two cracks in [90]- crack density in [90], [-45] and [+45] of 2.6 cm^{-1}, 0 cm^{-1}, and 0 cm^{-1} respectively at 43 MPa and 180°C

crack. The summation of transverse perturbations should be equal to zero as per the following equation.

$$\eta^{(+45)}V^{(+45)} + \eta^{(-45)}V^{(-45)} + \eta^{(90)}V^{(90)} = 0 \quad (5\text{-}8)$$

Applying this equation to the results in Figure 5-21 yields a value of 0.03 MPa. Despite its low magnitude, a non-zero value is indicative of the level of error in the predicted results. This error is believed to be due to the approximation used in obtaining the bounding values at crack locations for the axial perturbation as well as due to the error inherent in the variational analysis which searches for a lower bound rather than an accurate solution. Hence, this error can be minimized but not eliminated by the modeling approach developed in this thesis. A parametric study was done by varying a1 and b1 in equations (5-6) and (5-7) to determine the values that would minimize this error. The axial and transverse perturbation stresses around a crack for four sets of a1 and b1 are compared in Figure 5-23 for applied stress of 43 MPa at 180°C. The sum of transverse perturbation stresses, as per equation (5-8) are tabulated in Table 5-4 for sets of $\{a_1=1, b_1=0.5\}$, $\{a_1=2, b_1=0.5\}$, $\{a_1=3, b_1=0.5\}$, $\{a_1=6, b_1=0.5\}$. Among all sets, both sets of $\{a_1=1, b_1=0.5\}$, and $\{a_1=3, b_1=0.5\}$ provides 0.03 MPa for sum of transverse perturbations. Set of $\{a_1=1, b_1=0.5\}$ predicted 12 cracks at 43 MPa while set of $\{a_1=3, b_1=0.5\}$ predicted 13 cracks. It is expected that the error increases with increasing the number of cracks. Also, as discussed before, when [90] plies crack, the perturbations for [-45] and [+45] plies cannot be the same. Based on these reasons $\{a_1=3, b_1=0.5\}$ was selected.

The perturbation in in-plane shear stress in [-45] plies is equal and opposite in sign to that in [+45] plies, as shown in Figure 5-22. This is to be expected since the laminate is symmetric and balanced.

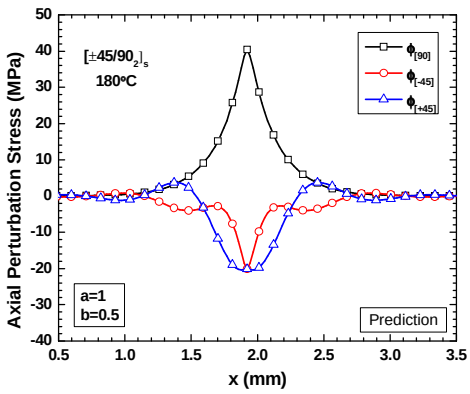
[±45/90$_2$]$_s$
180°C
$\phi_{[90]}$
$\phi_{[-45]}$
$\phi_{[+45]}$
a=1
b=0.5
Prediction
Axial Perturbation Stress (MPa)
x (mm)

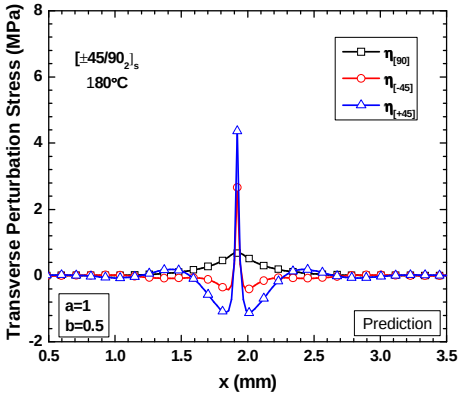
[±45/90$_2$]$_s$
180°C
$\eta_{[90]}$
$\eta_{[-45]}$
$\eta_{[+45]}$
a=1
b=0.5
Prediction
Transverse Perturbation Stress (MPa)
x (mm)

a)

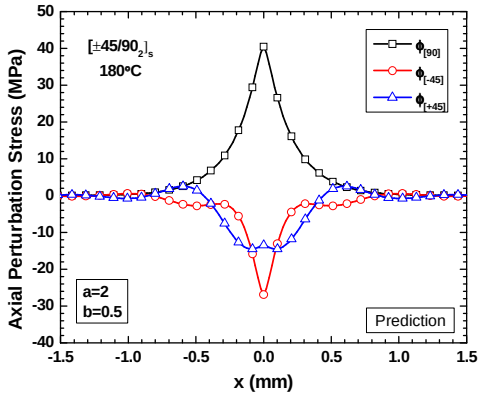
[±45/90$_2$]$_s$
180°C
$\phi_{[90]}$
$\phi_{[-45]}$
$\phi_{[+45]}$
a=2
b=0.5
Prediction
Axial Perturbation Stress (MPa)
x (mm)

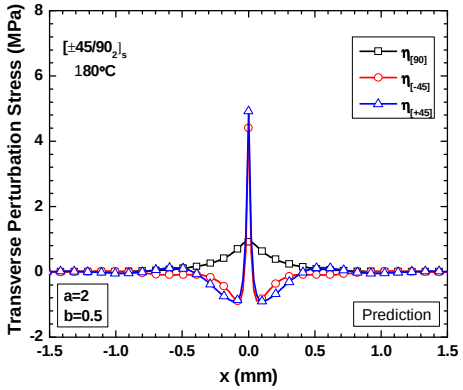
[±45/90$_2$]$_s$
180°C
$\eta_{[90]}$
$\eta_{[-45]}$
$\eta_{[+45]}$
a=2
b=0.5
Prediction
Transverse Perturbation Stress (MPa)
x (mm)

b)

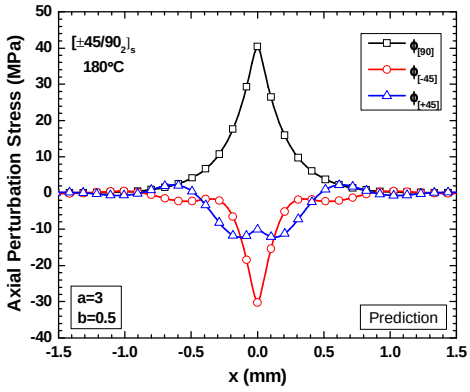
[±45/90$_2$]$_s$
180°C
$\phi_{[90]}$
$\phi_{[-45]}$
$\phi_{[+45]}$
a=3
b=0.5
Prediction
Axial Perturbation Stress (MPa)
x (mm)

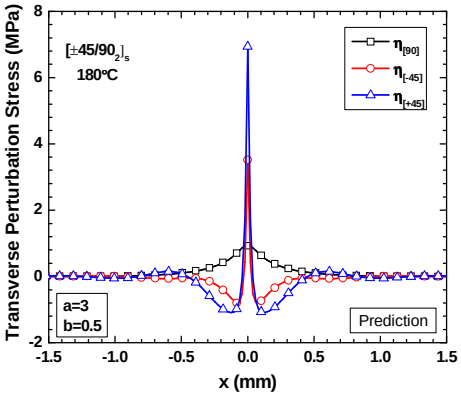
[±45/90$_2$]$_s$
180°C
$\eta_{[90]}$
$\eta_{[-45]}$
$\eta_{[+45]}$
a=3
b=0.5
Prediction
Transverse Perturbation Stress (MPa)
x (mm)

c)

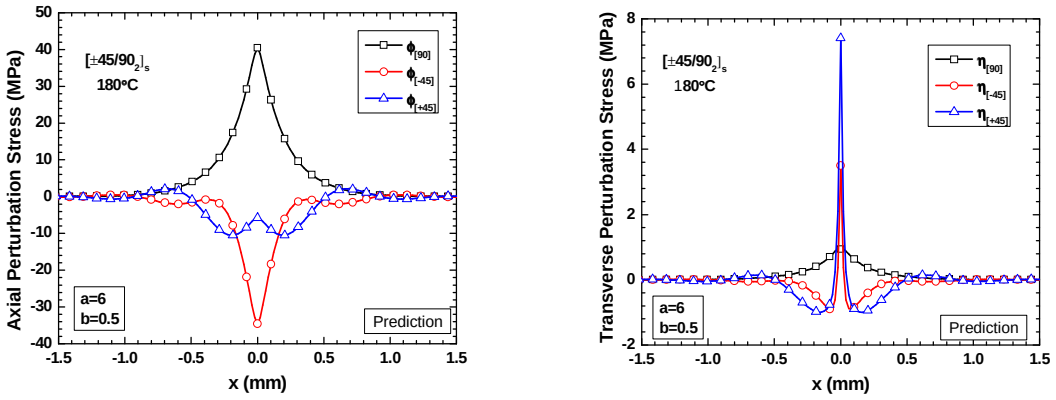

d)

Figure 5-23: Parametric study to investigate the impact of values of a and b on axial and transverse perturbations; a) a=1, b=0.5, b) a=2, b=0.5, c) a=3, b=0.5, and d) a=6, b=0.5

Table 5-4: Sum of transverse perturbations in 43 MPa and 180°C for four different sets of a, and b values

Set	Sum of transverse perturbation as eqn. (5-8)	Number of predicted cracks in [90]
a=1 b=0.5	0.03 MPa	12
a=2 b=0.5	0.04 MPa	13
a=3 b=0.5	0.03 MPa	13
a=6 b=0.5	0.05 MPa	13

Applying equation (5-9), the sum of shear perturbations stresses is zero. The shear stress is zero in [90] plies.

$$\psi^{(+45)}V^{(+45)} + \psi^{(-45)}V^{(-45)} = 0 \tag{5-9}$$

Using these results for axial distribution in eight perturbation stresses, the axial distribution in in-plane stresses around a crack in [90] plies were determined as per equations (3-25)-(3-42) and used in further analysis. The trend in these results is the inverse of the trend in Figure 5-20-Figure 5-22 and hence, are not presented for sake of brevity.

The axial distribution in out-of-plane stresses around a crack in [90] plies were determined using equations (3-25)-(3-42). These results for σ_{xz}, σ_{zz}, and σ_{yz} are plotted in Figure 5-24, Figure 5-25, and Figure 5-26 respectively. The plotted out-of-plane stresses were normalized with respect to the thickness (z) as per equations given in (3-25)-(3-42). Since they are functions of both axial and thickness directions. σ_{xz} is introduced in [90] plies to balance the perturbation in axial stresses near the crack. Due to the symmetry of the crack geometry, this is negative on one side and positive on the other side of the crack, as shown in Figure 5-24 (b). In order to balance this out-of-plane shear force, out-of-plane normal stress (σ_{zz}) is introduced in [90] plies as shown in Figure 5-25. There is no σ_{yz} in [90] plies since there is no in-plane shears stress in [90] plies. The out-of-plane stresses, σ_{xz}, σ_{zz}, in [±45] plies are introduced to balance the out-of-plane stresses introduced in [90] plies due to cracking. σ_{yz} is introduced to balance in-plane shear stresses according to equations (3-35) and (3-41), as shown in Figure 5-26. The summation of forces along z direction should be equal to zero since no load is applied along that direction. The summation of stresses in Figure 5-24-Figure 5-26 are zero and the observed trend are along expected trends.

Above discussion is focused on transverse cracking in [90] plies only. At higher applied

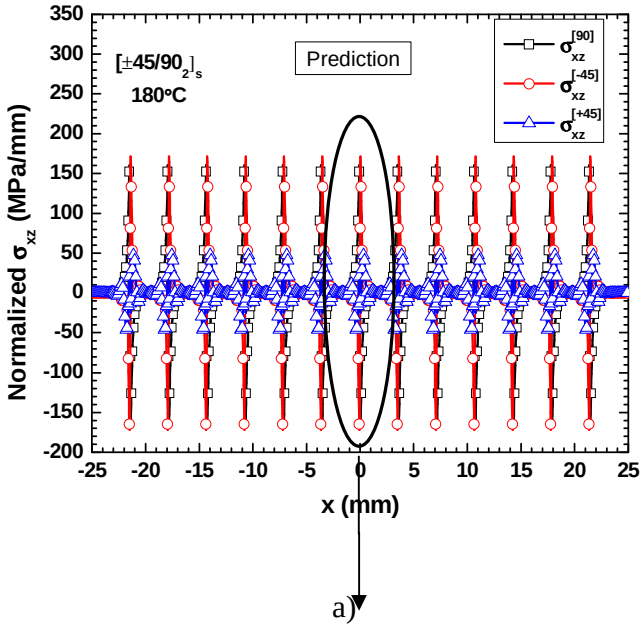

a)

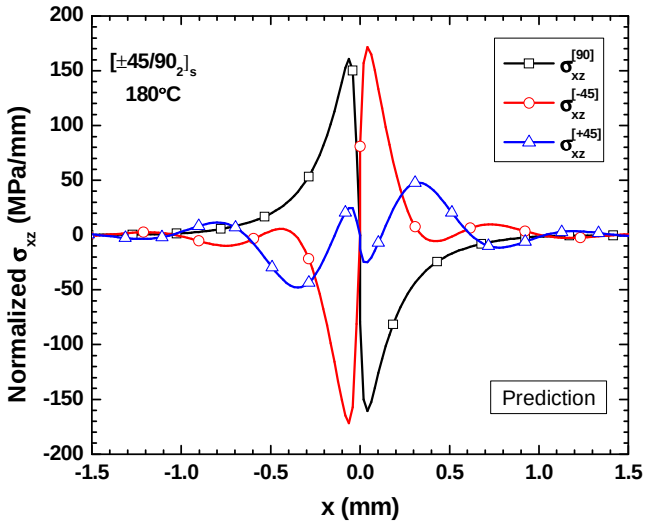

b)

Figure 5-24: Distribution of normalized out-of-plane shear stress (σ_{xz}) a) through the gauge length, b) between two cracks in [90]- crack density in [90], [-45] and [+45] of 2.6 cm^{-1}, 0 cm^{-1}, and 0 cm^{-1} respectively at 43 MPa and 180°C

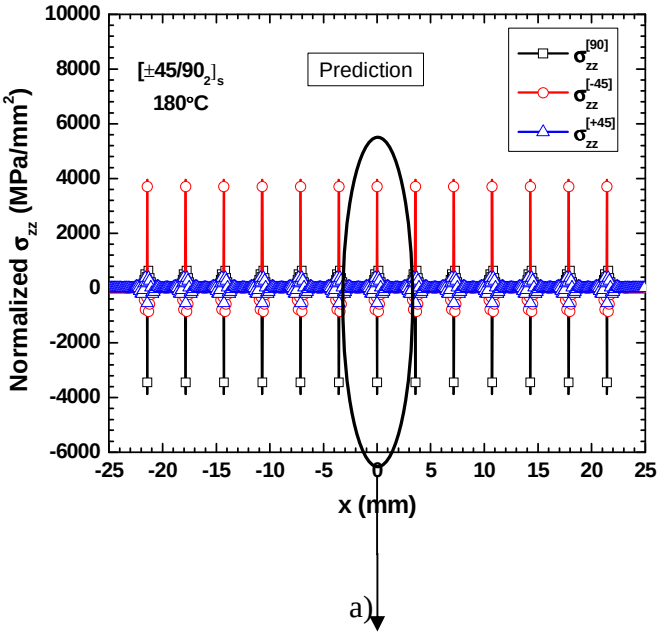

a)

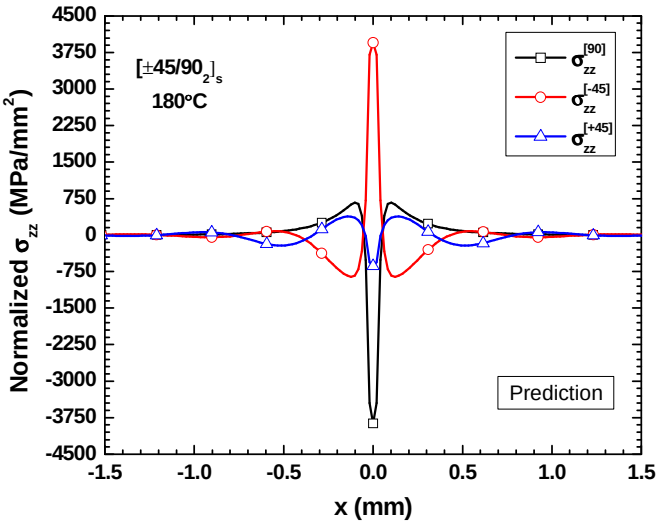

b)

Figure 5-25: Distribution of normalized out-of-plane normal stress (σ_{zz}) a) through the gauge length, b) between two cracks in [90]- crack density in [90], [-45] and [+45] of 2.6 cm^{-1}, 0 cm^{-1}, and 0 cm^{-1} respectively at 43 MPa and 180°C

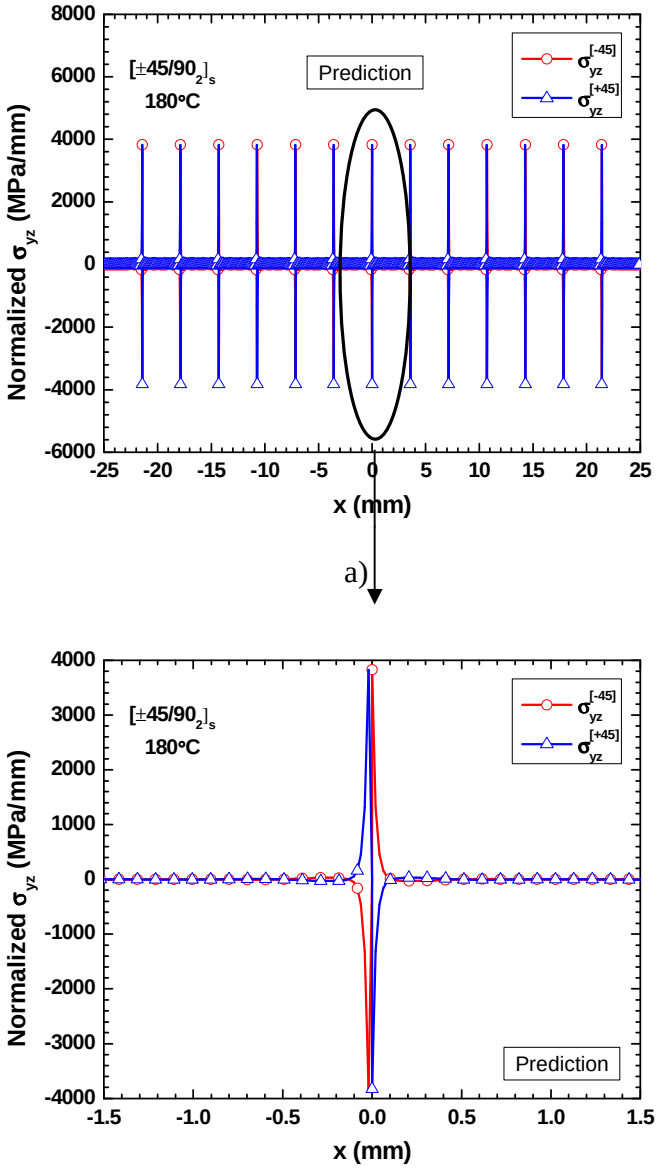

b)

Figure 5-26: Distribution of normalized out-of-plane shear stress (σ_{yz}) a) through the gauge length, b) between two cracks in [90]- crack density in [90], [-45] and [+45] of 2.6 cm^{-1}, 0 cm^{-1}, and 0 cm^{-1} respectively at 43 MPa and 180°C

loads, simultaneous transverse cracking of [±45] plies occurred. When [-45] plies cracked, the axial perturbation stress at the crack location within [-45] plies was taken to be the average stress state in the [-45] plies before cracking. The axial perturbation stress in [90] and [+45] plies at location below or above the cracks in [-45] plies was determined using equations (5-10) and (5-11).

$$\varphi^{(+45)} = b_2 . \left[\frac{\Delta\sigma}{V^{(+45)} + a_2 V^{(90)}} - \frac{V^{(-45)}\varphi^{(-45)}}{V^{(+45)} + a_2 V^{(90)}} \right] \tag{5-10}$$

$$\varphi^{(90)} = b_2 . a_2 \varphi^{(+45)} \tag{5-11}$$

The predicted axial perturbation stresses around a crack in [-45] plies are shown in Figure 5-27. The distribution of perturbation stresses is similar to the previous trends.

When [+45] plies cracked, the axial perturbation stress at the crack location within [+45] plies was taken to be the average stress state in the [+45] plies before cracking. The axial perturbation stress in [90] and [-45] plies at location below or above the cracks in [+45] plies was determined using equation (5-12) and (5-13).

$$\varphi^{(-45)} = b_3 . \left[\frac{\Delta\sigma}{V^{(-45)} + a_3 V^{(90)}} - \frac{V^{(+45)}\varphi^{(+45)}}{V^{(-45)} + a_3 V^{(90)}} \right] \tag{5-12}$$

$$\varphi^{(90)} = b_3 . a_3 \varphi^{(-45)} \tag{5-13}$$

The predicted axial perturbation stresses around a crack in [+45] plies are shown in Figure 5-28, where the distribution is similar to the trends observed before.

As a parametric study, sets of {a_2, a_3 =1/2, b_2, b_3=1/2}, {a_2, a_3 =1/3, b_2, b_3=1/2} and a combination of {{a_2 =1/3, b_2=1/2},{a_3 =1/6, b_3=1/2}} were examined to see the influence of varying a_m, b_m in equations (5-10) - (5-13) on TID evolution. All the results for TID for different sets were superposed. Hence, set of {a_2, a_3 =1/3, b_2, b_3=1/2} was selected.

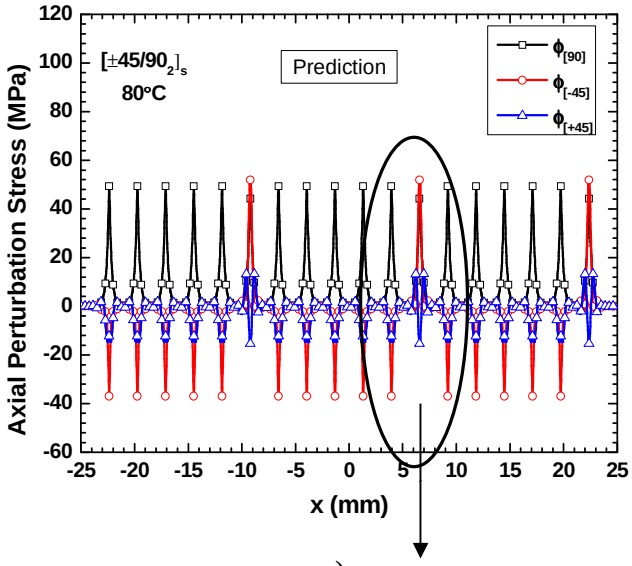

a)

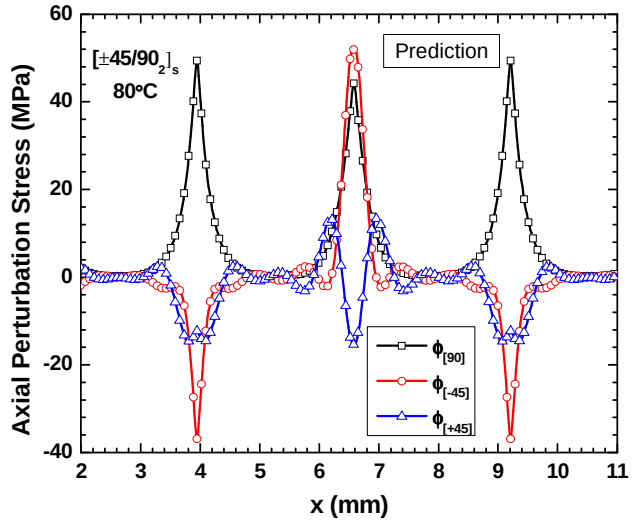

b)

Figure 5-27: Distribution of axial perturbation stress a) through the gauge length, b) between three cracks in [90] and one crack in [-45]- crack density in [90], [-45] and [+45] of 3.4 cm^{-1}, 0.6 cm^{-1}, and 0 cm^{-1} respectively at 48 MPa and 80°C

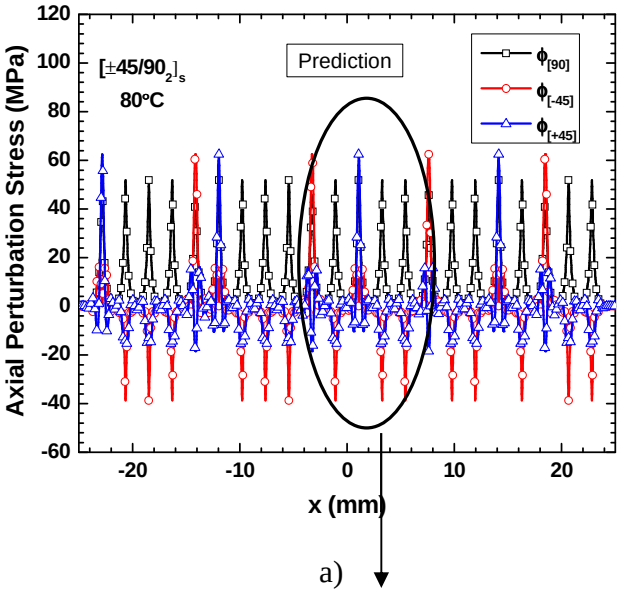

a)

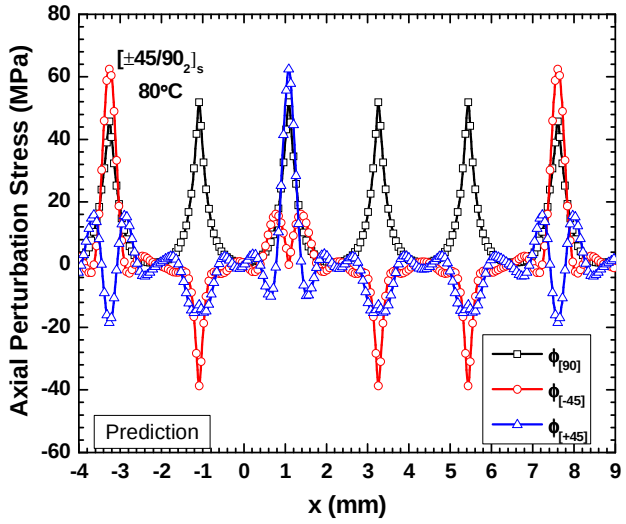

b)

Figure 5-28: Distribution of axial perturbation stress a) through the gauge length, b) between six cracks in [90] and two cracks in [-45] and one crack in [+45]- crack density in [90], [-45] and [+45] of 4.4 cm^{-1}, 1 cm^{-1}, and 0.8 cm^{-1} respectively at 52 MPa and 80°C

5.4.2 Evolution of stress, strain, stored elastic energy, and TID of the plies and laminate during quasi-static loading

The predicted stress-strain curve for the laminate, subjected to constant strain rate testing at 80°C, is plotted in Figure 5-29. The starting strain of -1422 micro strains is the process-induced strain. The average in-plane stresses and strains in the plies increase with applied stress as shown in Figure 5-30 and Figure 5-31 respectively. These values were used to calculate the stored elastic energy in the plies. When the stored elastic energy in [90] plies exceeded the critical value the [90] plies cracked and the stored elastic energy in [90] plies decreased to a value lower than the critical energy as shown in Figure 5-32. It should be noted that only stored energy per unit volume for each ply after cracking is plotted in Figure 5-32. This FPF in [90] plies occurred at 30 MPa as identified in Figure 5-29 (a) and the stress dropped at a constant strain as shown in Figure 5-29 (b) due to constant strain rate loading condition used in the model. With further increase in laminate stress, the [90] plies continued to crack when the stored elastic energy exceeded the critical stored elastic energy limit. Simultaneously, the stored elastic energy in [±45] plies also increased. When the stored elastic energy exceeded the critical stored elastic energy limit at about 46 MPa, FPF in [-45] plies occurred as shown in Figure 5-32 and Figure 5-29 (b). This is followed by FPF in [+45] plies at stress of 48 MPa as shown in Figure 5-32 and Figure 5-29 (b). The predicted evolution of TID with applied stress is plotted in Figure 5-33. The predicted FPF stress for transverse cracking varied as follows: $FPF^{(90)} < FPF^{(-45)} < FPF^{(+45)}$. The predicted crack at any applied stress varied as follows: $\lambda^{(90)} < \lambda^{(-45)} < \lambda^{(+45)}$. These are similar to the experimental trends discussed in Section 5.3.4.

During experiments, the final laminate failure was caused by damage modes other than transverse cracking. Since those damage modes were not modeled in this study, the current

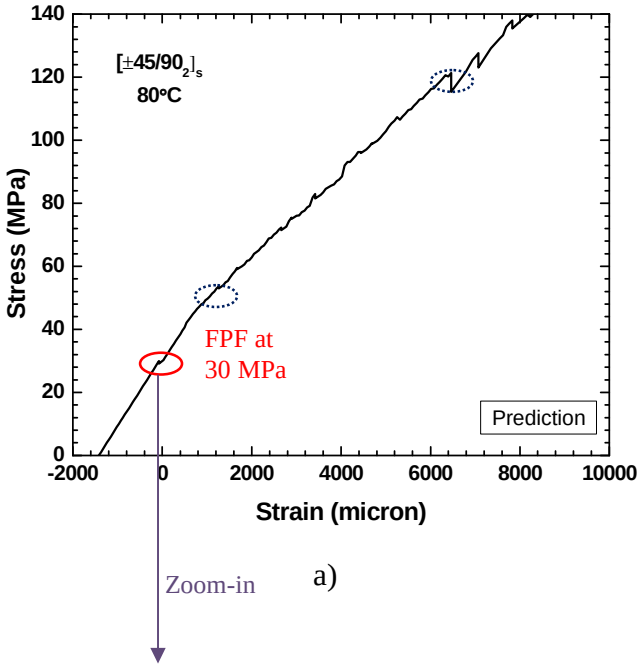

a)

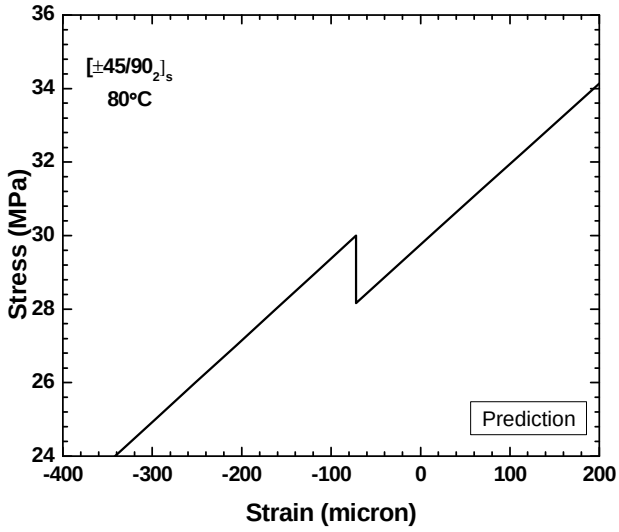

b)

Figure 5-29: Predicted stress-strain curve at $[\pm 45/90_2]_s$ at 80°C

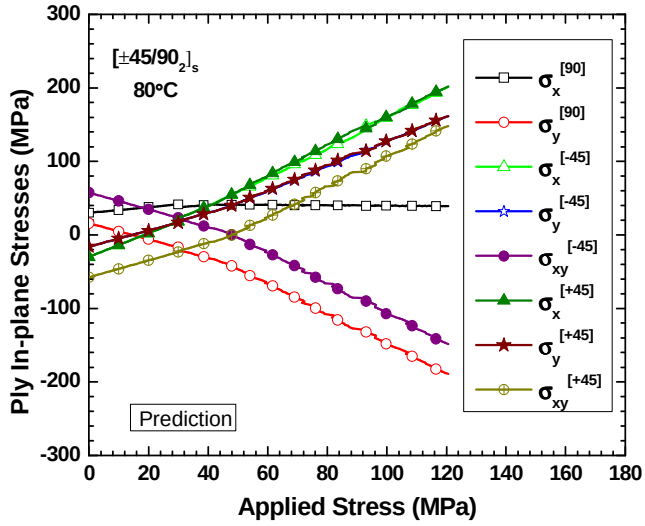

Figure 5-30: Predicted in-plane stresses in multiple plies as a function of the applied stress in $[\pm 45/90_2]_s$ laminate at 80°C

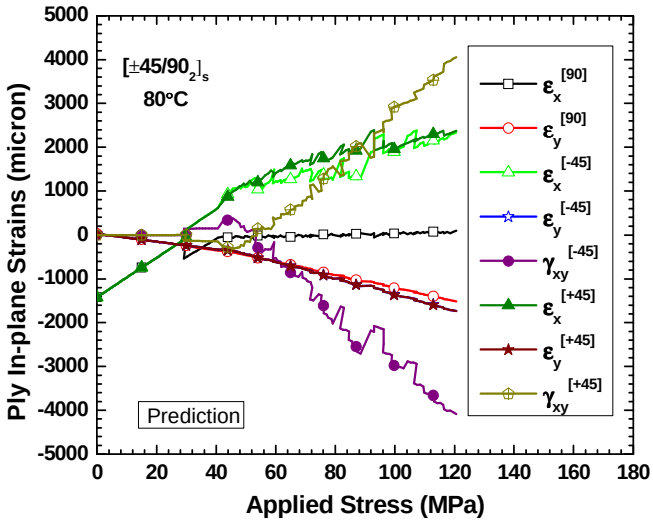

Figure 5-31: Predicted in-plane strains in multiple plies as a function of the applied stress in $[\pm 45/90_2]_s$ laminate at 80°C

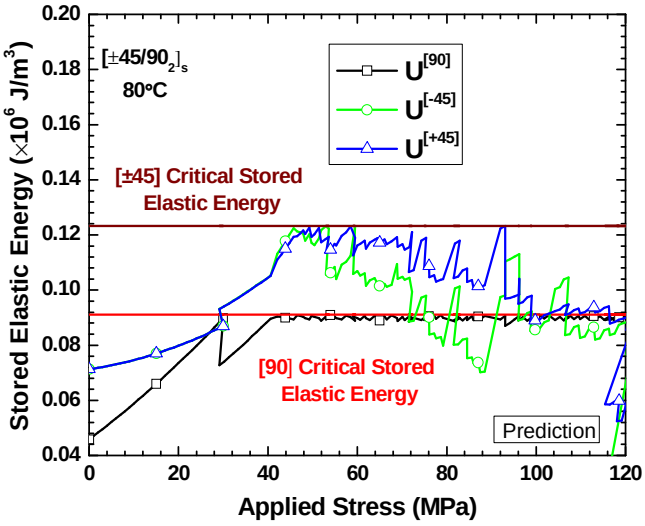

Figure 5-32: Variation of stored elastic energy in plies with applied stress in $[\pm 45/90_2]_s$ laminate at 80°C

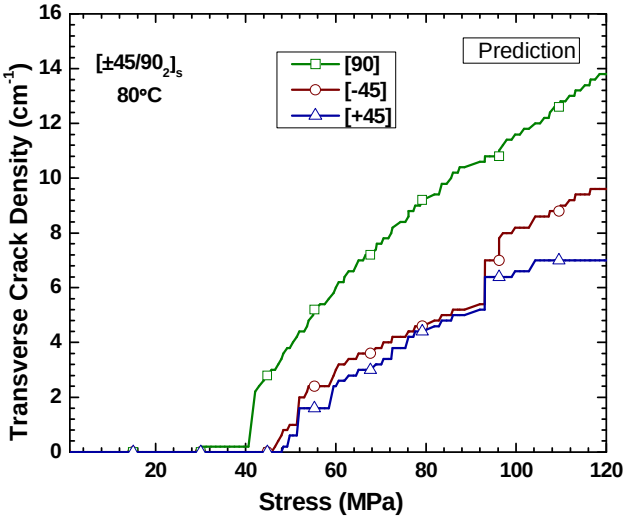

Figure 5-33: Predicted evolution of TID in multiple plies $[\pm 45/90_2]_s$ laminate with applied stress at 80°C

model is not capable of predicting the ultimate laminate failure. Hence, the simulation was arbitrarily stopped at an applied laminate stress of 140 MPa, as shown in Figure 5-29 (a). The average in-plane stresses and strains in Figure 5-30 and Figure 5-31 take into account the perturbation due to ply cracking and follow the expected trends. The axial laminate strain is compared with axial strains of plies in Figure 5-34. All the ply strains were superposed and equal to laminate strain until FPF in [90] plies. Beyond this, the axial strain of [90] plies was lower than that of the laminate strain due to decrease in average axial stresses in [90] plies with cracking. Similarly, the axial strains in [±45] plies started to deviate from laminate strain once they started cracking. This confirms the capability of the current model to predict behavior of the laminate under constant strain rate quasi-static loading. Similarly, the transverse ply strains were equal to the transverse strain of the laminate as shown in Figure 5-35 until cracking and both started to deviate after cracking. Since Poisson's ratio of the laminate was assumed to be unaffected by the transverse cracking of the plies, the transverse strains of the plies and the laminate should have superposed for the entire range of applied stress. The observed difference is due to error in the predicted transverse perturbation stress, discussed in the previous section.

Similar results were obtained at 180°C. The predicted results are plotted in Figure 5-36 to Figure 5-42. These results highlight the capability of the model to predict the quasi-static behavior of the model at any test temperature.

5.4.3 Influence of PIS

The model developed in this thesis takes into account the PIS. In order to demonstrate the importance of PIS to the accuracy of predicted results, simulations without PIS were also carried out at 80°C. The stress-strain curve and TID evolution, predicted without considering PIS, are compared with the predictions considering PIS at 80°C, in Figure 5-43 and Figure 5-44

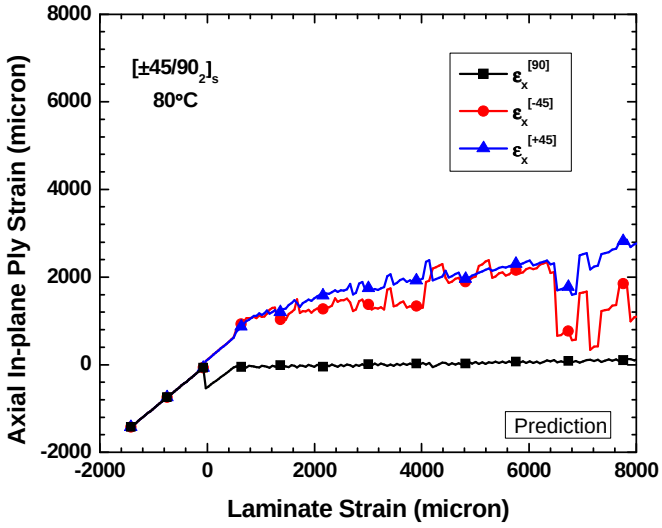

Figure 5-34: Comparison of predicted axial ply strains with the applied axial laminate strain in $[\pm 45/90_2]_s$ laminate at 80°C

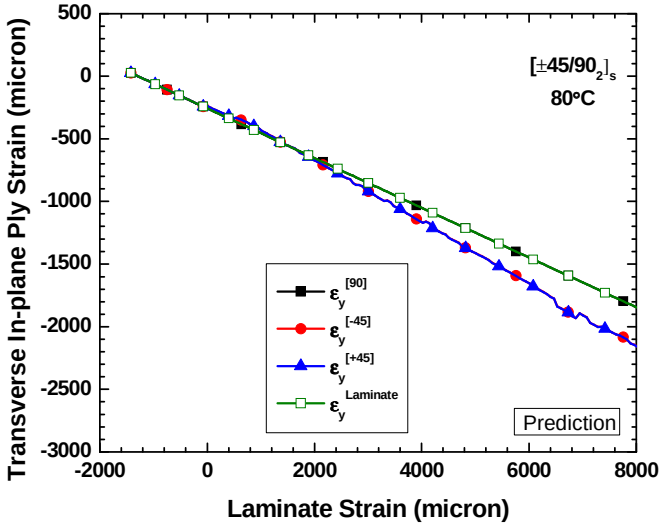

Figure 5-35: Comparison of predicted transverse ply strains with the applied axial laminate strain in $[\pm 45/90_2]_s$ laminate at 80°C

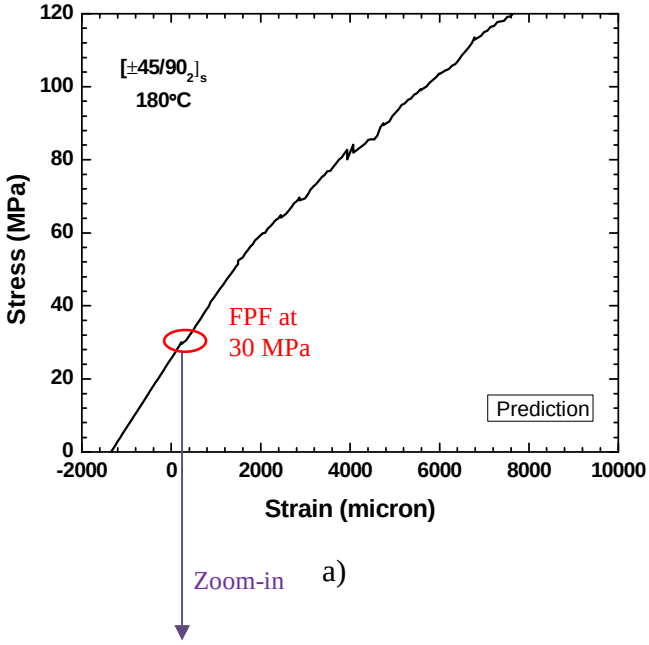

a)

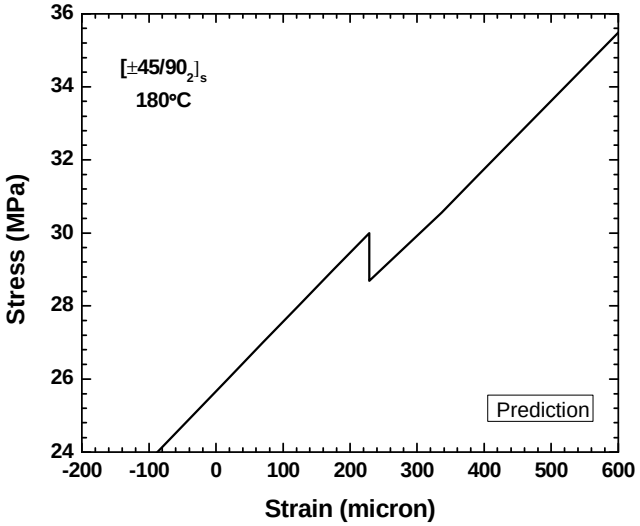

b)

Figure 5-36: Predicted stress-strain curve at $[\pm 45/90_2]_s$ at 180°C

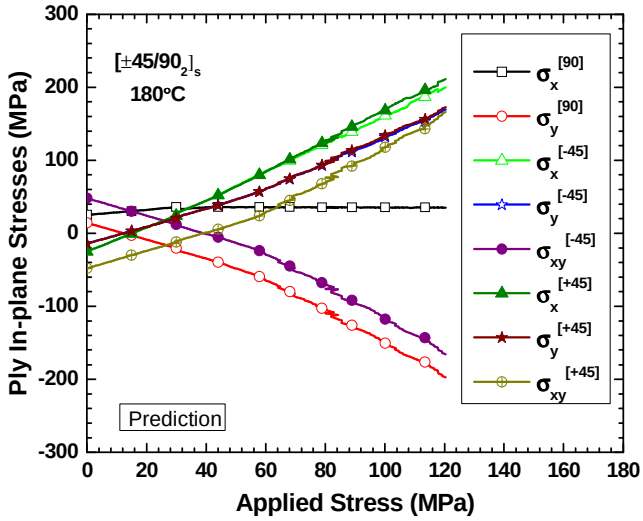

Figure 5-37: Predicted in-plane stresses in multiple plies as a function of the applied stress in $[\pm 45/90_2]_s$ laminate at 180°C

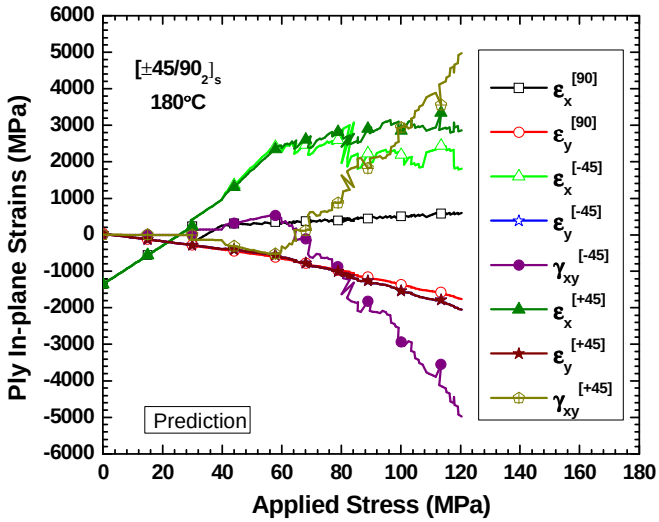

Figure 5-38: Predicted in-plane strains in multiple plies as a function of the applied stress in $[\pm 45/90_2]_s$ laminate at 180°C

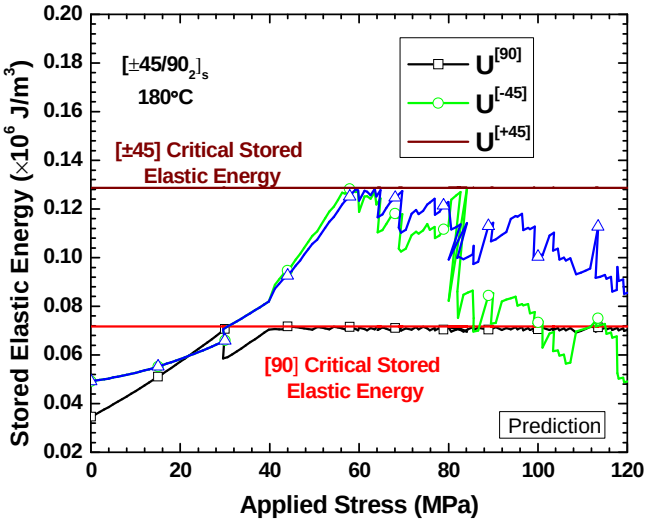

Figure 5-39: Variation of stored elastic energy in plies with applied stress in $[\pm 45/90_2]_s$ laminate at 180°C

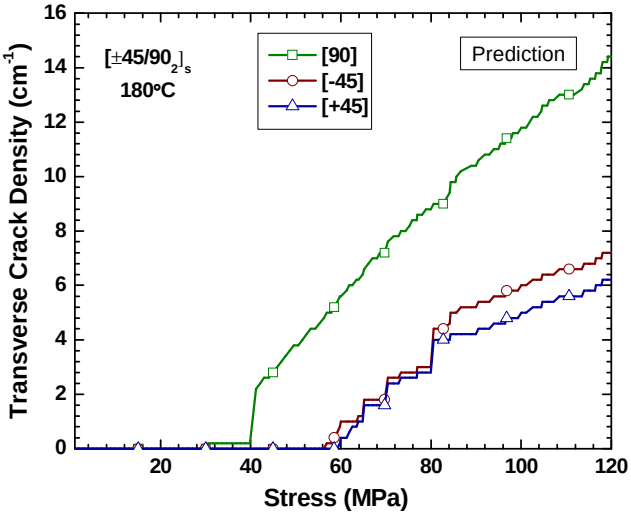

Figure 5-40: Predicted evolution of TID in multiple plies $[\pm 45/90_2]_s$ laminate with applied stress at 180°C

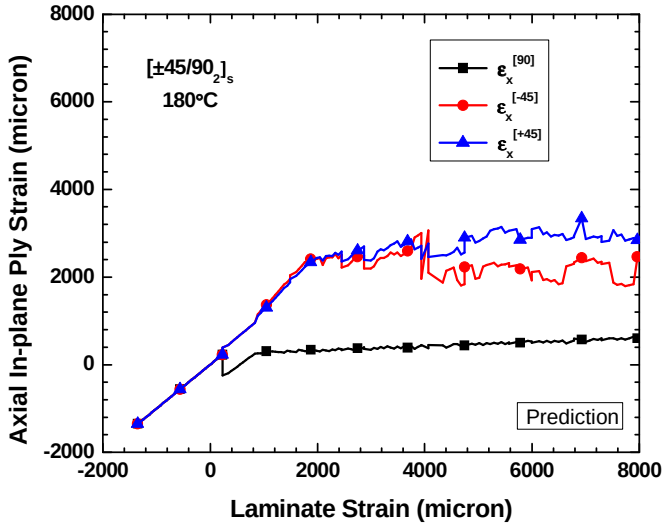

Figure 5-41: Comparison of predicted axial ply strains with the applied axial laminate strain in $[\pm 45/90_2]_s$ laminate at 180°C

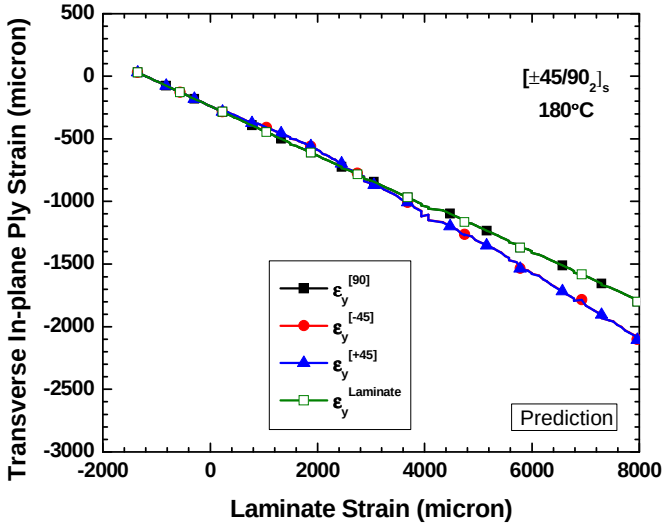

Figure 5-42: Comparison of predicted transverse ply strains with the applied axial laminate strain in $[\pm 45/90_2]_s$ laminate at 180°C

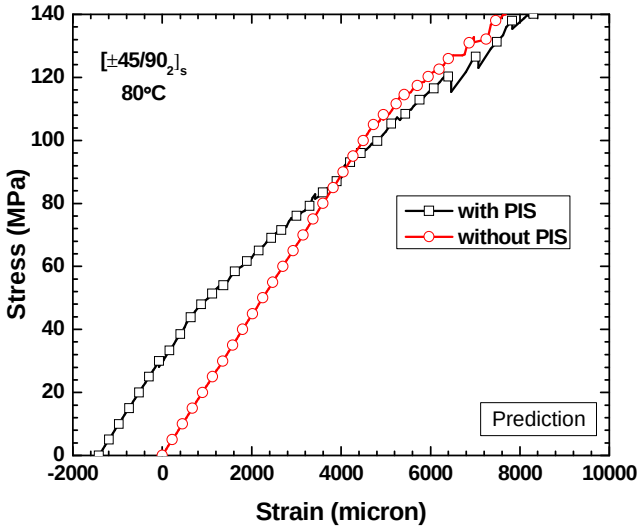

Figure 5-43: Predicted stress-strain curve for $[\pm 45/90_2]_s$ at 80°C with and without process-induced stress (PIS)

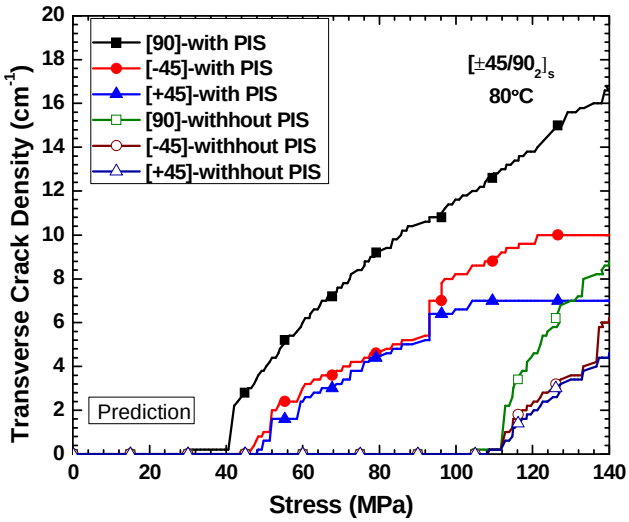

Figure 5-44: Evolution of transverse crack density in multiple plies predicted with and without residual stresses, as a function of the applied stress in $[\pm 45/90_2]_s$ at 80°C

respectively. The shape of the stress-strain curve is affected by PIS through its impact on crack evolution, which is evident in Figure 5-44. The PIS reduced the FPF stresses. The FPF stresses for [90], [-45], and [+45] plies were 104 MPa, 108 MPa, and 108 MPa respectively in the absence of PIS in contrast with 30 MPa, 46.5 MPa, and 48.3 when PIS is considered. The difference among FPF stresses for transverse cracking in various plies was small without PIS in the plies, which is to be expected since the PIS in [90] plies is opposite in sign to the PIS in [±45] plies. Due to this small difference, the crack evolution was more or less simultaneous resulting in a rate of crack evolution that is different from the crack evolution in a laminate with PIS. The predictions using PIS compared well with experimental results which will be discussed in the following section.

5.4.4 Validation of the model's ability to predict laminate behavior during quasi-static loading

The predicted stress-strain curves is compared with experimental results in Figure 5-45 and Figure 5-46 for 80^{o}C and 180^{o}C respectively. An excellent agreement is observed at stress levels less than ~ 80 MPa. The results deviated above this stress level due to occurrence of damage modes other than transverse cracking such as vertical cracking and delamination, which were not modeled in this study.

The predicted change in the laminate modulus with increase in the applied stress is compared with experimental results in Figure 5-47 and Figure 5-48 for 80^{o}C and 180^{o}C respectively. The modulus of the laminate degraded with increase in applied stress due to increase in transverse crack density in the plies. The predicted modulus is well within the scatter range of experimental results and the predicted rate of degradation in modulus with increase in

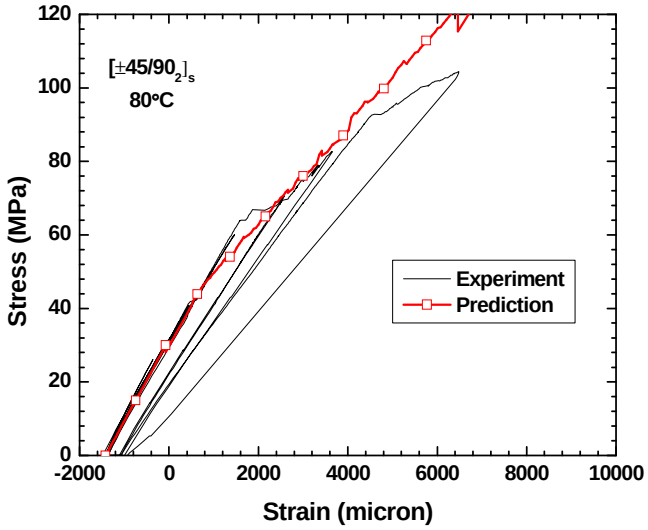

Figure 5-45: Experimental and predicted stress-strain curves in $[\pm 45/90_2]_s$ at 80°C

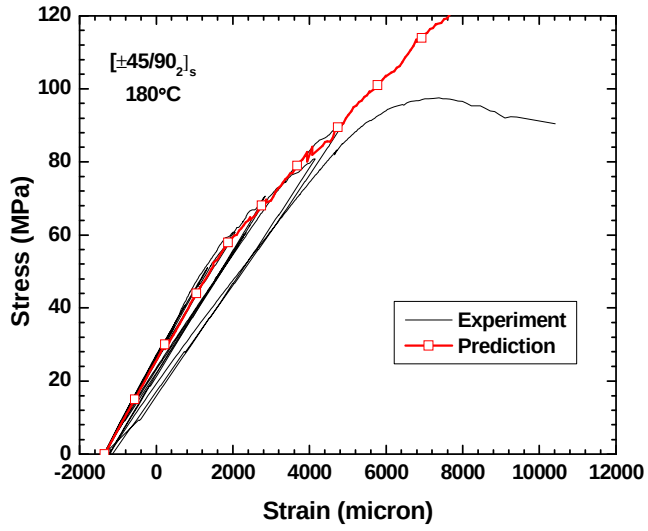

Figure 5-46: Experimental and predicted stress-strain curves in $[\pm 45/90_2]_s$ at 180°C

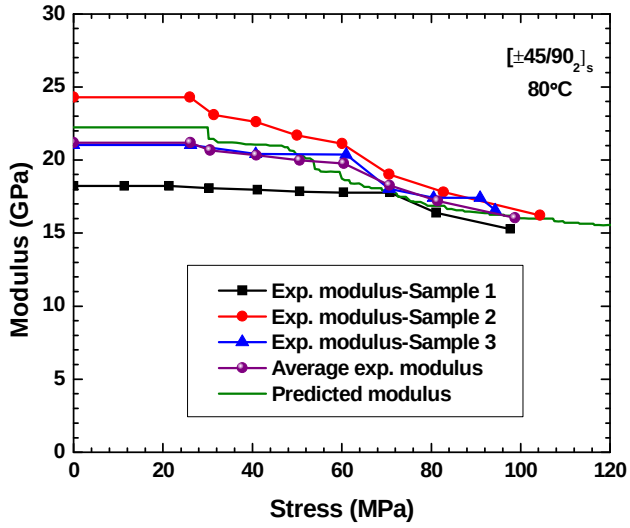

Figure 5-47: Experimental and predicted modulus of $[\pm 45/90_2]_s$ laminate at 80°C

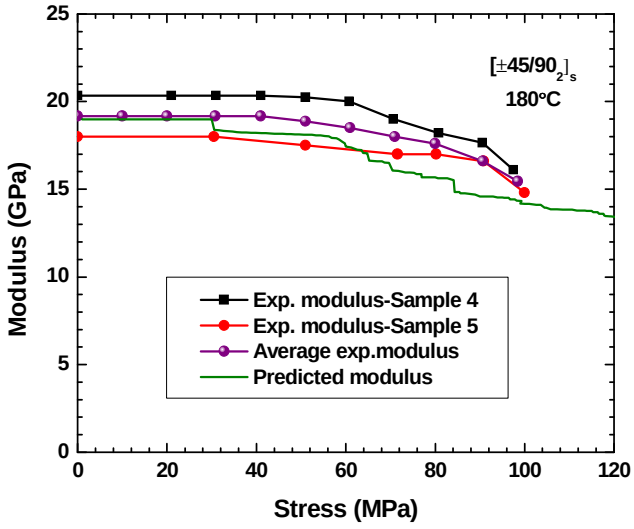

Figure 5-48: Experimental and predicted modulus of $[\pm 45/90_2]_s$ laminate at 180°C

applied stress compares very well with experimental results at stress levels below ~80 MPa when only transverse cracking of plies is observed.

The predicted values for TID in [90] plies at 80ºC are within the scatter range of experimental results and the predicted TID evolution is in a very good agreement with experimental results, as shown in Figure 5-49. The experimental FPF stress of 28±2 MPa is comparable to the predicted value of 30 MPa. While the experimental TID increases gradually, the predicted TID shows a sudden increase at ~ 40 MPa. This difference is believed to be due to the difference in crack density at FPF. In order to demonstrate this, the predicted number of cracks at FPF was increased arbitrarily by 3 (i.e., λ_{FPF} of 28 MPa) and subsequent TID evolution was predicted. The crack number of 3 was obtained using the minimum crack spacing in this stress level, as shown in Figure 5-7. This is compared with original prediction (with λ_{FPF} 30 MPa) in Figure 5-50. It can be observed that the predicted rate of increase in TID for λ_{FPF} of 28 MPa is more gradual than the original prediction with λ_{FPF} of 30 MPa. No sudden increase at 40 MPs is observed and the predicted results compare relatively better with experimental results than the original prediction with λ_{FPF} of 28 MPa. The difference in λ_{FPF} could be attributed to a number of possible causes such as the stochastic nature of cracking, stress concentration, etc., which were not considered in the model.

The predicted TID evolution in [-45] plies is compared with experimental results at 80ºC in Figure 5-51. While the experimental FPF stress is 45 ± 5 MPa, the predicted FPF stress is 45.7 MPa. Due the difference in $\lambda_{FPF,}$ the predicted TID increased more rapidly than the experimental TID at lower applied stress levels, which was discussed earlier in the parametric study. At higher stress levels (>~70 MPa), the predicted TID approached a constant value while the experimental TID continued to increase with applied stress. This difference may be attributed to the

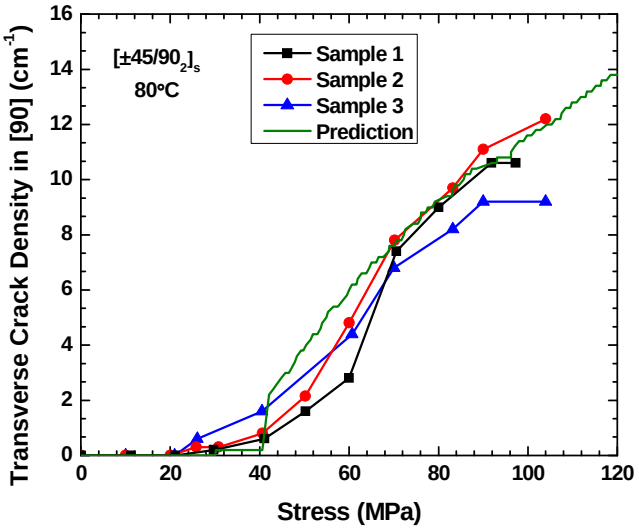

Figure 5-49: Experimental and predicted TID in [90] plies of $[\pm 45/90_2]_s$ during tensile loading at 80°C

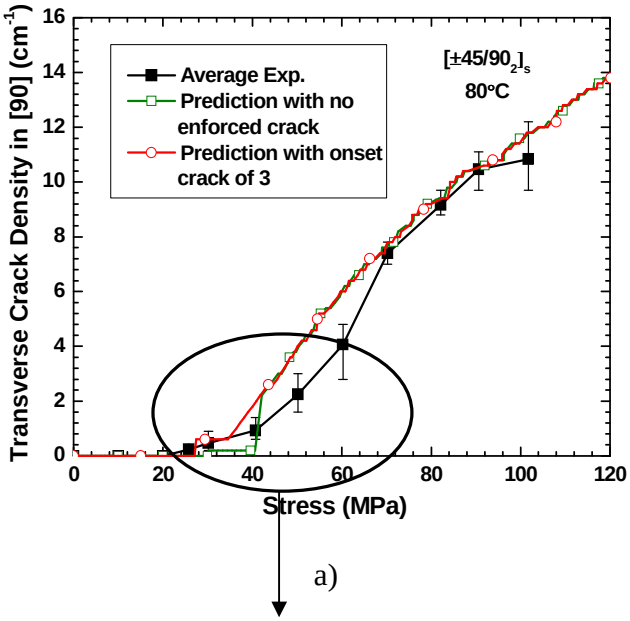

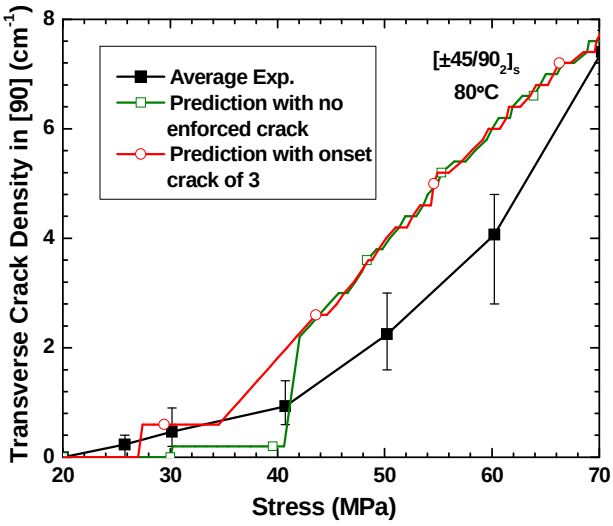

b)

Figure 5-50: The influence of λ_{FPF} on the evolution of cracks in [90] plies in $[\pm 45/90_2]_s$ at 80°C

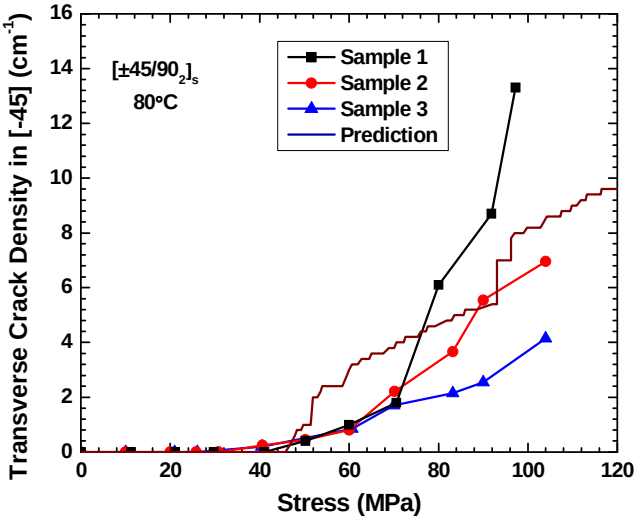

Figure 5-51: Experimental and predicted TID evolution in [-45] plies of $[\pm 45/90_2]_s$ during tensile loading at 80°C

occurrence of damage modes other than transverse cracking, which were not modeled in this thesis.

In view of these limitations, the predicted TID in [-45] plies is believed to compare well with experimental TID values for those stress levels in which only transverse cracking is observed. Similar conclusion can be drawn for predicted TID in [+45] plies, which is compared with experimental TID at 80^{o}C in Figure 5-52. The predictions shown in Figure 5-50, Figure 5-51, and Figure 5-52 were made using the average critical stored energy determined experimentally. In Figure 5-53, the effect of experimental scatter in the critical stored energy on predictions is highlighted. The original λ_{FPF} was used to obtain these predictions. The experimental scatter in TID compares very well with the scatter in the predicted TID due to experimental scatter in critical stored elastic energy.

The predicted TID in [90], [-45], and [+45] plies are compared with experimental TID at 180^{o}C in Figure 5-54, Figure 5-55, and Figure 5-56 respectively. The predicted trend and values for TID in [90] plies at 180^{o}C is in a good agreement with experimental results, as shown in Figure 5-54. The experimental FPF stress of 31±1 MPa is comparable to the predicted value of 30 MPa. The sudden increase in predicted TID at 180^{o}C at ~ 40 MPa is believed to be due to the difference in crack density at FPF, as discussed above.

The predicted TID evolution in [-45] plies is compared with experimental results at 180^{o}C in Figure 5-55. While the experimental FPF stress is 60 ± 30 MPa, the predicted FPF stress is 56.8 MPa. Due the difference in $\lambda_{FPF,}$ the predicted TID increased more rapidly than the experimental TID at applied stress levels lower than ~80 MPa. At higher stress levels (>~90 MPa), the predicted TID approached a constant value while the experimental TID increased rapidly with the applied stress. The occurrence of other damage modes, which was observed in

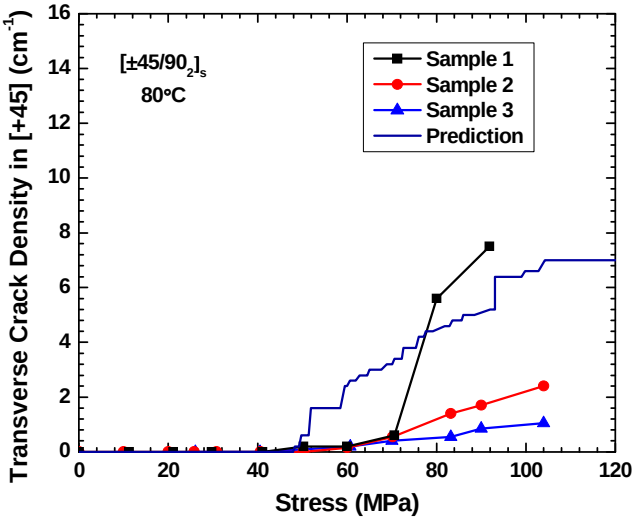

Figure 5-52: Experimental and predicted TID evolution in [+45] plies of $[\pm 45/90_2]_s$ during tensile loading at 80°C

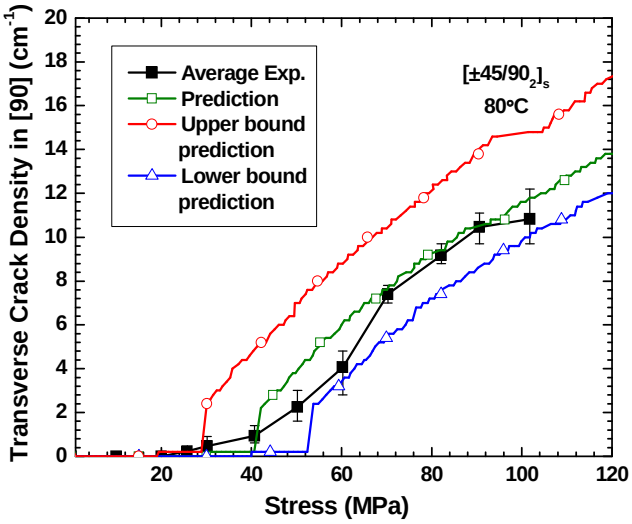

a)

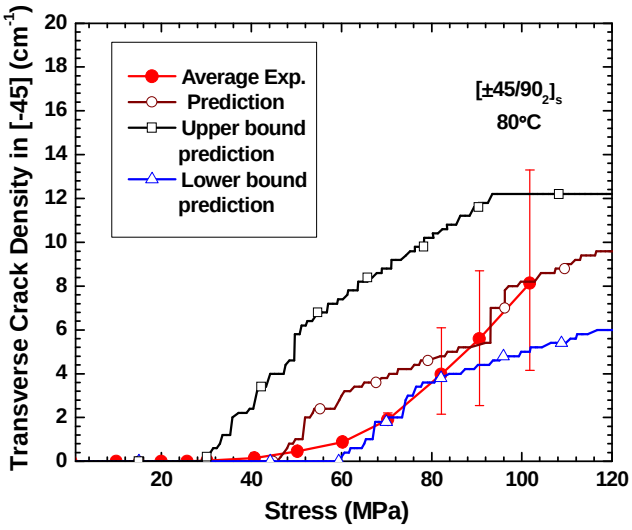

b)

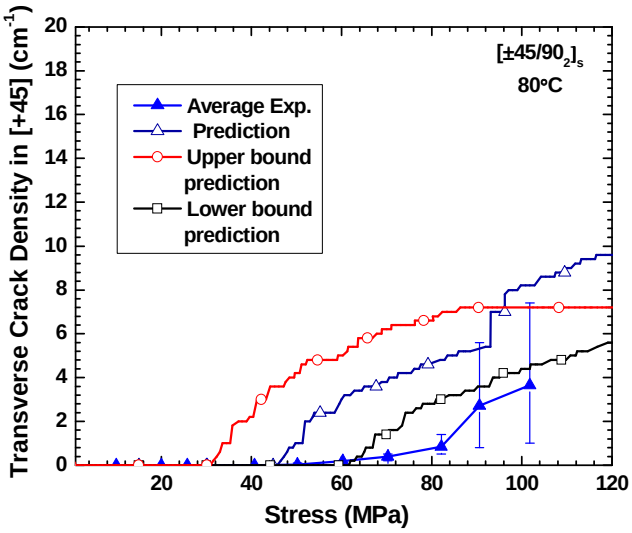

c)

Figure 5-53: Effect of experimental scatter in critical energy in TID evolution in a) [90], b) [-45] and c) [+45] plies of $[\pm 45/90_2]_s$ during tensile loading at 80°C

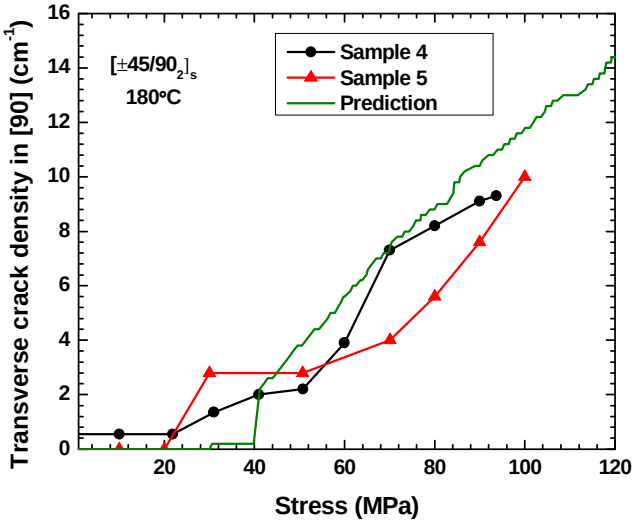

Figure 5-54: Experimental and predicted TID evolution in [90] plies of $[\pm 45/90_2]_s$ during tensile loading at 180°C

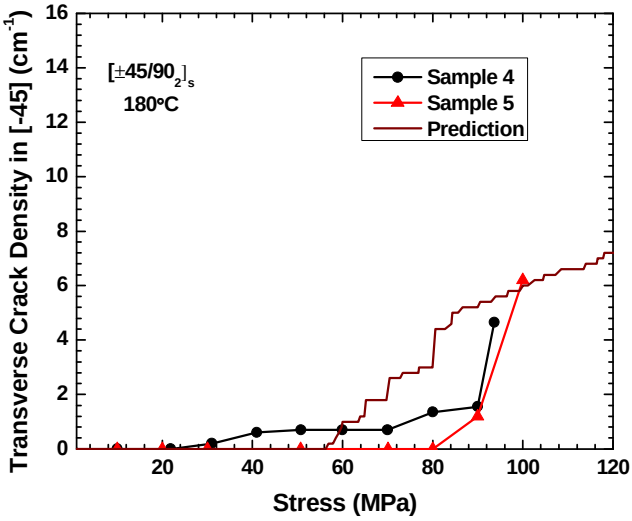

Figure 5-55: Experimental and predicted TID evolution in [-45] plies of $[\pm 45/90_2]_s$ during tensile loading at 180°C

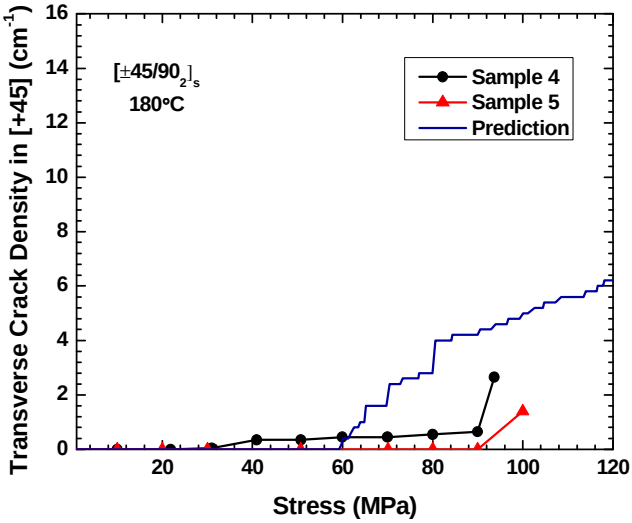

Figure 5-56: Experimental and predicted TID evolution in [+45] plies of $[\pm 45/90_2]_s$ during tensile loading at 180°C

the samples tested in 180ºC, is believed to be the reason of the difference between predictions and experimental results. Similar trend is observed for predicted TID in [+45] plies which is compared with experimental TID at 180ºC in Figure 5-56.

In summary, the predicted TID in all three plies are compared with average experimental TID at 80ºC and 180ºC in Figure 5-57 and Figure 5-58 respectively, to validate the ability of the proposed model to predict TID evolution during quasi-static loading.

5.5 Experimental Results for Time-Dependent Damage (TDD) Evolution and Creep

In this section, the experimental and predicted results for time-dependent evolution of transverse crack density and creep strain are presented and compared to validate the model, presented in Chapter 3.

5.5.1 Experimental creep results

Experimental creep strains measured at 80 °C are plotted in Figure 5-59 and Figure 5-60 for applied stresses of 45 MPa and 54 MPa respectively. These stress levels correspond to 45% and 54% of UTS (100 MPa) respectively. The strains upon loading were 3241 and 3576 micro strains for 45 MPa and 54 MPa respectively. The strain of the laminate increased from these initial values by 6.5% in 7.8 days at 45 MPa and by 7% in 10.4 days for 54 MPa. During the creep time, the transverse crack densities also increased, as tabulated in Table 5-5. At 45 MPa, the crack densities in [90], [-45] and [+45] were 2.1 cm^{-1}, 0 cm^{-1} and 0 cm^{-1}upon loading and 6.6 cm^{-1}, 0.2 $cm^{-1}$and 0.1 cm^{-1} upon unloading from the creep stress, respectively. At 54 MPa, the crack densities in [90], [-45] and [+45] were 2.5 cm^{-1}, 0 cm^{-1} and 0.1 cm^{-1}upon loading and 8.2 cm^{-1}, 0.2 $cm^{-1}$and 0.3 cm^{-1} upon unloading from the creep stress, respectively. Hence, the

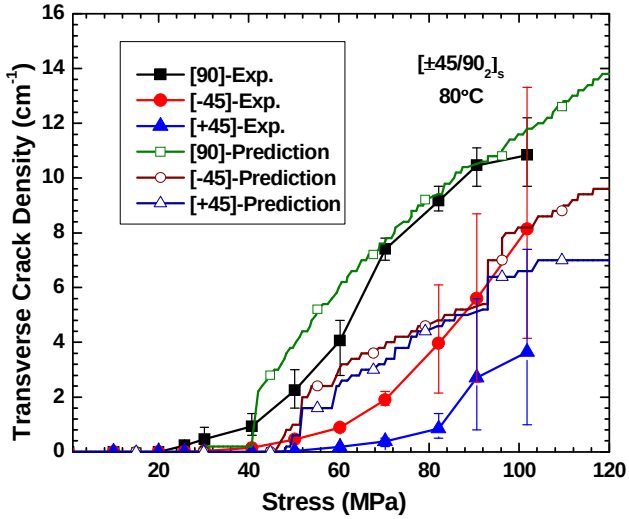

Figure 5-57: Comparison of average experimental and predicted TID evolution in [90], [-45], and [+45] of $[\pm 45/90_2]_s$ during tensile loading at 80°C

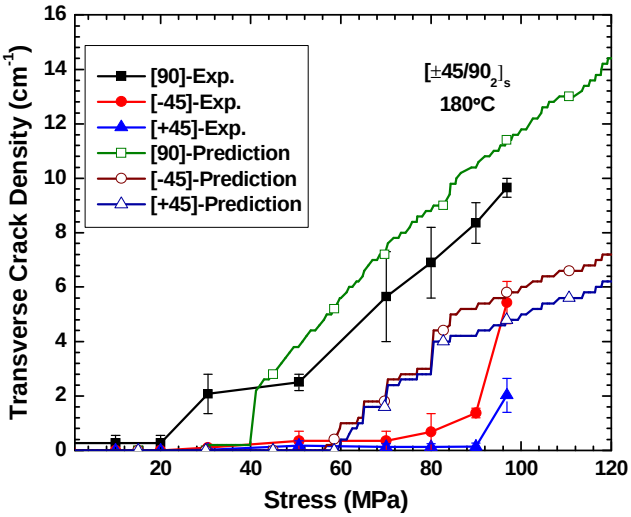

Figure 5-58: Comparison of average experimental and predicted TID evolution in [90], [-45], and [+45] of $[\pm 45/90_2]_s$ during tensile loading at 180°C

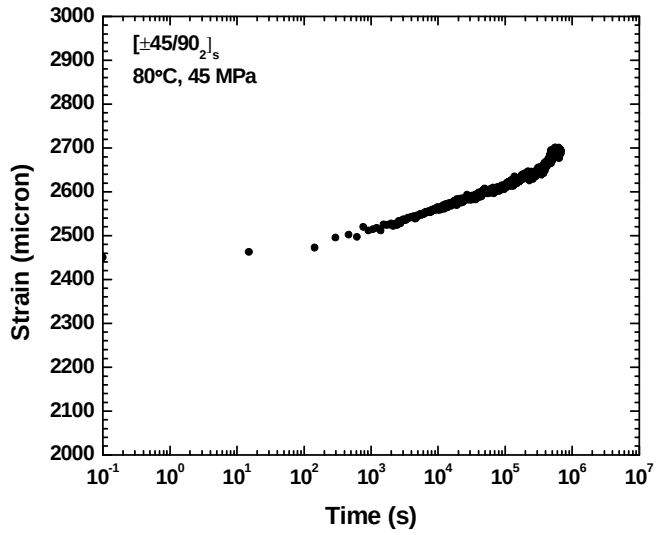

Figure 5-59: Experimental creep strain at 45 MPa and 80°C

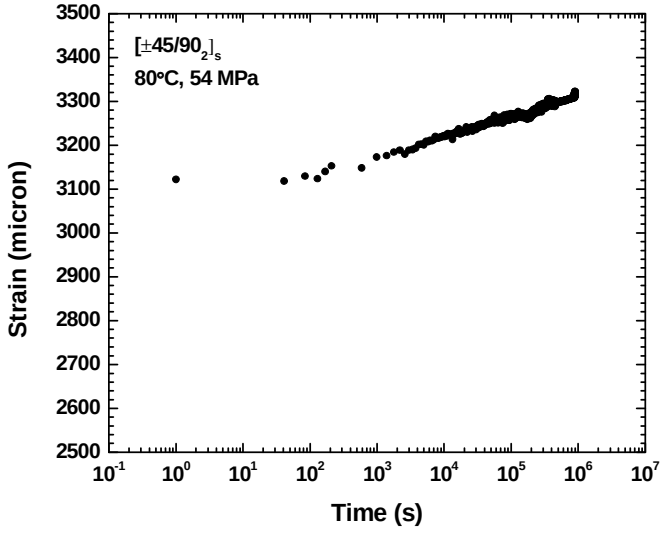

Figure 5-60: Experimental creep strain at 54 MPa and 80°C

Table 5-5: Transverse crack densitiy measured upon loading to creep load and unloading at the end of the creep test

Temperature & Stress		**Crack Density - Creep test**		
		[90] (cm^{-1})	**[-45] (cm^{-1})**	**[+45] (cm^{-1})**
80°C, 45 MPa	Upon loading	2.1	0	0
	End of test	6.6	0.2	0.1
80°C, 54 MPa	Upon loading	2.5	0	0.1
	End of test	8.2	0.2	0.3
180°C, 20 MPa	Upon loading	0	0	0
	End of test	6.4	0.8	0.4
180°C, 25 MPa	Upon loading	0	0	0
	End of test	5	2	0.5

increase in creep strain with time is due to contributions from both the creep of the lamina and the increase in crack density.

Despite the longer creep duration and the higher stress magnitude, the increase in creep strain at 54 MPa was higher than at 45 MPa only by 290 microns. Being non-linear viscoelastic, the creep of a ply depends on the stress acting on that ply. This stress changes with time due to difference in creep rate among various plies of the laminate, which can be attributed to the difference in fiber orientations. In addition, the time-dependent increase in crack density also alters the stress state of various plies. Hence, the difference in crack densities upon loading as well as in their evolution during creep, is believed to be the reason for the marginal difference between creep strains at both stress levels. The predicted ply stresses along loading axis upon loading as well as at the end of creep (before unloading) are tabulated in Table 5-6 for 45 MPa and 54 MPa. The stress in [90] plies at 54 MPa is lower than that at 45 MPa due to higher crack density. Hence, the starting creep rate at 54 MPa is lower than that at 45 MPa. Additionally, the decrease in axial stresses in [90] plies at 54 MPa is more than that in 45 MPa, for the same creep duration, due to relatively higher levels of cracking. Hence, the rate of decrease in creep rate in [90] plies at 54 MPa would be more than that at 45 MPa. It can be inferred from Table 5-6 that the axial stresses in [±45] plies at 54 MPa are higher than those at 45 MPa and the increase in ply stresses, due to cracking and creep during the same duration, is also higher. This suggests that the rate of increase in creep rate in [±45] plies would be higher at 54 MPa than at 45 MPa. However, [±45] plies creep less than [90] plies at an applied stress due to sharing of the applied load by the fibers. Therefore, the impact of higher rate of decrease in creep rate of [90] plies at 54 MPa on the overall laminate creep rate and creep strain would be more than the impact of higher rate of increase in creep rate in [±45] plies at 54 MPa. This is believed to be the reason for

Table 5-6: The predicted axial stresses in multiple plies upon loading and unloading at the end of the creep test (same creep period of 7.8 days)

	σ_x in [90] (MPa)		**σ_x in [-45] (MPa)**		**σ_x in [+45] (MPa)**	
Creep Stress and Temp.	t_0	t_{end}	t_0	t_{end}	t_0	t_{end}
45 MPa 80°C	41.2	37.0	48.8	58.1	48.0	57.7
54 MPa 80°C	37.6	31.3	65.6	69.8	67.9	72.5

the marginal difference between the laminate creep strains at 45 MPa and 54 MPa.

Experimental creep results at 180 °C are plotted in Figure 5-61 and Figure 5-62 for applied stresses of 20 MPa and 25 MPa respectively. These creep stresses were 20% and 25% of the UTS at this temperature. Creep strain at 180 °C increased substantially, by 85% at 20 MPa in 6.9 days and 123% at 25 MPa in 9.8 days. During the creep time, the transverse crack densities increased as tabulated in Table 5-6. Although the creep time for the sample at 25 MPa was 2.9 days longer than the sample at 20 MPa, higher crack density of 6.4 cm^{-1} in [90] plies at 20 MPa was observed compared to 5 cm^{-1} at 25 MPa. The possible reason can be inherent in the lower crack density of in [±45] plies at 20 MPa compared to 25 MPa at time of 6.9 days. However, this cannot be confirmed since the crack densities of the various plies of the sample tested in 25 MPa were not recorded at time of 6.9 days (i.e., equal to the creep time of the sample tested at 20 MPa).

5.5.2 *Experimental results for TDD*

Table 5-5 highlights the increase in crack density during creep. However, it does not provide any information on its evolution with time, Hence, separate specimens were used to obtain this data. The specimens were unloaded at pre-determined times and examined to record the crack density. One specimen was used per stress level.

The experimental data for the evolution of transverse crack density with time, in [90] and [±45] plies of a $[\pm 45/90_2]_s$ laminate, are plotted in Figure 5-63 and Figure 5-64 for creep stress levels of 45 MPa at 80°C and 25 MPa at 180°C, respectively. The values from Table 5-7 are also plotted in these figures to compare the results from both the creep tests and crack evolution characterization tests. The trend in TDD is similar to the trend previously observed in TID. The crack densities upon loading to 45 MPa at 80°C, in [90], [-45] and [+45] plies, were 1.6 cm^{-1}, 0.3

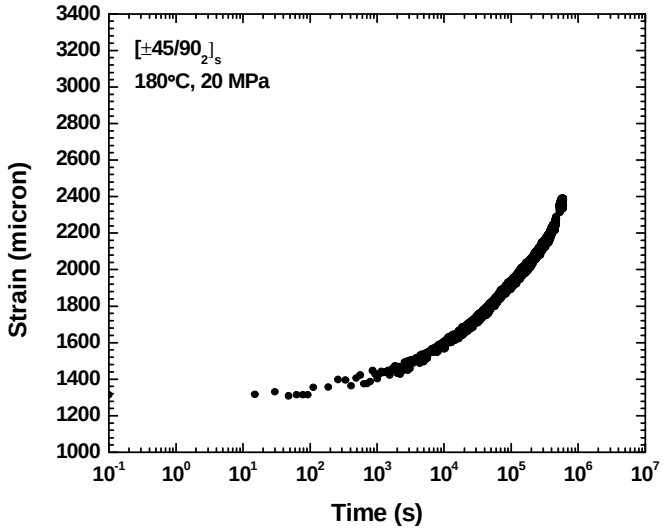

Figure 5-61: Experimental creep strain at 20 MPa and 180°C

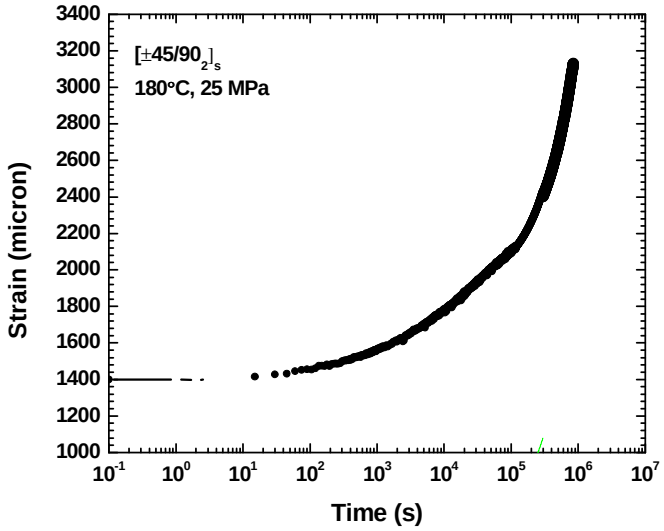

Figure 5-62: Experimental creep strain at 25 MPa and 180°C

Table 5-7: Comparison of transverse crack density in samples subjected to time-dependent damage characterization testing and creep testing

Temperature & Stress		Crack Density - Time-dependent damage characterization test			Crack Density - Creep test		
		[90] (cm^{-1})	[-45] (cm^{-1})	[-45] (cm^{-1})	[90] (cm^{-1})	[-45] (cm^{-1})	[+45] (cm^{-1})
80°C, 45 MPa	Upon loading	1.6	0.3	0	2.1	0	0
	End of test	5	1	0.6	6.6	0.2	0.1
180°C, 25 MPa	Upon loading	0	0	0	0	0	0
	End of test	5.5	1.3	0.5	5	2	0.5

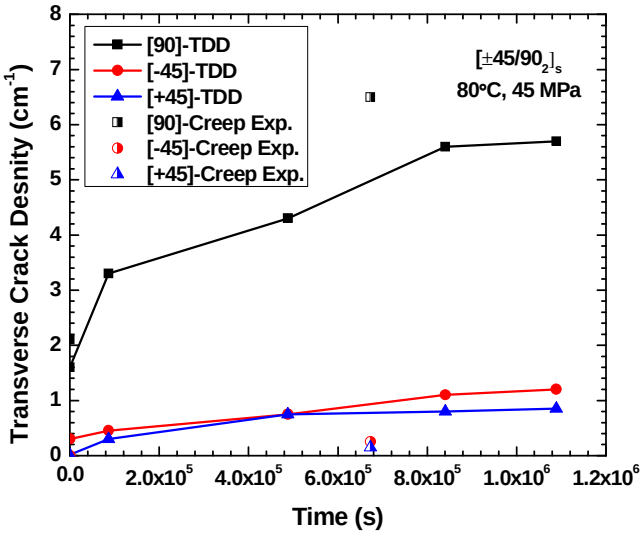

Figure 5-63: Experimental transverse crack density evolution with time in [90], [-45], and [+45] plies of $[\pm 45/90_2]_s$ laminate at 80°C and 45 MPa

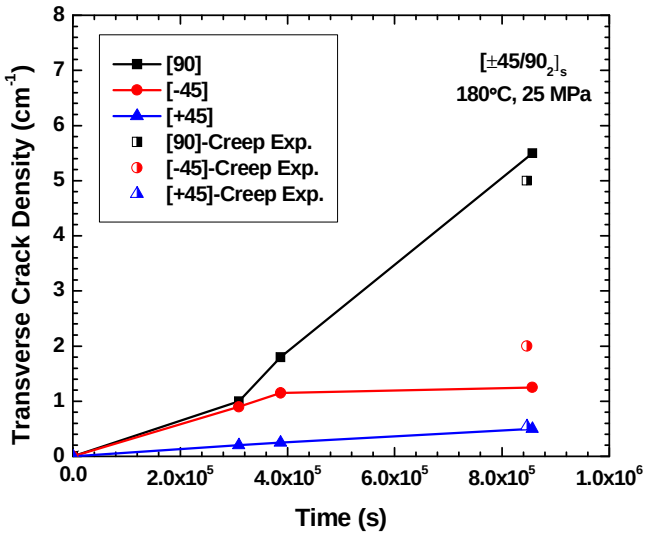

Figure 5-64: Experimental transverse crack density evolution with time in [90], [-45], and [+45] plies of $[\pm 45/90_2]_s$ laminate at 180°C and 25 MPa

cm^{-1}, and 0 cm^{-1} while the crack density values for the sample used in creep test were 2.1 cm^{-1}, 0 cm^{-1}, and 0 cm^{-1} respectively. The crack densities in the sample used for crack characterization test at a time corresponding to the end of creep (7.8 days) were 5 cm^{-1}, 1 cm^{-1}, and 0.6 cm^{-1} in [90], [-45] and [+45] plies respectively. The crack densities in [90], [-45] and [+45] plies of the creep sample at the end of creep tests at 45 MPa were 6.6 cm^{-1} and 0.2 and 0.1 cm^{-1} respectively. The time-dependent crack densities at the end of the both tests were of similar magnitude; the observed difference in crack densities upon loading to creep load (which can differ from sample to sample at an applied stress as discussed in the case of TID) is believed to have influenced the subsequent crack evolution.

At the creep stress of 25 MPa and 180°C, the laminate did not develop transverse cracks upon loading during both types of tests as shown in Table 5-7. The crack densities, in [90], [-45] and [+45] plies of the creep test sample, at the end of creep test (9.8 days) at 25 MPa and 180°C were 5 cm^{-1}, 2 cm^{-1}, and 0.5 cm^{-1}. The corresponding values form time-dependent characterization tests were 5.5 cm^{-1}, 1.3 cm^{-1}, and 0.5 cm^{-1}, respectively. In view of the difference in TID from sample to sample discussed in Section 5.3.4, the difference between these two sets of values in Table 5-7 is negligible. Hence, the repeated loading and unloading during crack characterization tests is believed to have not affected the TDD evolution obtained using these tests.

5.6 Predicted Results for TDD, Creep, and Model Validation

5.6.1 *Time-dependent transverse crack density evolution*

The perturbation of stresses in plies of the laminate due to time-dependent cracking is

similar to that discussed for the case of TID and hence, not presented here. The predicted in-plane stresses and strains in the plies varied with time as shown in Figure 5-65 to Figure 5-68 for a creep stress of 45 MPa at 80ºC and stress of 25 MPa at 180 respectively. The evolution of these with time is similar to the evolution of TID with applied stress. It can be inferred that the axial stresses in [90] plies decrease and that in [±45] plies increase with time, due to creep and increase in the transverse crack density. These stresses and strains were used to determine the time-dependent evolution of stored elastic energy in plies. When these exceeded the critical stored energy, cracking of those plies were predicted as shown in Figure 5-69 and Figure 5-70 for 80°C and 180°C respectively.

The predicted evolution of the transverse crack density with time, in multiple plies of $[\pm 45/90_2]_s$, are plotted and compared with experimental results in Figure 5-71 for a creep stress of 45 MPa at 80 ºC. The predicted transverse crack densities, upon loading, were 3 cm^{-1}, 0 cm^{-1} and 0 cm^{-1} [90], [-45] and [+45] plies, respectively, and the corresponding experimental crack densities were 1.8 cm^{-1}, 0.6 cm^{-1} and 0.3 cm^{-1} in [90], [-45] and [+45] plies, respectively. The simultaneous transverse cracking of [±45] plies had resulted in a lower crack density in [90] plies during experiments. However, the model predicts a higher crack density in [90] plies, with no cracking in [±45] plies upon loading to 45 MPa. The sample used in crack characterization test had process-induced cracks while no such cracking due to PIS was predicted by the model. The causes for such discrepancy have been discussed in Section 5.3.4.

The magnitude and the trend in crack evolution with time in [90] plies are in a good agreement with experimental results. The predicted crack density in [90] plies at a time corresponding to the end of crack characterization tests (12.6 days) is 5.2 cm^{-1} while the experimental crack density at this time was 5.7 cm^{-1}. The crack density in [90] ply measured in the sample used for creep

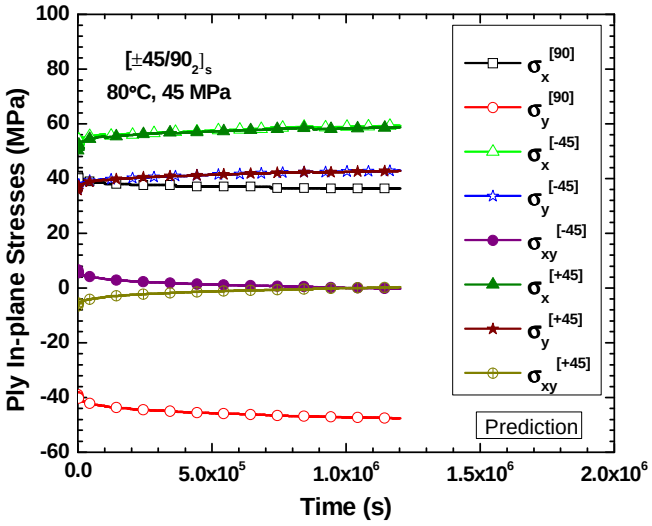

Figure 5-65: Predicted in-plane stresses with respect to time in $[\pm 45/90_2]_s$ at 80°C and 45 MPa

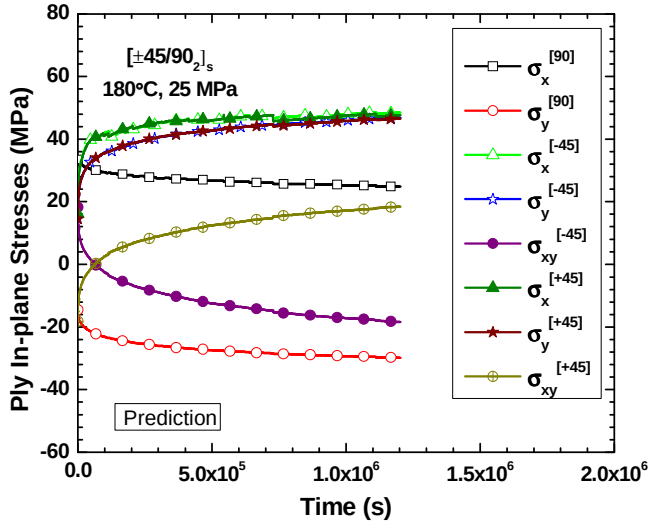

Figure 5-66: Predicted in-plane stresses with respect to time in $[\pm 45/90_2]_s$ at 180°C and 25 MPa

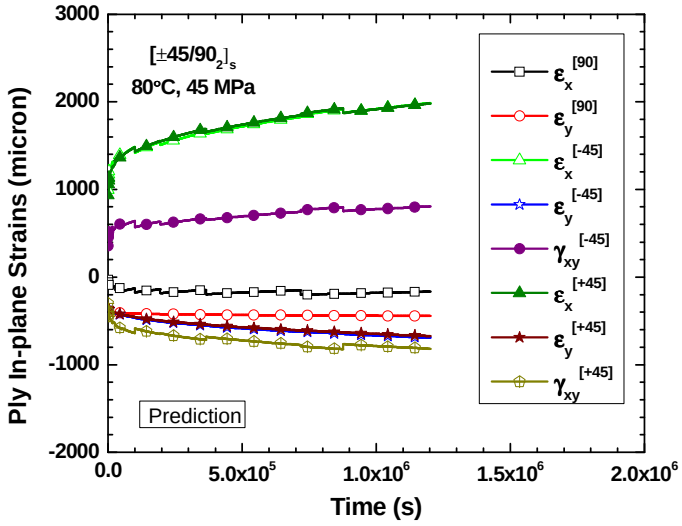

Figure 5-67: Predicted in-plane strains with respect to time in $[\pm 45/90_2]_s$ at 80°C and 45 MPa

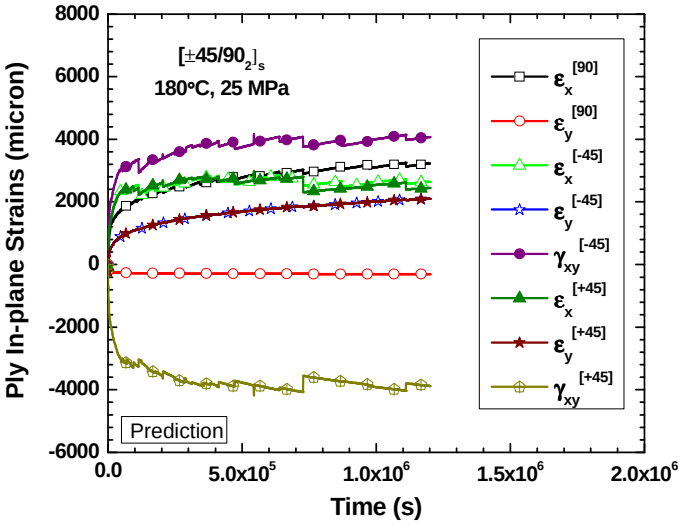

Figure 5-68: Predicted in-plane strains with respect to time in $[\pm 45/90_2]_s$ at 180°C and 25 MPa

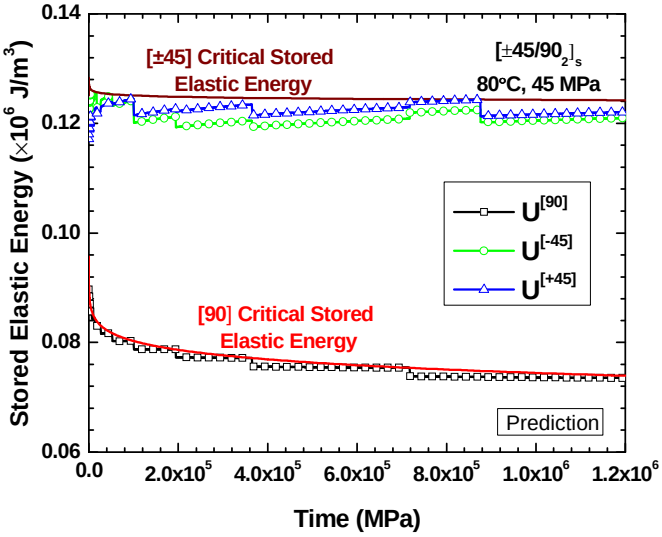

Figure 5-69: Evolution of stored elastic energy with time in various plies of $[\pm 45/90_2]_s$ at 80°C and 45 MPa

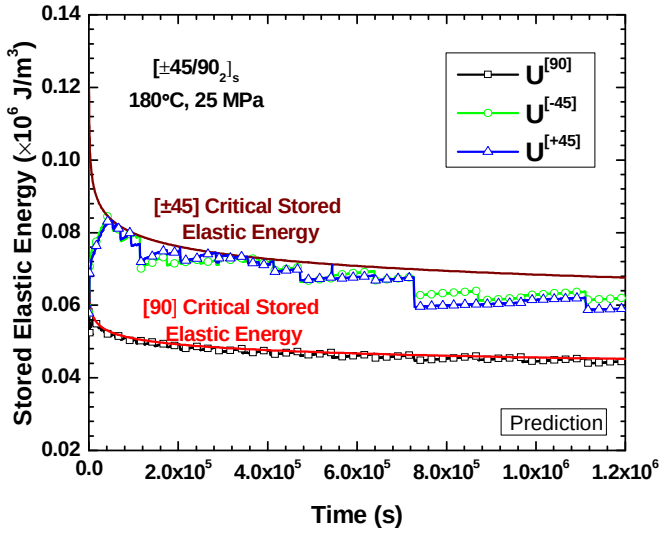

Figure 5-70: Evolution of stored elastic energy various plies of the $[\pm 45/90_2]_s$ laminate at 180°C and 25 MPa

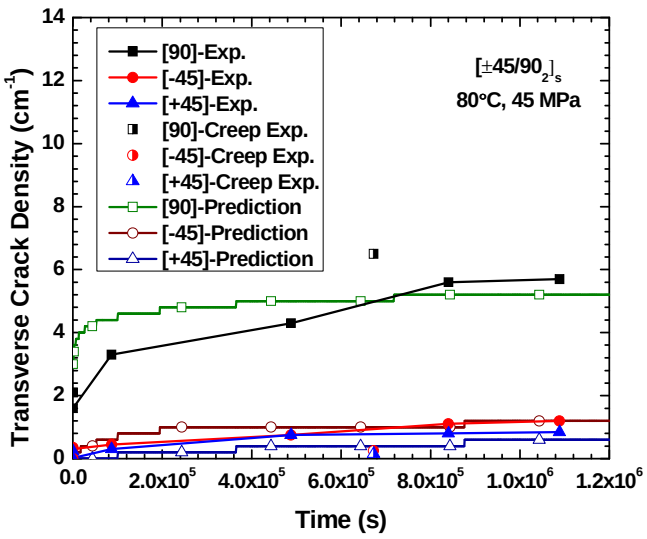

Figure 5-71: Comparison of experimental and predicted evolution of transverse crack density with time in multiple plies of $[\pm 45/90_2]_s$ at 80°C and 45 MPa

experiment was 6.6 cm^{-1} at a time of 7.8 days while the corresponding predicted value is 5 cm^{-1}.

The predicted magnitude and the trend in the evolution of transverse cracking in [-45] and [+45] plies are also in a good agreement with the experimental results generated by crack characterization tests. While the predicted crack density at the end of the test are 1.2 cm^{-1} and 0.6 cm^{-1} in [-45] and [+45] plies respectively, the experimental values were 1.2 cm^{-1} and 0.9 cm^{-1}. The transverse crack density values measured in the creep sample were 0.3 cm^{-1} and 0.2 cm^{-1} differed from the predicted results which are 0.3 cm^{-1} and 0.9 cm^{-1} at the day of 7.8. It is believed that the influence of cracking evolution of the plies on one another, discussed in 5.3.4, resulted in a higher crack density in [90] plies and lower crack density in [±45] plies in the sample tested in creep compared to the predicted results.

Figure 5-72 compares the predictions with experimental results for the time-dependent evolution of transverse crack density in multiple plies of $[\pm 45/90_2]_s$ laminate at 25 MPa and 180ºC. The experimental crack densities in all the plies for both samples tested for creep and crack characterization were zero upon loading to 25 MPa which similar to the predicted values at time equal to zero. The predicted crack densities after 9.9 days corresponding to the end of crack characterization tests, in [90], [-45], and [+45] plies, are 7 cm^{-1}, 5.8 cm^{-1}, 4.2 cm^{-1} respectively. The values obtained by crack characterization tests at this time were 5.5 cm^{-1}, 1.25 cm^{-1}, and 0.5 cm^{-1}. The values recorded in the creep test in day of 9.8 were 5 cm^{-1}, 2 cm^{-1}, and 0.5 cm^{-1} while the predicted values are 7 cm^{-1}, 5.8 cm^{-1}, 4.2 cm^{-1} at the corresponding time for [90], [-45], and [+45] plies respectively. The obtained experimental values are lower than the predicted values. In addition, the predicted rate of evolution of crack density is different from the experimental rate of evolution of crack density. These differences are believed to be due to occurrence of damage modes other than transverse cracking. Extensive vertical cracking and delamination were

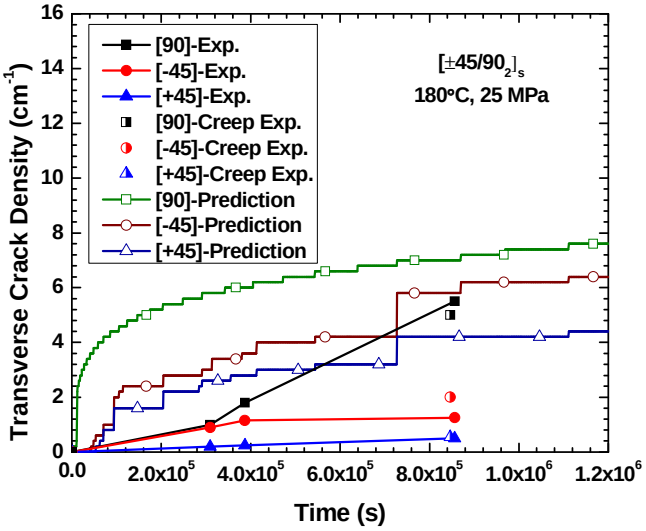

Figure 5-72: Evolution of experimental and predicted transverse crack density with time in multiple plies of $[\pm 45/90_2]_s$ at 180°C and 25 MPa

observed in the samples tested at 180°C for both creep and crack characterization tests.

5.6.2 *Creep*

The predicted creep strains of the multidirectional laminate, are compared with experimental results in Figure 5-73 (a) and Figure 5-74 (a) for two creep stress levels of 45 MPa and 54 MPa, respectively at 80°C. The predicted and experimental strain values at the start of creep after loading to creep stress of 45 MPa are 682 and 2450 micro strains and creep stress of 54 MPa are 1263 and 3120 micro strains respectively. While the prediction takes into account the process-induced thermal strain, the experimental values does not include since strain gages were bonded to the test coupons only after manufacturing. Hence, the process-induced strain of -1422 micro strains was added to the experimental creep strain and this shifted the experimental curve down as shown in Figure 5-73 (b) and Figure 5-74 (b) for 45 MPa and 54 MPa respectively. The difference between the instantaneous strains after applying this correction is 346 micro strains at 45 MPa and 435 micro strains at 54 MPa at t_o. This difference is believed to be due to the difference between the predicted and experimental moduli discussed in Section 5.3.5. In order to confirm this, the experimental instantaneous strain was shifted to match the instantaneous strain at t_0 corresponding to the maximum and minimum moduli for 54 MPa at 80°C. According to Figure 5-18, the scatter range of the experimental modulus of the laminate in 54 MPa and 80°C is within 17.7 GPa and 23.5 GPa. After adding the thermal strain, the instantaneous strain corresponding to the minimum (17.7 GPa) and maximum (21.3 GPa) experimental modulus is 1628 (3050-1422) and 1133 (2535-1422) micro strains respectively. The shifted instantaneous strain corresponding to these values are plotted in Figure 5-74 (b) demonstrating that the predicted and experimental creep instantaneous strain are between the scatter range of the

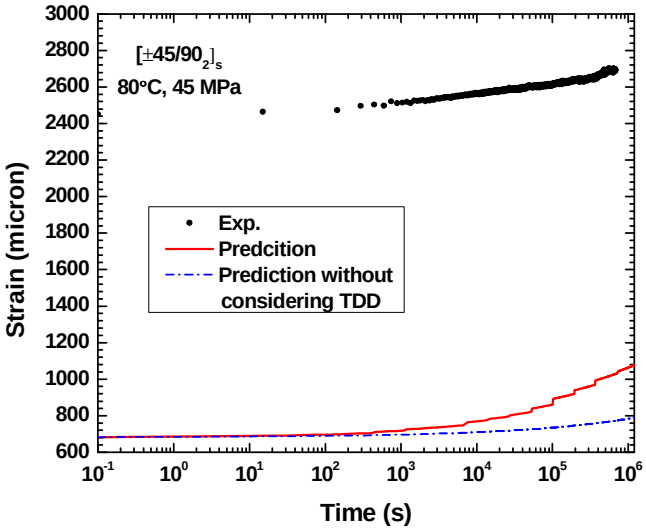
[±45/90$_2$]$_s$
80°C, 45 MPa
Exp.
Predcition
Prediction without considering TDD
Strain (micron)
Time (s)

a)

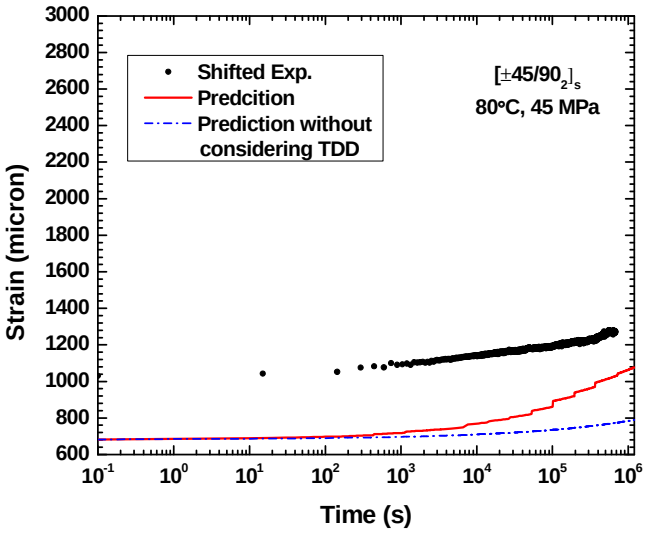
Shifted Exp.
Predcition
Prediction without considering TDD
[±45/90$_2$]$_s$
80°C, 45 MPa
Strain (micron)
Time (s)

b)

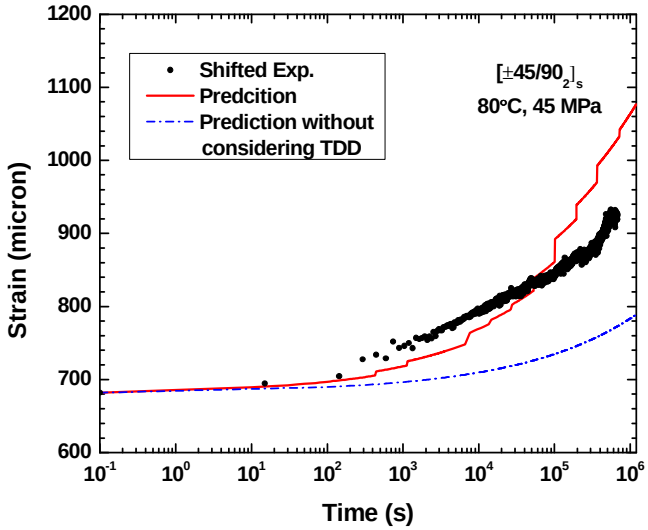

c)

Figure 5-73: Comparison of predicted strain with total experimental strain, a) without adding the thermal strain to the experimental strain, b) after adding the thermal strain to the experimental strain, and c) after eliminating the difference at t_0 for 45 MPa and 80°C

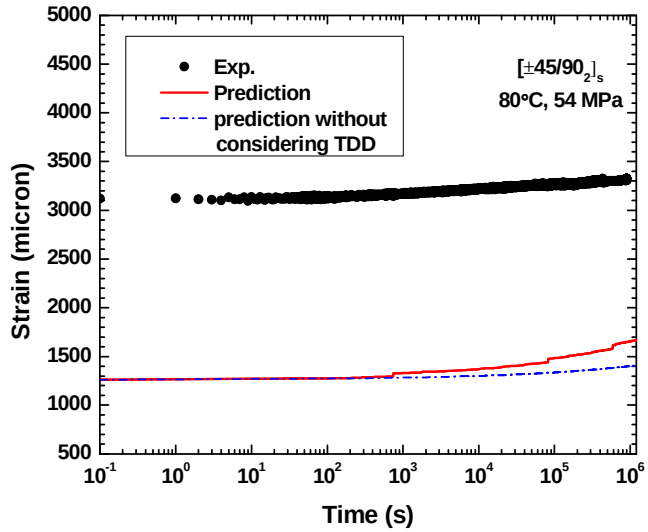

a)

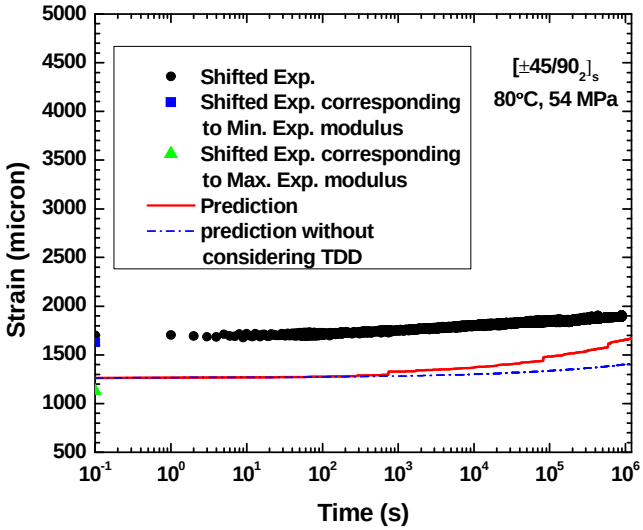

b)

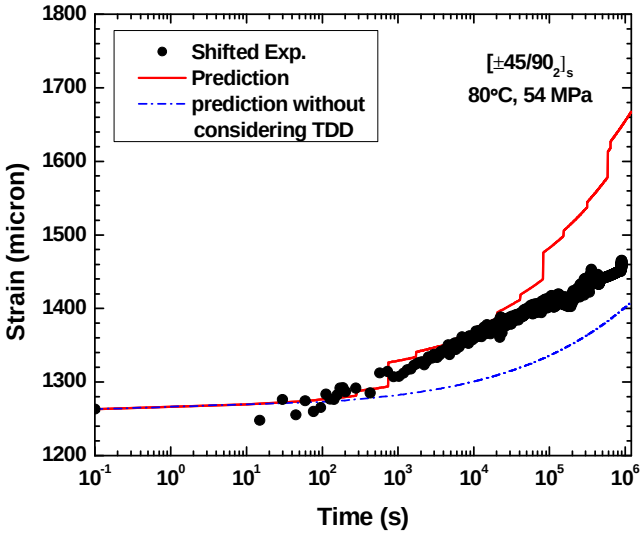

c)

Figure 5-74: Comparison of predicted strain with total experimental strain, a) without adding the thermal strain to the experimental strain, b) after adding the thermal strain to the experimental strain, and c) after eliminating the difference at t_0 for 54 MPa and 80°C

experimental creep strain.

While the predicted shape of the creep curve is similar to the shape of the experimental creep curve, a better comparison could be made if the above mentioned difference in the instantaneous strain (i.e. at t_o) is eliminated. Hence, the experimental and predicted curves were superposed by shifting the curves vertically by an amount equal to the difference in instantaneous strain as shown in Figure 5-73 (c) and Figure 5-74 (c). The maximum difference between the predicted creep and experimental creep strain at a time of 7.8 days corresponding to the end of creep experiment is 7.3 % at 45 MPa and time of 10.4 days is 11.8 % at 54 MPa. In order to highlight the contribution from TDD on creep, creep strain at these stresses were also predicted without allowing the plies to crack. These predictions without TDD, plotted in Figure 5-73 and Figure 5-74, clearly demonstrate the role played by TDD on creep.

Similarly, the predicted creep strains for two stress levels of 20 MPa and 25 MPa at 180°C are compared with experimental results in Figure 5-75 (a) and Figure 5-76 (a) respectively. After adding the process-induced strain of -1352 micro strains to the experimental creep strain, the resulting curves are as shown in Figure 5-75 (b) and Figure 5-76 (b). The difference in the instantaneous strains (i.e. at to) after applying this correction is 260 microns at 20 MP and 83 microns at 25 MPa, which is due to the difference between the predicted and experimental moduli. For a better comparison of the curve shape and the maximum error, the difference in the instantaneous strain (i.e. at t_o) was eliminated and the experimental and predicted curves were superposed by shifting the curves vertically by an amount equal to the difference in instantaneous strain as shown in Figure 5-75 (c) and Figure 5-76 (c). It is seen that there is a good agreement between experimental and predicted strain curves. The maximum difference between experimental and predicted creep strains is 17% at a time of 6.9 days for 20

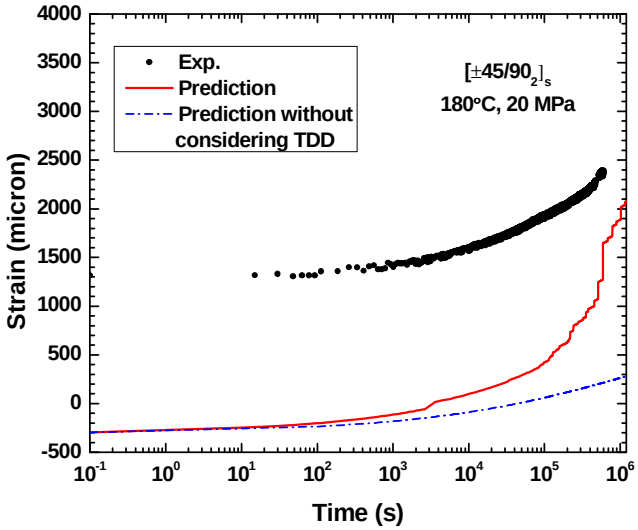
Exp.
Prediction
Prediction without considering TDD
[±45/90$_2$]$_s$
180°C, 20 MPa
Strain (micron)
Time (s)

a)

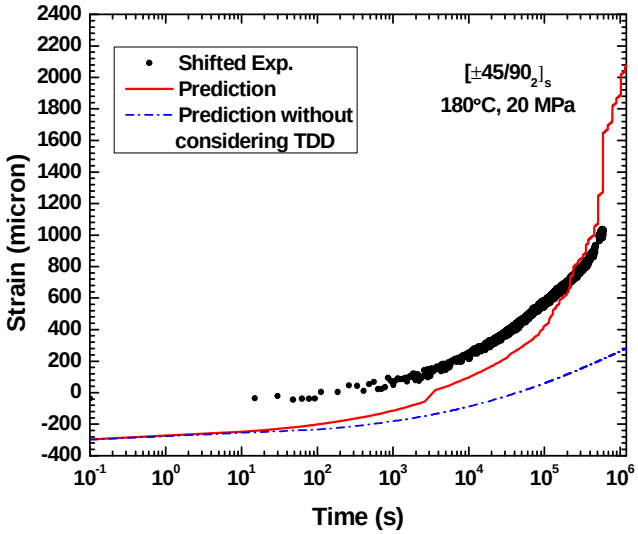
Shifted Exp.
Prediction
Prediction without considering TDD
[±45/90$_2$]$_s$
180°C, 20 MPa
Strain (micron)
Time (s)

b)

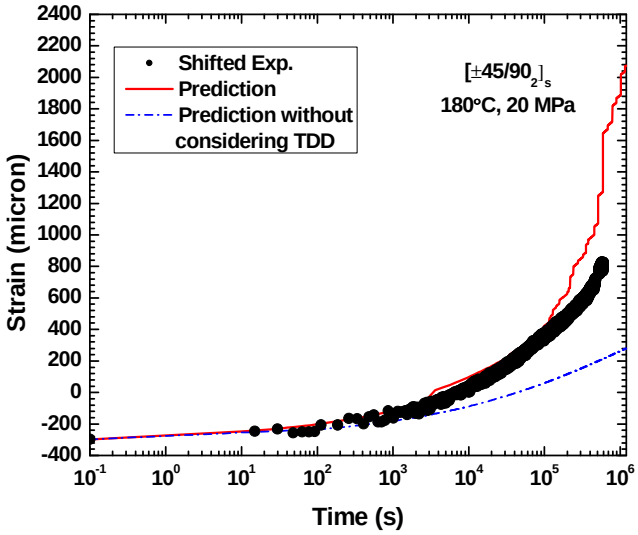

c)

Figure 5-75: Comparison of predicted strain with total experimental strain, a) without adding the thermal strain to the experimental strain, b) after adding the thermal strain to the experimental strain, and c) after eliminating the difference at t_0 for 20 MPa and 180°C

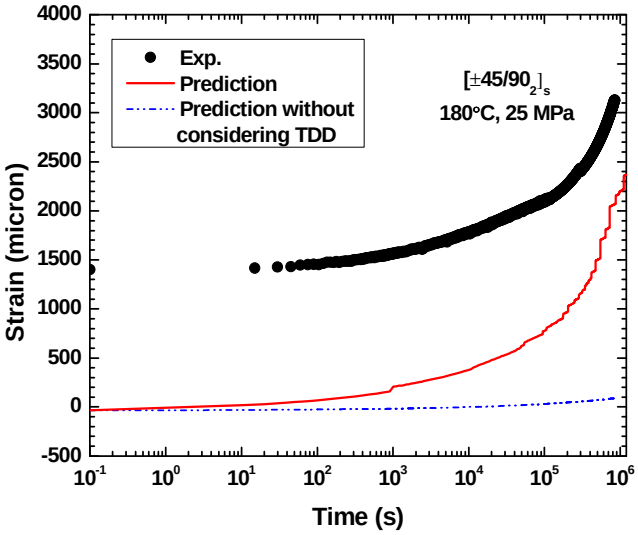

a)

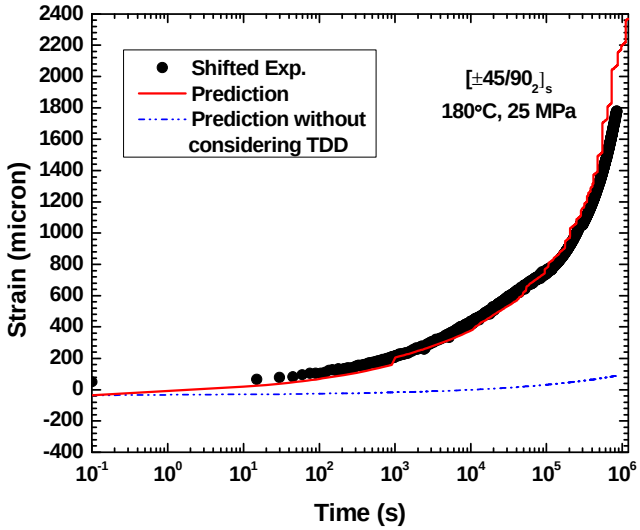

b)

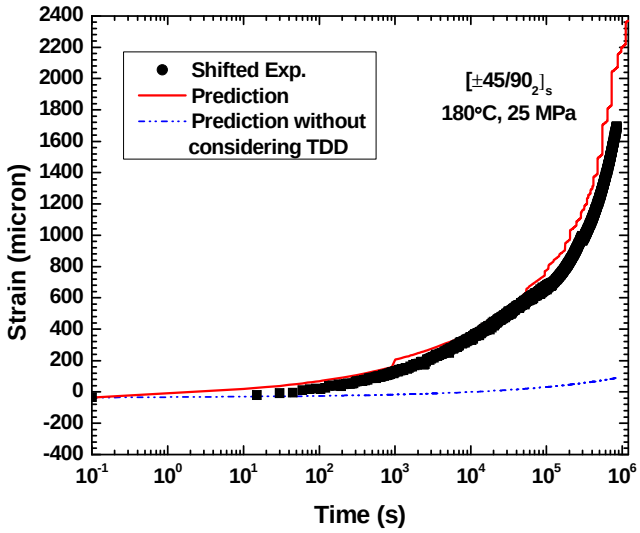

c)

Figure 5-76: Comparison of predicted strain with total experimental strain, a) without adding the thermal strain to the experimental strain, b) after adding the thermal strain to the experimental strain, and c) after eliminating the difference at t_0 for 25 MPa and 180°C

MPa and 8% at a time of 9.8 days for 25 MPa. Predictions without considering TDD are also plotted in Figure 5-75 and Figure 5-76 which clearly demonstrate the role of TDD on creep.

Good superposition between experimental and predicted results in Figure 5-73 (c), Figure 5-74 (c), Figure 5-75 (c), and Figure 5-76 (c) validates the ability of the model developed in this thesis to predict creep of laminates with TDD.

CHAPTER 6. CONCLUSION

A model to predict the evolution of time-independent damage (TID) that develops due to process-induced stresses and during loading to the service load, the evolution of time-dependent damage (TDD) in in multiple plies during creep, and their influence on creep response of multidirectional polymer composite laminates has been developed and validated using experimental results. The predominant damage mode, transverse cracking, was considered in the modeling. The model consists of four modules, PIS, QSL, SL, and VA. The PIS, the QSL, and the SL modules predict changes in ply stresses and stored elastic energy for incremental change in temperature, stress, and time respectively, and compare the stored elastic energy with a critical stored elastic energy criterion to determine whether a crack occurs. The variational analysis-based VA module predicts the crack density of each ply and the associated perturbation in ply stresses due to cracking in that ply. The model predictions for a $[\pm 45/90]_s$ laminate, at two test temperatures (80^{o}C and 180^{o}C) and four stresses in the range of 20–54 MPa, compare very well with experimental results, for TID and TDD evolution, modulus, stress-strain curve and creep strain, validating the model. Therefore, it is concluded that all the three objectives of this thesis, stated in 2.5, have been successfully achieved.

6.1 Summary

A summary of accomplished tasks are presented below

1) A model has been developed for predicting the time-independent evolution of transverse cracking simultaneously in multiple plies of a multidirectional polymer composite laminate and the influence of this TID on the modulus of the laminate.

This model also accounts for process-induced stress and any TID due to this process-induced stress.

- Tensile stress–strain curves, and time-independent evolution of transverse cracking in multiple plies and its influence on time-independent modulus in $[\pm 45/90]_s$ laminate have been generated at 80°C and 180°C and used to validate the model predictions.
- An excellent agreement is observed between the predicted and the experimental stress-strain curves at 80°C and 180°C below 80 MPa. Beyond this stress level, the predictions deviate from the experimental results due to the development of other damage modes, such as vertical cracking and delamination, which has not been accounted for model.
- The predicted trend in TID evolution is similar to the experimental trend and the predicted magnitudes of TID in [90], [-45], and [+45] plies, at any applied stress, are within the scatter range of experimental results and hence, compare very well.
- Although, the process-induced stress (PIS) did not result in TID upon cooling from the cure temperature, its influence on TID evolution was substantial. The predicted results compare well with experimental results only if the PIS is taken into account. The predicted time-independent moduli, at any applied stress below 80 MPa, are within the experimental scatter range and compare well with experimental moduli. However, it deviates beyond this stress level due to the occurrence of the other damage modes not modeled in this study.

2) A model has been developed for predicting the time-dependent evolution of transverse cracking simultaneously in multiple plies of a multidirectional polymer composite laminate.

   - Time-dependent evolution of transverse cracking in multiple plies of a $[\pm 45/90]_s$ laminate at 45 MPa and 80°C and at 25 MPa and 180°C has been generated and used to validate the model. Additional crack density data, obtained from creep specimens after the end of the test, have also been used in the validation.
   - The predicted results for TDD at 45 MPa and 80°C compare very well with experimental results. However, the predicted magnitude and the predicted rate of increase in TDD, at 25 MPa and 180°C, are higher than the experimental results due to the occurrence of damage modes other than transverse cracking.

3) A model has been developed to predict the creep of a multidirectional polymer composite laminate with both the TID and the TDD.

   - Creep results for $[\pm 45/90]_s$ laminate at four stresses and two temperatures, i.e., 45 MPa and 54 MPa at 80°C, and 20 MPa and 25 MPa at 80°C, have been generated and used to validate the model.
   - The instantaneous strain, upon to loading to creep stresses, were higher than the predicted values due to non-inclusion of the process-induced residual strain in the experimental strain.
   - After adding the residual strain to the experimental strain, the experimental curves are shifted down towards the predicted curves. The predicted creep strains compare very well with the experimental results. The range of error in prediction is 7.3%-17%.

4) Parametric analyses have been done to evaluate the influence of various assumptions used in the model.
    - The most important assumption, affecting the accuracy of the model, is the boundary values used in the VA module to solve for the stress perturbation in the plies of the laminate. The parametric analyses have been used to identify the optimal values.
    - A parametric analysis of the effect of experimental scatter in stored elastic energy on TID evolution confirms the validity of the use of average value obtained from experiments.
    - The influence of additional assumptions such as constant crack spacing and placement of cracks in all plies at the same location, has not been evaluated due to lack of ability of the model, developed in this thesis, to simulate this influence.
    - The model also assumes that the perturbation is constant across the thickness and width of the plies. While the effect of this has been indirectly studied through the parametric study of boundary values, the current model does not have the capability to study the effect of this assumption directly.

6.2 Original Contributions

To the best knowledge of the author, the following contributions are the first in this area.

a) An analytical model for predicting time-independent evolution of transverse cracking simultaneously in multiple plies of a composite taking into account the influence of process-induced stresses.

b) An analytical model for predicting time-dependent evolution of transverse cracking, simultaneously, in multiple plies of a composite.

c) An analytical model to predict the creep compliance of a composite with both TID and TDD.

6.3 Recommendation for Future Work

In order to improve the accuracy of prediction and eliminate various assumptions mentioned in the previous section, the following is recommended for future work.

1) To develop the VA module using the principle of minimum potential energy.

The variational analysis model developed in this research work is based on the principle of minimum complementary energy. Since this approach tries to determine a stress state to minimize the complementary energy, the solution provides an upper bound for the actual stress field. Hence, the modulus determined by this method is a lower bound to the actual modulus. Based on this, the following is recommended for the future work:

An approach based on the principle of minimum potential energy is recommended to provide a solution for strain field of the cracked laminate and a lower bound for the cracked laminate's modulus. Normally, the actual solution would lie in between the two bounds. In general, the variational analysis based on the principle of minimum complementary energy solves for stress perturbation without any consideration for strain in the plies. The lamination theory requires that the strains in the plies far away from the cracks have to be same and should be equal to the strain of the laminate. While the variational analysis used in the VA module does not impose this, the solution methodology imposed it. In view of this, it would be interesting to see the accuracy of solution using the principle of minimum potential energy.

2) The boundary values were approximated in this research work. It is recommended that the perturbation in ply stresses at the crack locations are experimentally measured.
3) To develop a time-dependent failure criteria for a ply within a laminate.

In this research work, the critical stored elastic energy for [90] and [±45] plies were experimentally obtained using unidirectional plies tested under uniaxial state of stress. However, a time-dependent failure criterion for a ply embedded in a laminate under multi-axial state of stress is lacking and is recommended

REFERENCES

1 Birur, A., Gupta, A., Raghavan, J., "Creep rupture of multidirectional polymer composite laminates-Influence of time-dependent damage", *Engineering Materials and Technology*, Vol. 128 (4), pp. 611-617 (2006).

2 Dillard, D. A., Morris, D. H., Brinson, H F., "Creep and creep-rupture of laminated graphite/epoxy composites", *Report VPI-E-81-3*, Blacksburgh, USA: Virginia Polytechnic (1981).

3 Balachander, M., "Individual and interactive influence of temperature, stress, physical aging and moisture on creep, creep rupture and fracture of epoxy matrix and its composite*", M.Sc. Thesis, Winnipeg, MB, Canada*; University of Manitoba (2001).

4 Raghavan, J., Meshii, M., "Time-dependent damage in carbon-fiber reinforced polymer composites, *Composites*, Vol. 27 (A), pp. 1223-1227 (1996).

5 Nairn, J., "Matrix microcracking in composites", *Comprehensive Composite Materials Handbook*, Amsterdam, Elsevier, pp. 403-432 (2002).

6 Daniel, I. M., Ishai, O., "Engineering Mechanics of Composite Materials", *Oxford University Press*, Oxford ,New York, pp. 173 (1994).

7 Asadi, A., Raghavan, J., "Influence of time-dependent damage on creep of multidirectional polymer composite laminates", *Composites: Part B.*, Vol. 42, pp. 489-498 (2011).

8 Wang, A. S. D., and Crossman, F.W., "Initiation and growth of transverse cracks and edge delamination in composite laminates; Part 1. An energy method", *Journal of Composite Materials Supplement*, Vol. 14, pp. 71-86 (1980).

9 Wang, A. S. D., "Growth mechanisms of transverse cracks and ply delamination in composite laminates", *Advanced Composites Materials, Proceedings in International Conference of Composite Materials, ICCM, 3rd*, Paris, France, Vol. 1, pp. 170-185 (1980).

10 Nairn. J., and Hu, S., "The initiation and growth of delamination induced by matrix microcracks in laminated composites", *International journal of fracture*, Vol. 57, pp. 1-24 (1992).

11 Crossman, F.W., Warren, W. J., and Wang, A. S. D., "Influence of ply thickness on damage accumulation and final fracture", *Advanced Aerospace Structures, Materials, and Dynamics, A Symposium in Composites*, Boston, USA, pp. 215-226 (1983).

12 Wang, A. S. D. and Crossman, F.W., "Fracture mechanics of transverse cracks and ply delaminations in composite laminates", *Advances in composite materials, Proceedings of the 3rd international conference on composite materials,* Paris, France, pp. 170-185 (1980).

13 Corum, J. M., Battiste, R. L., Liu, K. C., and Ruggles, M. B., "Basic properties of reference cross-ply carbon fiber composite" *Oak-Ridge National Laboratory Report, ORNL/TM – 2000/29,* pp. 27-35, (2000).

14 Corum, J. M., Battiste, R. L., Deng, S., Liu, K. C., Ruggles, M. B. and Weistsman,Y.J., "Durability based design properties of reference cross-ply carbon fiber composite", *Oak-Ridge National Laboratory report, ORNL/TM – 2000/322*, pp. 10-1 – 10-9 (2001).

15 Viswanathan, C., "Individual and interactive influence of temperature, stress, physical aging, moisture and fiber volume fraction on creep, creep-rupture and fracture of epoxy

matrix and its composites", *MSc. Thesis, Winnipeg, MB, Canada*; University of Manitoba (2001).

16 Abhishek, G., "Creep of Plain Weave Polymer Matrix Composites", *Ph.D. Dissertation, Winnipeg, MB, Canada*; University of Manitoba (2009).

17 Zeng, X. and Raghavan, J., "Role of tool-part interaction in process-induced warpage of autoclave-manufactured composite structures", *Composites Part A*, Vol. 41 (9), pp. 1174 -1183 (2010).

18 Doner, D. R., and Novak, R. C., "Structural Behavior of Laminated Graphite Filament", *Composites 24th Annual Technical Conference, Reinforced Plastics/Composites Division, the Society of the Plastics Industry, Inc 3*; Quackenbush, NE, USA (1969).

19 Gentz, M., Armentrout, D., Rupnowski, P., Kumosa, L., Shin E., Sutter, J. K., Kumosa M., "In-plane shear testing of medium and high modulus woven graphite fiber reinforced/polyimide composites", *Composites Science and Technology*, Vol. 64, pp. 203-220 (2004).

20 Hahn, H. T., "Residual Stresses in Polymer Matrix Composite Laminates", *Journal of Composite Materials*, Vol. 10, pp. 266 (1976).

21 Nimmer, R. P., "Fiber-matrix interface effects in the presence of thermally induced residual stress", *Journal of Composites science and Technology*, Vol. 12, pp. 65 (1990).

22 Wisnom, M. R., "Factors affecting the transverse tensile strength of unidirectional continuous silicon carbide fibre reinforced 6061 aluminum", *Journal of Composites Materials*, Vol. 24, pp. 707-726 (1990).

23 Adams, D. S., Bowles, D. E., and Herakovich, C. T., “Thermally induced transverse cracking in graphite-epoxy cross-ply laminates”, *Journal of Reinforced Plastics and Composites*, Vol. 5, pp. 152-169 (1986).

24 Park, C. H., and McManus, H. L., "Thermally induced damage in composite laminates: Predictive methodology and experimental investigation”, *Composites Science and Technology*, Vol. 56, pp.1209-1219 (1996).

25 Herakovich, C. T., Hyer, and M. W., “Damage-induced property changes in composites subjected to cyclic thermal loading”, *Engineering Fracture Mechanics*, Vol. 25, pp. 779-791 (1985).

26 Zhao, L.G., Warrior, N.A., Long, A.C., “A micromechanical study of residual stress and its effect on transverse failure in polymer-matrix composites”, *International Journal of Solids Structures*, Vol. 43, pp. 5449-5467 (2006).

27 Lange, J., Toll, S., Manson, J. A. E., Hult, A., “Residual stress build-up in thermoset films cured above their ultimate glass transition temperature” *Polymers*, Vol. 36, pp. 3135-3141 (1995).

28 Flores, F., Gillespie, J. W., Bogetti, T. A., “Experimental investigation of the cure-dependent response of vinyl ester resin”, *Polymer Engineering and Science*, Vol. 42, pp. 582-590 (2002).

29 Hahn, H. T., and Pagano, N. J., “Curing stresses in composite laminates”, *Journal of Composites Materials*, Vol. 9, pp. 91-106 (1975).

30 Zewi, I. G., Daniel, I. M., and Gotro, J.T., “Residual stresses and warpage in woven-glass/epoxy laminates”, *Experimental Mechanics*, Vol. 27 (1), pp. 44-50 (1987).

31 Jun, W. J., and Hong, C. S., "Cured shape of unsymmetric laminates with arbitrary layup angles", *Journal of Reinforced Plastics and Composites*, Vol. 11 (12), pp.1352-1366 (1992).

32 Tseng, S. C., and Osswald, T. A., "Prediction of shrinkage and warpage of fiber reinforced thermoset composite parts", *Journal of Reinforced Plastics and Composites*, Vol. 13 (8), pp. 698-721 (1994).

33 Kim, K. S., and Hahn, H. T., "Residual stress development during processing of graphite/epoxy composites", *Composites Science and Technology*, Vol. 36 (2), pp. 121-132 (1989).

34 Wang, T. M., Daniel, I. M., and Gotro, J. T., "Thermoviscoelastic analysis of residual stresses and warpage in composite laminates", *Journal of Composites Materials*, Vol. 26 (6), pp. 883-899 (1992).

35 Zhu, Q., Guebelle, P. H., Li, M., and Tucker III, L., "Dimensional Accuracy of Thermoset Composites: Simulation of Process-Induced Residual Stresses", *Journal of Composites Materials*, Vol. 35, pp. 2171-2225 (2001).

36 Weitsman, Y., "Residual thermal stresses due to cool-down of epoxy-resin composites", *Journal of Applied Mechanics*, Vol. 46 (3), pp.563-567 (1979).

37 Harper, B. D., and Weitsman, Y., "Residual thermal stresses in an unsymmetrical cross-ply graphite/epoxy laminate", *Proceedings of 22nd AIAA/ASME/ASCE/AHS Structures, Structural Dynamics and Materials Conference*, Atlanta, GA, pp. 325-332 (1981).

38 White, S. R. and Hahn, H. T., "Process modeling of composite materials: Residual stress development during cure. I. Model formulation", *Journal of Composites Materials*, Vol. 26 (16), pp. 2402-2422 (1992).

39 White, S. R. and Hahn, H. T., “Process modeling of composite materials: residual stress development during cure. II. Experimental validation. *J. of Composites Materials*, Vol. 26 (16), pp. 2423-2453 (1992).

40 Lee, S., and Sohn, Y. S., “Viscoelastic analysis of residual stresses in a unidirectional laminate”, *Structures and Engineering Mechanics*, Vol. 2(4), pp. 383-393 (1994).

41 Bogetti, T.A., and Gillespie Jr., J. W., “Process-induced stress and deformation in thick-section thermoset composite laminates”, *Journal of Composites Materials*, Vol. 26 (5), pp. 626-660 (1992).

42 Eom, Y., Boogh, L., and Michaud, V., “Time-cure-temperature superposition for the prediction of instantaneous viscoelastic properties during cure”, *Polymer Engineering and Science*, Vol. 40 (6), pp. 1281-1292 (2000).

43 Simon, S.L., McKenna, G.B., Sindt, O., “Modeling the evolution of the dynamic mechanical properties of a commercial epoxy during cure after gelation”, *Journal of Applied Polymer and Science*, Vol. 76 (4), pp.495-508 (2000).

44 O’Brien, D., Mather, P.T., White, S.R., “Viscoelastic properties of an epoxy resin during cure”, *Journal of Composites Materials*, Vol. 35 (10), pp. 883-904 (2001).

45 Rebeire, J. L., Gamby, D., “A criterion for modeling, initiation and propagation of matrix cracking and delamination in cross-ply laminates”, *Composites Science and Technology*, Vol. 64, pp. 2239-2250 (2004).

46 Nairn. J., “Fracture mechanics of composite with residual stresses, imperfect interfaces, and traction-loaded cracks”, *Composites Science and Technology*, Vol. 61, pp. 2159-2167 (2001).

47 Lim, S-H., and Li, S., “Energy release rates for transverse cracking and delaminations induced by transverse cracks in laminated composites”, *Composites: Part A*, Vol. 36, pp. 1467-1476 (2005).

48 Garrett, K. W., and Bailey, J. E., “Multiple transverse failure in 90° cross-ply laminate of a glass fiber reinforced polyester”, *Journal of Material Science*, Vol. 12, pp. 157-68 (1977).

49 Bader, M. G., Bailey, J. E., Curtis P. T., and Parvizi A., “Mechanisms of initiation and development of damage in multi-axial fibre-reinforced plastics laminates” *in Proceedings of International Conference on Mechanical Behavior of Materials*, Cambridge, UK, pp. 227-239 (1979).

50 Parvizi, A., Garret K, Bailey J. E., "Constrained cracking in glass fibre-reinforced epoxy cross-ply laminates", *Journal of Material Science*, Vol. 13, pp. 195-201 (1978).

51 Bailey, J. E., Curtis, P. T., Parvizi, A., “On the transverse cracking and longitudinal splitting behavior of glass and carbon fiber reinforced epoxy cross ply laminates and the effect of Poisson and thermally generated strain”, *Proceedings of The Royal Society of London, Series A: Mathematical and Physical Science*s, Vol. 366 pp. 599-623 (1979).

52 Bailey, J. E, and Parvizi, A. “On fiber debonding effects and the mechanism of transverse-ply failure in cross-ply laminates of glass fiber/thermoset composites”, *Journal of Materials Science*, Vol. 16 (3), pp. 649-659 (1981).

53 Jones, R., Wheatley, A. R., and Bailey, J. E., “Composite Structures”, edition I., H. Marshall, Applied Science Publishers, Barking, UK, pp. 415-429 (1981).

54 Takeda, N., and Ogihara, S., “Initiation and growth of delamination from the tips of cracks in CFRO cross-ply laminates”, *Composite Science and Technology*, Vol. 52 (3), pp. 309-318 (1994).

55 Wang, A. S. D. and Law, C.E., “An energy method for multiple transverse cracks in graphite epoxy laminates”, *TRRL Supplementary Report*, pp. 17-29 (1979).

56 Wang, A. S. D., Crossman, F.W., “Some new results on edge effects in symmetric composite laminates”, *Journal of Composite Materials*, Vol. 11, pp. 92-106 (1977).

57 Highsmith, AL and Reifsnider, KL, "Stiffness Reduction Mechanisms in Composites," Damage in Composite Materials, ASTM STP 775, ASTM, Philadelphia, pp.103-117 (1982).

58 Nairn, J., Hu. S., “The formation and effect of outer-ply microcracks in cross-ply laminates, a variational approach”, *Engineering Fracture Mechanics*, Vol. 41 (3), pp. 203-221 (1992).

59 Fan, J. and Zhang, J., “In-situ damage evolution and micro/macro transition for laminated composites”, *Composites Science and Technology*, Vol. 47. pp. 107-118 (1992).

60 Kashtalyan, M., Soutis, C., “Stiffness degradation in cross ply laminates damaged by transverse cracking and splitting”, *Composites, Part A*, Vol. 31, pp. 335-351 (1999).

61 Kashtalyan, M., Soutis, C., “The effect of delamination induced by transverse cracks and splits on stiffness properties of composite laminates”, *Composites, Part A*, Vol. 31, pp. 107-119 (2000).

62 Hinton, M. J., Kaddour, A. S., Soden, P. D., “A comparison of the predictive capabilities of current failure theories of composite laminates, judged against experimental evidence”, *Composites Science and Technology*, Vol, 62, pp. 1725-1797 (2002).

63 Hinton, M. J., Kaddour, A. S., Soden, P. D., "A further assessment of the predictive capabilities of current failure theories for composite laminates: comparison with experimental evidence", *Composites Science and Technology*, Vol. 64, pp. 549-588 (2004).

64 Kumar, R. S. and Talreja, R., "A continuum damage model for linear viscoelastic composite materials", *Mechanics of Materials*, Vol. 35, pp. 463-480 (2003).

65 Herakovich, C. T., "Mechanics of Fibrous Composites", *John Wiley and Sons*, New York, pp. 332 (1998).

66 McCartney, L. N., "Physically based damage models for laminated composites", *Proceedings of the Institution of Mechanical Engineers, Part L (Journal of Materials: Design and Applications)*, Vol. 217 (Part I), pp. 163-199 (2003).

67 Lee, J. W., Daniel, I. M. "Progressive transverse cracking of cross-ply composite laminates", *Journal of Composite Materials*, Vol. 24, pp. 1225-43 (1990).

68 Daniel, I. M., Tsai, C., "Analytical/experimental study of cracking in composite laminates under biaxial loading", *Composites Engineering*, Vol. 1, pp. 355-359 (1991).

69 Hashin, Z., "Analysis of cracked laminate: a variational approach", *Mechanics of Materials*, Vol. 4, pp. 121–36 (1985).

70 Nairn, J., "The strain energy release rate of composite microcracking: A variational approach", *Journal of Composite materials*, Vol. 23, pp. 1106-1129 (1989).

71 Cox, C. L., "The elasticity and strength of paper and other fibrous materials", *British Journal of Applied Physics*, Vol. 3 (3), pp. 72-79 (1952).

72 Nuismer, R. J., Tan, S. C., "Constitutive relations of a cracked composite lamina", *Journal of Composite Materials*, Vol. 22(4), pp.306-21 (1988).

73 Laws, N., and Dvorak, G., "Progressive transverse cracking in composite laminates", *Journal of Composite Materials*, Vol. 22, pp. 900-916 (1988).

74 McCartney, L. N., "Theory of stress transfer in a cross-ply laminate containing a parallel array of transverse cracks", *Journal of the Mechanics and Physics of Solids*, Vol. 40 (1), pp. 27-68 (1992).

75 Flaggs, D. L., "Prediction of tensile matrix failure in composite laminates", *Journal of Composite Materials* Vol. 19 (1), pp. 29–50 (1985).

76 Han, Y. M., Hahn, H.T., "Ply cracking and property degradations of symmetric balanced laminates under general in plane loading", *Composites Science Technology*, Vol. 35(4), pp. 377–97 (1989).

77 Fukunaga, H., Cho, T. W., Peters, P. W. M. and Schulte, K., "Probabilistic failure strength analysis of graphite/epoxy cross-ply laminates", *Composites Science Technology*, Vol. 18, pp. 339-356 (1984).

78 Lim, G. and Hong, C. S., "Prediction of transverse cracking and stiffness reduction in cross-ply laminated composites", *J. of Composite Materials*, Vol. 23, pp. 695-713 (1989).

79 Lu, X., and Liu, D., "Interlayer shear slip theory for cross-ply laminates with nonrigid interfaces", *AIAA J.*, Vol. 30, No. 4, pp. 1063-1073 (1992).

80 Berthelot J M. "Analysis of the transverse cracking of cross ply laminates; a generalized approach" *Journal of Composite Materials*, Vol. 31(18), pp. 1780–805 (1997).

81 Kashtalyan, M., Soutis, C., "Modeling stiffness degradation due to matrix cracking in angleply composite laminates", *Plastics, Rubber and Composites*, Vol. 29 (9), pp. 482-488 (2000).

82 Henaff-Gardin, C., Lafarie-Frenot, M. C., Gamby, D., "Doubly period matrix cracking in composite laminates Part 1: general in-plane loading", *Composite Structures*", Vol. 36, pp. 113–130 (1996).

83 Hashin, Z., "Finite thermoelastic fracture criterion with application to laminate cracking analysis", *Journal of the Mechanics and Physics of Solids*, Vol. 44, pp. 1129-1145 (1996).

84 Lanczos, C., "The variational principles of mechanics", *University of Toronto press*, Fourth edition, (1962).

85 Varna, J., and Berglund, L., "Multiple transverse cracking and stiffness reduction in cross-ply laminates", *Journal of Composites Research and Science*, Vol. 13 (2), pp. 92-106 (1991).

86 Anderssen, R., Gradin, P.A. and Gustafson, C.G., "Prediction of the stiffness degradation in cross-ply laminates due to transverse matrix-cracking: An energy method approach", *Advanced Composite Materials*, Vol. 7 (4), pp. 325–346. (1998).

87 Zhang, H., Minnetyan, L. "Prediction of Effective Stiffness in $[\theta_m/90_n]_s$ Laminates due to Transverse Cracking", *Journal of Composite Materials*, Vol. 41, pp. 81-109 (2007).

88 Farge, L., Varna, J., Ayadi, Z., "Damage characterization of a cross-ply carbon fiber/epoxy laminate by an optical measurement of the displacement field", *Composites Science and Technology*, Vol. 70, pp. 94–101 (2010).

89 Vinogradov, V., Hashin, Z., "Variational analysis of cracked angle-ply laminates", *Composites Science and Technology*, Vol. 70, pp. 638–646 (2010).

90 Nairn, J., and Hu, S., and Bark, J., "A critical evaluation of theories for predicting microcracking in composite materials", *Journal of Materials and Science*, Vol. 28, pp. 5099-5111 (1993).

91 Peters, P. W. M., "The strength distribution of 90◦ plies in 0/90/0 graphite-epoxy laminates", *Journal of Composite Materials*, Vol. 18(6), pp. 545–556 (1984).

92 Flaggs D. L., Kural M. H., "Experimental determination of the in situ transverse laminate strength in graphite/epoxy laminates", *Journal of Composite Materials*, Vol. 16, pp. 103-116 (1982).

93 Fukunaga, H., Chou, T.W., Peters, P.W.M., and Schulte, K., "Probabilistic failure strength analyses of graphite/epoxy cross-ply laminates", *Journal of Composite Materials*, Vol. 18, pp. 339 – 356 (1984).

94 Dillard, D. A., Morris, D H, Brinson, H F., "A numerical procedure for predicting creep and delayed failures in laminated composites", *Long Term Behaviour of Composites, ASTM STP 813,*Philadelphia, pp. 23-27 (1983).

95 Moore, R. H., Dillard, D. A., "Time-dependent matrix cracking in cross-ply laminates", *Composite Science and Technology*, Vol. 39, pp. 1-12 (1990).

96 Nguyen, H., and Gamby, D., "Effects of nonlinear viscoelastic behaviour and loading rate on transverse cracking in CFRP laminates", *Composite Science and Technology*, Vol. 67, pp. 438–452 (2007).

97 Schapery, R. A., "On the characterization of nonlinear viscoelastic materials", *Polymer Engineering and Science*, Vol. 9 (4), pp. 295-310 (1969).

98 Schapery, R. A., "Nonlinear viscoelastic and viscoplastic constitutive equations with growing damage", *International Journal of Fracture*, Vol. 97, pp. 33-66 (1999).

99 Schapery, R. A., "Homogenized constitutive equations for linear viscoelastic unidirectional composites with growing transverse cracks" *Mechanics of Time-dependent Materials*, Vol. 6, pp. 101-131 (2002).

100 Ahci, E., and Talreja, R., "Characterization of viscoelasticity and damage in high temperature polymer matrix composites", *Journal of Composite Science and Technology*, Vol. 66, pp. 2506-2519 (2006).

101 Gupta, A., Raghavan, J., "Creep of plain weave polymer matrix composites under on-axis and off-axis loading", *Composites Part A*, Vol. 41 (9), pp. 1289-1300 (2010).

102 Ogi, K. and Takao, Y., "Modeling of time-dependent behavior of deformation and transverse cracking in cross-ply laminates", *Advanced Composite Materials*, Vol. 10, pp. 39-62 (2001).

103 Ogi, K. and Kim, H. S., "Creep deformation of a cross-ply laminate with constant transverse crack density", *Materials Science Research International, Special Technical Publication-2*, pp. 261-265 (2001).

104 Ogi, K. and Smith, P. A., "Modeling creep and recovery behavior of a quasi-isotropic laminate with transverse cracking", *Advanced Composite Materials*, Vol. 11, pp. 81-93 (2002).

105 Akshantala, N. V., and Brinson, L. C., "A damage evolution model for viscoelastic composite laminates", *Journal of composites Technology and Research*, Vol. 23 (1), pp. 3-14 (2001).

106 Raghavan, J., "Fracture Criteria to Predict Creep Rupture of Polymer Composites", *Trends in Polymer Science*, Vol. 5, pp. 5:116-22 (1997).

107 Raghavan, J., and Meshii, M., "Creep rupture of polymer composites", *Composite Science and Technology*, Vol. 57, pp. 1673-1688 (1997).

108 Washizu, K., "Variational methods in elasticity and plasticity", *Pergamon Press*, Oxford-New York (1975).

109 Mura, T., Koya, T., "Variational methods in mechanics", *Oxford university press*, New York (1992).

110 Raghavan, J., and Meshii, M., "Prediction of creep rupture of unidirectional carbon fiber reinforced polymer composite", *Materials Science and Engineering*, Vol. 197, pp. 237-249 (1995).

111 Raghavan, J., and Meshii, M., "Creep of polymer composites", *Composite Science and Technology*, Vol. 57, pp. 1673-1688 (1997).

112 Raghavan, J., and Meshii, M., "Activation theory for creep of matrix resin and carbon fiber-reinforced polymer composites", *Journal of Materials Science*, Vol. 29, pp. 5078-5084 (1994).

113 Jayaraman, R., "Creep and creep rupture of carbon fiber reinforced polymer composite", *Ph.D. Thesis, Evanston, IL, USA*; Northwestern University (1994).

114 Standard test methods for density and specific gravity (relative density) of plastics by displacement, *ASTM D 792-00*, v08.01, 2001.

115 http://www.mathworks.com/help/matlab/ref/bvp4c.html

APPENDIX A. LAMINATION THEORY

A-1 Lamination theory

The fiber orientation in each layer, with respect to loading direction x shown in Figure 3-1 (b), is normally varied to obtain desired properties. The coordinate system convention used for the lamina (i.e. ply) is illustrated in Figure 3-1 (b) as well. 1-2-3 corresponds to the principal coordinate system of the ply, wherein 1 coincides with the longitudinal axis of the fiber, and 2 & 3 correspond to axes oriented perpendicular to the fiber axis. x-y-z is the global coordinate system. θ is the angle of orientation of the fibers in a lamina with respect to the loading (global) x-axis.

A multidirectional composite made using tape lamina is referred to as "multidirectional non-woven composite/ laminate $[\theta_m/\delta_n]_{s,"}$ as shown in Figure 1-1, while a multidirectional composite made of fabric lamina is referred to as "multidirectional woven composite/laminate $[\theta_m, (\theta+90)_m/ \delta_n, (\delta_n+90)_n]_{s,"}$ as shown in Figure 1-1. The subscript "s" corresponds to "symmetric" and θ and δ are in the range of 0 to 90°. Also, "m, n" are the number of the plies. A symmetric laminate is one in which the laminate layup sequence on one side of a reference plane is a mirror image of the laminate layup sequence on the other side. In other words, for each lamina layer on one side of the reference plane, there is a corresponding lamina layer on the other side at equal distance from the reference plane with identical thickness, orientation and properties. For example, $[0/90]_s$ corresponds to [0/90/90/0].

Since a single lamina (tape or fabric) is difficult to test, normally a laminate made up of several laminas with same fiber orientation in all layers (known as a unidirectional laminate $[\theta]_n$) is manufactured and tested to measure the properties of a lamina. A thin unidirectional lamina is

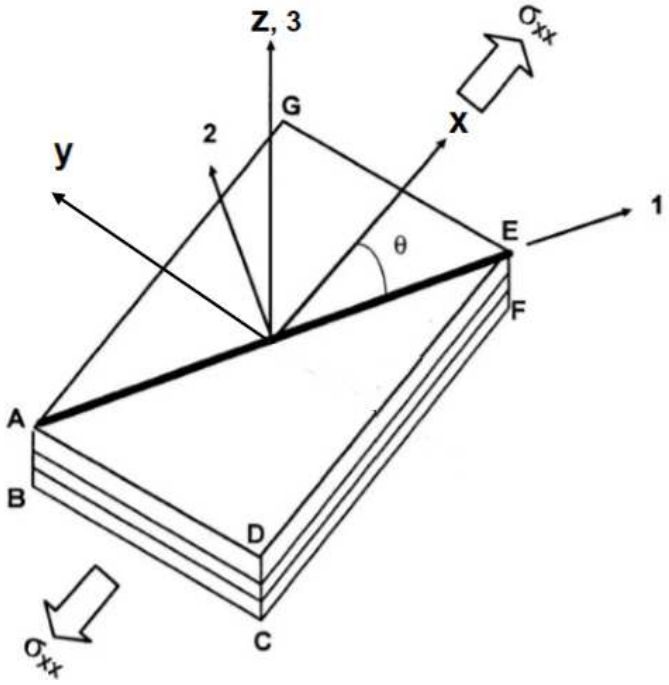

Figure 2-1: Laminate coordinate system [1]

assumed to be under a state of plane stress. The in-plane stress and strain components are related to each other by compliance (or stiffness) along the principal axes of the material, as follows:

$$\begin{bmatrix} \varepsilon_{11} \\ \varepsilon_{22} \\ \gamma_{66} \end{bmatrix} = \begin{bmatrix} S_{11} & S_{12} & 0 \\ S_{12} & S_{22} & 0 \\ 0 & 0 & S_{66} \end{bmatrix} \begin{bmatrix} \sigma_{11} \\ \sigma_{22} \\ \tau_{66} \end{bmatrix} \tag{A-1}$$

or

$$\begin{bmatrix} \sigma_{11} \\ \sigma_{22} \\ \tau_{66} \end{bmatrix} = \begin{bmatrix} Q_{11} & Q_{12} & 0 \\ Q_{12} & Q_{22} & 0 \\ 0 & 0 & Q_{66} \end{bmatrix} \begin{bmatrix} \varepsilon_{11} \\ \varepsilon_{22} \\ \gamma_{66} \end{bmatrix} \tag{A-2}$$

where σ_{11} and ε_{11} are longitudinal stress and strain (along the fiber direction), σ_{22} and ε_{22} are transverse stress and strain (perpendicular to fiber), and τ_{66} and γ_{66} are shear stress and strain. S_{11}, S_{22}, and S_{66} are longitudinal, transverse, and shear compliances respectively. S_{12} is the compliance which relates longitudinal/transverse loading to transverse/longitudinal deformation. Q_{11}, Q_{22}, and Q_{66} are longitudinal, transverse, and shear stiffness, respectively. Similar to S_{12}, Q_{12} is a stiffness term to relate the longitudinal/transverse loading to transverse/longitudinal deformation.

Thus, a unidirectional lamina can be fully characterized by four independent compliance constants. Compliances can be expressed in terms of engineering constants, as follows:

$$S_{11} = \frac{1}{E_{11}} \qquad S_{22} = \frac{1}{E_{22}} \qquad S_{12} = \frac{\nu_{12}}{E_{11}} = -\frac{\nu_{21}}{E_{22}} \qquad S_{66} = \frac{1}{G_{12}} \tag{A-3}$$

where E_{11}, E_{22}, G_{12}, and ν_{12} are axial, transverse, shear moduli, and major Poisson's ratio, respectively.

The engineering constants are experimentally determined from uniaxial tests (tension, compression or shear tests) on specimens cut parallel ([0]) and perpendicular ([90]) to the fiber direction of a unidirectional composite, respectively. E_{11} and E_{22} are determined using [0] and

[90] specimens respectively. E_{12} can be determined using either specimen by generating additional strain data along the direction transverse to the loading axis. G_{12} is determined typically using either torsional testing of a [0] specimen or tensile testing of an off-axis specimen (e.g. [+45]). There are other test methods such as rail-shear test.

The classical lamination theory is used to predict the overall behaviour of a multidirectional composite laminate as a function of the properties and stacking sequence of the individual layers. Consider an individual layer k in a multidirectional laminate whose mid-plane is at a distance of z_k from the laminate reference plane, as shown in Figure A-1. The stress-strain relationship for this layer in the global coordinates, in terms of its properties along principal coordinates, can be determined using

$$\begin{bmatrix} \sigma_{xx} \\ \sigma_{yy} \\ \sigma_{xy} \end{bmatrix}^{(k)} = \begin{bmatrix} Q_{xx} & Q_{xy} & Q_{xs} \\ Q_{xy} & Q_{yy} & Q_{ys} \\ Q_{xs} & Q_{ys} & Q_{ss} \end{bmatrix}^{(k)} \begin{bmatrix} \varepsilon_{xx} \\ \varepsilon_{yy} \\ \gamma_{xy} \end{bmatrix}^{(k)} \tag{A-4}$$

Equation (A-4) can be rewritten in terms of compliance as well.

$$\begin{bmatrix} \varepsilon_{xx} \\ \varepsilon_{yy} \\ \gamma_{xy} \end{bmatrix}^{(k)} = \begin{bmatrix} S_{xx} & S_{xy} & S_{xs} \\ S_{xy} & S_{yy} & S_{ys} \\ S_{xs} & S_{ys} & S_{ss} \end{bmatrix}^{(k)} \begin{bmatrix} \sigma_{xx} \\ \sigma_{yy} \\ \tau_{xy} \end{bmatrix}^{(k)} \tag{A-5}$$

The strain at any point in the laminate is related to the reference plane strain and the laminate curvature as per equation (A-6)

$$\begin{bmatrix} \varepsilon_{xx} \\ \varepsilon_{yy} \\ \gamma_{xy} \end{bmatrix} = \begin{bmatrix} \varepsilon_{xx}^{0} \\ \varepsilon_{yy}^{0} \\ \gamma_{xy}^{0} \end{bmatrix} + z \begin{bmatrix} \kappa_{xx} \\ \kappa_{yy} \\ \kappa_{xy} \end{bmatrix} \tag{A-6}$$

where ε_{jl}, ε_{jl}^{0}, and κ_{jl} (j, l=x,y,z) are total laminate strain, reference plane strain and laminate curvature with respect to global coordinate axes. Substituting equation (A-6) into

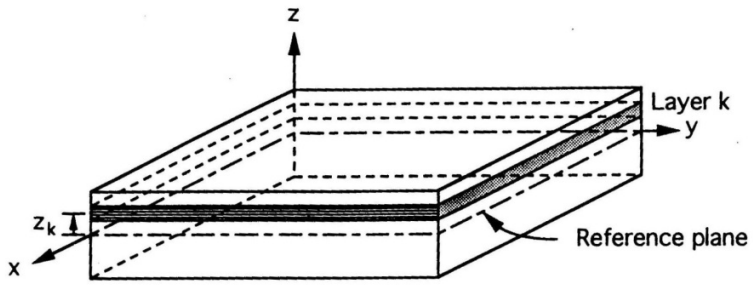

Figure A-1: Layer k in a multidirectional laminate [6]

equation (A-4),results in equation (A-7) for each layer.

$$\begin{bmatrix}\sigma_{xx}\\ \sigma_{yy}\\ \tau_{xy}\end{bmatrix}^{(k)} = \begin{bmatrix}Q_{xx} & Q_{xy} & Q_{xs}\\ Q_{xy} & Q_{yy} & Q_{ys}\\ Q_{xs} & Q_{ys} & Q_{ss}\end{bmatrix}^{(k)}\begin{bmatrix}\varepsilon^0_{xx}\\ \varepsilon^0_{yy}\\ \gamma^0_{xy}\end{bmatrix} + z\begin{bmatrix}Q_{xx} & Q_{xy} & Q_{xs}\\ Q_{xy} & Q_{yy} & Q_{ys}\\ Q_{xs} & Q_{ys} & Q_{ss}\end{bmatrix}^{(k)}\begin{bmatrix}\kappa_{xx}\\ \kappa_{yy}\\ \kappa_{xy}\end{bmatrix} \tag{A-7}$$

Since the stresses in each layer are not the same, it is more convenient to deal with stresses of the laminate. Thus, for n-ply laminate the force and moment resultants can be written in the following form:

$$\begin{bmatrix}N_{xx}\\ N_{yy}\\ N_{xy}\end{bmatrix} = \sum_{k=1}^{n}\left\{\begin{bmatrix}Q_{xx} & Q_{xy} & Q_{xs}\\ Q_{xy} & Q_{yy} & Q_{ys}\\ Q_{xs} & Q_{ys} & Q_{ss}\end{bmatrix}_k\begin{bmatrix}\varepsilon^0_{xx}\\ \varepsilon^0_{yy}\\ \gamma^0_{xy}\end{bmatrix}\int_{h_{k-1}}^{h_k} dz + z\begin{bmatrix}Q_{xx} & Q_{xy} & Q_{xs}\\ Q_{xy} & Q_{yy} & Q_{ys}\\ Q_{xs} & Q_{ys} & Q_{ss}\end{bmatrix}_k\begin{bmatrix}\kappa_{xx}\\ \kappa_{yy}\\ \kappa_{xy}\end{bmatrix}\int_{h_{k-1}}^{h_k} z dz\right\} \tag{A-8}$$

$$\begin{bmatrix}M_{xx}\\ M_{yy}\\ M_{xy}\end{bmatrix} = \sum_{k=1}^{n}\left\{\begin{bmatrix}Q_{xx} & Q_{xy} & Q_{xs}\\ Q_{xy} & Q_{yy} & Q_{ys}\\ Q_{xs} & Q_{ys} & Q_{ss}\end{bmatrix}_k\begin{bmatrix}\varepsilon^0_{xx}\\ \varepsilon^0_{yy}\\ \gamma^0_{xy}\end{bmatrix}\int_{h_{k-1}}^{h_k} z dz + z\begin{bmatrix}Q_{xx} & Q_{xy} & Q_{xs}\\ Q_{xy} & Q_{yy} & Q_{ys}\\ Q_{xs} & Q_{ys} & Q_{ss}\end{bmatrix}_k\begin{bmatrix}\kappa_{xx}\\ \kappa_{yy}\\ \kappa_{xy}\end{bmatrix}\int_{h_{k-1}}^{h_k} z^2 dz\right\} \tag{A-9}$$

where $[N]_{x,y}$ and $[M]_{x,y}$ are force and moment resultants for the laminate. In equations (A-8) and (A-9), since in-plane strains, $[\varepsilon^0]_{x,y}$ and curvatures, $[\kappa]_{x,y}$ are not functions of z, they can be taken out of the integration. Thus, the equation (A-8) and equation (A-9) can be rewritten in the form of equations (A-10) and (A-11):

$$\begin{aligned}[N]_{x,y} &= \left[\sum_{k=1}^{n}[Q]^k_{x,y}\int_{h_{k-1}}^{h_k} dz\right]\left[\varepsilon^0\right]_{x,y} + \left[\sum_{k=1}^{n}[Q]^k_{x,y}\int_{h_{k-1}}^{h_k} z dz\right][\kappa]_{x,y}\\ &= \left[\sum_{k=1}^{n}[Q]^k_{x,y}(h_k - h_{k-1})\right]\left[\varepsilon^0\right]_{x,y} + \left[\frac{1}{2}\sum_{k=1}^{n}[Q]^k_{x,y}(h_k^2 - h_{k-1}^2)\right][\kappa]_{x,y}\\ &= [A]_{x,y}\left[\varepsilon^0\right]_{x,y} + [B]_{x,y}[\kappa]_{x,y}\end{aligned} \tag{A-10}$$

$$\begin{aligned}[M]_{x,y} &= \left[\frac{1}{2}\sum_{k=1}^{n}[Q]^k_{x,y}(h_k^2 - h_{k-1}^2)\right]\left[\varepsilon^0\right]_{x,y} + \left[\frac{1}{3}\sum_{k=1}^{n}[Q]^k_{x,y}(h_k^3 - h_{k-1}^3)\right][\kappa]_{x,y}\\ &= [B]_{x,y}\left[\varepsilon^0\right]_{x,y} + [D]_{x,y}[\kappa]_{x,y}\end{aligned} \tag{A-11}$$

where

$$A_{jl} = \sum_{k=1}^{n} [Q]_{x,y}^{k} (h_k - h_{k-1})$$
$$B_{jl} = \frac{1}{2} \sum_{k=1}^{n} [Q]_{x,y}^{k} (h_k^2 - h_{k-1}^2) \quad \text{(A-12)}$$
$$D_{jl} = \frac{1}{3} \sum_{k=1}^{n} [Q]_{x,y}^{k} (h_k^3 - h_{k-1}^3)$$

and j, l = x, y. In other words, the relationship between force and moment resultants for the laminate and the reference plane strains and curvatures can be written in the form of equation (A-13).

$$\begin{bmatrix} N \\ \cdots \\ M \end{bmatrix} = \begin{bmatrix} A & B \\ \cdots\cdots & \\ B & D \end{bmatrix} \begin{bmatrix} \varepsilon^0 \\ \cdots \\ \kappa \end{bmatrix} \quad \text{(A-13)}$$

Here, [A], [B] and [D] are laminate stiffness matrices. Equation (A-13) can be inverted to determine laminate strain and curvature in response to applied load and moment:

$$\begin{bmatrix} \varepsilon^0 \\ \cdots \\ \kappa \end{bmatrix} = \begin{bmatrix} a & b \\ \cdots\cdots & \\ c & d \end{bmatrix} \begin{bmatrix} N \\ \cdots \\ M \end{bmatrix} \quad \text{(A-14)}$$

where [a], [b], [c], and [d] are laminate compliance matrices and obtained from stiffness matrices, as follows:

$$[a] = [A^{-1}] - \{[B^*][D^{*-1}]\}[C^*]$$
$$[b] = [B^*][D^{*-1}] \quad \text{(A-15)}$$
$$[c] = [-D^{*-1}][C^*]$$
$$[d] = [D^{*-1}]$$

where

$$
\begin{aligned}
&[A^{-1}] = inverse\ of\ \ matrix\,[A] \\
&[B^*] = -[A^{-1}][B] \\
&[C^*] = [B][A^{-1}] \\
&[D^*] = [D] - \{[B][A^{-1}]\}[B]
\end{aligned}
\tag{A-16}
$$

The strain-force relation for the laminate can be written in terms of engineering constants as follows:

$$
\begin{bmatrix} \varepsilon_{xx}^0 \\ \varepsilon_{yy}^0 \\ \gamma_{xy}^0 \end{bmatrix} = \begin{bmatrix} \frac{1}{\bar{E}_{xx}} & \frac{-\bar{\nu}_{yx}}{\bar{E}_{yy}} & \frac{\bar{\eta}_{sx}}{\bar{G}_{xy}} \\ \frac{-\bar{\nu}_{xy}}{\bar{E}_{xx}} & \frac{1}{\bar{E}_{yy}} & \frac{\bar{\eta}_{sy}}{\bar{G}_{xy}} \\ \frac{\bar{\eta}_{xs}}{\bar{E}_{xx}} & \frac{\bar{\eta}_{ys}}{\bar{E}_{yy}} & \frac{1}{\bar{G}_{xy}} \end{bmatrix} \begin{bmatrix} N_{xx} \\ N_{yy} \\ N_{xy} \end{bmatrix} \frac{1}{h}
\tag{A-17}
$$

where

$\bar{E}_{xx}, \bar{E}_{yy}$= Effective Young's moduli of the laminate in the x and y directions, respectively;

$\bar{\nu}_{xy}$, $\bar{\nu}_{yx}$ =Effective Poisson's ratios of the laminate;

$\bar{\eta}_{xs}, \bar{\eta}_{ys}, \bar{\eta}_{sx}, \bar{\eta}_{sy}$ =Effective shear coupling coefficients of the laminate;

The laminate's effective moduli and Poisson's ratio can be obtained from compliance matrices, as follows.

$$
\begin{aligned}
&\bar{E}_{xx} = \frac{1}{h\,a_{xx}}, \qquad \bar{E}_{yy} = \frac{1}{h\,a_{yy}}, \qquad \bar{G}_{xy} = \frac{1}{h\,a_{ss}} \\
&\bar{\nu}_{xy} = -\frac{a_{yx}}{a_{xx}}, \qquad \bar{\nu}_{yx} = -\frac{a_{xy}}{a_{yy}}, \qquad \bar{\eta}_{sx} = \frac{a_{xs}}{a_{ss}} \\
&\bar{\eta}_{xs} = \frac{a_{sx}}{a_{xx}}, \qquad \bar{\eta}_{ys} = \frac{a_{sy}}{a_{yy}}, \qquad \bar{\eta}_{sy} = \frac{a_{ys}}{a_{ss}}
\end{aligned}
\tag{A-18}
$$

This lamination theory, represented by equation (A-14), has been adapted and used in this thesis.

APPENDIX B. EULER-LAGRANAGE EQUATIONS' CONSTANTS

$$A_1 = \frac{94th^5}{15E_{yy}^{(90)}}$$

$$A_2 = \frac{-20\nu_{xy}^{(90)}th^3}{15E_{yy}^{(90)}} - \frac{8th^3}{13G_{xy}^{(90)}}$$

$$A_3 = \frac{2th}{E_{xx}^{(90)}}$$

$$A_4 = \frac{5th^5}{5E_{yy}^{(90)}}$$

$$A_5 = \frac{-3\nu_{xy}^{(90)}th^3}{E_{xx}^{(90)}}$$

$$A_6 = \frac{-10\nu_{yz}^{(90)}th^3}{E_{yy}^{(90)}}$$

$$A_7 = \frac{-2\nu_{xy}^{(90)}th}{E_{yy}^{(90)}}$$

$$A_8 = \frac{2th}{E_{yy}^{(90)}}$$

$$A_9 = \frac{9th^5}{2E_{yy}^{(90)}} - \frac{th^5}{20E_{yy}^{(-\theta)}}$$

$$A_{10} = \frac{-th^3}{3G_{xy}^{(-\theta)}} - \frac{\nu_{xy}^{(-\theta)}th^3}{3E_{xx}^{(-\theta)}}$$

$$A_{11} = \frac{th}{E_{xx}^{(-\theta)}}$$

$$A_{12} = \frac{5th^5}{24E_{yy}^{(-\theta)}}$$

$$A_{13} = \frac{-th^3}{2G_{xy}^{(-\theta)}} - \frac{\nu_{xy}^{(-\theta)}th^3}{E_{xx}^{(-\theta)}}$$

$$A_{14} = \frac{5th^5}{E_{yy}^{(\theta)}}$$

$$A_{15} = \frac{\nu_{yz}^{(-\theta)}th^3}{6E_{yy}^{(-\theta)}}$$

$$A_{16} = \frac{-\nu_{xy}^{(-\theta)}th}{E_{xx}^{(-\theta)}}$$

$$A_{17} = \frac{-3\nu_{yz}^{(90)}th^3}{E_{yy}^{(90)}}$$

$$A_{18} = \frac{th}{E_{yy}^{(-\theta)}}$$

$$A_{19} = \frac{13th^5}{12E_{yy}^{(-\theta)}} + \frac{th^5}{10E_{yy}^{(\theta)}}$$

$$A_{20} = \frac{-\nu_{xy}^{(\theta)}th^3}{3E_x^{(\theta)}} - \frac{th^3}{3G_{xy}^{(\theta)}} - \frac{th^3}{G_{xy}^{(-\theta)}}$$

$$A_{21} = \frac{th}{E_{xx}^{(\theta)}}$$

$$A_{22} = \frac{-\nu_{yz}^{(\theta)}th^3}{6E_{yy}^{(\theta)}}$$

$$A_{23} = \frac{-\nu_{xy}^{(\theta)}th}{E_{xx}^{(\theta)}}$$

$$A_{24} = \frac{th}{E_{yy}^{(\theta)}}$$

$$A_{25} = \frac{\eta_{xs}^{(-\theta)}th}{2E_{xx}^{(-\theta)}}$$

$$A_{26} = \frac{\eta_{zs}^{(-\theta)}th}{12E_{yy}^{(-\theta)}}$$

$$A_{27} = \frac{\eta_{ys}^{(-\theta)}th}{2E_y^{(-\theta)}}$$

$$A_{28} = \frac{\eta_{zs}^{(-\theta)}th^3}{2E_{yy}^{(-\theta)}}$$

$$A_{29} = \frac{-\eta_{zs}^{(\theta)}th^3}{12E_{yy}^{(\theta)}}$$

$$A_{30} = \frac{-\eta_{xs}^{(\theta)}th}{2E_{xx}^{(\theta)}}$$

$$A_{31} = \frac{-\eta_{ys}^{(\theta)}th}{2E_{yy}^{(\theta)}}$$

$$A_{32} = \frac{-th^3}{3G_{yz}^{(-\theta)}}$$

$$A_{33} = \frac{th}{3G_{xy}^{(-\theta)}}$$

$$A_{34} = \frac{-th_3}{2G_{yz}^{(-\theta)}}$$

$$A_{35} = \frac{\eta_{xs}^{(-\theta)}th}{2E_{xx}^{(\theta)}}$$

$$A_{36} = \frac{\eta_{zs}^{(-\theta)}th}{2E_{yy}^{(-\theta)}}$$

$$A_{37} = \frac{th^3}{3G_{yz}^{(\theta)}} - \frac{th^3}{G_{yz}^{(-\theta)}}$$

$$A_{38} = \frac{-th}{G_{xy}^{(\theta)}}$$

$$A_{39} = \frac{-th^3}{2G_{yz}^{(-\theta)}}$$

$$A_{40} = \frac{\eta_{zs}^{(\theta)}th}{2E_{yy}^{(\theta)}}$$

$$A_{41} = \frac{\eta_{ys}^{(\theta)}th}{2E_{yy}^{(\theta)}}$$

$$A_{42} = \frac{\eta_{xs}^{(\theta)}th}{2E_{xx}^{(\theta)}}$$